# Applicability of Quantitative Functional MRI Techniques for Studies of Brain Function at Ultra-High Magnetic Field

Von der Fakultät für Physik und Geowissenschaften
der Universität Leipzig
genehmigte

**DISSERTATION**

zur Erlangung des akademischen Grades
doctor rerum naturalium
(Dr. rer. nat.)
vorgelegt

von Dipl. Phys. Steffen Norbert von Smuda geb. Krieger
geboren am 11.02.1985 in Frankfurt am Main, Deutschland

| | |
|---|---|
| Gutachter: | Prof. Robert Turner |
| | Prof. Fahmeed Hyder |

| | |
|---|---|
| Tag der Einreichung: | 29.10.2014 |
| Tag der Verteidigung: | 05.02.2015 |
| Tag der Verleihung: | 23.02.2015 |

# Bibliographische Beschreibung

von Smuda, Steffen Norbert

Applicability of Quantitative Functional MRI Techniques for Studies of Brain Function at Ultra-High Magnetic Field

Universität Leipzig, Dissertation
150 pages, 258 references, 51 figures, 4 tables

**Referat:**

This thesis describes the development, implementation and application of various quantitative functional magnetic resonance imaging (fMRI) approaches at ultra-high magnetic field including the assessment with regards to applicability and reproducibility.

Functional MRI (fMRI) commonly uses the blood oxygenation level dependent (BOLD) contrast to detect functionally induced changes in the oxy-deoxyhaemoglobin composition of blood which reflect cerebral neural activity. As these blood oxygenation changes do not only occur at the activation site but also downstream in the draining veins, the spatial specificity of the BOLD signal is limited. Therefore, the focus has moved towards more quantitative fMRI approaches such as arterial spin labelling (ASL), vascular space occupancy (VASO) or calibrated fMRI which measure quantifiable physiologically and physically relevant parameters such as cerebral blood flow (CBF), cerebral blood volume (CBV) or cerebral metabolic rate of oxygen ($CMRO_2$), respectively.

In this thesis a novel MRI technique was introduced which allowed the simultaneous acquisition of multiple physiological parameters in order to beneficially utilise their spatial and temporal characteristics. The advantages of ultra-high magnetic field were utilised to achieve higher signal-to-noise and contrast-to-noise ratios compared to lower field strengths. This technique was successfully used to study the spatial and temporal characteristics of CBV, CBF and BOLD in the visual cortex. This technique is the first one that allows simultaneous acquisition of CBV, CBF and BOLD weighted fMRI signals in the human brain at 7 Tesla.

Additionally, this thesis presented a calibrated fMRI technique which allowed the quantitative estimation of changes in cerebral oxygen metabolism at ultra-high field. $CMRO_2$ reflects the amount of thermodynamic work due to neural activity and is therefore a significant physical measure in neuroscience. The calibrated fMRI approach presented in this thesis was optimised for the use at ultra-high field by adjusting the MRI parameters as well as implementing a specifically designed radio-frequency (RF) pulse. A biophysical model was used to calibrate the fMRI data based on the simultaneous acquisition of BOLD and CBF weighted MRI signals during a gas-breathing challenge.

The reproducibility was assessed across multiple brain regions and compared to that of various physiologically relevant parameters. The results indicate that the degree of intra-subject variation for calibrated fMRI is lower than for the classic BOLD contrast or ASL. Consequently, calibrated fMRI is a viable alternative to classic fMRI contrasts with regards to spatial specificity as well as functional reproducibility. This calibrated fMRI approach was also compared to a novel direct calibration technique which relies on complete venous oxygenation saturation during the calibration scan via a gas-breathing challenge.

This thesis introduced several reliable quantitative fMRI approaches at 7 Tesla and the results presented are a step forward to the wider application of quantitative fMRI.

# Table of Contents

# 1 Introduction

Magnetic resonance imaging (MRI) is the currently most versatile imaging technique in the medical environment (Lauterbur, 1973). Whereas the main application is based on imaging internal structures of the body, MRI can also provide information about biological tissue composition, function, diffusion, haemodynamics and several other characteristics.

MRI is based on the phenomenon of nuclear magnetic resonance (NMR) which relies on the interaction of spin angular momentum of nuclei with external magnetic fields. Typically a static magnetic field is used to split up the Zeeman energy configurations. Transitions from one energy level to another are usually induced by external electromagnetic fields and for example relaxation effects, spin density, diffusion or perfusion are used to characterise the samples. In MRI, magnetic field gradients are utilised in at least three directions to introduce spatial encoding. Data is acquired in Fourier space and MR images are calculated via a Fourier transformation.

Functional MRI (fMRI) in the brain relies on the same physical basis as MRI but uses secondary, mostly haemodynamic, effects accompanying neuronal cerebral activity (Kim & Ogawa, 2012; Ogawa et al., 1990). Compared to structural MRI scans, functional MRI offers increased temporal but usually reduced spatial resolution. Fast image acquisition techniques are applied which can introduce noise and artefacts (Griswold et al., 2002; Mansfield, 1977). Whereas a structural MRI scan only consists of one high-resolution image, functional scans include a series of sequentially acquired images. Specifically designed functional tasks are used to modulate brain activity and induce haemodynamic changes. These changes can be detected via fMRI and therefore represent a surrogate marker of the neuronal response. Due to the simplicity of this technique and the fact that MRI scanner hardware has become more and more available around the world, fMRI has had a significant impact on neuroscience. Some of the main advantages of fMRI compared to other imaging techniques are its non-invasive nature, its minimal harmful impact on biological tissue, high spatial resolution and high coverage.

After the discovery of fMRI 20 years ago several important technological and methodological innovations have helped to push the limits of spatial and temporal resolution, increase signal-to-noise ratio (SNR) and contrast-to-noise ratio (CNR), improve spatial localisation and specificity, and simplify the use of these techniques. Some of these innovations were used in this thesis, for example: the application of ultra-high static magnetic field strength (Turner et al., 1993), strong gradients, parallel imaging (Griswold et al., 2002; Heidemann et al., 2001; Pruessmann et al., 1999), and optimised acquisition techniques (Mansfield, 1977). The main benefit of higher static magnetic

field strengths is the increase in signal per 3D pixel (voxel) due to the direct mathematical relationship of MR signal and magnetic field (Duyn, 2012). An increase in SNR allows smaller voxels or less averaging. FMRI also utilises the changes in longitudinal relaxation times that are related with increased field strengths (Yacoub et al., 2001).

Beside these theoretical advantages of ultra-high magnetic fields there are several challenges that have to be overcome in order to actually improve the image quality obtained via fMRI. The change in relaxation times is not only an advantage, but also a problem when it comes to signal acquisition. Smaller transverse relaxation times require fast readout techniques that use intelligent readout acceleration approaches. Beside that, energy deposition in tissue is a major issue at ultra-high field. Increased static magnetic fields require RF pulses with higher frequencies and therefore higher energies. MRI pulse sequences that use several RF pulses may be not applicable at ultra-high fields because of the increased heating of soft tissue. Precise safety estimations have to be performed before any novel MRI hardware or software can be used.

The currently most widely used fMRI contrast is the blood oxygenation level-dependent (BOLD) signal. BOLD signal changes can be measured via gradient-echo (GRE) or spin-echo (SE) MRI sequences. The good availability of GRE and SE approaches and high sensitivity characteristics of the BOLD contrast are the main reasons why BOLD is still the most popular fMRI contrast although there are several major issues with this technique. First, the BOLD signal originates from simultaneous changes in cerebral blood volume (CBV), cerebral blood flow (CBF) and cerebral metabolic rate of oxygen (CMRO$_2$) (Uludağ et al., 2009; Hyder et al., 2001). The complicated quantitative relationship between these parameters is not fully known yet, although there have been efforts to develop detailed biophysical models (Buxton, 2012; Mandeville et al., 1999; Hyder & Rothman, 2010). Therefore BOLD signal changes and results obtained via the BOLD technique have to be interpreted with caution (Shulman et al., 2007; Hyder & Rothman, 2011; Kida & Hyder, 2006). Furthermore, BOLD signal changes can occur at sites that are far away from the origin of neuronal activity changes. This is due to the fact that the BOLD signal relies on the oxy-deoxyhaemoglobin composition of blood which not only changes at the activation site but also downstream in the draining veins (Turner, 2002). Therefore, the spatial specificity of the BOLD contrast is limited.

Due to these drawbacks there have been efforts to develop alternative fMRI techniques that use a single physiological parameter rather than a combination of many. Arterial spin labelling (ASL) is a technique that uses spin inversion to label blood water and therefore to generate an endogenous tracer of CBF (Detre et al., 1992; Williams et al., 1993). The advantage compared to BOLD is that

changes in CBF occur mainly in the capillary and arterial vessel compartments. Therefore ASL signals provide an improved spatial specificity compared to BOLD signals (Wang et al., 2003). However, despite the theoretical advantages of ultra-high magnetic fields, the implementation and application of ASL at these field strengths is challenging. Sequence optimisations and the application of modern saturation techniques are necessary to obtain reliable ASL time series. ASL was successfully applied in this thesis and was used in all experiments that are presented.

Recently, MRI studies of human brain function have begun to investigate changes in CBV and use CBV as a marker of neuronal activity. An effective technique to measure functionally induced changes in CBV is vascular space occupancy (VASO) MRI (Lu et al., 2003). Similar to ASL, VASO relies on spin inversion but unlike ASL, VASO images are acquired at the time point when the blood signal is nulled. With this concept it is possible to measure changes in total CBV without the contribution of CBF. As the main part of functionally induced CBV changes occur in the capillary and arterial vessel compartments the spatial specificity of VASO is believed to be closer to the site of neuronal activation than BOLD.

In this thesis a novel MRI technique is presented that enables the simultaneous acquisition of CBV, CBF and BOLD weighted MRI signals at ultra-high magnetic field. The development of this sequence was based on a previously published approach at 3 Tesla (Yang et al., 2004). Simultaneous acquisition of multiple MRI parameters allows the combination of the spatial and temporal advantages of each technique (Hyder, 2009) without adding any scan time to the study. Whereas the original approach at 3 Tesla already found a series of applications (Gu et al., 2005; Lin et al., 2009; Lin et al., 2008), the optimised technique introduced in this thesis may lead to a wider range of applications by utilising the advantages that ultra-high field strengths have to offer. Simultaneously acquired quantitative physiological parameters (CBV and CBF) can be used to evaluate theoretical models of the BOLD signal, brain dynamics and brain physiology in a physical reasonable and quantitative manner.

Beside the work on the simultaneous acquisition technique, the main focus of my work was on the quantitative measurement of changes in cerebral oxygen metabolism via calibrated fMRI at ultra-high field (Davis et al., 1998). Calibrated fMRI relies on the simultaneous acquisition of BOLD and CBF weighted MRI signals during a gas-breathing challenge. A biophysical model with a set of assumptions is used to first calculate a calibration parameter and then estimate the functionally induced changes in oxygen metabolism (Hoge et al., 1999). Changes in oxygen metabolism are directly related to the amount of thermodynamic work due to neuronal activity. Consequently calibrated fMRI is temporally, spatially and physiologically closer to neuronal activation than the

BOLD contrast. Furthermore calibrated fMRI offers physiologically and physically quantifiable measures compared to BOLD signals, which are somewhat arbitrarily scaled . However, due to the greater complexity with regards to MRI and hardware setup, acquisition time and data analysis, calibrated fMRI has not yet been extensively used, especially at ultra-high magnetic fields or combined with low-contrast functional tasks such as typically used in cognitive and psychological studies. The main goal of this thesis was therefore to assess the applicability of calibrated fMRI at ultra-high field combined with low-contrast task (such as common in cognitive neuroscience). I further aimed to contribute to the improvement of the calibrated fMRI method by comprehensively assessing the technical characteristics of this approach. Finally, an alternative direct calibration technique was assessed and compared with the modelling approach (Gauthier et al., 2011).

The structure of the thesis is as follows: Chapter 2 introduces the mathematical, physical and physiological background that is necessary to understand the techniques used in the thesis. Chapter 3 describes the general experimental setup used for the studies presented. Also software developments and technical optimisations that were performed during the studies of this thesis are described. Chapters 4 and 5 are based on calibrated fMRI and chapter 6 describes the simultaneous acquisition technique. Additional information on materials and methods that were specifically used in each study can be found in these chapters. Finally, chapter 7 summarises the obtained results and provides an outlook for future research on the topics investigated in this thesis.

# 2 Background to Functional Magnetic Resonance Imaging

## *2.1 Magnetic Resonance*

### 2.1.1 Quantum Mechanics

The basic principle of nuclear magnetic resonance (NMR) and therefore magnetic resonance imaging (MRI) relies on the interaction of spin angular momenta of nuclei with external magnetic and electric fields. Most nuclei have a non-zero spin momentum $\hat{I}$ which is coupled to the magnetic momentum $\hat{\mu}$ .

$$\hat{\mu} = \gamma \hbar \hat{I} \tag{1}$$

The coupling constant $\gamma$ is the gyromagnetic ratio which is different for each nuclei. The gyromagnetic ratio is a crucial factor with regards to sensitivity of NMR and MRI experiments with the larger the constant the higher the sensitivity of the NMR and MRI experiments. The typical NMR experiment uses a static magnetic field $B_0$ with the coupling of nuclear spin and external field described via the Hamilton operator $\hat{H}$ .

$$\hat{H} = -\hat{\mu} B_0 \tag{2}$$

The direction of $B_0$ is usually referred to the z-axis of the experiment. By solving the Schrödinger equation for the specific system one obtains the Zeeman energy values which are proportional to the external magnetic field.

$$E_m = -m \gamma \hbar B_0 \tag{3}$$

For nuclei with $I = \frac{1}{2}$ (such as protons) there are two possible energy configurations:

$$m = [-\frac{1}{2}, +\frac{1}{2}] \tag{4}$$

A transition from one energy level to the other can be induced by electromagnetic waves in the radio frequency range for static magnetic field strengths up to 20 Tesla. The so-called Larmor

frequency $\omega_0$ is proportional to the static magnetic field $\boldsymbol{B_0}$.
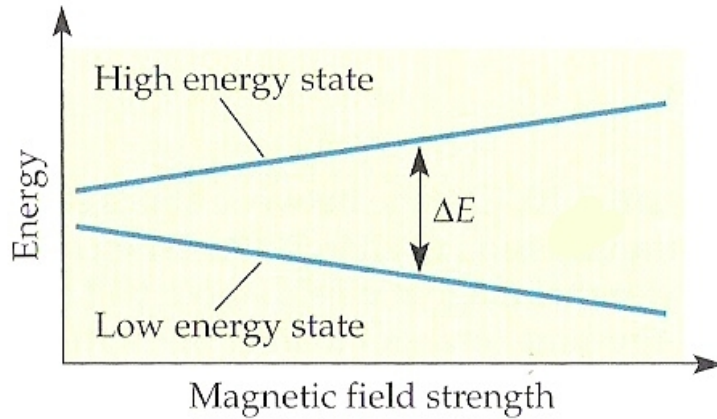


*Figure 1: The energy difference of the Hamilton eigenstates depends linearly on the static magnetic field strength. Reprint from (Huettel, 2009).*

$$\omega_0 = \gamma B_0 \tag{5}$$

The behaviour of the spin momentum $\hat{\boldsymbol{I}}$ in a time-varying magnetic field can be described as

$$\frac{d\hat{\boldsymbol{I}}}{dt} = \frac{i}{\hbar}[\hat{\boldsymbol{H}}, \hat{\boldsymbol{I}}] \tag{6}$$

The introduction of a time-dependent magnetic field $\boldsymbol{B}$ leads to the following formulation of the Hamilton operator.

$$\hat{\boldsymbol{H}} = -\gamma \hbar \boldsymbol{B} \hat{\boldsymbol{I}} \tag{7}$$

When an MRI experiment is performed, the whole probe's spin-system has to be taken into account. If the spins were evenly distributed between the two energy states, there would be no net magnetization. Fortunately, in an external magnetic field there are more parallel than anti-parallel eigenstates, and thus a net magnetization. The relative proportion of the two spin states depends on their energy difference $\Delta E = \hbar \omega_0$ (see Fig 1) and the temperature. This proportion can be expressed using Boltzmann's constant $k$ .

$$p_m = \frac{N_m}{N} \sim e^{\frac{-E_m}{kT}} \qquad (8)$$

$N_m$ describes the number of spins with eigenfunction $\Psi_m$. $N$ stands for all spins available in the spin system. This energy distribution leads to a finite expectation value of the dipole moment $\hat{\mu}$.

$$\langle \hat{\mu} \rangle = \sum_{-\frac{1}{2}}^{+\frac{1}{2}} \hat{\mu}_m \, p_m \qquad (9)$$

and the macroscopic measurable magnetisation (see Fig 2) in thermal equilibrium which is parallel to the external magnetic field $\boldsymbol{B_0}$ is

$$-\boldsymbol{M}_\infty = N \cdot \langle \hat{\bar{\mu}} \rangle \hat{e}_z \qquad (10)$$
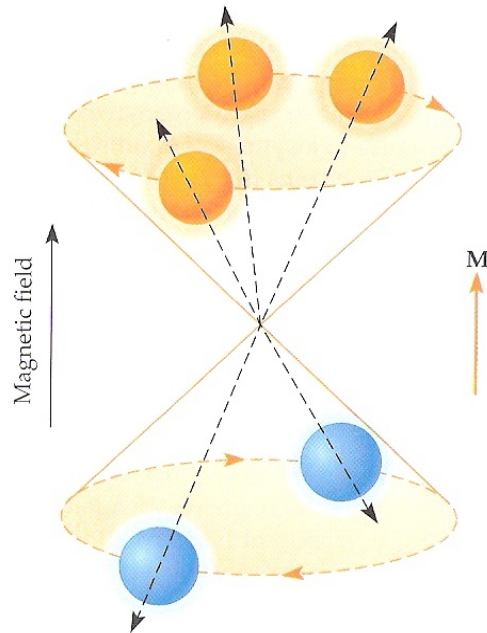


*Figure 2: The resulting measurable magnetisation depends explicitly on the Boltzman constant which links the temperature with the energy distribution of the spin system. Reprint from (Huettel, 2009).*

## 2.1.2 The Classical Point of View

As NMR and MRI is usually based on a two-energy states system a semi-classical formulation is valid. The external magnetic field $B_0$ generates a torque $D$, which affects the nuclei's magnetic moment $\mu$. The magnetic moment is related to an angular momentum $J$ via the law of conservation of angular momentum.

$$D = \mu \times B_0 = \frac{dJ}{dt} \tag{11}$$

The torque $D$ produces a change in angular momentum $J$ where $\frac{\mu}{\gamma} = J$.

$$\frac{d\mu}{dt} = \gamma \mu \times B_0 \tag{12}$$

When assuming a static magnetic field in z-direction the Cartesian components of the magnetic momentum can be obtained

$$\begin{aligned}
\dot{\mu}_x &= \gamma B_0 \mu_y \\
\dot{\mu}_y &= -\gamma B_0 \mu_x \\
\dot{\mu}_z &= 0
\end{aligned} \tag{13}$$

This set of differential equations can be solved by defining $\mu_+ = \mu_x + i\mu_y$ :

$$\begin{aligned}
\mu_x(t) &= \mu(0)\cos(\omega_0 t) \\
\mu_y(t) &= -\mu(0)\sin(\omega_0 t) \\
\mu_z(t) &= const
\end{aligned} \tag{14}$$

The solutions in the laboratory frame describe a dipole which is precessing around the static magnetic field $B_0$ with the Larmor frequency $\omega_0$. At this point it is useful to introduce the concept of the rotating frame, which means, that now the observer rotates around the z-axis with a frequency $\omega_{rot}$. The transformation from the laboratory to the rotating frame is given by

$$\left(\frac{d\boldsymbol{\mu}}{dt}\right)_{rot}=\frac{d\boldsymbol{\mu}}{dt}-\boldsymbol{\omega}_{rot}\times\boldsymbol{\mu} \tag{15}$$

and equation 15 simplifies to

$$\left(\frac{d\boldsymbol{\mu}}{dt}\right)_{rot}=\Delta\boldsymbol{\omega}\times\boldsymbol{\mu} \tag{16}$$

where $\Delta\omega=\omega_0-\omega_{rot}$ (see Fig 3). In the case of resonance $\omega_{rot}=\omega_0=-\gamma\boldsymbol{B_0}$ equation 16 simplifies to

$$\left(\frac{d\boldsymbol{\mu}}{dt}\right)_{rot}=0 \tag{17}$$
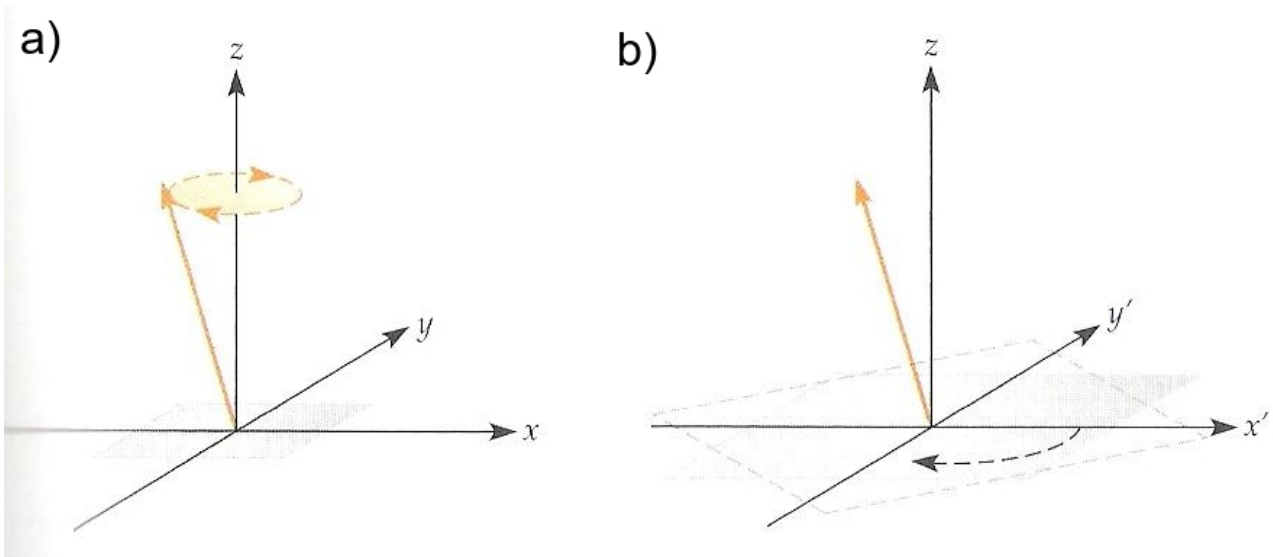


*Figure 3: A rotating net magnetisation in the laboratory frame (a) appears stationary in the rotating frame (b). Reprint from (Huettel, 2009).*

A simplified description could be obtained by using the rotating frame instead of the laboratory frame. When a temporally varying magnetic field $\boldsymbol{B_1}$ with frequency $\omega_{rf}\approx\omega_0$ orthogonal to $\boldsymbol{B_0}$ is applied the net magnetisation can be tipped. With $\boldsymbol{B_1}(t)=(B_1\sin(\omega_{rf}t),B_1\cos(\omega_{rf}t),0)$ the magnetic field becomes

$$\boldsymbol{B}(t) = (B_1 \sin(\omega_{rf} t), B_1 \cos(\omega_{rf} t), B_0) \tag{18}$$

When using $\boldsymbol{\omega_{rot}} = (0, 0, \omega_{rf})$ together with equation 16 the effective magnetic field becomes

$$\boldsymbol{B_{eff}} = \left(0, B_1, B_0 + \frac{\omega_{rot}}{\gamma}\right) \tag{19}$$

$$\boldsymbol{\omega_{eff}} = (0, \omega_1, \Delta\omega) \tag{20}$$

with $\omega_1 = -\gamma \boldsymbol{B_1}$ and $\Delta\omega = \omega_0 - \omega_{rot}$.

In NMR and MRI experiments the macroscopic magnetisation is manipulated via external radio-frequency fields. A mathematical description is used to find the equations of motion.

$$\boldsymbol{M} = \sum_i \boldsymbol{\mu_i} \tag{21}$$

$$\left(\frac{d\boldsymbol{M}}{dt}\right)_{rot} = (\boldsymbol{\omega_{eff}} \times \boldsymbol{M}) \tag{22}$$

The components of equation 22 are

$$\begin{aligned}
(\dot{M}_x)_{rot} &= (-\Delta\omega M_y + \omega_1 M_z)_{rot} \\
(\dot{M}_y)_{rot} &= (-\Delta\omega M_x)_{rot} \\
(\dot{M}_z)_{rot} &= (-\omega_1 M_x)_{rot}
\end{aligned} \tag{23}$$

## 2.1.3 Radio Frequency Pulses

The macroscopic magnetisation can be manipulated by applying an on-resonant RF pulse. RF pulses are generated by RF coils which are placed orthogonal to the magnetic field $\boldsymbol{B_0}$. Starting at time $t = 0$ the total magnetization is $\boldsymbol{M} = (0, 0, M_0)$. When the RF pulse is generated, the magnetization in the rotating frame changes to $\boldsymbol{M} = (0, M_0 \sin(\omega_1 t), M_0 \cos(\omega_1 t))$ which means that in the rotating frame, the magnetization is precessing around $\boldsymbol{B_1}$ with $\omega_1 = -\gamma \boldsymbol{B_1}$ (Fig 4).

Depending on the duration of the pulse $t_p$ the magnetization has flipped by the angle $\alpha$, which is proportional to $\boldsymbol{B_1}$ and $t_p$.

$$\alpha = \gamma B_1 t_p \qquad\qquad (24)$$

In NMR and MRI especially the 90° and the 180°-pulses are important. This means, that $t_p$ and $\boldsymbol{B_1}$ are set up such, that the flip angle becomes 90° or 180° degrees.
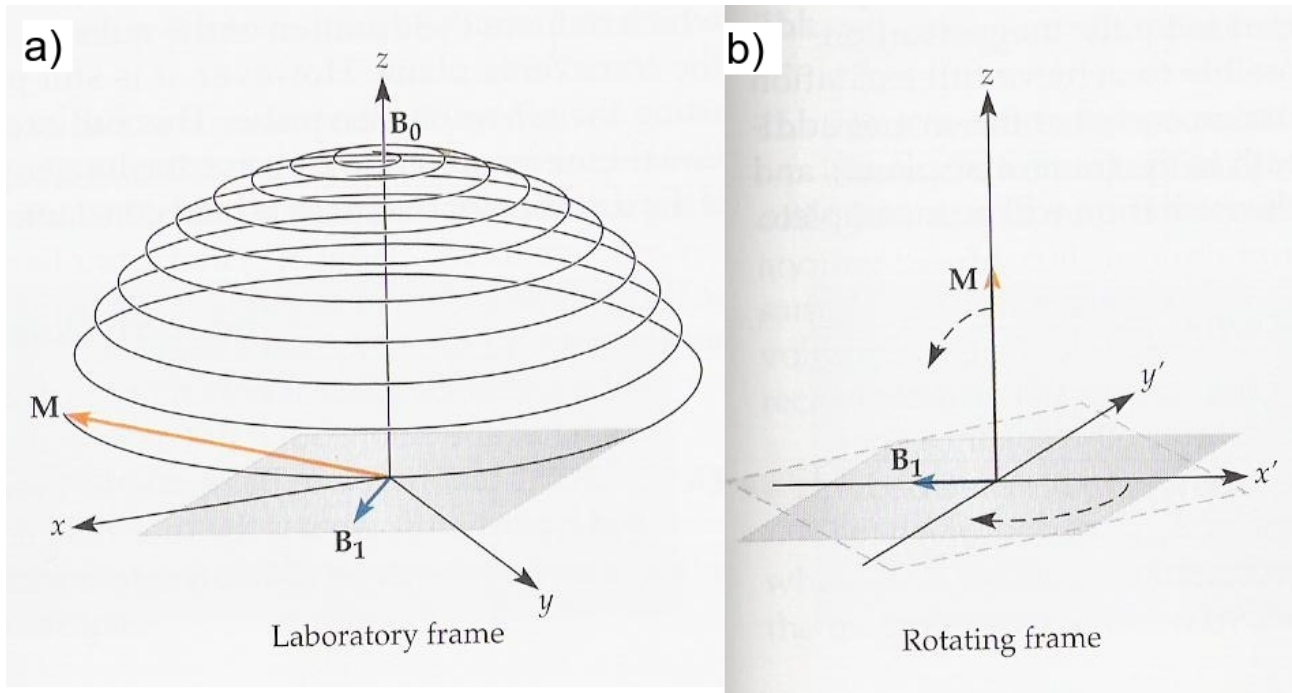


*Figure 4: When applying an RF pulse the method of a rotating frame becomes valuable. The delivery of an excitation pulse causes the longitudinal magnetisation to be tipped into the transverse plane. In the rotating frame (b) this looks like a simple rotation downwards. In the laboratory frame (a) the magnetisation has a complex trajectory which is known as nutation. Reprint from (Huettel, 2009).*

## 2.1.4 Relaxation Effects

In most cases spins cannot be assumed to be isolated. Nuclei interact with each other (e.g. via magnetic coupling) and with their environment (e.g. chemical shift). These interactions are constant in time and lead to a material specific frequency distribution, which can be used to study the material and its properties. On the other hand there are time-dependent perturbations, caused by temperature effects, which for example lead to relaxation effects after an RF-pulse.

*Spin-Lattice relaxation and longitudinal relaxation time $T_1$*

After the RF pulse (excitation pulse), the spin system gradually loses the energy absorbed during the excitation. This is caused by interaction of the system with the surrounding atoms, which leads to lattice oscillations within the studied material. This energy loss can be observed via the net magnetization, which gradually returns to its thermodynamical equilibrium. This process is called spin-lattice relaxation or longitudinal relaxation and is characterized by the time constant $T_1$ (Fig 5).

From the quantum mechanical point of view, during spin-lattice relaxation the spins return from the high-energy state to their low-energy state. As the net magnetization can be interpreted as the vector sum of spins, each flip from a high to a low energy state leads to a change of this quantity. Longitudinal relaxation obeys the following law.

$$M_z = M_0 \left( 1 - e^{-\frac{t}{T_1}} \right) \tag{25}$$
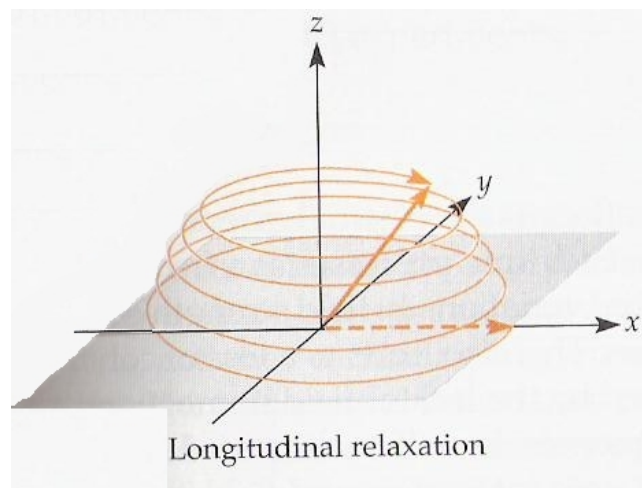


*Figure 5: The time constant $T_1$ governs the rate at which longitudinal magnetisation recovers. Reprint from (Huettel, 2009).*

*Spin-Spin Relaxation and transversal relaxation time $T_2$*

After the net magnetization is tipped into the transverse plane by an excitation pulse, it is initially coherent. The spins in the sample are precessing around the main field vector at the same phase. Over time, this coherence between the spins is gradually lost and they fall out of phase. This phenomena is known as transverse relaxation. In general there are two main causes for transverse relaxation, one intrinsic and the other extrinsic. The intrinsic cause is spin-spin interaction: when many spins are excited at once, there is a loss of coherence due to their effects on one another. The

signal loss of this intrinsic mechanism, which is also called $T_2$-decay, is characterised by the time constant $T_2$ (Fig 6).

$$M = M_0 e^{-\frac{t}{T_2}}$$ (26)

An extrinsic source of differential spin effects is the external magnetic field, which is usually inhomogeneous. Because each spin precesses at a frequency proportional to its local field strength, spatial variations in field strength cause spatial differences in precession frequencies. This also leads to a loss of coherence. But in contrast to spin-lattice relaxation effects, this lack of field homogeneity can be reversed by special pulse sequences, as will be discussed later. The combined effects of spin-spin interaction and field inhomogeneity lead to signal loss known as $T_2^*$-decay, characterized by time constant $T_2^*$. $T_2^*$ decay is always faster than $T_2$ and plays a critical role in BOLD contrast methods.
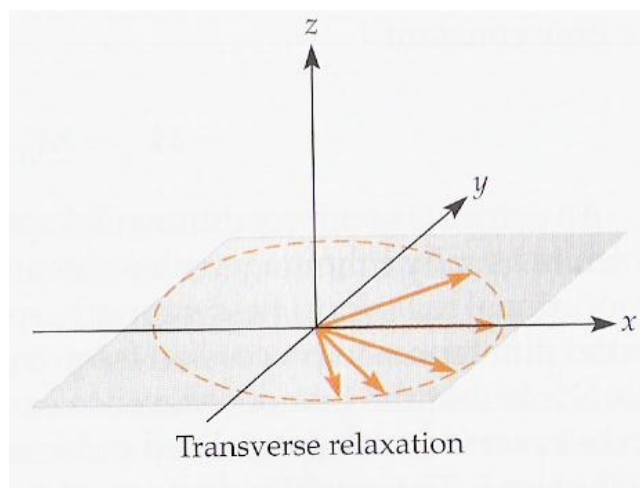


*Figure 6: The time constant $T_2$ represents the rate at which transversal magnetisation decays. Reprint from (Huettel, 2009).*

## 2.1.5 The Bloch Equations

The equation of motion 22 can be modified such that the relaxation parameters $T_1$ and $T_2$ are included. The resulting equations are called the Bloch equations.

$$\left(\dot{M}_x\right)_{rot} = \left(-\Delta\omega\, M_y + \omega_1 M_z - \frac{1}{T_2}M_x\right)_{rot}$$

$$\left(\dot{M}_y\right)_{rot} = \left(\Delta\omega\, M_x - \frac{1}{T_2}M_y\right)_{rot} \tag{27}$$

$$\left(\dot{M}_z\right)_{rot} = \left(-\omega_1 M_x - \frac{1}{T_1}\left(M_z - M_0\right)\right)_{rot}$$

$M_0$ represents the the net magnetisation for $t \to \infty$. For $\Delta\omega = 0$ and $B_1 = 0$ equation 27 becomes

$$\left(\dot{M}_x\right)_{rot} = \left(\frac{-1}{T_2}M_x\right)_{rot}$$

$$\left(\dot{M}_y\right)_{rot} = \left(\frac{-1}{T_2}M_y\right)_{rot} \tag{28}$$

$$\left(\dot{M}_z\right)_{rot} = \left(\frac{-1}{T_1}\left(M_z - M_0\right)\right)_{rot}$$

## *2.2 Magnetic Resonance Imaging*

MRI is an imaging technique that utilises material dependent magnetisation density and its relaxation behaviour to visualize detailed internal structures of biological tissue. Magnetic field gradients cause magnetization at different locations to precess at different frequencies. Spatial encoding of magnetization can be obtained by using gradients in three direction.

### 2.2.1 Data Acquisition

Signal detection is achieved by the implementation of a receiver coil, in which a current is induced due to electromagnetic coupling. The receiver coil can be the same as the transmit coil. During the application of an RF pulse the net magnetization is tipped into the transverse plane. Its precession at the Larmor frequency sweeps across the receiver coil, causing the density of magnetic flux experienced by the receiver coil to change over time. This flux-change induces an electromotive force in the coil. The electromotive force $F_{em}$ induces an electrical potential that can be used to drive a current through a circuit.

$$F_{em} = \frac{d\Phi}{dt} \tag{29}$$

$$\Phi = \int_s B \ dS \qquad \qquad (30)$$

The solution of equation 29 shows the time dependency of the electromotive force $F_{em}$ which oscillates with the Larmor frequency $\omega_0$. Therefore the coil has to be tuned to the resonance frequency to be able to detect an MR signal.

## 2.2.2 Image Formation

The main goal of magnetic resonance imaging is the formation of an image by mapping the spatial distribution of a certain property of the atomic nuclei within the sample. This property might reflect e.g. the spin density, the diffusion-coefficient, or the $T_1$ and $T_2$ relaxation constants. To resolve spatial information in three dimensions, three magnetic gradient fields in three orthogonal directions are required. In MRI, the static magnetic field $B_0$ is oriented along the z-axis which is parallel to the scanner bore. The gradient magnetic fields along the x-,y- and z-directions indicate how the strength of that static magnetic field changes in each direction and so, the spatial dependence of the Larmor frequency. Instead of turning on all gradients at the same time, one has to implement a sequence of gradient changes to create an image. First, the so called slice selection is used to define a two-dimensional slice of the object and then the remaining two dimensions within this slice are systematically resolved by frequency encoding and phase encoding, to obtain the final image.

To describe an MRI experiment, we use a pulse sequence diagram, which gives a quick and clear overview of what pulses are used. The upper line represents RF excitation pulse and sometimes data readout is represented here (Fig 7). For readability reasons, in our case, data readout is visualized separately in the last line of the diagram. The other three lines represent the different gradients' time courses. If more than one MRI experiment is performed *TR* represents the time between two excitations of the spin system.

### 2.2.2.1 Slice Selection

Most structural MRI and fMRI studies involve the construction of three-dimensional images from a set of two-dimensional slices. Thus a first common step is dimensional reduction. This can be realized by the slice selection technique. The key element is to ensure that there is a match between the precession frequency of the spins within the desired slice and the RF excitation pulse. This can be realized via a magnetic gradient in the z-axis during excitation (Fig 7). The effect of such a gradient is, that only the spins with the appropriate Larmor frequency get excited by the RF pulse, which means, that only spins in one slice are available for MR signal detection. If a field gradient is

turned on along the z-axis, it will cause a continuous change in field strength and so one slice will contain spins with a range of frequencies. To match this frequency band, the excitation RF pulse will need to contain the same frequency range. Commonly this is realized by setting up the RF frequency as the centre frequency of the slice and configure the bandwidth as desired. Every gradient causes a spin-dephase in the gradient's direction. So after the slice selection pulse there is a negative rephasing gradient applied, so that the spins within the slice are rephased again.
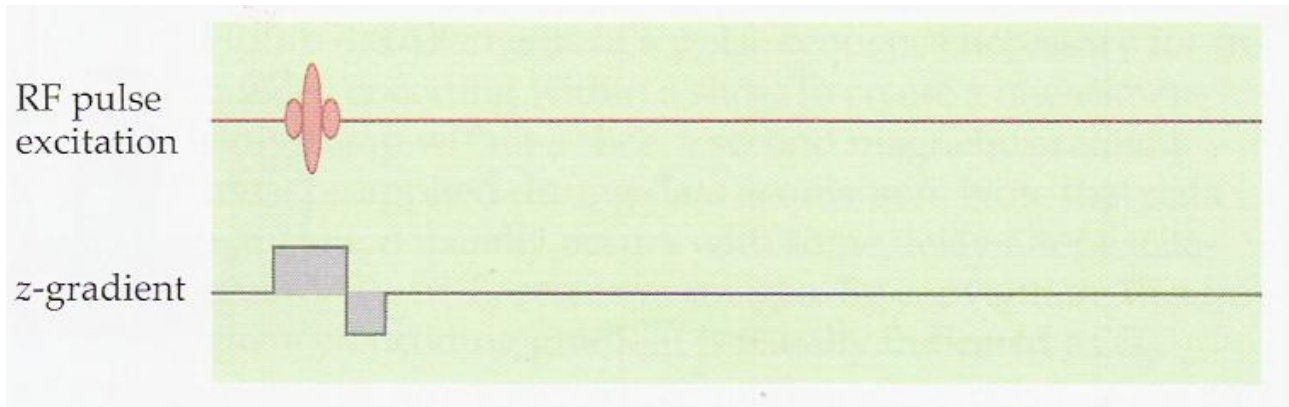


Figure 7: To select a slice of an object , an excitation RF pulse is applied while a magnetic gradient is turned on in z-direction. Reprint from (Huettel, 2009).

### 2.2.2.2 Frequency Encoding

To obtain spatial encoding within the selected slice, two additional orthogonal gradients are necessary. During signal detection the so-called read (or frequency encoding) gradient is applied (Fig 8). This leads to a linear dependency between spatial locations and recorded frequencies. The readout is performed via gradient echo. An additional field gradient is applied inverse to the read gradient, before the latter is switched on. This inverse gradient induces a dephase of the excited spins and the read gradient rephases them again. After the time between excitation and readout (time of echo $TE$ ) the so-called gradient echo evolves. As each frequency is directly related with a specific location, spatial information can be obtained via Fourier transformation of the detected signal.
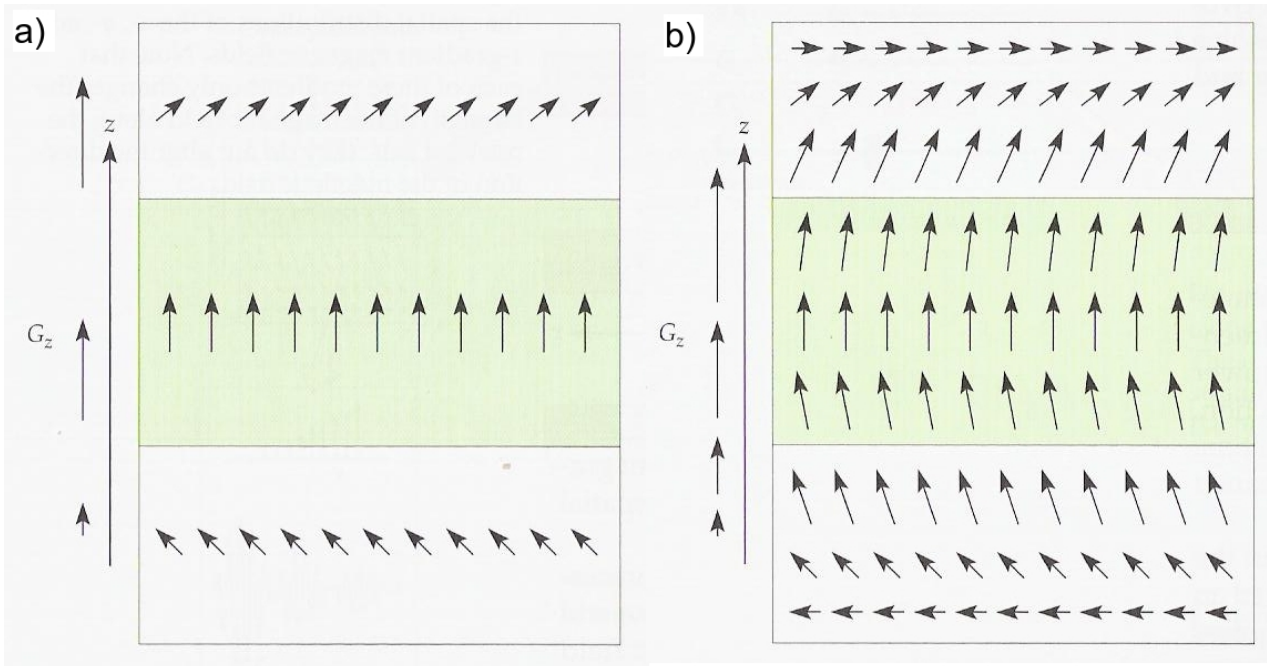
*Figure 8: One slice contains a continuum of spin frequencies so that it is common use to set the RF frequency as the centre frequency and configure the bandwidth as desired. Exciting a well defined slice therefore depends on correct pulse shaping and bandwidth. Reprint from (Huettel, 2009).*

### *2.2.2.3 Phase Encoding*

In order to encode the second direction within the slice, the so-called phase gradient must be applied between the excitation pulse and signal detection. As this gradient must be orthogonal to the read and the slice selection gradient. The phase gradient induces, similar to the frequency gradient, a phase dispersion between the excited spins. But, as this dephase is not rephased, it produces a spatial dependency of phases in the direction of the gradient (Fig 9). As signal detection of all spins is performed simultaneously, phases add up and so the phase-location dependency is lost. Thus, a series of measurements with different phase gradient amplitudes are performed. Via Fourier analysis, spin density in y-direction can be obtained and combined with the frequency-location. Thus, full spatial encoding can be achieved.
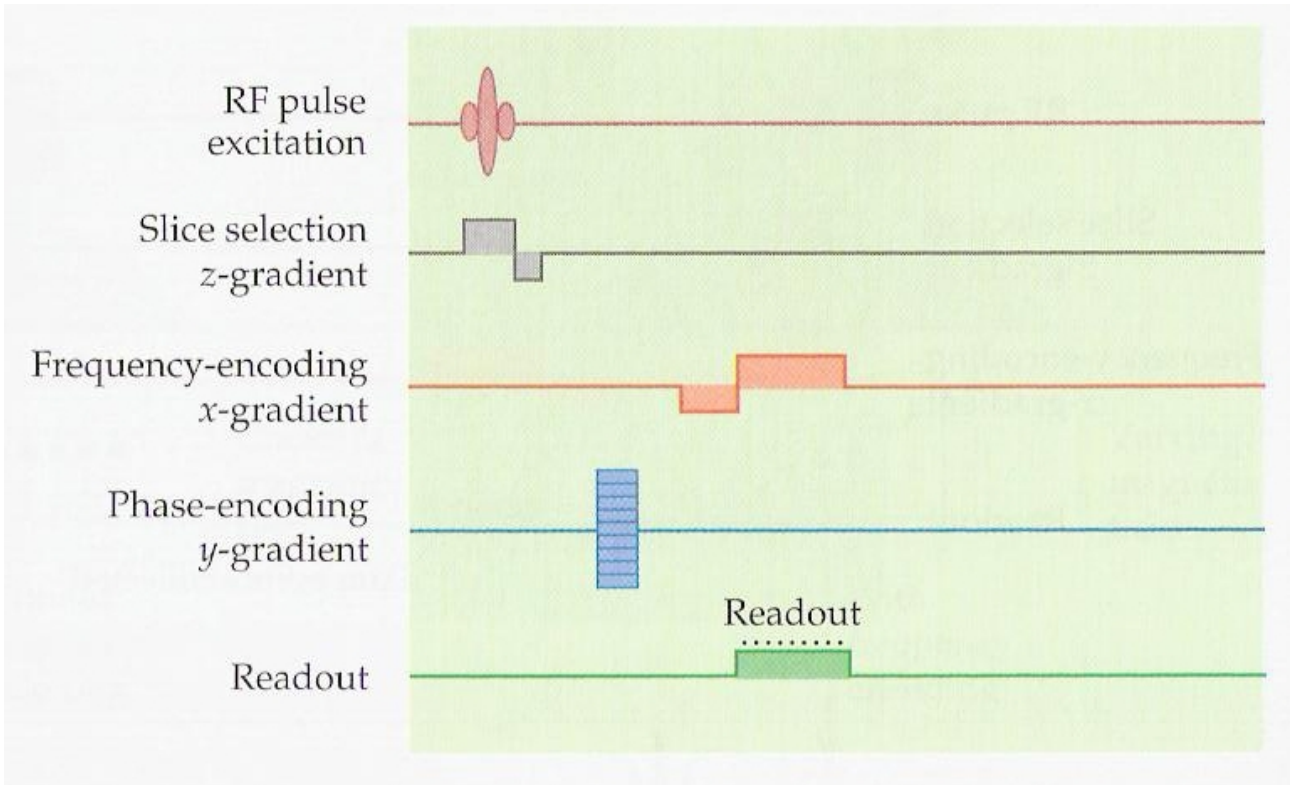
*Figure 9: Sequence diagram of an MRI experiment. Reprint from (Huettel, 2009).*

### *2.2.2.4 Mathematics of Image Formation*

In order to understand the process of image formation quantitatively, we will need to characterize how the MR signal changes as a function of the particular magnetic field gradients that are applied. Equation 31 shows the Bloch equation in laboratory frame, where $B$ stands for the gradient components of the magnetic field plus the static magnetic field, as explained in the next paragraph.

$$\frac{d\boldsymbol{M}}{dt} = \gamma\,\boldsymbol{M}\times\boldsymbol{B} + \frac{1}{T_1}(M_0 - M_z) - \frac{1}{T_2}(M_x - M_y) \tag{31}$$

with its components

$$\frac{dM_x}{dt} = M_y\,\gamma\,B - \frac{M_x}{T_2}$$
$$\frac{dM_y}{dt} = -M_x\,\gamma\,B - \frac{M_y}{T_2} \tag{32}$$
$$\frac{dM_z}{dt} = \frac{-M_z + M_0}{T_1}$$

which describe the changes in magnetization over time in x and y directions with time constant $T_2$ and in z-direction, specified by the relaxation constant $T_1$. By solving the equations above one obtains the behaviour of longitudinal and transverse magnetization depending on time.

$$M_x(t)=(M_{x,0}\cos(\omega t)+M_{y,0}\sin(\omega t))e^{-\frac{t}{T_2}}$$
$$M_y(t)=(-M_{y,0}\sin(\omega t)+M_{x,0}\cos(\omega t))e^{-\frac{t}{T_2}} \qquad (33)$$
$$M_z(t)=M_{z,0}(1-e^{-\frac{t}{T_1}})$$

Although especially the time course of the magnetization in x-y-plane looks very complex, it is quite easy to understand. When combining the two components by writing them in complex form, where magnetization decays over time with the factor $e^{-\frac{t}{T_2}}$, we describe a one dimensional projection of a circular motion.

$$M_{xy}(t)=M_{xy,0}\cdot e^{-\frac{t}{T_2}}e^{-i\omega t} \qquad (34)$$

After the spin excitation, the magnetic field $\boldsymbol{B}$ experienced by spins at a given spatial location will depend on the large static field $\boldsymbol{B_0}$ and a smaller gradient field $\boldsymbol{B_g}$. We can describe the total magnetic field at a given spatial location $(x,y,z)$ and time point $\tau$ as a linear combination of the static magnetic field and the gradient fields as follows:

$$B(\tau)=B_0+G_x(\tau)x+G_y(\tau)y+G_z(\tau)z \qquad (35)$$

We can substitute the $\omega$ term in equation 34 using $\omega=-\gamma B$ and obtain the following expression

$$M_{xyz}(t)=M_{xy,0}\cdot e^{-\frac{t}{T_2}}\cdot e^{-i\gamma B_0 t}\cdot e^{-i\gamma\int_0^t (G_x(\tau)x+G_y(\tau)y+G_z(\tau)z)d\tau} \qquad (36)$$

In summary, the transverse magnetisation for a given location $(x, y, z)$ at a given time $\tau$ depends on

- the original magnetisation at that location, $M_{xy}(x, y, z, t=0)$

- the signal loss due to $T_2$ effects, $e^{-\frac{t}{T_2}}$

- the accumulated phase due to the main magnetic field, $e^{-i\gamma B_0 t}$

- the accumulated phase due to the gradient fields $e^{-i\gamma \int_0^t (G_x(\tau)x + G_y(\tau)y + G_z(\tau)z)d\tau}$

### 2.2.2.5 Signal Formation

The spatial summation of the MR signal from every voxel gives the measured MR signal $S(t)$.

$$S(t) = \int_x \int_y \int_z M_{xy}(x, y, z, t)\, dx\, dy\, dz \qquad (37)$$

When equation 37 is combined with equation 36 the fundamental MR signal equation is obtained.

$$S(t) = \int_x \int_y \int_z M_{xy,0}(x, y, z) \cdot e^{-\frac{t}{T_2}} \cdot e^{-i\gamma B_0 t} \cdot e^{-i\gamma \int_0^t (G_x(\tau)x + G_y(\tau)y + G_z(\tau)z)d\tau}\, dx\, dy\, dz \qquad (38)$$

As the signal equation in its current form is difficult to solve the concept of k-space is introduced, which is a description of MR experiments in Fourier space. Within a slice, $k_x$ and $k_y$ represent the time integrals of the gradient waveforms.

$$k_x = \frac{\gamma}{2\pi} \int_0^t G_x(\tau)\, d\tau \qquad (39)$$

$$k_y = \frac{\gamma}{2\pi} \int_0^t G_y(\tau)\, d\tau \qquad (40)$$

Equation 39 and 40 substitute the appropriate expressions in equation 38 which becomes

$$S(t) = \int_x \int_y \int_z M(x, y)e^{-i2\pi k_x(t)x} \cdot e^{-i2\pi k_y(t)y}\, dx\, dy \qquad (41)$$

Equation 41 depicts the direct relationship between image space and k-space via a Fourier transformation. Any signal change over time can be constructed from a series of frequencies and therefore any image can be constructed from a series of components in the spatial-frequency domain.

By altering the gradient parameters, the sampling path within k-space can be manipulated. For example, by changing the strength of different gradients over time a trajectory can be traced through k-space (Fig 10). Whereas straight lines are usually preferred for k-space sampling, theoretically any trajectory is possible.
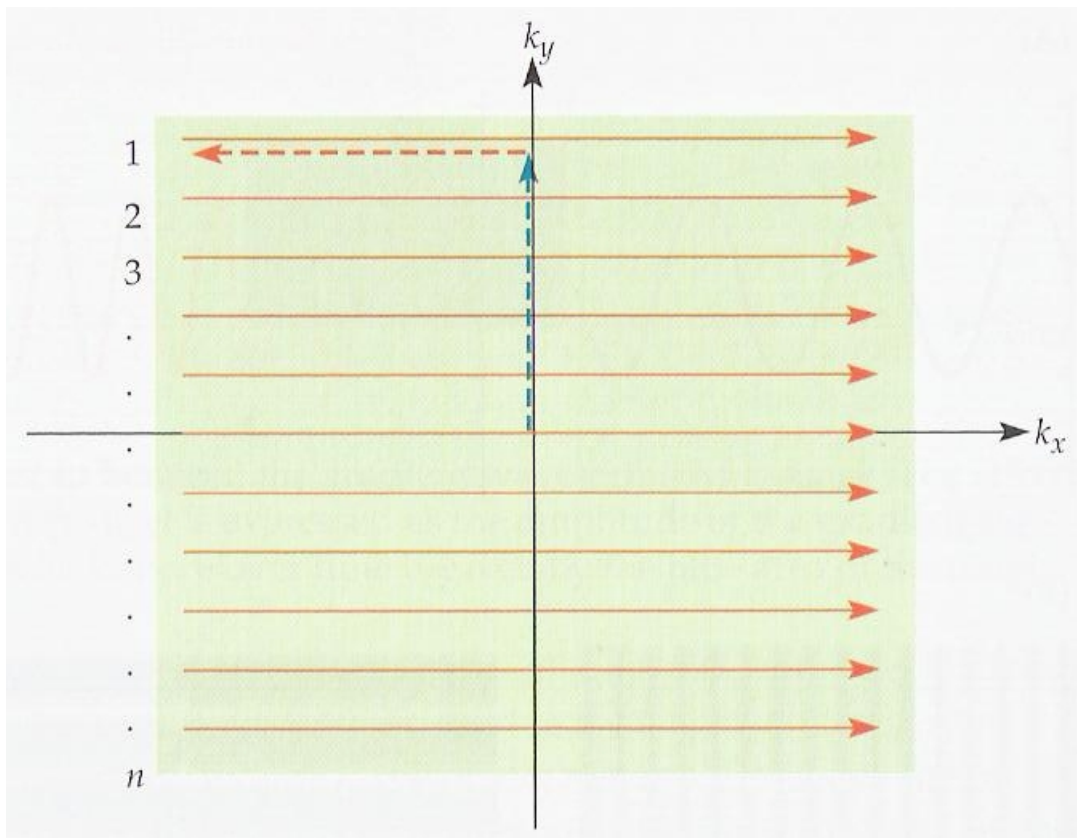


*Figure 10: Scanning k-space in an MRI experiment. Reprint from (Huettel, 2009).*

Standard imaging sequences fill one k-space line at one time. K-space lines are selected via the $G_y$ gradient following each excitation while the $G_x$ gradient is applied during data acquisition. Different $G_y$ gradient strengths will result in the acquisition of different k-space lines which are acquired continuously whereas the $k_x$ trajectory is naturally discrete. However, as MR data acquisition is usually performed digitally both trajectories become discrete in the end.

After filling the k-space a Fourier transformation is necessary to obtain the MRI images. It is

important to know about the inverse proportionality of k-space and image space. This means for example that larger k-space improves the spatial resolution in image space and that finer k-space sampling results in a larger field-of-view (FOV). The FOV is defined as the total size of an image in the image space.

$$FOV_x = \frac{1}{\Delta k_x} = sampling\ rate\ along\ k_x = \frac{2\pi}{\gamma(\Delta G_x t)}$$
$$FOV_x = \frac{1}{\Delta k_y} = sampling\ rate\ along\ k_y = \frac{2\pi}{\gamma(\Delta G_y t)}$$

(42)

The voxel size can be calculated as follows

$$\frac{FOV_x}{M_x} = \frac{1}{2 k_{x,max}}$$
$$\frac{FOV_y}{M_y} = \frac{1}{2 k_{y,max}}$$

(43)

## *2.3 Advanced Imaging Methods*

### 2.3.1 Echo-Planar Imaging (EPI)

Echo-planar imaging (EPI) is the most common fMRI acquisition method. In contrast to standard gradient echo or spin echo approaches, EPI enables acquisition of multiple k-space lines after a single RF excitation (Mansfield, 1977). Usually, single-shot EPI is used which means that data of a whole imaging slice is acquired after one RF excitation. Although the concept of EPI has been around for a long period of time, it was not used routinely until the 1990s.

A slice selective gradient in z-direction is played at the same time as the RF excitation pulse. After the excitation pulse, read gradients are applied with alternating polarity. Each read gradient generates a gradient echo. At those times when the polarity of the read gradients is switched a so-called "blip", which is a small gradient, is applied in the phase-encoding direction. These blips are responsible for the shifts in k-space along the phase-encoding direction. If a single-shot EPI approach is used these blips are applied until the whole of k-space is covered. Usually k-space data is acquired in a rectangular sampling scheme. The changing polarity of the read gradient leads to an alternating direction of the read trajectory in k-space. However, other trajectories through k-space are possible, such as zig-zag forms, spiral readouts (Law & Glover, 2009) or centre-out EPI variants (Hetzer et al., 2011). The echo time *TE* is, however, always defined as the temporal distance

between the RF excitation pulse and the centre of k-space.

## 2.3.2 Partial Fourier Acquisition

Data acquisition time can be reduced by exploiting k-space symmetries. Partial k-space (or partial Fourier) acquisition is based on the assumption that the Fourier transform of an object is hermitian (Feinberg et al., 1986).

$$S\left(k_x, k_y, k_z\right) = S^*\left(-k_x, -k_y, -k_z\right) \tag{44}$$

For ideal acquisition circumstances only half of the k-space is required to reconstruct an object. However, phase shifts cause half of k-space to be insufficient for proper image reconstruction and typically three quarters or at least five eights of k-space data is sampled in MRI, including the k-space centre which contains the most crucial data for image reconstruction. Typically, partial k-space acquisition methods are applied in the phase-encoding direction, as this is the most time consuming acquisition part. However, the reduction in acquisition time results in decreased SNR. The symmetric parts of k-space contain randomly distributed noise. This noise averages out during image reconstruction of full k-space. In case of partial k-space acquisition symmetry is used to copy k-space information and therefore random noise distribution cannot be guaranteed any more which results in lower SNR of the reconstructed images.

## 2.3.3 Generalised Autocalibrating Partially Parallel Acquisition (GRAPPA)

Beside partial k-space acquisition, parallel imaging approaches have become an important tool to reduce scan time and therefore improve spatial resolution, temporal resolution, SNR and scanner efficiency. In parallel MR imaging, reduced k-space data is acquired in phase encoding direction by combining the signals of multiple coil arrays. Spatial information from the separate coil elements is used to reduce the amount of Fourier encoding.

Before each parallel acquisition scan, a full reference scan is necessary to assess the sensitivity of the coil elements. This information is used later during image reconstruction. Parallel imaging image reconstruction is based on a separate reconstruction of data from each coil element before a full FOV image is created.

Generalised autocalibrating partially parallel acquisitions (GRAPPA) is the currently most common parallel acquisition technique (Griswold et al., 2002) and is an extension of VD-AUTO-SMASH (Heidemann et al., 2001) and PILS (Griswold et al., 2000). In GRAPPA, more than one k-space line

is acquired in each single coil of an array. Data from each line and each coil is then used together with the sensitivity maps acquired earlier to reconstruct the missing k-space line. It is important to mention that although GRAPPA can principally improve SNR, excessively high acceleration factors will ultimately lead to decreased SNR.

## 2.3.4 Inversion Recovery (IR)

Most of the techniques used in this work are based on the inversion recovery (IR) technique. IR can be used to prepare the MR signal with a $T_1$ weighting which is necessary for the various cerebral blood flow and blood volume based MRI techniques that will be described further below.

The inversion recovery technique uses a 180° inversion pulse which flips the z-magnetisation from the equilibrium state $M_z$ to the inverted signal state $-M_z$. Grey matter, white matter, cerebral blood volume and cerebrospinal fluid all have different characteristic $T_1$ relaxation times and therefore a contrast emerges comparable to $T_2$ or $T_2^*$ weighted MRI sequences. After the inversion time $TI$ MRI data is acquired.

## 2.3.5 Adiabatic Inversion

Especially at ultra-high static magnetic field strengths RF interactions with the human body are a crucial problem as the RF wavelength used at these field strengths approaches the size of the target object. Consequently, interference and diffraction effects of RF waves occur which can cause blurred imaging quality and SNR problems (Vaughan et al., 2001). For conventional RF pulses the flip angle is directly proportional to the magnitude (see equation 24).

$B_1$ inhomogeneities however can cause strong flip angle variations within the image. Inversion recovery based MRI techniques rely on a good inversion efficiency as well as a sharp inversion profile and so adiabatic inversion pulses are commonly used.

Adiabatic RF pulses are based on the adiabatic principle (Abragam, 1983). In contrast to conventional RF pulses, adiabatic pulses do not obey equation 24 but rely on how the $B_1$ magnetic field varies its amplitude, frequency and phase.

Adiabatic MR pulse durations are commonly between 5 and 20ms long which is longer than typical conventional RF pulses. While the pulse is being played out, the amplitude and frequency of the RF field is modulated such that the orientation of the effective magnetic field $B_{eff}$ is manipulated. The magnetisation precesses on the surface of a thin cone around $B_{eff}$ and therefore changes in direction of $B_{eff}$ result in a changed orientation of the precessing cone. Usually, adiabatic RF pulses start with

a frequency below resonance $\omega_{rf} \ll \omega_0$ , so $\boldsymbol{B_{eff}}$ is parallel to $\boldsymbol{B_0}$ . With changing RF frequency $\omega_{rf}$ , $\boldsymbol{B_{eff}}$ starts rotating into the transverse plane and the longitudinal component vanishes when $\omega_{rf}$ approaches the Larmor frequency. At this time $\boldsymbol{B_{eff}}$ is in the transverse plane and therefore independent of the field strength $\boldsymbol{B_1}$ (adiabatic half passage). For a full 180° adiabatic pulse the frequency $\omega_{rf}$ is swept beyond resonance until $\boldsymbol{B_{eff}}$ is parallel to the -z direction. The amplitude modulation function of the adiabatic pulse starts with 0, rises to a maximum and drops back to 0 at the end of the pulse. The macroscopic magnetisation will follow the change of the effective magnetic field $\boldsymbol{B_{eff}}$ if this change is slow enough (adiabatic condition). However, as transverse and longitudinal relaxation processes occur during inversion, the inversion duration must not be too long.

The angle $\alpha$ between $\boldsymbol{B_{eff}}$ and $\boldsymbol{B_1}$ is defined as:

$$\alpha = \arctan\left(\frac{B_0 - \frac{\omega}{\gamma}}{B_1}\right) = \arctan\left(\frac{B_{z,eff}}{B_1}\right) \tag{45}$$

Fig 11 shows a depiction of the relationship between $\boldsymbol{B_{eff}}$ and $\boldsymbol{B_1}$ . Based on equation 45 the adiabatic condition requires the change in direction of $\boldsymbol{B_{eff}}$ to be small compared to the rate at which the magnetisation precesses around $\boldsymbol{B_{eff}}$ .

$$\left|\frac{d\alpha}{dt}\right| \ll \gamma |\boldsymbol{B_{eff}}| \tag{46}$$

Adiabatic inversion cannot work properly if the adiabatic condition is not obeyed. A measure of how well the inversion will work is given by the adiabaticity $\beta$ , whereas the adiabatic condition is met for $\beta \gg 1$ .

$$\beta = \frac{|\gamma \boldsymbol{B_{eff}}|}{\left|\frac{d\alpha}{dt}\right|} \tag{47}$$
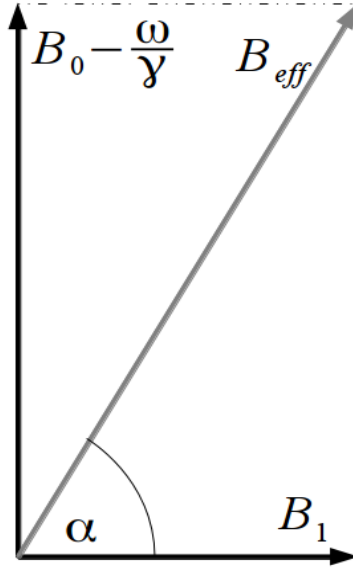
*Figure 11: Visualisation of the effective magnetic field and magnetisation during the adiabatic passage.*

### 2.3.5.1 Hyperbolic Secant (HS) RF pulses

If a spatially restricted inversion is required rather than a global one, an additional gradient must be applied. The range in which the magnetisation is affected by the inversion pulse corresponds to the slab perpendicular to the gradient vector. The classic adiabatic inversion pulse uses a hyperbolic secant function to describe the pulse frequency and amplitude (Silver et al., 1984).

$$\widetilde{B_1^{HS}}(t) = B_1^{HS}(t=0)\left(sech(\beta t)\right)^{1+i\mu} \Rightarrow \begin{array}{c} B_1^{HS}(t) = B_1(t=0)\,sech(\beta t) \\ G^{HS} = const \\ \Delta\omega^{HS}(t) = -\mu\beta\tanh(\beta t) \end{array} \qquad (48)$$

$G$ represents the gradient, $\boldsymbol{B_1}$ is the RF pulse amplitude and $\Delta\omega$ denotes the z-component of $\boldsymbol{B_{eff}}$. The temporal and frequency dependent properties of the inversion pulse are described via the parameters $\mu$ and $\beta$.

### 2.3.5.2 Time Resampled Frequency Offset Corrected Inversion (tr-FOCI) RF Pulses

In order to reduce the amount of energy that is deposited in tissue during the inversion the peak amplitude can be reduced. As a permanent reduction in RF amplitude might decrease the inversion efficiency a new type of adiabatic pulse has been developed. Frequency offset corrected inversion (FOCI) pulses use amplitude modulations over time in order to achieve high inversion efficiencies

while providing sharp inversion profiles (Ordidge et al., 1996). The magnetic field $\boldsymbol{B_1}(t)$, the gradient strength $G(t)$ and the resonance frequency offset $\Delta\omega(t)$ of the FOCI pulse are based on the hyperbolic secant pulses (equation 48) but multiplied with a shaping function $A(t)$.

$$
\begin{aligned}
B_1^{FOCI}(t) &= A(t) * B_1^0 \, sech(\beta t) \\
G^{FOCI}(t) &= A(t) * G^{HS}(t) \\
\Delta\omega^{FOCI}(t) &= -A(t) * \mu\beta\tanh(\beta t)
\end{aligned}
\tag{49}
$$

$G^{HS}$ is the slice selective gradient corresponding to a hyperbolic secant inversion pulse. $A(t)$ varies in time, starting with a high value, decreases until one half of the inversion pulse duration and increases again to its original value.

An improved insensitivity to field inhomogeneities in inversion efficiency is offered by the time-resampled FOCI (tr-FOCI) pulse (Hurley et al., 2010). These numerically optimised adiabatic inversion pulses were tailored specifically for magnetisation inversion at ultra-high static magnetic field strengths where inhomogeneities are still a major issue. A time resampling function $T(t)$, is used for optimisation of $\boldsymbol{B_1}(t)$ and $\Delta\omega(t)$. The shapes and equations of this modulation function can be found in the original publication (Hurley et al., 2010).
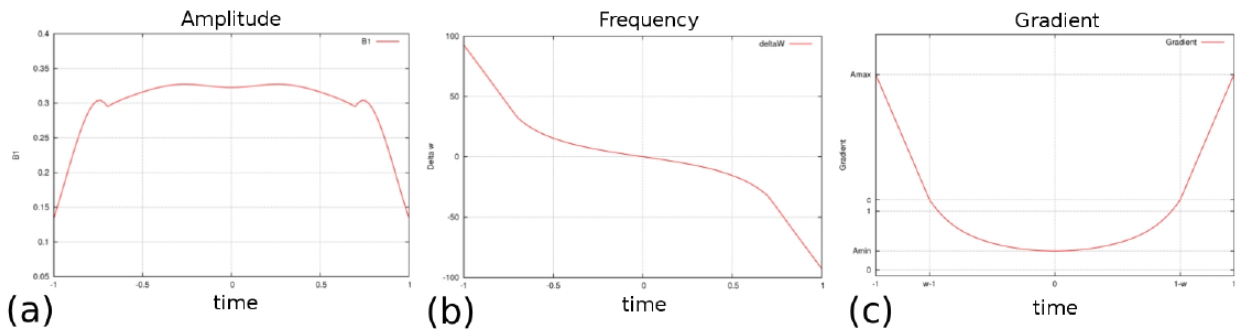


*Figure 12: Visualisation of the tr-FOCI pulse modulation functions for amplitude (a), frequency (b) and gradient (c).*

## *2.4 Physiological Background*

The goal of functional MRI is to detect changes in the activity of the human brain. In order to understand the techniques that can be used to measure these changes a good understanding of the functional organisation of the brain is required. The techniques used in this thesis do not detect neuronal activity directly, but measure physiological correlates of brain activation. The most important physiological parameters can be introduced as follows:

- Cerebral blood volume (CBV): $\dfrac{ml_{blood}}{100\,g_{tissue}}$

- Cerebral blood flow (CBF): $\dfrac{ml_{blood}}{100\,g_{tissue}\cdot min}$

- Cerebral metabolic rate of oxygen (CMRO$_2$): $\dfrac{\mu\,mol_{oxygen}}{100\,g_{tissue}\cdot min}$

- Cerebral metabolic rate of glucose (CMRGlc): $\dfrac{\mu\,mol_{glucose}}{100\,g_{tissue}\cdot min}$

- Oxygen extraction fraction (OEF): $\dfrac{ml_{oxygen,extracted}}{ml_{oxygen,inflow}}$

## 2.4.1 Neuronal Activity

The basic information processing unit inside the brain is the neuron. Neurons are nerve cells which consist basically of three parts: axon, soma and dendrites. The axon transmits an electrical impulse via an action potential from the soma (cell body) to the synapse, where the transfer to other neurons takes place. The dendrites are the signal reception units and forward these signals to the soma. The soma itself is responsible for the metabolic and structural properties of a neuron and contains organelles, cytoplasm and the cell nucleus with the DNA. The general structure of all neurons is similar. However, categorisation is based on the neurons' connections (sensory-, motor- or interneurons) or structure (e.g. pyramidal or stellate neurons). Beside the neurons, there are the glia cells. Glia cells are not directly involved into the cerebral information process, but offer support-mechanisms, like the synapse formation or the regulation of the chemical environment of the neurons which they surround.

The inactive neuron carries a potential difference between the intracellular and the extracellular space. This potential results from the different ion composition and, when setting the extracellular level to 0mV, one can detect an intracellular potential of -70mV. Passive ion channels and active ion pumps are responsible to keep up this dynamic ionic equilibrium. Passive ion channels are protein complexes that span the membrane and let specific ions pass in the direction of the ionic gradient only under certain conditions. This means that the opening of such an ion channel depends either on chemical substances, called neurotransmitters or on a threshold voltage between the intra- and the extracellular space. In the case of the threshold voltage dependent ion channels, an appropriate electric impulse leads directly to the opening of these channels. In contrast, the neurotransmitter based ion channels can either open up directly when docking to their matching transmitter or start

second messenger cascades.

Beside their job of maintaining the potential at rest, active ion pumps are especially responsible for restoring this potential after an activation process. Ions are transported against the ionic concentration gradient, whereas the needed energy comes from hydrolysis from ATP to ADP.

When neurons become activated, the potential between the intra- and the extracellular space changes from its resting potential of -70mV to +40mV. When this so-called action potential arrives at the synaptic end of an axon, the neuron's membrane becomes depolarized and voltage dependent $Ca^{2+}$ ion channels open up. Special vesicles, which contain the neurotransmitters are now able to fuse with the neuron's membrane and release the transmitters into the synaptic cleft, an intracellular space between two neurons. Within the synaptic cleft, the transmitters bind with receptors on the post-synaptic neuron, causing passive ion-channels to open either directly or through g-protein cascades, for an ion-flow from the synapse into the post-synaptic cell. This leads to a change of the potential within the post-synaptic cell (because of the charge of the transferred ions). The resulting potential change of the post-synaptic cell is a summation of the transferred ions from the synapse into the cell.

After activation, the neuron restores its resting potential via ionic pumps. These pumps have an extensive need of energy, which is offered by adenosine triphosphate (ATP), which in turn is generated by the glycolysis process. The vascular system of the brain is responsible for the transport of glucose and oxygen, which are the starting substances for the glycolysis process and so changes within the vascular system of the brain reflect changes in brain function.

## 2.4.2 Energy Metabolism

Although the human brain only contributes about 2% to the total weight of the human body, it is responsible for approximately 20% of the total energy consumption (Attwell & Laughlin, 2001). Most energy generating processes are based on glucose and oxygen which are delivered to the brain by blood flow. Glucose is transported in the blood plasma. However, only about 30% of the glucose that is delivered into the capillary bed is actually extracted from the blood (Oldendorf, 1971). As the concentration of glucose in blood is higher than in tissue, glucose diffuses along this gradient into the tissue though channels in the capillary wall. Next, the glucose enters the interstitial space separating the blood vessels and the cells, and enters the cells where the first steps of glycolysis take place. However, as approximately half of the glucose diffuses back into the blood stream only around 15% of the delivered glucose is actually metabolised (Gjedde, 1987).

In contrast to glucose, oxygen is carried by the erythrocytes, the red blood cells, where most of it is

bound to haemoglobin. Only a small fraction is dissolved in the blood plasma (~2%). However, oxygen supply of tissue relies on diffusion from blood plasma rather than haemoglobin and therefore the concentration of oxygen in blood plasma is indeed important. In the blood, the pools of oxygen bound to haemoglobin and that dissolved in plasma are in fast equilibrium. Therefore oxygen diffusing out of the capillaries is quickly replenished by the release of haemoglobin-bound oxygen.

The fraction of oxygen that is extracted into the tissue (oxygen extraction fraction = OEF) has been studied in healthy human subjects and is in the range of 0.3 to 0.4 (Bulte et al., 2012; Carpenter et al., 1991; Gauthier et al., 2012; He & Yablonskiy, 2007; Ito et al., 2004; Jain et al., 2010; Lu & Ge, 2008; Qin et al., 2011; Raichle et al., 2001; Wise et al., 2013). At rest no significant differences across brain regions could be found (Gusnard et al., 2001). However, the potential effects of pathologies that impact OEF are yet unclear. For example, decreases in OEF have been found after brain injuries (Diringer et al., 2000).

Experiments in primates found that three quarters of the total energy used by the brain, accounts for recovery from the post-synaptic potentials at the dendrites (Attwell & Iadecola, 2002; Attwell & Laughlin, 2001). Neurons prepare for the next action potential by restoring the ionic composition of the extracellular and the intracellular space, especially $Na^+$ recycling. Another neuronal process that consumes energy is the recovery on the pre-synaptic side. Neurotransmitters are recycled and $Ca^{2+}$ ions are cleared (Iadecola & Nedergaard, 2007).

### 2.4.3 Physiological Changes During Brain Activation

Brain activation describes a localised rise in electrical signalling. The regional increase in CBF that accompanies these increases in cerebral information processing is the physiological basis for functional MRI. CMRGlc and CBF changes have been found in activated brain areas (Fox et al., 1988; Ginsberg et al., 1988; Ginsberg et al., 1987; Yarowsky & Ingvar, 1981). However, the CBF response varies with stimulus strength. Changes in CBF observed in the visual cortex depend on the flicker rate of a flashing checkerboard stimulus (Fox & Raichle, 1984) and in the auditory cortex changes in CBF depend on the stimulus rate (Binder et al., 1994). Therefore the haemodynamic response might reflect not only the location of the activated area but also the degree of activation. Furthermore, there is evidence that 50% of the glucose that diffuses through the capillary wall is not metabolised but diffuses back into the blood stream (Gjedde, 1987). Therefore glucose metabolism could double without further increase in CBF. Additionally CBF was found to remain constant throughout a state of hypoglycemia (Powers et al., 1996). These results are supported by an animal

model that showed that blocking of NO production in the neurons suppressed CBF changes during activation states but did not change glucose metabolism (Cholet et al., 1997).

Changes in cerebral oxygen metabolism are generally smaller than changes in CBF or glucose metabolism and several studies have quantified the ratio of the change in CBF to $CMRO_2$ between two to three (Hoge et al., 1999; Marrett & Gjedde, 1997; Roland et al., 1989; Roland et al., 1987; Seitz & Roland, 1992; Vafaee et al., 1999; Vafaee et al., 1998). The imbalance of CBF and $CMRO_2$ can be characterised by the oxygen extraction fraction OEF via Fick's principle, where $[O_2]_a$ is the concentration of oxygen in arterial blood in units of moles per millilitre.

$$CMRO_2 = OEF \cdot CBF \cdot [O_2]_a \qquad (50)$$

According to equation 50 OEF decreases in order to compensate for strong CBF increases compared with changes in oxygen metabolism during functional activation. There is also experimental evidence for this (Fox & Raichle, 1986). The reduction of OEF during cerebral functional activation combined with increases in CBF, CBV and $CMRO_2$ are the physiological basis of the BOLD effect. Although numerous studies have investigated the origins of the BOLD signal and its contributors, the functional significance of changes in OEF remain less well understood.

Beside changes in blood flow, oxygen metabolism, glucose metabolism and oxygen extraction fraction, changes in cerebral blood volume have been observed during functional activation. Cerebral blood volume is defined as the fraction of the tissue volume that is occupied by blood vessels. Typical values of total blood volume ($CBV_t$) are in the range of 4 to 6% (Gu et al., 2006; Ito et al., 2004; Lu et al., 2005). More careful measurements indicate an arterial ($CBV_a$) contribution of 15% to 25%, a capillary ($CBV_c$) contribution of 35% to 45% and a venous ($CBV_v$) contribution of 40% to 55% to the total cerebral blood volume (An & Lin, 2002b; An & Lin, 2002a; Donahue et al., 2009; Kim & Kim, 2005; Pawlik et al., 1981). Total blood volume changes during activation processes have been measured to be typically around 30%. When assuming arterial blood volume changes of approximately 80% (Lee et al., 2001), capillary changes of 20% (Krieger et al., 2012) and venous changes of about 5% (Berwick et al., 2005; Chen & Pike, 2009; Drew et al., 2011; Hillman et al., 2007), the arterial, capillary and venous contribution to functionally induced changes in blood volume will be 60%, 30% and 10% of the total CBV change, respectively.

The velocity with which blood is moving ranges from 10 to 50cm/s in large arteries down to 1mm/s in the capillaries. A functionally induced regional increase in CBF is usually associated with an increase in blood velocities (Bereczki et al., 1993) which causes a local decrease in the mean transit

time (MTT) and the arterial arrival time (AAT) (Mildner et al., 2014; Mildner et al., 2003).

## 2.4.4 The BOLD Contrast

The physiological parameters CBV, CBF, $CMRO_2$, and OEF affect the concentration of deoxyhaemoglobin inside the blood vessels. Deoxyhaemoglobin in turn produces magnetic field gradients within and around blood vessels that decrease the MR signal. During cerebral functional activation, changes in MR signals due to changes in deoxyhaemoglobin concentration can be measured via the so-called blood oxygenation level dependent (BOLD) contrast (Ogawa et al., 1990). Deoxyhaemoglobin plays an important role as endogenous contrast agent that induces a susceptibility difference between the extravascular and intravascular space.

The formation of BOLD signal changes as a physiological response to functional activation is rather counter-intuitive (Hyder et al., 2001; Buxton, 2012). An increase in neuronal activity increases oxygen metabolism which is accompanied by an increase in deoxyhaemoglobin which in turn reduces the BOLD signal. However, the local increase in CBF overcompensates the decrease in oxygen which produces a washout effect (Kida et al., 2004; Uludağ et al., 2009). Thus, brain activation is characterised by a decrease in local concentration of deoxyhaemoglobin and therefore an increase in MR signal (BOLD signal) (Fig 13) (Kim & Ogawa, 2012).
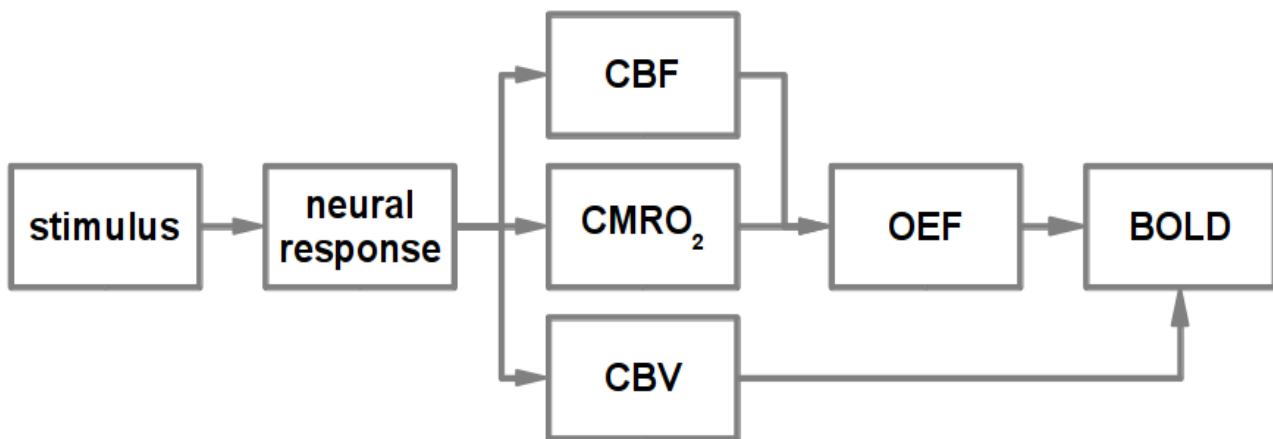


*Figure 13: The BOLD signal arises from changes in CBV, CBF and CMRO₂. CBF and CMRO₂ determine the temporal dynamics of OEF.*

The temporal shape of the BOLD signal has been characterised by numerous studies. For the first few seconds after the onset of the functional stimulus the BOLD signal does not increase significantly. Some studies even report an initial dip, potentially corresponding to an initial decrease in oxyhaemoglobin concentration before the haemodynamic response comes into play (Buxton, 2010). The initial dip is followed by a strong rise in BOLD signal. Some studies observed an

overshoot in BOLD signal before the plateau was reached after 5 to 10 seconds. After stimulus offset, the BOLD signal usually decreases below baseline which is called post stimulus undershoot (Poser et al., 2011; Hoge et al., 1999). This undershoot has suggested to originate from sustained elevated CBV or prolonged oxygen consumption (Buxton, 2010; Chen & Pike, 2010; Dechent et al., 2011; Mandeville et al., 1999; Poser et al., 2011; Schroeter et al., 2006). However, despite the intense study of the temporal features of the BOLD signal, there is no consensus on whether the over- and undershoot observed are based on neural, vascular or metabolic effects (Poser et al., 2011), especially since the precise shape of the BOLD signal depends on the activated brain area, the stimulus paradigm (Chen & Pike, 2009) and the cortical layers and vascular compartments (Kim & Kim, 2011).

## 2.4.5 Disadvantages of the BOLD Contrast

The BOLD signal is still the most widely used functional MRI contrast due to its good sensitivity. However, the BOLD effect is not a direct measure of neuronal activity but rather a secondary or even tertiary effect as BOLD relies on simultaneous changes in CBV, CBF, CMRO$_2$ and OEF which in turn are a physiological response to changes in neuronal activity states. The results obtained via cognitive, medical or psychological studies that use the BOLD signal as functional MRI contrast must therefore be interpreted with caution.

The most severe constraint in BOLD based fMRI, however, arises from the fact that the concentration in deoxyhaemoglobin not only changes at the spot of functional activation but also in the veins draining these brain areas (Turner, 2002). Changes in blood oxygenation arising from local brain activity-related changes in blood flow propagate downstream in veins and can give rise to spurious activation at sites remote from neuronal activity. The BOLD effect is most pronounced on GE-images, indicating that the effect is primarily an increase of the local value of $T_2^*$. At higher fields the intra vascular blood signal is suppressed because $T_2$ and $T_2^*$ of venous blood shortens with increasing field strength (Buxton, 2009). Although the BOLD contrast is the favoured fMRI technique, CBF and CBV approaches are finding wider appeal because these methods are affected less by the complicating factors that contribute to BOLD.

## *2.5 Arterial Spin Labelling (ASL)*

Using cerebral blood flow as indicator of brain activation provides several advantages compared to BOLD. Beside the fact that only one physiological parameter is utilised and therefore ambiguities in interpreting the MRI signal can be avoided, cerebral blood flow changes usually show an arterial and capillary weighting in contrast to BOLD, which is prone to venous downstream effects.

Therefore CBF based fMRI approaches are believed to be closer to the actual locations of cerebral activation than the BOLD signal.

A common method to measure either absolute values of CBF or flow changes in ASL. ASL uses blood water as an endogenous tracer. Blood water spins are tagged before they arrive in the tissue, and the amount of labelled blood delivered to the tissue is then measured (Detre et al., 1992). The most striking advantage of ASL is that ASL provides non-invasive images of local CBF with better spatial and temporal resolution compared to contrast agent injection techniques.

Although there is a large variety of ASL approaches and labelling schemes, the basic principle is always based on the subtraction of two consecutively acquired images. The first image (tag image) is usually acquired after tagging of blood water spins upstream to the area of interest, either via saturation (Detre et al., 1992; Pell et al., 1999) or inversion (Edelman et al., 1994; Williams et al., 1993). The second image (control image) is acquired without spin preparation and the subtraction of both images provides information about the amount of labelled blood magnetisation that flows into the imaging slab. By adding a delay called inversion time *TI* between labelling and signal acquisition, the labelled blood water can reach the capillary bed where it exchange with tissue water (see Fig 14).

The signal difference between tag and control image is only about 0.5% to 1.5% of the total MR signal and depends on many parameters such as cerebral blood flow, longitudinal relaxation time of blood and tissue, arterial arrival time and inversion time. Sufficient SNR is usually achieved by repeating the experiment and biophysical models are used to quantify absolute perfusion and estimated perfusion changes.

The different ASL techniques can be distinguished by the tagging approach, the acquisition of control and tag images and the handling of potential systematic errors such as bolus width definition. Classically two ASL techniques have been developed: continuous ASL (CASL) and pulsed ASL (PASL). In CASL the blood is labelled continuously below the imaging slab commonly in a supplying artery such as the carotid, thereby providing a temporally well defined bolus. In contrast, PASL uses an inversion slab which is labelled at a single instance using an RF inversion pulse. Imaging in PASL is performed after a time long enough for the spatially labelled blood to reach the tissue and exchange in the region of interest. In the studies of this thesis only the PASL technique has been applied.
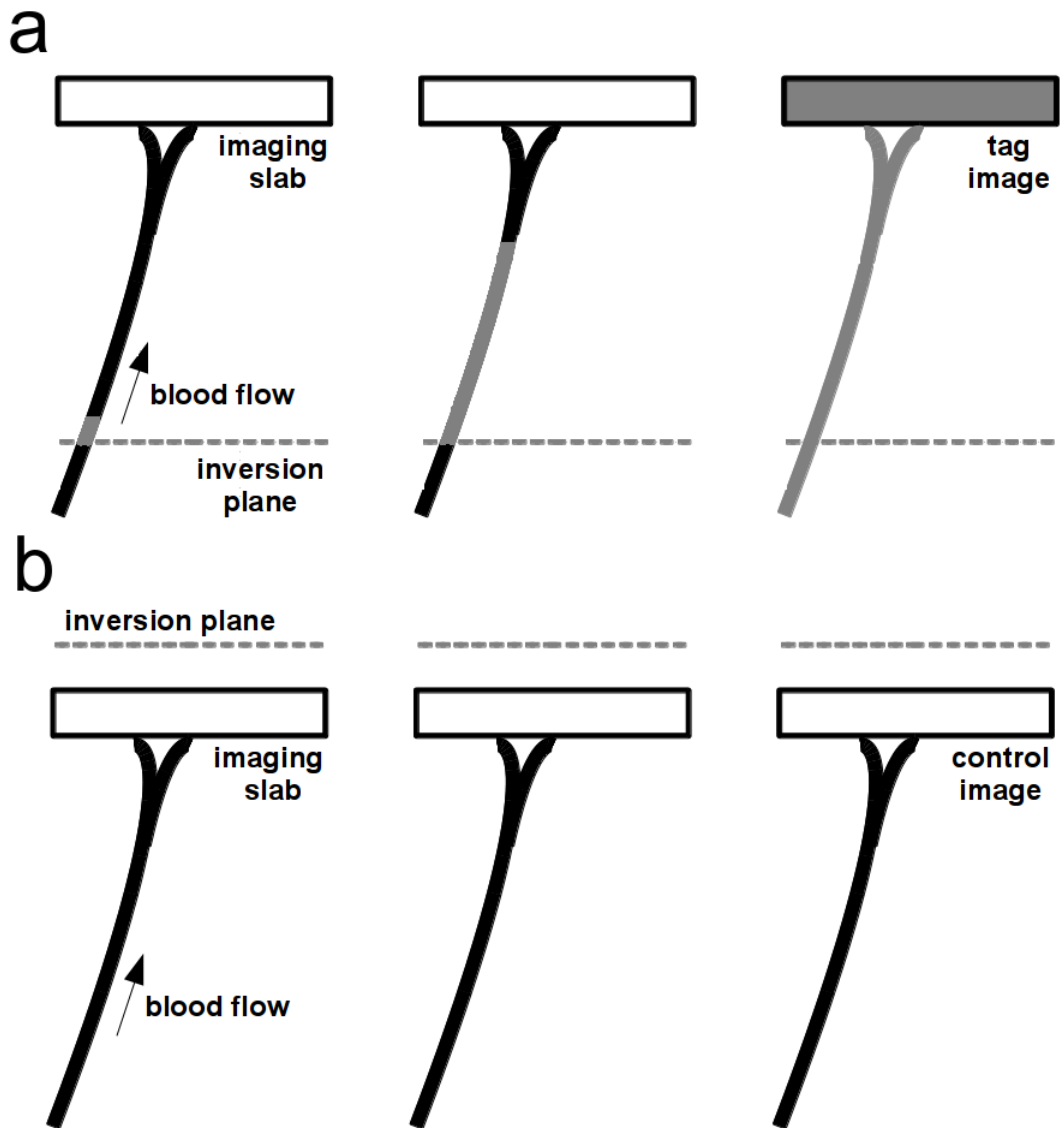
*Figure 14: Basic arterial spin labelling experiment. The magnetisation of arterial blood is inverted below the inversion plane via an RF pulse in the tag experiment (a). The inverted blood flows into the imaging slab where the MR image is acquired. In the control experiment (b) no spin inversion takes place.*

## 2.5.1 Pulsed Arterial Spin Labelling

In PASL, a single spatially selective 180° RF inversion pulse is applied which spatially defines the tagging bolus. Compared to CASL, a reduction of magnetisation transfer (MT) effects can be achieved, although, not completely avoided. PASL approaches can be subdivided into two categories, symmetrical and asymmetrical techniques.

Most symmetrical PASL techniques are based on the flow sensitive alternating inversion recovery (FAIR) (see Fig 15) labelling scheme (Kim, 1995; Kwong et al., 1995; Schwarzbauer et al., 1996). In FAIR, spin tagging is applied by using a non-selective inversion pulse while the control pulse is slab selective using an inversion slab width that is slightly larger than the imaging slab. The

symmetric nature of this labelling scheme automatically compensates for MT-effects.

Asymmetrical PASL techniques were introduced via the echo-planar MR imaging and signal targeting with alternating radio frequency (EPISTAR) labelling scheme (Edelman et al., 1994). EPISTAR uses a tagging band that is usually 10-15cm thick below the imaging slice while leaving a gap of 1cm between the edge of the band and the edge of the imaged slices. An identical inversion pulse is applied above the imaging slice. As MT effects are only compensated in a single slice, an improved version has been introduced via the PULSAR labelling scheme (Golay et al., 2005). Instead of a single inversion control pulse above the imaging slab, two 180° pulses with half of the power are applied also below the imaging slab.
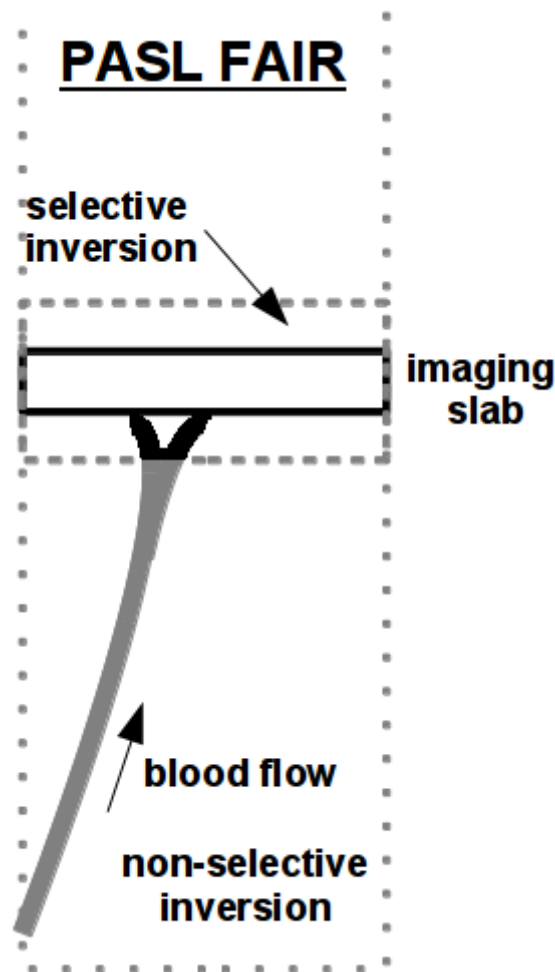


*Figure 15: The PASL FAIR labelling scheme.*

A major problem with PASL is venous blood back-flow into the imaging slab which potentially leads to an overestimation of CBF. A solution to this problem might be the proximal inversion with a control for off-resonant effects (PICORE) approach (Wong et al., 1997). The labelling RF pulse is

applied during the control phase (similar to EPISTAR) but the tag RF inversion pulse is applied with shifted frequency and no gradient. The image slab therefore experiences the same off-resonance RF pulse in tag and control images but due to the off-resonant frequency used in the tag condition no inversion actually takes place.

Most PASL techniques use a gap of about 1 to 2cm between the imaging and the labelling slab in order to limit the influence of imperfections in the inversion profile. This gap increases the arrival time of the tagged blood into the imaging slab which leads to a decreased contrast due to $T_1$ relaxation. The gap between imaging slab and inversion slab can be minimised by optimising the inversion profile by using improved inversion pulses such as the tr-FOCI for ultra-high magnetic field strengths (Hurley et al., 2010).

A major source of error in estimating CBF via PASL techniques is the difference of arterial arrival times (AAT) between brain regions. Although arterial arrival times can be estimated by using different inversion times most functional studies cannot use this approach as it would decrease the temporal resolution dramatically. In order to make the PASL technique more insensitive to differences in AAT, saturation pulses have been introduced after a first inversion time $TI_1$ in order to precisely define the labelling bolus length in temporal units, such as in CASL techniques. The MR images are acquired after a second inversion time $T_2$. There are two major saturation schemes that can be used: either a single saturation pulse is applied in the area below the imaging slab (QUIPSSII) (Wong et al., 1998b) or a high number of small saturation pulses is applied from $TI_1$ to $T_2$ (Q2TIPS) (Luh et al., 1999). Whereas Q2TIPS has been found to provide better results compared to QUIPSSII, Q2TIPS is hardly applicable at ultra-high magnetic field MR scanners due to its high energy deposition.

There are two requirements for the QUIPSSII technique to work properly. First, the saturation pulse must be applied before fresh blood flows into the imaging slab. Second, the delay after the saturation pulse must be long enough to allow blood water exchange through the capillary walls. Also it is advisable to adjust the acquisition scheme such that the most distal slice with the longest arterial arrival time is acquired last. However, this proximal to distal acquisition order can create problems with large supplying arteries that run through more proximal slices. Therefore it is important that the second inversion time $TI_2$ is long enough to allow blood that is running through these supplying arteries to be cleared (Detre et al., 1998; Yang et al., 1998; Ye et al., 1997).

Arterial spin labelling experiments are usually described via the general kinetic model which takes into account the $T_1$ relaxation time differences between tissue and blood, the arterial transit time

from the tagging to the imaging slab and the spatial appearance of the tagging bolus (Buxton et al., 1998). The magnetisation difference between label and control experiment is defined via equation 51. $M_{a,0}$ represents the equilibrium magnetisation of a voxel containing arterial blood, $c(\tau)$ is the arterial input function (AIF), $r(t-\tau)$ is the residue function which represents the clearance of labelled spins from a voxel and $m(t-\tau)$ describes the longitudinal relaxation effects.

$$\Delta M(t) = 2 M_{a,0} CBF \int_0^t c(\tau) r(t-\tau) m(t-\tau) d\tau \tag{51}$$

This model is flexible and allows the description of CASL and PASL experiments by adjusting $c(\tau)$, $r(t-\tau)$ and $m(t-\tau)$. When defining $T_{ex}$ as the time of exchange of blood water into the extravascular space, $\tau_d$ as the delay of water arriving in the voxel and $\tau_a$ as the arterial transit time the following expressions are obtained for the PASL experiment.

$$c(t) = \begin{cases} 0 & t < \tau_a \\ \alpha e^{-\frac{t}{T_{1,a}}} & \tau_a \le t \le \tau_d \\ 0 & t \ge \tau_d \end{cases} \tag{52}$$

$$r(t) = e^{-\frac{CBF \cdot t}{\lambda}} \tag{53}$$

$$m(t) = \begin{cases} e^{-\frac{t}{T_{1,a}}} & t < T_{ex} \\ e^{-\frac{T_{ex}}{T_{1,a}}} e^{-\frac{t-T_{ex}}{T_{1,t}}} & t > T_{ex} \end{cases} \tag{54}$$

Water exchange through the capillary wall is modelled as an instantaneous process $T_{ex} = \tau_a$. Therefore labelled blood water spins relax with $T_{1,a}$ before the exchange and with $T_{1,t}$ after the exchange and equations 50 to 54 become

$$\Delta M(t) = \begin{cases} 0 & t < \tau_a \\ \dfrac{-2aM_{a,0} CBF}{\delta R} e^{-R_{1,a}t} \left(1 - e^{-\delta R(t-\tau_a)}\right) & \tau_a \le t \le \tau_d \\ \dfrac{-2aM_{a,0} CBF}{\delta R} e^{-R_{1,a}\tau_d} \left(1 - e^{-\delta R(t-\tau_a)}\right) e^{-R_{1,app}(t-\tau_d)} & t \ge \tau_d \end{cases} \tag{55}$$

where $R_{1,a}=\dfrac{1}{T_{1,a}}$, $\delta R = R_{1,a} - R_{1,app}$ and $R_{1,app} = R_{1,t} + \dfrac{CBF}{\lambda}$. The parameters $\tau_a$, $\lambda$, $M_{a,0}$, $R_{1,a}$,

$R_{1,t}$ need to be either measured or assumed in order to quantify CBF. Equation 55 describes the longitudinal magnetisation before a gradient or spin echo is generated via an excitation RF pulse. During the echo time SNR is decreased by $T_2$ or $T_2^*$ signal decay and it is therefore important to obtain short *TE* in PASL experiments.

## 2.5.2 Arterial Spin Labelling at Ultra-High Field

The most obvious advantage of higher field strengths is based on the theoretical increase in SNR due to the direct relationship of MR signal to static magnetic field strength. Especially low SNR techniques such as ASL could benefit from increased static magnetic fields due to the assumed linear increase in SNR with the main magnetic field. Especially inversion recovery based MR techniques furthermore benefit from increased longitudinal relaxations times $T_1$ (Rooney et al.,

2007; Zhang et al., 2013). $T_1$ has actually been suggested to have the dependence $T_1 \sim \omega^{\frac{1}{3}}$ (Golay & Petersen, 2006; Wang et al., 2002). However, decreased relaxations times $T_2$ and $T_2^*$ of tissue and blood with higher field strengths counteract the signal increase due to increased $T_1$ (Teeuwisse et al., 2010). Therefore it is crucial at ultra-high field MRI to achieve minimal echo times.

The most severe problem, especially at 7 Tesla and higher field strengths is inhomogeneities in the magnetic field. Differences in resonance frequencies between brain and large arteries become larger with higher field strengths which could cause irregular profiles across large arteries (Teeuwisse et al., 2010). Magnetic field inhomogeneities can also affect the flip angle of excitation or inversion RF pulses which could negatively influence the accuracy of PASL techniques (Gardener et al., 2009). Current ultra-high field MR systems use an RF head coil which has intrinsically limited width of the labelling slab because the $\boldsymbol{B_1}$ field decreases towards the end of the coil. In order to avoid CBF underestimation these limitations must be accounted for by either using techniques to precisely define the labelling bolus, such as QUIPSSII or Q2TIPS, or by assessing the labelling profile in the same scan.

Higher field strength MR systems are also more vulnerable to physiological noise which scales with field strength. Larger voxel sizes translate directly into better SNR but simultaneously increase the amplitude of physiological noise (Krüger & Glover, 2001; Triantafyllou et al., 2005). Also, the temporal stability of a typical voxel size used for ASL techniques at lower field strengths does not increase due to physiological noise (Triantafyllou et al., 2005). However, labelling efficiency can be

reduced when Larmor frequency fluctuations due to breathing are not corrected.

Another restriction at ultra-high magnetic fields arises from the radio-frequency transmitting hardware (Duyn, 2012; Yacoub et al., 2001). Whereas at lower field strengths a body coil or a neck coil is used to label arterial spins globally in PASL sequences, or selectively label spins in the carotid arteries in CASL sequences, such equipment is not readily available at 7 Tesla. Therefore ASL at ultra-high field may suffer from reductions in functional SNR.

## *2.6 Vascular Space Occupancy (VASO)*

Recently, MRI studies of human brain function have begun to investigate changes in cerebral blood volume (CBV) in addition to CBF and BOLD based methods. CBV has been measured as blood plasma volume ($CBV_p$) via blood pool contrast agents (Leite et al., 2002; Zhao et al., 2001) and volume of haemoglobin ($CBV_h$) via optical techniques (Devor et al., 2008; Hudetz, 1997; Kennerley et al., 2005). The recently invented VASO (Vascular Space Occupancy) technique allows the estimation of total blood volume ($CBV_t$) without exogenous tracers (Lu et al., 2003). VASO is an inversion recovery technique which is based on the nulling of the blood signal when acquiring MRI data. The magnetization signal originates only from the tissue and the CSF of each voxel. During neuronal activity, CBV increases at the expense of the tissue which leads to a decreasing MRI signal during neuronal activation processes. Therefore, the VASO contrast can be used to dynamically detect neuronal activity based changes of CBV and quantitatively estimate CBV contents of each voxel. A sequence diagram and the corresponding z-magnetisation of grey matter, CSF and blood can be found in Fig 16. Equation 56 shows the VASO signal dependence when using a gradient echo readout sequence.

$$S_{VASO} \sim M(TI) e^{-\frac{TE}{T_2^*}} = M_0 [1 - 2 e^{-\frac{TI}{T_1}} + e^{-\frac{TR}{T_1}}] e^{-\frac{TE}{T_2^*}} \tag{56}$$

VASO signal changes are described by vessel diameter changes and an opposite change in grey matter signal in a voxel. The vascular space occupancy of a vessel is defined as

$$\xi_i = \frac{CBV_i}{V_{par}} = \frac{CBV_i}{V_{tissue} + \sum_i CBV_i} \tag{57}$$

with $_i$ representing the vessel and $_{par}$ the parenchyma. When defining $\xi = \sum_i \xi_i$ as the total microvascular space occupancy the VASO signal change due to neuronal activity becomes (in the

case of flow independent inversion):

$$\frac{\Delta S_{VASO}}{S_{VASO}} = \frac{S_{par}^{act} - S_{par}^{rest}}{S_{par}^{rest}} = \frac{\left(C_{par} - \xi^{act} C_{blood}\right)e^{-\frac{TE}{T_{2,tissue}^{*,act}}} - \left(C_{par} - \xi^{rest} C_{blood}\right)e^{-\frac{TE}{T_{2,tissue}^{*,rest}}}}{\left(C_{par} - \xi^{rest} C_{blood}\right)e^{-\frac{TE}{T_{2,tissue}^{*,rest}}}} \tag{58}$$
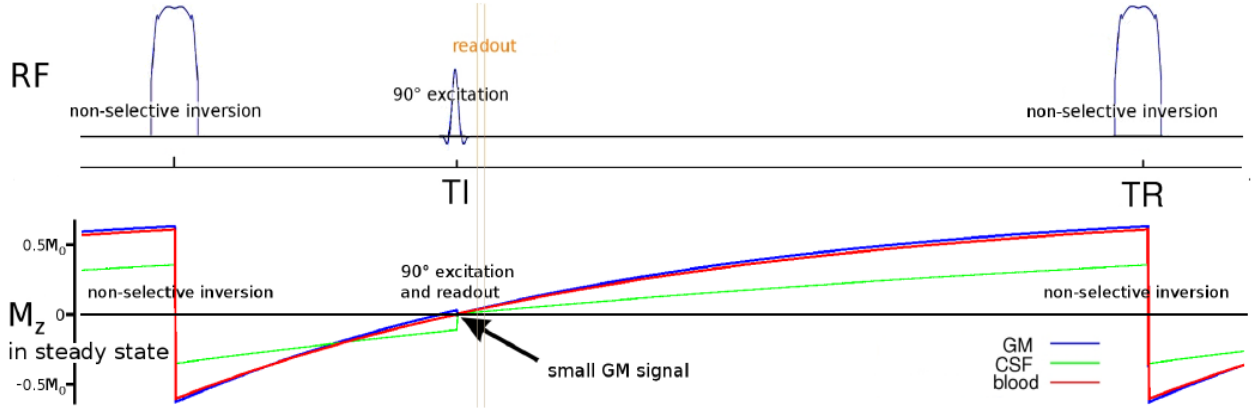
with $C$ being the water density of blood or tissue.



*Figure 16: Sequence diagram of classic VASO including the corresponding steady-state z-magnetisation of grey matter (blue line), CSF (green line) and blood (red line). The functional contrast of VASO originates from changes in residual tissue signal at the blood nulling time point.*

The original VASO technique was proposed as a single slice method based on a gradient echo EPI readout (Lu et al., 2003). Consequently, the original VASO technique was restricted to functional MRI studies of large cortical areas such as motor or visual cortex only. During the last decade, significant improvements of the VASO technique have been proposed. Spin-echo EPI (Donahue et al., 2006) and HASTE (Poser & Norris, 2007) readout techniques have enhanced the sensitivity of the VASO technique. Magnetization transfer preparation (Hua et al., 2009) increases SNR and CNR significantly. Magnetization transfer effects take place predominantly in tissue rather than blood which leads to a faster recovery process of tissue magnetization. Consequently, the signal difference of blood and tissue increases which leads to an improved signal-to-noise ratio. Better cortical-layer specificity could be reached via an adaptation for high-resolution scans on small animals (Jin & Kim, 2008). The limited volume coverage of the original VASO technique could be improved by using a global inversion cycling scheme (MAGIC) (Lu, van Zijl, et al., 2004). This technique could be extended to whole-brain coverage (Scouten & Constable, 2007) and was utilized in functional MRI studies with visual, motor and auditory stimulation.

An alternative whole-brain VASO approach is based on the 3D gradient and spin-echo readout technique (Poser & Norris, 2009). This readout method has already been used for arterial spin labelling techniques (Fernández-Seara et al., 2005; Tan et al., 2011). 3D GRASE is a very fast readout technique and allows acquisition of a 3D volume within several tens of milliseconds. Consequently, $T_1$ decay during the readout is not an issue. However, $T_2$ decay is a problem as the readout duration is in the range of $T_2$ which can lead to distortions in the reconstructed MRI images. 3D GRASE VASO has also been combined with the VASO-FLAIR technique (Donahue et al., 2009).

Beside the fact that the BOLD contrast is a quite robust and easily applicable technique with high SNR, its major disadvantage lies in its bad spatial specificity. As oxygenation changes do not only appear at the site of neuronal activity, but also at distant regions of large draining veins, the BOLD contrast usually shows activation patterns which largely extend the area of neuronal activation (Iadecola, 2002; Turner, 2002). Comparative fMRI measurements of VASO and BOLD in humans at 3T have confirmed this theoretical prediction (Lu & van Zijl, 2012) and functional high-resolution MRI scans of the cat brain verified these findings (Jin & Kim, 2008). BOLD activation patterns cover broad areas of cortical layers and brain regions containing large vessels, whereas VASO reveals distinct areas of neuronal activity. Additionally, VASO signal peaks have been found to originate from layer IV of the visual cortex during visual stimulation whereas the BOLD signal originates equally from all layers (Jin & Kim, 2008). Therefore, VASO can provide clearer boundaries between adjacent visual cortices than BOLD contrast (Lu & van Zijl, 2005).

## 2.6.1 VASO at Ultra-High Field

VASO techniques at ultra-high field strengths (such as 7T) provide four major challenges. First, blood and grey matter $T_1$ converge at high field strengths (Jin & Kim, 2008; Rooney et al., 2007). Despite the absolute increase of $T_1$ times, this results in a very small tissue signal at the blood nulling time-point. Second, increasing BOLD signal at high field strengths can counteract the VASO image (Lu & van Zijl, 2005). Gradient echo BOLD is known to have both intra-vascular and extra-vascular contributions, but since the blood signal is nulled in VASO experiments only the extra-vascular BOLD effect can contribute to the VASO contrast. This extras-vascular part has been found to increase with higher field strengths compared to its intra-vascular counterpart (Faro & Mohamed, 2010). Therefore, for long echo times the VASO signal change may even change sign and become positive due to large BOLD signal contributions (Lu & van Zijl, 2005). Third, magnetic field inhomogeneities and limits in the specific absorption rate of the transmitted energy hamper

spin inversion efficiency which is an issue for all inversion recovery based MR techniques. Fourth, unlike at lower field strengths only head coils are available for RF transmission at ultra-high fields which results in reduced inversion volume. Therefore the likelihood of fresh blood inflow during the nulling time is increased. Furthermore, the blood nulling time is increased at ultra-high fields compared to lower field strengths due to increased blood $T_1$ which increases the possibility of inflow effects in VASO.

## 2.6.2 Slice-Saturation Slab-Inversion (SS-SI) VASO

Due to the issues discussed above VASO was only recently implemented successfully at ultra-high magnetic field. Hua et al. used an off-resonant magnetisation transfer pulse to increase the tissue signal by up to a factor of 1.5 (Hua et al., 2012; Hua et al., 2009). In another study the steady-state z-magnetisation of VASO was increased by adapting $TR$ and $TI$ appropriately (Jin & Kim, 2008; Shen et al., 2009; Wu et al., 2008; Wu, Buxton, et al., 2007).

However, there is evidence that the z-magnetisation cannot approach a steady state at ultra-high fields when using short $TR$ as required for fMRI (Jin & Kim, 2006). A slab selective inversion which matches the volume included by the coil coverage was therefore used. Blood z-magnetisation was maintained in a non-steady state and the blood nulling time is adjusted accordingly. Simulations of this approach showed a significant increase in the remaining tissue signal (Jin & Kim, 2008).

Following this idea the slice-saturation slab-inversion VASO (SS-SI-VASO) technique was introduced recently (Huber, Ivanov, et al., 2014). A slab-selective inversion pulse is applied to increase SNR compared to the original VASO approach (see Fig 17). In humans, the arterial arrival time is similar to the blood nulling time which enables adjustment of the $TI$ and the inversion slab thickness mutually so that all blood in the microvasculature is nulled which reduces potential inflow contamination of the VASO contrast. The stationary grey matter magnetisation at the blood nulling time is further increased by applying additional 90° RF pulses in the imaging slices just before the slab selective inversion. The z-magnetisation of tissue at inversion time results in an increased at the blood nulling time.

The increase in tissue signal is achieved by manipulating the z-magnetization of flowing blood differently from that of grey matter. $TR$, $TI_1$, $TI_2$, inversion efficiency and inversion slab thickness are adjusted such that no non-inverted blood enters the microvasculature of the imaging region during $TI_1$. Furthermore, the microvasculature of the imaging slice is refreshed by spins outside the imaging slice of between $TI_2$ of the previous $TR$ and $TI_1$ of the of the present $TR$. Increased tissue

signal in SS-SI-VASO originates primarily from the small z-magnetisation of grey matter at the inversion time which increases until the MR image is acquired. An additional signal increase comes from the increased blood nulling time of once-inverted compared with steady-state blood, providing the z-magnetization of the neighbouring tissue more time to undergo longitudinal relaxation.
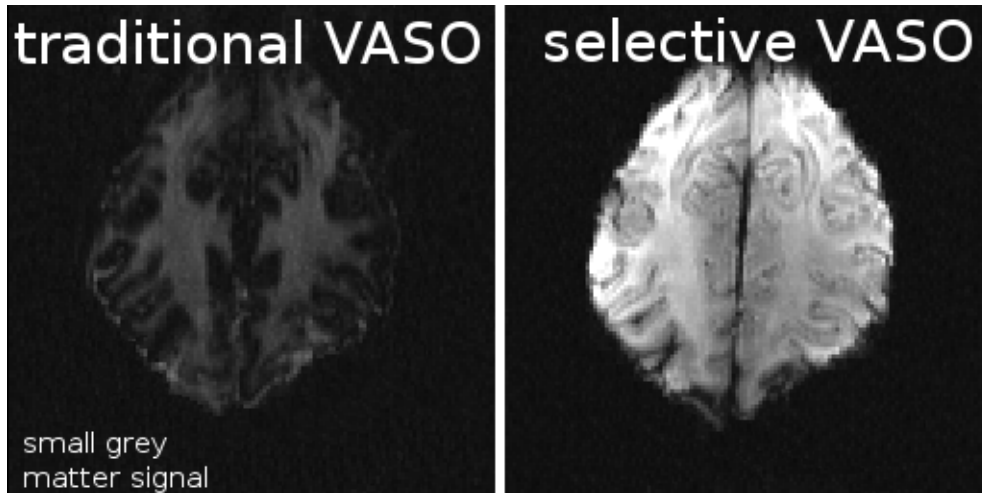


*Figure 17: Traditional VASO (a) and SS-SI-VASO (b) images acquired at ultra-high field. Both images were acquired with the same imaging parameters: $TR = 1.5s$, spatial isotropic resolution=1.5mm, $TE = 19ms$. The blood nulling time used for (left) was $TI = 604ms$ and for (right) was $TI = 1328ms$. The grey matter signal obtained via SS-SI-VASO is much higher than they grey matter signal obtained via original VASO.*

When assuming a blood $T_1$ at 7 Tesla of 2100ms (Dobre et al., 2007; Zhang et al., 2013) the blood nulling time can be calculated via $TI_1 = \ln(2) \cdot T_{1,blood} = 1450ms$. The inversion slab must be large enough that no fresh blood reaches the imaging slice during that time. In humans, the arterial arrival time of the occipital lobe is approximately 1500-2000ms (Chen et al., 2012; Wong et al., 1997). These numbers suggest that the blood-nulling time used by SS-SI-VASO at 7 Tesla is shorter than the AAT of fresh blood, and it takes longer than $TI_1$ for non-inverted blood magnetization to arrive in the microvasculature of the imaging slice.

SS-SI-VASO relies on blood water signal that has experienced a single inversion only and therefore the technique is based on a refill condition. The period between two image acquisitions must be longer than the refill time of the vasculature of the imaging slice in order to avoid spin history and saturation effects. Detailed studies of the microvasculature revealed refill times of 1-1.5s (Hillman et al., 2007; Kleinfeld et al., 1998; Pawlik et al., 1981) and due to higher flow rates in larger vessels refill times in arteries can be assumed to be even smaller. SS-SI-VASO can therefore be assumed to show negligible spin history effects when assuming typical $TR$.

## *2.7 Calibrated Functional Magnetic Resonance Imaging*

As discussed in the previous chapters, using CBV and CBF as endogenous markers of neuronal activity can provide advantages regarding spatial localisation and specificity as compared to the BOLD signal. However, haemodynamic responses to changes in brain activity are indirect measures of neuronal activity. Brain activity changes are accompanied by changes in oxygen metabolism. Measuring changes in CMRO$_2$ directly could produce measurements spatially and temporally closer to the sites of neuronal activation (Hyder et al., 2010).

Calibrated BOLD fMRI is a non-invasive MRI technique that enables estimation of CMRO$_2$ (Davis et al., 1998; Hoge et al., 1999). The classic approach is based on simultaneous acquisition of CBF and BOLD weighted MRI images during a gas-breathing manipulation. Based on these signals the calibration constant $M$ can be calculated which is then used to estimate changes in oxygen metabolism during an additional functional scan.

## 2.7.1 The Davis Model

Various calibrated fMRI approaches have advantages and disadvantages with regards to sensitivity, stability, reproducibility and applicability (Blockley, Griffeth & Buxton, 2012; Blockley, Griffeth, Simon, et al., 2012; Bulte et al., 2012; Driver et al., 2012; Gauthier et al., 2012; Gauthier et al., 2011; Herman et al., 2013; Hyder et al., 2001; Kim et al., 1999; Liu, Xu, et al., 2013; Mark et al., 2011; Tancredi & Hoge, 2013; Wise et al., 2013; Xu et al., 2009). The original and probably most commonly used technique was introduced in 1998 and is based on a hypercapnic gas-breathing challenge and a biophysical model as detailed below (Davis et al., 1998; Hoge et al., 1999).

For a gradient echo sequence the MR signal can be described via a single compartment model

$$S = S\left(TE = 0\right) \sim e^{-TE \cdot R_2^*} \tag{59}$$

where $S\left(TE = 0\right)$ is the intrinsic signal and $R_2^*$ the transverse relaxation net rate. $R_2^*$ can be decomposed into two parts, one relaxation rate caused by deoxyhaemoglobin $R_2^*|_{dHb}$ and another one based on all other sources.

$$R_2^* = R_2^*|_{dHb} + R_2^*|_{other} \tag{60}$$

Furthermore, $R_2^*|_{dHb}$ can be related to venous CBV and the venous deoxyhaemoglobin content of blood via the following equation (Boxerman et al., 1995).

$$R_2^*|_{dHb} = A \cdot CBV \cdot [dHb]_v^\beta \qquad (61)$$

where $R_2^*|_{dHb}$ is a constant that is field strength and sample dependent, $\beta$ is a constant in the range of $1 \leqslant \beta \leqslant 2$ ( $\beta \approx 1.3$ for 3 Tesla and $\beta \approx 1.0$ for 7 Tesla).

Changes in $R_2^*|_{dHb}$ can be induced by changes in CBF and CBV (for example due to functional activation).

$$\Delta R_2^*|_{dHb} = A \left( CBV \cdot [dHb]_v^\beta - CBV_0 \cdot [dHb]_{v_0}^\beta \right) \qquad (62)$$

The subscript zero represents the baseline values of each quantity. Changes in the $T_2^*$ weighted MR images due to changes in transverse relaxation rate can be expressed as

$$\frac{\Delta\,\mathrm{BOLD}}{\mathrm{BOLD}_0} \sim e^{-TE\,\Delta R_2^*|_{dHB}} - 1 \approx -TE\,\Delta R_2^*|_{dHb} \qquad (63)$$

whereas the last term is based on a linear approximation for small transverse relaxation rate changes. $\Delta R_2^*|_{dHb}$ can be substituted by via equation 62.

$$\frac{\Delta\,\mathrm{BOLD}}{\mathrm{BOLD}_0} \approx TE \cdot A \cdot CBV_0 \cdot [dHb]_{v_0}^\beta \left( 1 - \frac{CBV}{CBV_0} \frac{[dHb]_v}{[dHb]_{v_0}} \right)^\beta \qquad (64)$$

The first part of equation 64 is the maximum attenuation of the BOLD signal due to elimination of all deoxyhaemoglobin of the sample. Henceforth, this attenuation is referred to as $M$ .

$$M = TE \cdot A \cdot CBV_0 \cdot [dHb]_{v_0}^\beta \qquad (65)$$

When assuming a negligible concentration of deoxyhaemoglobin in arterial blood, Fick's principle relates oxygen metabolism, cerebral blood flow and venous concentration of deoxyhaemoglobin via mass conservation.

$$[dHb]_v = \frac{1}{4} \frac{CMRO_2}{CBF} \qquad (66)$$

Fractional changes in deoxyhaemoglobin can therefore be expressed via changes in CMRO$_2$ and CBF.

$$\frac{[dHb]_v}{[dHb]_{v_0}} = \frac{CMRO_2}{CMRO_2|_0} \frac{CBF_0}{CBF}$$

(67)

When using equation 65 and equation 67 to replace the appropriate expression in equation 64 relative BOLD signal changes can be expressed via changes in CBV, CBF and CMRO$_2$.

$$\frac{\Delta BOLD}{BOLD_0} \approx M \cdot \left(1 - \frac{CBV}{CBV_0} \frac{CMRO_2}{CMRO_2|_0} \frac{CBF_0}{CBF}\right)^\beta$$

(68)

Although several techniques have been introduced to simultaneously measure CBV, CBF and CMRO$_2$ (Yang et al., 2004) the more common MRI techniques either measure CBF and BOLD weighted signals or CBV and BOLD weighted signals, and therefore the classic Davis model uses the Grubb equation 69 to eliminate CBV from equation 68 and obtain equation 70 (Grubb et al., 1974).

$$\frac{CBV}{CBV_0} = \left(\frac{CBF}{CBF_0}\right)^\alpha$$

(69)

$$\frac{\Delta BOLD}{BOLD_0} = M \cdot \left(1 - \left(\frac{CMRO_2}{CMRO_2|_0}\right)^\beta \cdot \left(\frac{CBF}{CBF_0}\right)^{\alpha-\beta}\right)$$

(70)

Equation 70 can be used to estimate changes in oxygen metabolism during a functional stimulus based on measurements of BOLD and CBF weighted MRI signals if the calibration parameter $M$ is well known.

$$\frac{CMRO_2}{CMRO_2|_0} = \left(1 - \left(\frac{\frac{\Delta BOLD}{BOLD_0}}{M}\right)\right)^{\frac{1}{\beta}} \left(\frac{CBF}{CBF_0}\right)^{1-\frac{\alpha}{\beta}}$$

(71)

When using Davis' calibrated BOLD approach, $M$ is estimated via an additional MRI scan without

functional stimulus but with a hypercapnic breathing challenge. Hypercapnia is assumed not to influence oxygen metabolism and therefore equation 70 simplifies to

$$\frac{\Delta \text{BOLD}}{\text{BOLD}_0} = M \cdot \left(1 - \left(\frac{CBF}{CBF_0}\right)^{\alpha-\beta}\right)$$

(72)

Once $M$ has been estimated via hypercapnia and equation 72, functionally induced changes in $CMRO_2$ can be easily calculated via equation 71.

## 2.7.2 The Chiarelli Model

An alternative calibrated fMRI approach based on hyperoxia rather than hypercapnia has been introduced in order to avoid increased discomfort occurring when breathing $CO_2$ gas mixtures. Breathing oxygen enriched gas mixtures induces measurable changes in the concentration of oxygenated capillary and venous haemoglobin. The hyperoxia based calibration approach requires the measurement of BOLD signal changes and end-tidal $O_2$ values. Additional CBF data is used to correct for small amounts of CBF changes during oxygen inhalation.

The theoretical model used to obtain the hyperoxia based calibration parameter $M$ relies on the same concept as the Davis model (see equation 64). However, small changes in CBF due to hyperoxia are accounted for by the CBV and $[dHb]$ correction terms in equation .

$$\frac{\Delta \text{BOLD}}{\text{BOLD}_0} = M \left(1 - \frac{CBV}{CBV_0} \left(\frac{[dHb]_v}{[dHb]_{v_0}} + \frac{\Delta[dHb]_v}{[dHb]_{v_0}}\right)^{\beta}\right)$$

(73)

When using Fick's principle and the Grubb relation similar to the Davis model one obtains the Chiarelli model for hyperoxia calibrated fMRI.

$$\frac{\Delta \text{BOLD}}{\text{BOLD}_0} = M \left(1 - \left(\frac{CBF}{CBF_0}\right)^{\alpha} \left(\frac{[dHb]_v}{[dHb]_{v_0}} + \frac{CBF_0}{CBF} - 1\right)^{\beta}\right)$$

(74)

In contrast to the Davis model, the Chiarelli model does not substitute the expression for deoxyhaemoglobin in equation 74 with equation 67 but uses standard physiological equations of oxygen transport to estimate $[dHb]_v$ and $[dHb]_{v_0}$ via measured end-tidal oxygen values.

The fractional arterial oxygen saturation $Sa_{O_2}$ is related to $Pa_{O_2}$ via the Severinghaus equation

(Severinghaus, 1979a; Severinghaus, 1979b).

$$Sa_{O_2} = \cfrac{1}{\cfrac{23400}{Pa_{O_2}^3 + 150\left(Pa_{O_2}\right)} + 1} \tag{75}$$

Based on equation 75 the arterial oxygen content can be calculated. The left term of equation 76 represents the contribution from oxygen that is bound to haemoglobin and the right term is the contribution from oxygen dissolved in blood plasma.

$$Ca_{O_2} = \left(\varphi \cdot [Hb] \cdot Sa_{O_2}\right) + \left(Pa_{O_2} \cdot \epsilon\right) \tag{76}$$

where $\varphi$ is the oxygen carrying capacity of haemoglobin which is species dependent and $\epsilon$ is the solubility coefficient of oxygen in blood. In humans the following values can be used: $\varphi = 1.34 \, ml_{O_2}/g\,Hb$ , $\epsilon = 0.0031 \, ml_{O_2}/\left(dl_{blood} \cdot mmHg\right)$ .

When assuming a resting oxygen extraction fraction (OEF) the venous oxygen content can be calculated.

$$Cv_{O_2} = Ca_{O_2} - \left(Ca_{O_2}|_0 \cdot OEF\right) \tag{77}$$

As the extracted oxygen remains constant during hyperoxia the venous oxygen saturation can be calculated as follows.

$$Sv_{O_2} = \cfrac{Cv_{O_2} - \left(Pv_{O_2} \cdot \epsilon\right)}{\varphi \cdot [Hb]} \tag{78}$$

$$Cv_{O_2} = \left(\varphi \cdot [Hb] \cdot Sv_{O_2}\right) + \left(Pv_{O_2} \cdot \epsilon\right) \tag{79}$$

When solving equation 78 for $[Hb]$ and estimating $Sv_{O_2}$ via $Cv_{O_2}$ the calibration constant $M$ can be estimated via equation 74. $Pv_{O_2}$ is usually assumed to be negligible.

As the meaning of $M$ in the Chiarelli model is the same as in the Davis model, equation 71 is still

valid and changes in oxygen metabolism can be calculated via equation 71.

## 2.7.3 The Generalised Calibration Model (GCM)

The hyperoxia model introduced in the last section is valid for small or no changes in cerebral blood flow during gas inhalation. The generalised calibration model (GCM) has been derived from the Chiarelli model to allow arbitrary changes in CBF during the calibration procedure rendering it valid for breathing challenges that require combined hypercapnia-hyperoxia (Gauthier & Hoge, 2013).

In the GCM, equation 77 is is replaced by the following expression.

$$CBF \cdot Cv_{O_2} = CBF \cdot Ca_{O_2} - CBF_0 \cdot \left( Ca_{O_2}|_0 \cdot OEF_0 \right) \tag{80}$$

The resting oxygen extraction fraction $OEF_0$ is assumed constant across brain regions and subjects. Equation 80 describes the temporal flux of oxygen at the capillary level and when solved for the venous oxygen concentration equation 80 becomes

$$Cv_{O_2} = Ca_{O_2} - \frac{Ca_{O_2}|_0 \cdot OEF_0}{\dfrac{CBF}{CBF_0}} \tag{81}$$

Based on equation 81 and equations 76, 75 and 78 the calibration parameter $M$ can be estimated for arbitrary changes of CBF:

$$M = \frac{\dfrac{\Delta BOLD}{BOLD_0}}{1 - \left( \dfrac{CBF}{CBF_0} \right)^\alpha \dfrac{1 - Sv_{O_2}}{1 - Sv_{O_2}|_0}} \tag{82}$$

Once $M$ is estimated changes in oxygen metabolism can be calculated as usual via equation 71.

# 3 Materials and Methods

## *3.1 Scanner Setup*

All experiments were performed on a Siemens Magnetom 7 Tesla whole body MR scanner Siemens Healthcare, Erlangen, Germany). The software baseline used for all experiments was VB 17A. MR sequence modifications and developments were necessary for the projects described in the following three chapters. These modifications will be described in detail in chapter 3.3 below. A 25 channel head coil (NOVA Medical Inc, Wilmongton, MA, USA) was used for signal transmission and reception. A CP volume transmission coil and 24-element receive array were arranged in a helmet-like geometry. The coil is designed to tightly fit the subject's head to provide a high fill factor giving good SNR characteristics.

The functional stimuli used in this study were developed in and presented with the Presentation 14 (Neurobehavioral Systems Inc, Albany, CA, USA) software, installed on a local PC running Microsoft Windows XP. The optical pulses that were sent by the MR scanner during the EPI acquisition were converted into an electric pulse by an in-house built electronic box. In this way the Presentation software was synchronized with the scanner acquisition. The functional stimuli were presented on a translucent screen from the front end of the scanner via a projector (Sanyo Pro XTRAX PLC-X20L) using a mirror system. The screen was positioned 20cm from the front end of the coil over the chest of the subjects. The close distance to the eyes resulted in a large visual field covered by the stimulus of approximately 27° horizontally and 21° vertically. Glasses were provided to some of the subjects, who needed them, to correct their vision to normal. Further details of the scanner setup or modifications from this basic setup are described in the chapters of each specific experiment.

## *3.2 Gas Delivery and Physiological Monitoring System*

A number of the experiments described in the following chapters included gas-breathing challenges which required the delivery of various gas mixtures to the subjects. Special ethics approval from the ethics committee of the University of Leipzig was required as well as MR-compatible gas delivery equipment. Ethics approval was granted under the condition that a medical doctor was present in the scanner room during the gas manipulation experiments. The doctors monitored the physiological parameters of the subjects and manually controlled the gas delivery to the subjects according to a predefined protocol. In the case of hyperventilation of the subject or a respiratory volume increase an appropriate adjustment of the gas flow could be initiated by the medical doctor. One gas mixture, provided by Westfalen AG (Münster, Germany) was used in a number of the experiments: 7% $CO_2$,

93% $O_2$ (carbogen-7). The gas cylinders were stored in the basement of the institute and the gas was delivered via pipes into the scanner room, where wall mounts were installed. An appropriate connector for these mounts was installed and a flow-meter was added to deliver gas at flows up 16 litres per minute. Gas flow rates could be manually adjusted via a hand knob. The device has two ports with a rubber bag to temporarily store excess gas attached to one and a plastic tube attached to the other. The plastic bag port has a two-way valve installed which ensures continuous air delivery even if the bag is completely empty during the inspiration phase. The tube is connected through a series of other plastic tubes and connectors to a three-way valve which is constructed to separate the inhaled and the exhaled air. Removal of the expired gas was ensured by an additional plastic tube at the expiratory end of the valve. This prevented a change in susceptibility of the surrounding air during the gas experiments which could lead to significant changes in magnetic field (Streicher et al., 2012). Subjects used a mouthpiece to inhale the gas mixtures while wearing a nose clip. A connector with a luer-lock port between the subject's mouth and the valve allowed sampling of both the inspiratory and expiratory gas concentrations.

End-tidal oxygen and carbon-dioxide values were recorded via the $O_2$, and $CO_2$ modules of the MP150 BIOPAC physiological monitoring system (BIOPAC systems Inc, Goleta, CA, USA). The BIOPAC system was connected to a local PC running Microsoft Windows XP via a network adapter. The computer was running BIOPAC Acqknowledge 4.0 software and had two monitors connected – one at the scanner console and the other one inside the scanner room to present the information to the medical doctor. No artefacts in the MR images were found due to the monitoring system. The following modules were connected to the MP150 unit: OXY100C, O2100C, CO2100C and DA100C with TSD 160A. The first module allowed sampling of heart rate, pulse waveform and blood oxygen saturation via a finger pulse-oxymeter. The second and third modules were used to determine the oxygen and carbon-dioxide partial pressures, respectively. The O2100C and CO2100C modules were calibrated before every scanning session using two fixed-concentration gas mixtures. The DA100C module was used to measure the respiration rate through a pressure pad which was attached to the subject's body in the area of the rips. A ten metre long cable connected the pulse-oxymeter and the pressure pad to the appropriate BIOPAC modules which were located outside of the scanner iron shield. Further, the two other BIOPAC modules were connected to the gas delivery setup via a 10 metre sampling line. Beside the continuous sampling of the physiological data from the volunteers, the optical pulses sent by the scanner with each EPI acquisition, were also recorded by the Acknowledge software which allowed synchronization with the MR data. This was achieved using the same electronic box as for the Presentation

synchronization. A delay time of approximately half a second was determined for the pressure pad. The physiological data was exported from the Acknowledge software to Matlab format (MathWorks, Natick, MA, USA) and there further processed and analysed using in-house developed software. The other software and techniques used for the analysis of the specific studies included in this thesis are described in the corresponding chapters.

## *3.3 MRI Sequence Developments*

The MRI techniques used in the experiments of this study required modifications of existing MR sequences or novel developments. These implementations are described in detail in the following chapters.

## 3.3.1 Tr-FOCI Adiabatic Inversion

The standard inversion recovery based sequence which has been used for all experiments of this study utilised the hyperbolic secant inversion pulse scheme. In order to achieve optimal inversion efficiency and sharp inversion profiles at ultra-high magnetic field a tr-FOCI pulse was implemented under Siemens IDEA VB17a (Fig 18) (Hurley et al., 2010).

The inversion efficiency $\xi$ is defined as the ratio of the change in z-magnetization to the largest possible change in z-magnetization. Full inversion gives gives $\xi = 100\%$. The inversion efficiency of a saturation pulse is $\xi = 50\%$. The z-magnetisation after the inversion pulse is defined as

$$M_{z,after\ Inversion} = -\chi\, M_{z,before\ Inversion} \tag{83}$$

and the inversion efficiency becomes

$$\xi = \frac{M_0 - M_{z,after\ Inversion}}{2\,M_0} = \frac{1-\chi}{2} \tag{84}$$

The MR-signal of an inversion recovery sequence is given by equation 85 with *T* denoting the pulse duration of the adiabatic inversion pulse.

$$M(TI) = M_0 - e^{-\frac{TI}{T_1}}\left(M_0 - M(t=T)\right) \tag{85}$$

The inversion efficiency becomes

$$\xi = \frac{M_0 - M_{z, \text{after Inversion}}}{2 M_0} = \frac{\frac{e^{TI}}{T_1}(M(TI) - M_0)}{2 M_0}$$ (86)

Equation 86 shows that for long $TI$ the inversion efficiency can be estimated if $T_1$ is known.
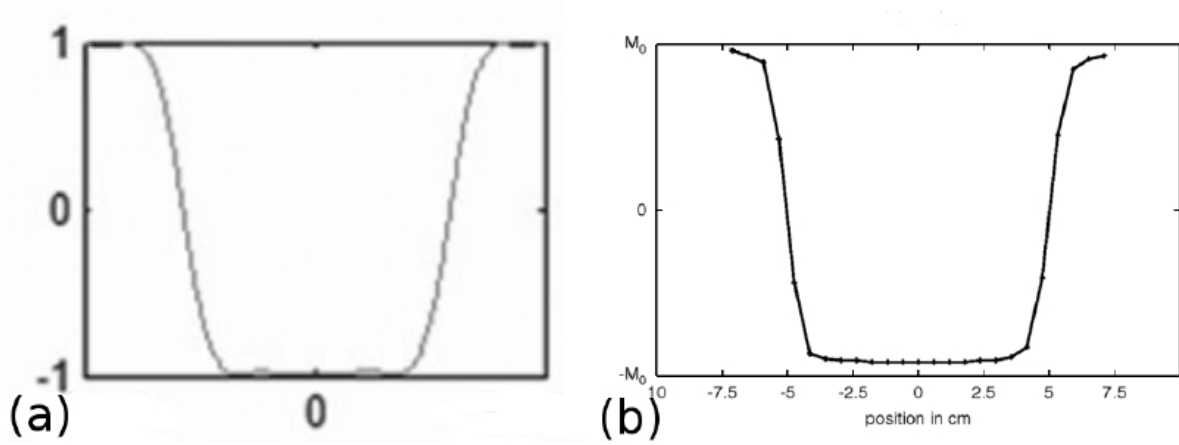


*Figure 18: The slice profiles in the original study by Hurley (a) is compared to our implementation (b) using the same pulse parameters. The sharpness of both profiles is similar.*

In addition to a high inversion efficiency a sharp inversion profile is a desired attribute for RF inversion pulses. In order to be able to properly adjust the inversion profile and the inversion efficiency most parameters of the tr-FOCI pulse implemented were kept variable and could be adjusted via the scanner console. In order to evaluate the dependencies of these parameters, the inversion profile was studied as a function of these pulse variables. An oil phantom was used for these scans in order to minimize $B_1$ inhomogeneities. The relaxation times for this phantom are $T_1 \approx 932$ms and $T_2 \approx 37$ms . Our implementation was validated using identical pulse parameters as in the original study of the tr-FOCI pulse (Hurley et al., 2010). The pulse duration was adjusted to 5ms and the inversion slab thickness to 100mm (see Fig 18).

*RF Magnetic Field $B_1$*

The inversion profile of the tr-FOCI pulse was measured with different RF magnetic field strengths using an oil phantom (see Fig 19). The reference $B_1$ magnitude was $25.91 \mu T$ .
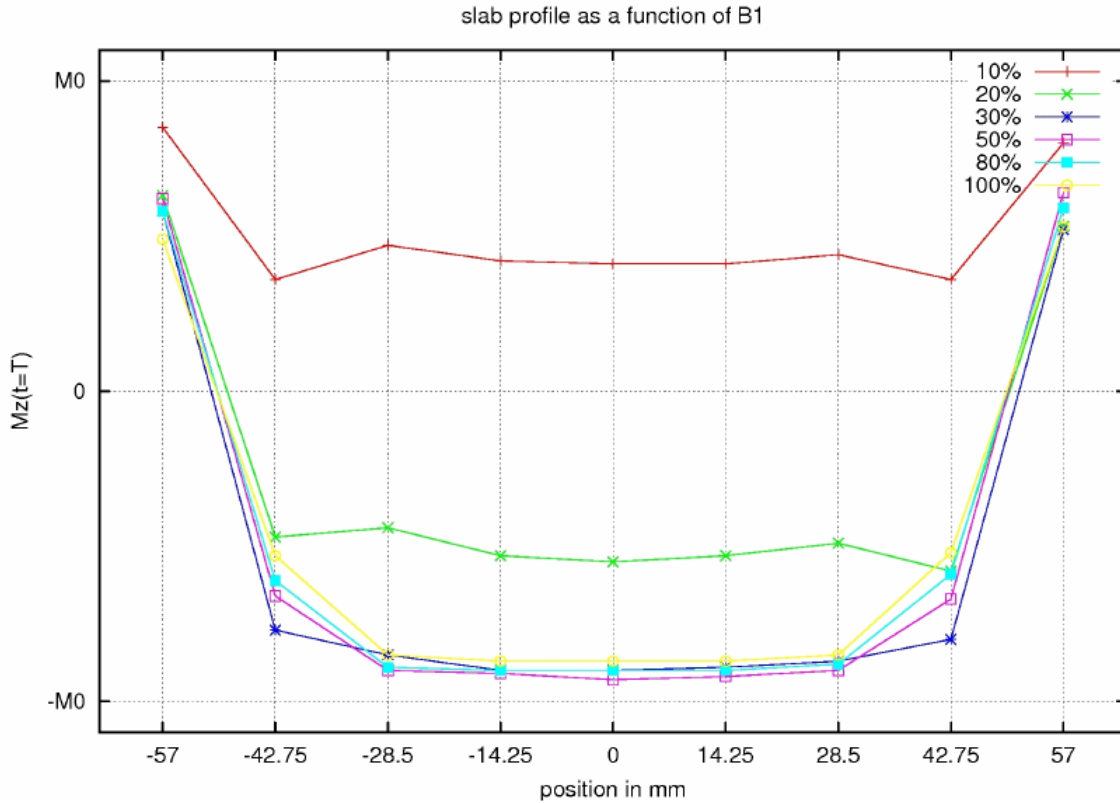
*Figure 19: Inversion profile of the tr-FOCI pulse as a function of the RF magnetic field $B_1$. The maximum inversion efficiency is reached for RF field strengths above 30%.*

The accuracy of the inversion profile is not affected by changes in $B_1$. However, the inversion efficiency was found to be $B_1$ dependent, especially for small $B_1$ values for which the adiabatic condition $\beta \gg 1$ in relation to equation 47 is not met. As long as the adiabatic condition is not fulfilled, the inversion efficiency is $B_1$ dependent. In our implementation an inversion efficiency of more than 95% is achieved for $B_1 > 7.8 \mu T$ which is in accordance with the literature (Hurley et al., 2010).

*Bandwidth* $\mu$

The inversion profile of the tr-FOCI pulse was assessed as a function of bandwidth $\Delta \omega = 2 A_{max} \mu \beta$ (see Fig 20). The reference bandwidth was defined as $\mu = 6.3 \, kHz$ which was was found to provide the best profile for an inversion pulse duration of 5ms. In order to keep the inversion slab thickness constant for different bandwidths, the gradient strength was adapted respectively.

Fig 20 illustrates that the inversion profile becomes sharper for higher bandwidths. However, the inversion efficiency decreases for very high and very low bandwidths. The optimal inversion pulse bandwidth was found to be around 200% of the reference bandwidth.
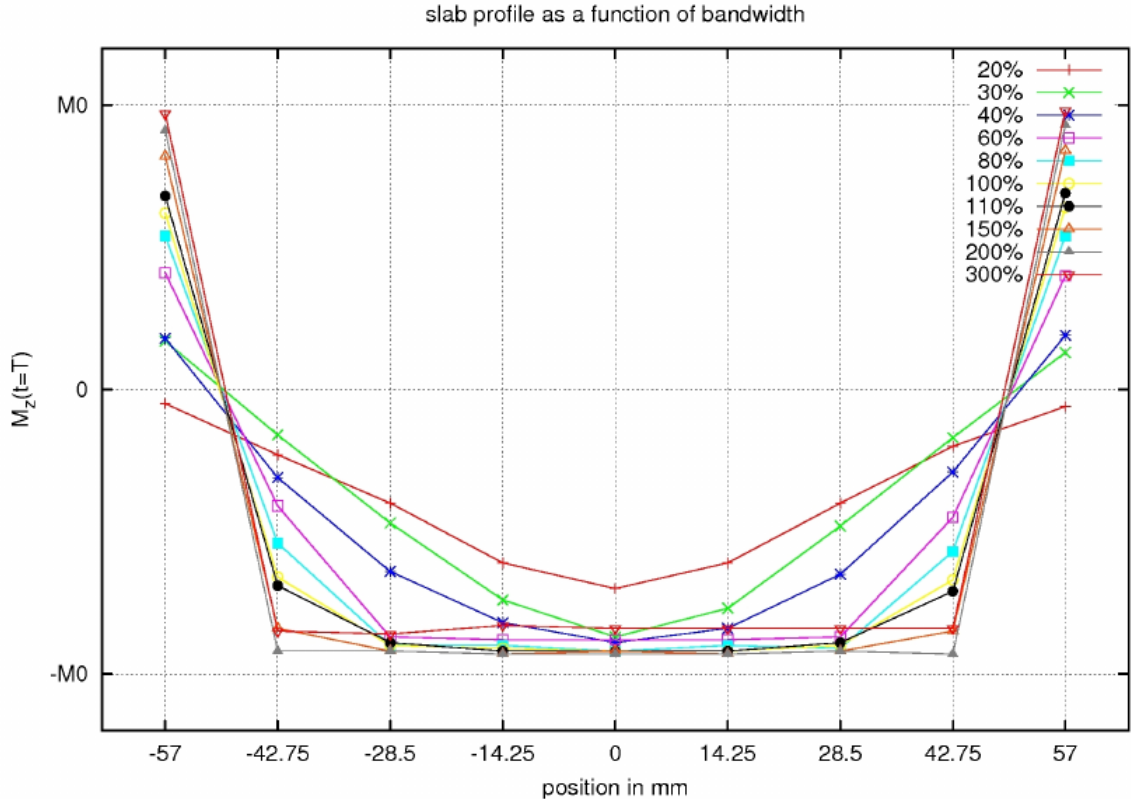
*Figure 20: Slice profile of the tr-FOCI pulse as a function of the pulse bandwidth. The percentage numbers denote the percentage of the bandwidth. The reference bandwidth (100%) is 6.355kHz. The inversion profile becomes sharper for higher bandwidths. The inversion efficiency becomes worse for large and small bandwidths.*

The dependence of the inversion profile on the RF bandwidth is illustrated by Fig 21. If the spins at the margin of the inversion slab (transition zone) do not experience an adiabatic inversion pulse with frequencies much above resonance, the angle $\alpha$ between effective magnetic field $B_{eff}$ and z-magnetisation is not zero (see Fig 21a). The angle $\alpha$ can be calculated via equation 45.

In this case a large angle $\alpha$ creates a large cone of precession around the z-magnetisation which translates into an incomplete inversion after the inversion pulse is administered (see Fig 21b).

The transition effects occur for a limited range of frequencies $\Delta\omega_{on-res}$ related to the gradient strength applied during the RF pulse.

$$\Delta z_{on-res} = \frac{\gamma G}{\Delta\omega_{on-res}} \tag{87}$$

$\Delta z$ denotes the inversion slab thickness. Larger frequency differences result in smaller transition zones as the gradient becomes larger too and therefore the slab profile becomes sharper. However,

58

the adiabaticity $\beta$ decreases with higher $\Delta\omega_{on-res}$ (see equation 47) which explains the decreasing inversion efficiency for high bandwidths in Fig 20.
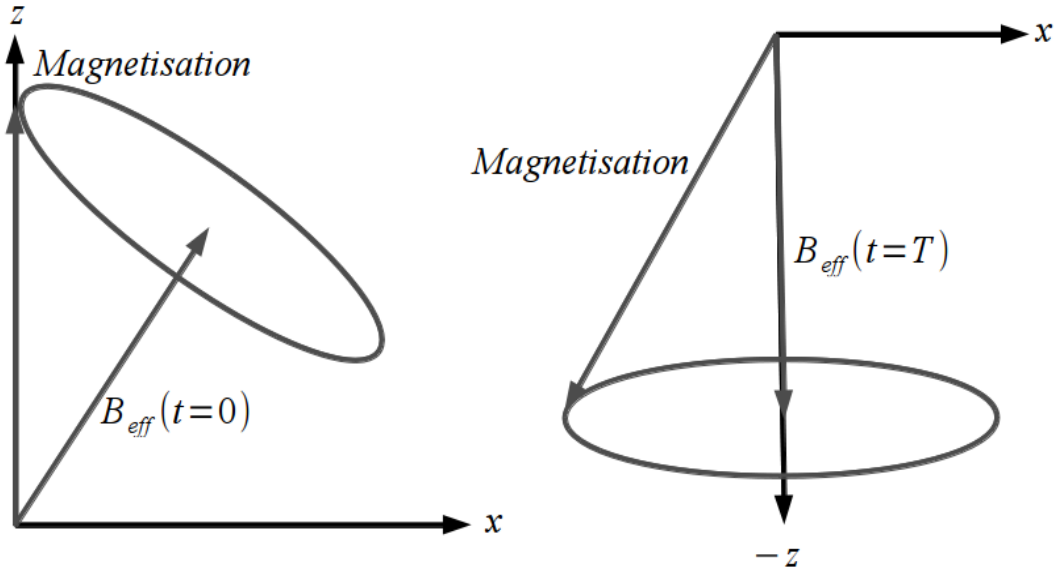


*Figure 21: Incomplete inversion for spins at the borders of the inversion profile based on insufficient off-resonance.*

*Duration T:*

The adiabatic principle (see equation 47) requires minimisation of the duration of an adiabatic RF inversion pulse. Furthermore the specific absorption rate (SAR) increases with the duration of the RF pulse. Therefore short duration adiabatic inversion pulses are profitable. Decreasing inversion efficiency in Fig 22 can be explained with $T_2$ and $T_1$ relaxation effects during the adiabatic inversion. The relaxation during the adiabatic inversion is given by equation 88 whereas the $T_1$ relaxation is negligible for short pulse durations.

$$\frac{dM_\rho}{dt} = -\frac{1}{\frac{1}{T_1}(\cos^2(\alpha) + \sin^2(\alpha)\frac{T_1}{T_2})}(M_\rho - \frac{M_0\cos(\alpha)}{(\frac{\cos^2(\alpha)}{T_1} + \frac{\sin^2(\alpha)}{T_2})T_1}) \tag{88}$$

$M_\rho$ denotes the magnetisation pointing along the effective magnetic field $B_{eff}$.
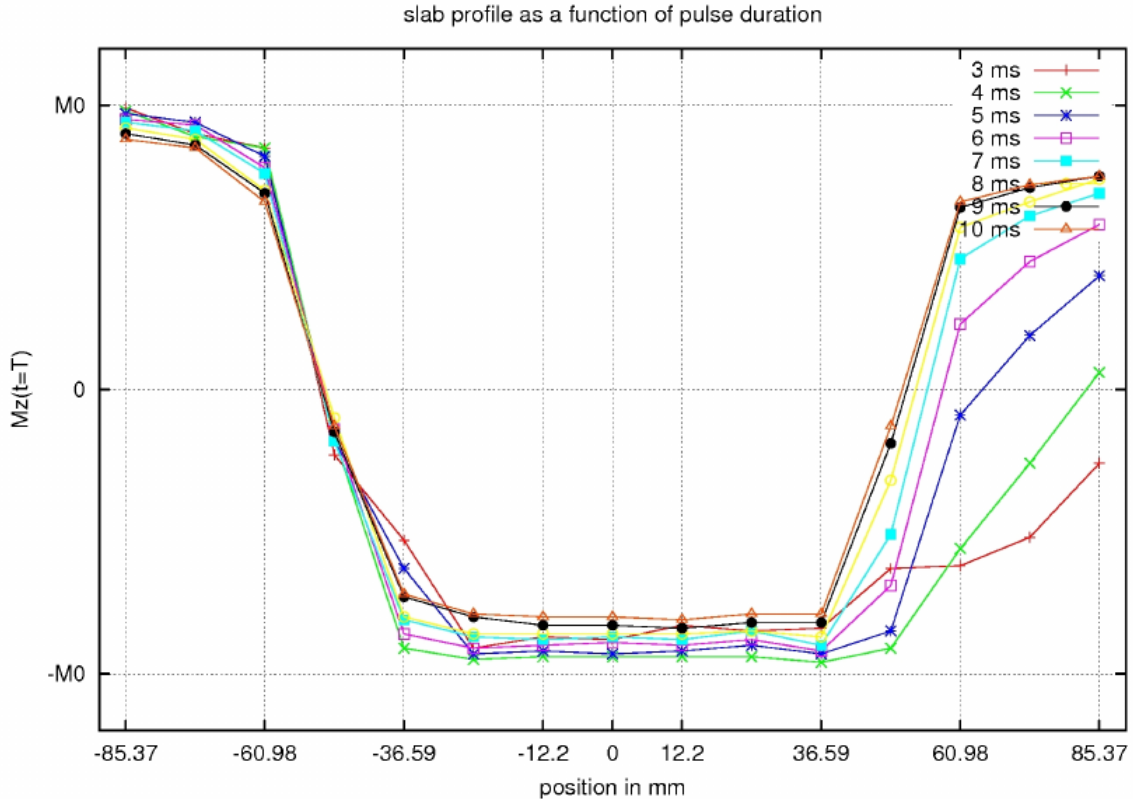
*Figure 22: Measured inversion profile as a function of the RF pulse duration using an oil phantom. The best inversion efficiency is obtained for an RF pulse duration of 4-5ms.*

*Inversion slab  thickness:*

The inversion slab thickness is given by the RF bandwidth of the pulse and the gradient (compare Equation 89).

$$\Delta\omega=\gamma\,G\,\Delta z \tag{89}$$

Fig 23 illustrates the inversion profile for multiple inversion slab thicknesses.

## 3.3.2 Optimisation of the PASL FAIR QUIPSSII Sequence Parameters

The Siemens IDEA VB17a product sequence PASL FAIR QUIPSSII (see Fig 24) has been used as a basis for all experiments performed in this study. In order to obtain optimal results the inversion efficiencies of the hyperbolic secant and the tr-FOCI RF pulse were compared for multiple parameter sets. The sequence parameters used for this comparison were:

$TR=4s$, $TE=8.1ms$, GRAPPA factor 3, partial Fourier factor 6/8, 25 slices (=75mm imaging slab), 3mm isotropic nominal spatial resolution, ascending acquisition, reference voltage=270V.
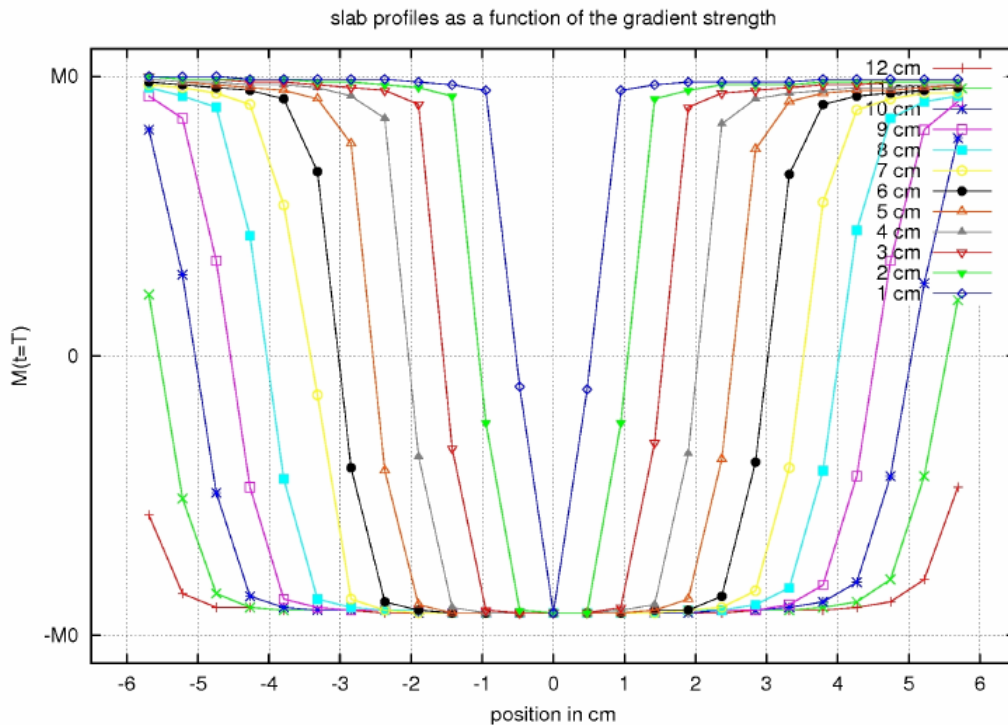
*Figure 23: Inversion slab thickness as a function of the gradient strength measured in an oil phantom.*
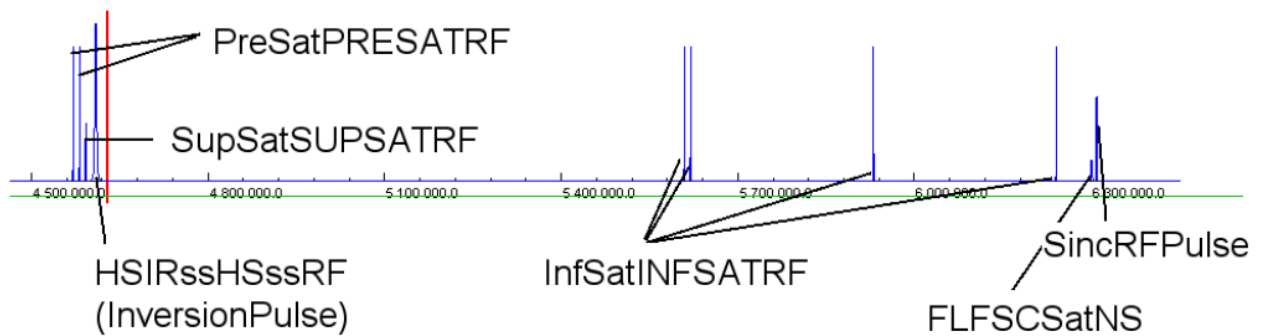


*Figure 24: The RF pulse diagram of the PASL FAIR QUIPSSII sequence. This is a screenshot from the IDEA VB17a development environment. The inversion pulse (HSIRssHSssRF), the QUIPSSII saturation pulses (InfSatINFSATRF) and the 90 degree excitation pulse (SincRFPulse) are the most important ones in the figure.*

Fig 25 shows the performance of the HS pulse for varying RF amplitudes. At least 350-400V are necessary for an RF pulse duration of 16ms to obtain maximum inversion efficiency. In contrast, the tr-FOCI pulse provides maximum inversion efficiency from 200V onwards for 10ms RF pulse duration and 250V onwards for 10ms pulse duration (see Fig 26).
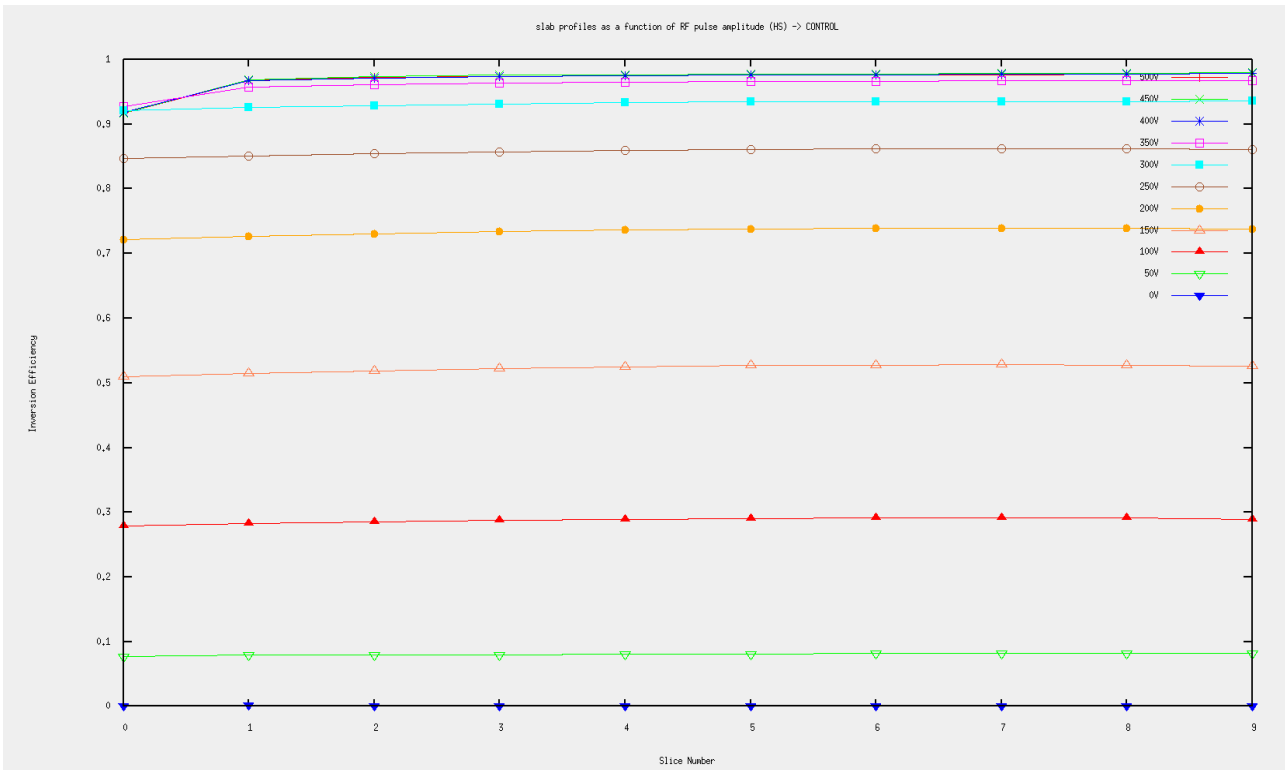
*Figure 25: Hyperbolic secant: Inversion efficiency for multiple inversion pulse RF amplitudes*
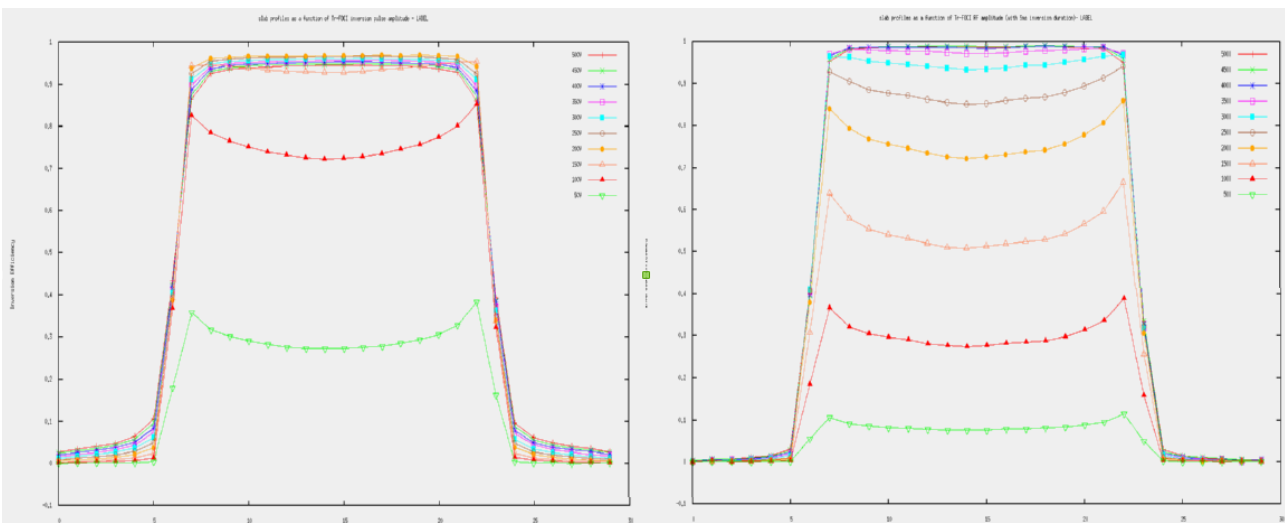


*Figure 26: Tr-FOCI: Inversion efficiency for multiple inversion pulse RF amplitudes using a pulse duration of 10ms (left) and 5ms (right).*

These results are confirmed by *in-vivo* perfusion weighted images (Fig 27) obtained using the same sequence parameters. The tr-FOCI inversion pulse leads to better grey matter – white matter contrast compared to the hyperbolic secant (HS) pulse. This trend is confirmed by the subtracted raw images which can be found in Fig 28.
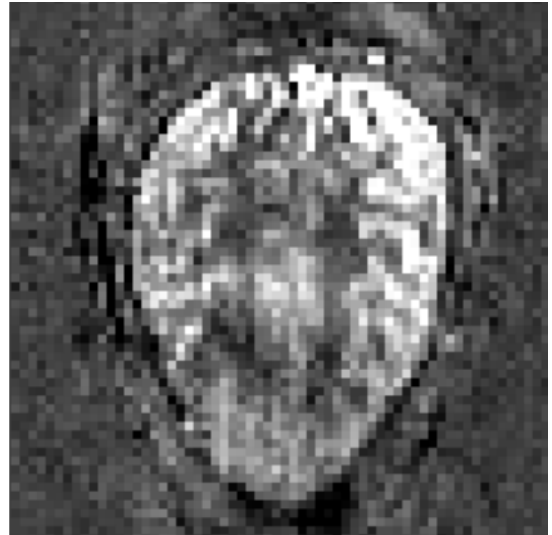
*Figure 27: Perfusion weighted images calculated by the 7T Siemens scanner based on: left – tr-FOCI inversion pulse; right – Hyperbolic secant inversion pulse. PASL FAIR QUIPSSII sequence with tr-FOCI shows better inversion maps (better GM-WM contrast in perfusion images).*
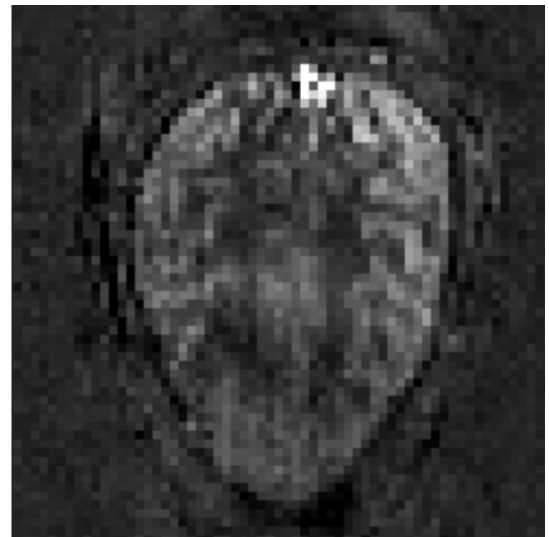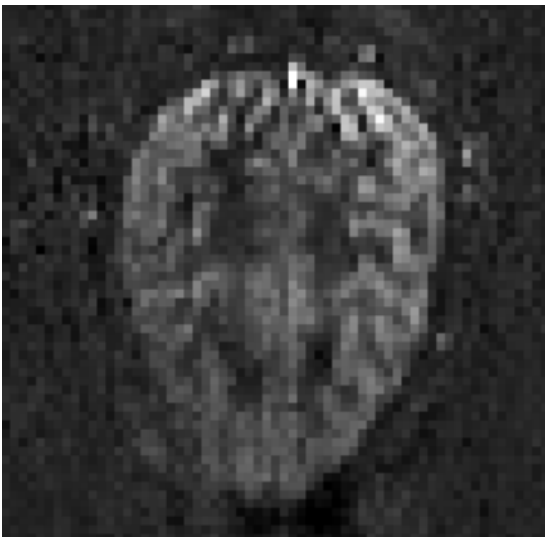


*Figure 28: Simple subtraction of control -label images results in these perfusion images for: left tr-FOCI based sequence and right for HS based sequence. Tr-FOCI shows better GM-WM contrast and consequently better perfusion weighting.*

In order to find the best combination of inversion times multi- $TI$ scans were performed by varying both inversion times simultaneously and keeping the inversion time difference constant (see Fig 29). Short $TI_1$ leads to a small tagging bolus and therefore to a small MR signal after subtraction. The goal is to maximise $TI_1$. However, if $TI_1$ becomes too long fresh blood will flow into the imaging slab before image acquisition which counteracts the perfusion signal. The best combination of inversion times was found as $TI_1 / TI_2 = 700\text{ms} / 1700\text{ms}$ providing the best grey matter − white

matter contrast.

In order to find the best $\Delta TI$ another multi- $TI$ experiment was performed and the results can be found in Fig 30. $TI_1$ was then adjusted to the optimum (Fig 29). Longer $\Delta TI$ leads to perfusion from larger vessels into microvasculature (capillaries) and tissue space. For short $\Delta TI$ mainly large vessels are visible in the subtraction images whereas an increase in $\Delta TI$ leads to similar contrast in all GM voxels. For very large $\Delta TI$, $T_1$ decay leads to minimal contrast of GM-WM (eg $TI_1 / TI_2 = 700\,ms / 1700\,ms$ ).

### 3.3.3 Multi-TE Multi-TI EPI

Beside the RF pulse based developments described above which were necessary for all experiments of this study, some additional implementations were necessary for the experiments which will be described in chapter 6.

The Siemens VB17a PASL FAIR QUIPSSII sequence code was extended such that multiple EPI readouts could be performed after one single excitation. Furthermore an option to enable and disable the 90° excitation pulse was implemented. The resulting MR sequence is very flexible as it allows an unlimited number of readouts and excitations within one $TR$.

In order to assess the performance of the multi-echo EPI readout multiple echoes from multiple separately performed readouts were acquired and $T_2^*$ was estimated via fitting this parameter to the appropriate MR relaxation equation. Scans of an oil phantom were acquired both without (Fig 31) and with acceleration (Fig 32) techniques. Multiple echo times originating from multiple excitations were fitted to a single relaxation curve for both the accelerated and not accelerated cases. An application of this technology can be found in chapter 6.
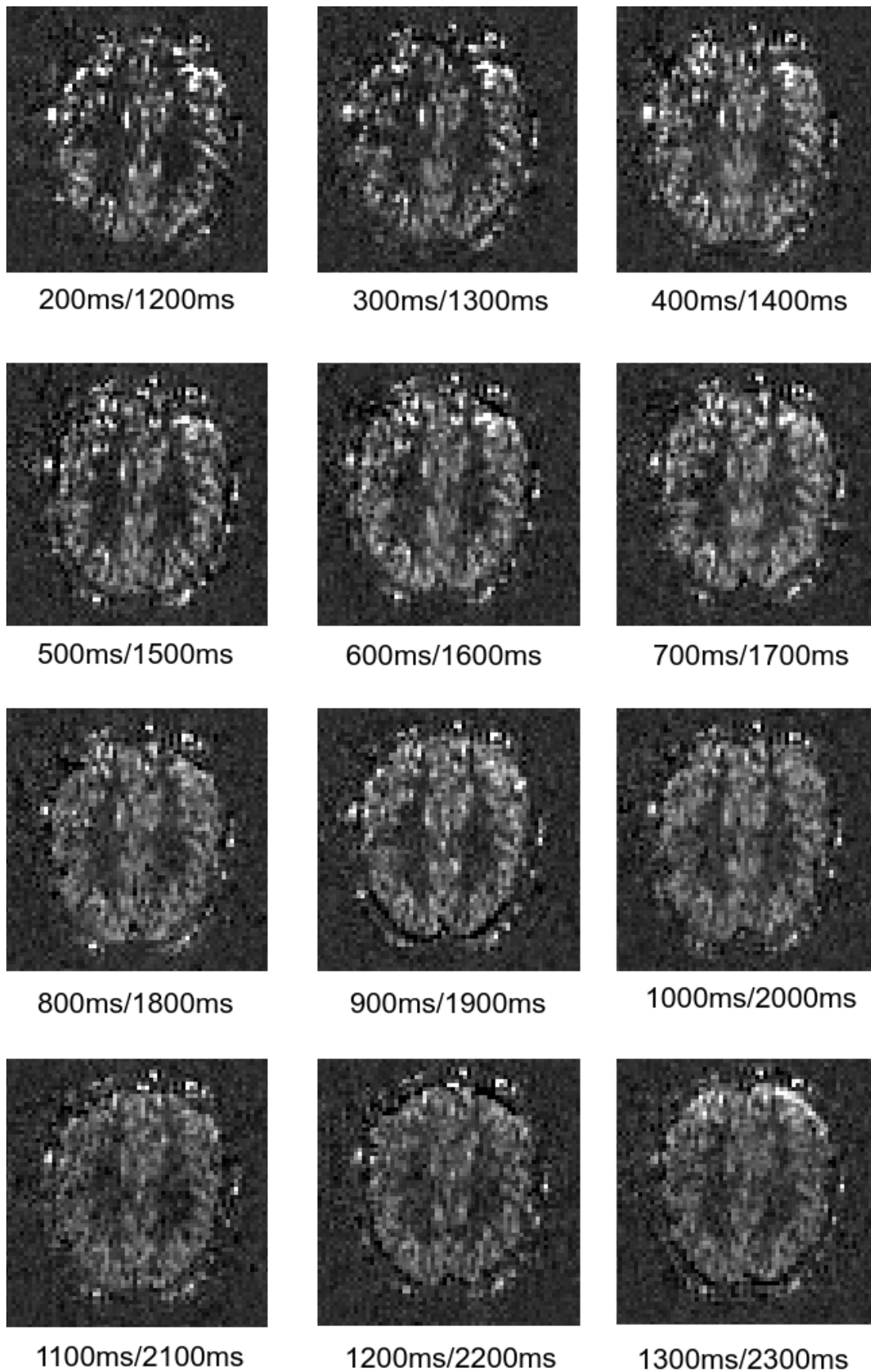
*Figure 29: Subtraction images acquired via PASL FAIR QUIPSSII using the tr-FOCI pulse with multiple $TI_1/TI_2$ combinations and constant $\Delta TI$. These images are averages over $3min$ ($=45$ repetitions with $TR=4s$). Short $TI_1$ results in short tagging bolus. The best results were obtained with $TI_1/TI_2=700ms/1700ms$.*
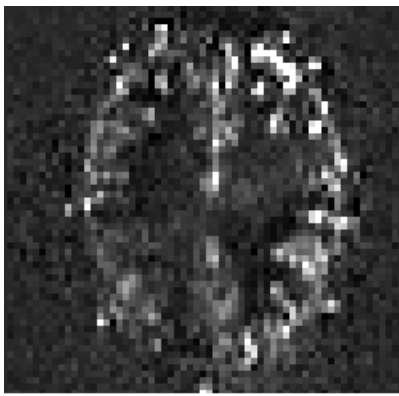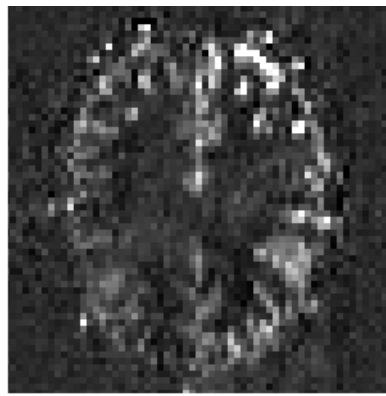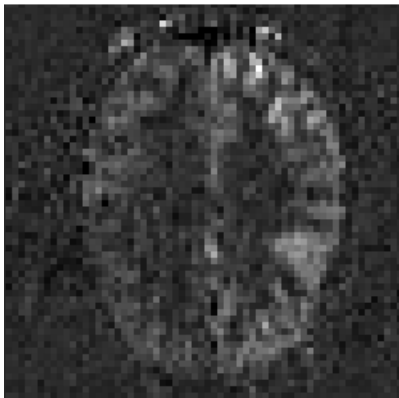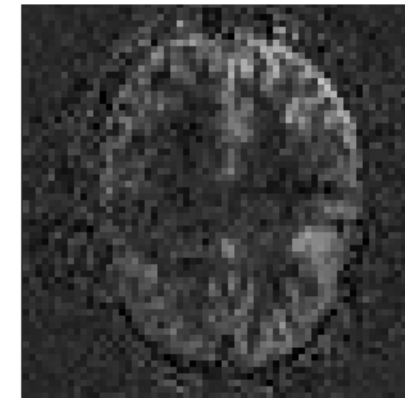
700ms/1100ms 700ms/1200ms 700ms/1300ms
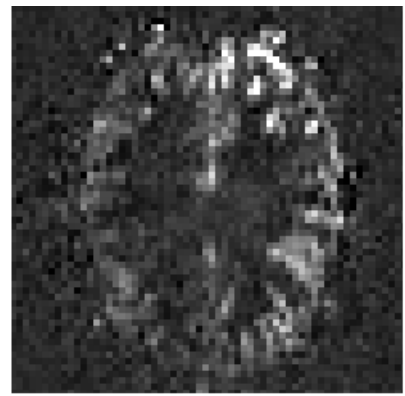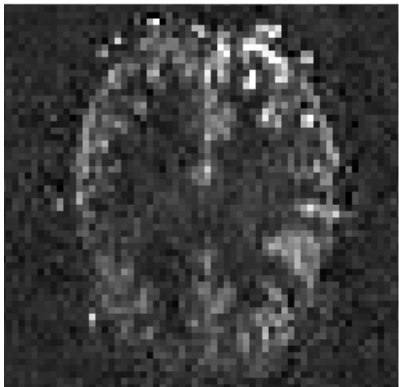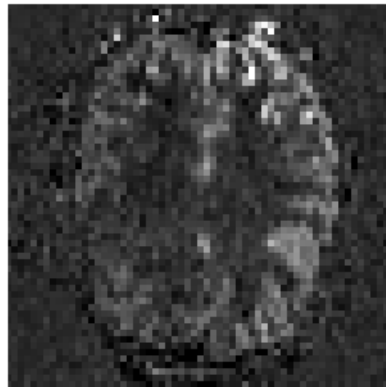
700ms/1400ms 700ms/1500ms 700ms/1600ms
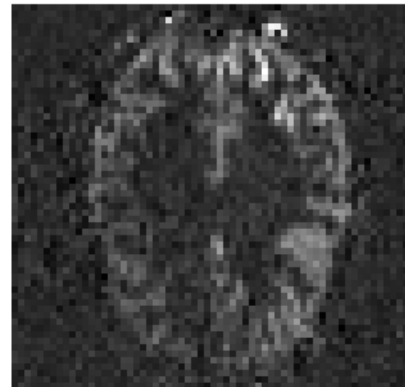
700ms/1700ms 700ms/1800ms 700ms/1900ms

*Figure 30: Subtraction images acquired via PASL FAIR QUIPSSII using the tr-FOCI pulse with multiple $TI_1 / TI_2$ combinations and constant $TI_1$. These images are averages over 3min (=45 repetitions with $TR = 4s$). Longer $\Delta TI$ leads to blood perfusion from larger vessels into the microvasculature (capillaries) and tissue space. For short $\Delta TI$ GM with large vessels is bright. For longer $\Delta TI$ (eg $\Delta TI = 1000\,ms$) all GM voxels have similar contrast values. For very large $\Delta TI$, $T_1$ decay leads to minimal contrast of GM/WM (eg $TI_1 / TI_2 = 700\,ms / 1700\,ms$).*
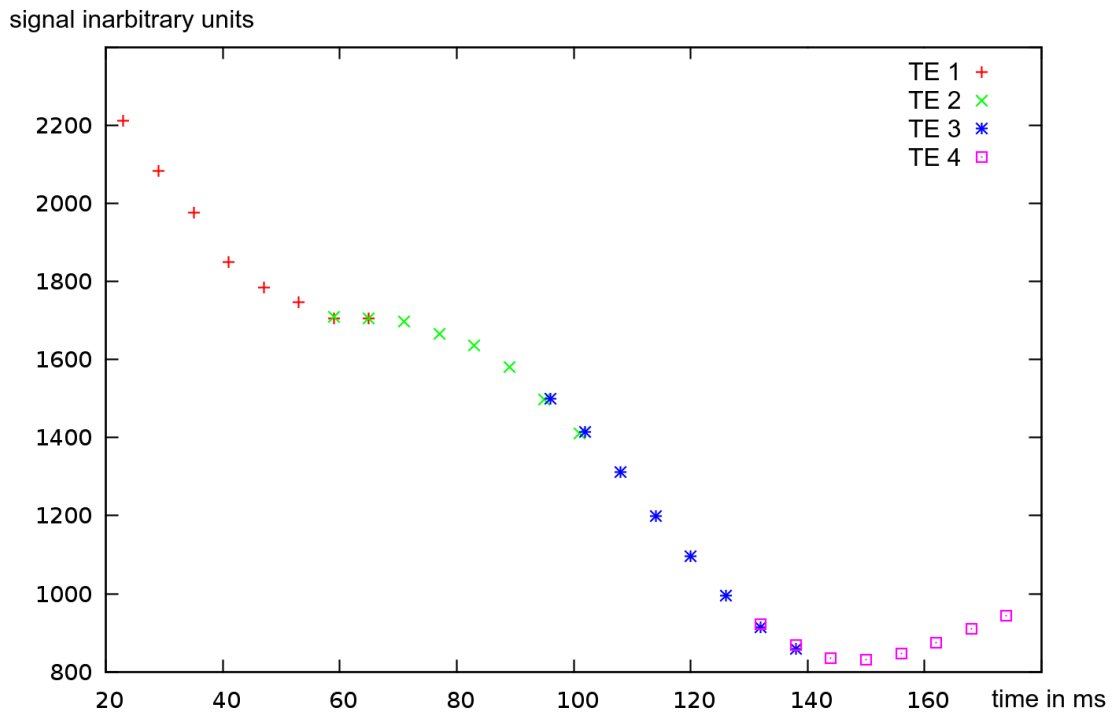
*Figure 31: $T_2^*$ plots for multiple echoes without GRAPPA and without partial Fourier.*
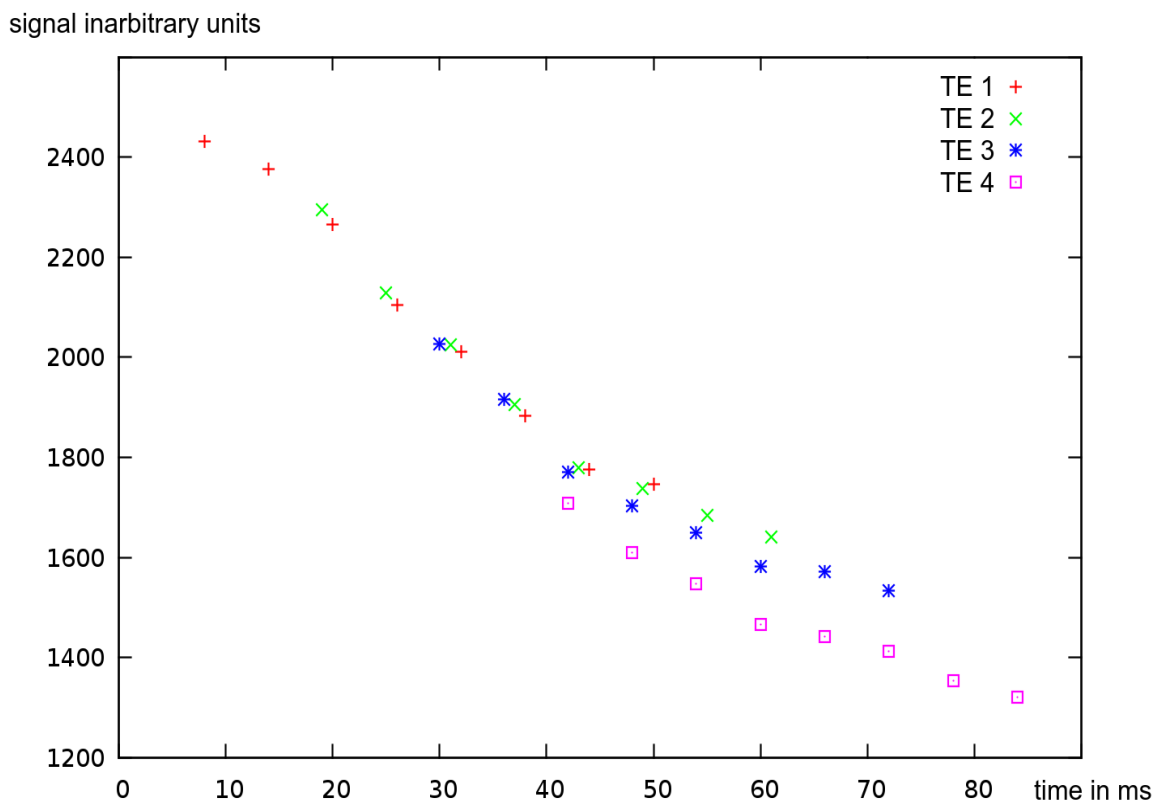


*Figure 32: $T_2^*$ plots for multiple echoes using GRAPPA 3 and partial Fourier 6/8.*

# 4 Experiment I: Comparison of Direct and Modelled fMRI Calibration

This study has been published in Neuroimage (2014) 84:605-14.

## 4.1 Background Information

The BOLD contrast is widely used in functional magnetic resonance imaging (fMRI) to map neuronal activity in the brain (Ogawa et al., 1990; Buxton, 2012). BOLD contrast relies on a complex interplay between changes in CBF, CBV and $CMRO_2$. The quantitative relationship between these parameters has not, however, been fully elucidated (Turner, 2002; Buxton, 2010; Aguirre et al., 1998). Additionally, since the BOLD response is a relative change from an unknown baseline, differences in baseline physiology may influence BOLD signal changes, precluding truly quantitative BOLD response comparisons across subjects, or within the same subject across days (Gauthier et al., 2011; Lu et al., 2008). However, more physiologically-specific MRI-based methods have been proposed to detect functional activity in the brain. These are typically based on measuring a single physiological quantity rather than an ambiguous combination of several quantities (Lu et al., 2003; Williams et al., 1993; Davis et al., 1998). Of these physiological quantities, $CMRO_2$ is believed to provide one of the most direct indices of neural activity mapping since it reflects oxidative energy consumption of the tissue (Hoge et al., 1999).

Calibrated fMRI techniques used to quantify $CMRO_2$ in the brain commonly rely on the combined acquisition of CBF and BOLD signals during a gas-breathing manipulation. Either hypercapnic ($CO_2$) (Hoge et al., 1999; Davis et al., 1998) or hyperoxic ($O_2$) (Chiarelli, Bulte, Wise, et al., 2007) breathing challenges are used to elevate venous saturation and thereby the BOLD signal. The BOLD signal increase measured during this gas breathing manipulation is extrapolated to its theoretical maximum $M$ via a biophysical calibration model. The recently introduced generalized calibration model (GCM) extends the hyperoxia calibration model (Chiarelli, Bulte, Wise, et al., 2007), making it valid for combined hypercapnia and hyperoxia breathing challenges (Gauthier & Hoge, 2013).

Common to all models is a dependence on accurate estimation of the calibration parameter $M$ to obtain valid $CMRO_2$ estimates. Previous studies using hypercapnia, hyperoxia or a combination of both have yielded a large range of estimated $M$-values (Ances et al., 2009; Ances et al., 2008; Bulte et al., 2012; Bulte et al., 2009; Chen & Parrish, 2009; Chiarelli, Bulte, Piechnik, et al., 2007; Chiarelli, Bulte, Wise, et al., 2007; Driver et al., 2012; Gauthier et al., 2012; Gauthier, Krieger, et

al., 2013; Gauthier & Hoge, 2013; Hall et al., 2013; Huber et al., 2013; Ivanov et al., 2012; Leontiev et al., 2007; Leontiev & Buxton, 2007; Lin et al., 2008; Mark et al., 2011; Mark & Pike, 2012; Mohtasib et al., 2012; Perthen et al., 2008). Some of the variance between studies may be explained by differences in haemodynamic and physiological properties across brain regions and subjects (Lu et al., 2008; Ances et al., 2008; Chiarelli, Bulte, Gallichan, et al., 2007; Aguirre et al., 1998) or the dependence of $M$ on specific measurement parameters, such as $TE$ or static magnetic field strength ($B_0$) (Hoge et al., 1999; Uludağ et al., 2009). However, some uncertainty in $M$ is also expected due to the relatively high probability of extrapolation error when starting from noisy measurements or poorly estimated parameters (Chen & Pike, 2010; Chiarelli, Bulte, Piechnik, et al., 2007).

A recently introduced technique uses carbogen mixtures with high $CO_2$ and $O_2$ content (10% $CO_2$, 90% $O_2$) to saturate the BOLD signal by elevating venous $O_2$ saturation close to 100% (Gauthier et al., 2011). This approach can be used to directly measure the calibration constant $M$ and circumvent the disadvantages associated with $M$-value modelling. However, $CO_2$ concentrations in the range of 10% can lead to a significant level of discomfort (Banzett et al., 1996; Gauthier et al., 2011) and are therefore not a viable alternative for routine calibrated BOLD studies. In this study we applied the direct $M$-value estimation approach at 7 T using a moderate $CO_2$ concentration of 7% with simultaneous visuo-motor activation, based on previous work in our lab (Ivanov et al., 2012). Since breathing discomfort is known to be related to $CO_2$ concentration (Banzett et al., 1996; Gauthier et al., 2011; Gauthier & Hoge, 2013), this lower $CO_2$ concentration is expected to be more tolerable for participants. The directly estimated results are compared to GCM-based $M$-value modelling also based on carbogen-7 inhalation. Furthermore, this work is the first to quantitatively assess the direct and GCM-based $M$-value estimation techniques at ultra-high field in the same experiment. Benefits and drawbacks of both techniques are analysed and compared to assess their feasibility for future calibrated fMRI studies.

## *4.2 Methods*

Data were acquired in 15 healthy participants (7 women, 26 ± 3 years) using the scanner setup described in chapter 3. All participants gave written informed consent for participation in this study. Ethics approval was obtained from the local review board (Ethics Commission, Leipzig University).

## 4.2.1 Experimental Design

Each participant underwent a ten minute MRI acquisition in which CBF and BOLD-weighted MRI signals were measured simultaneously. This acquisition consisted of a one-minute block design with

rest and visuo-motor stimuli interspersed. During this same 10-minute acquisition, a combined hypercapnia-hyperoxia gas-breathing challenge was used, starting after two minutes of acquisition and lasting for five minutes. The experimental design is shown schematically in Fig 33. This design was chosen to assess the presence of BOLD signal saturation while retaining the possibility of estimating $M$ via modelling, and thereby consists of alternating periods of combined gas manipulation and task with periods of gas inhalation only.
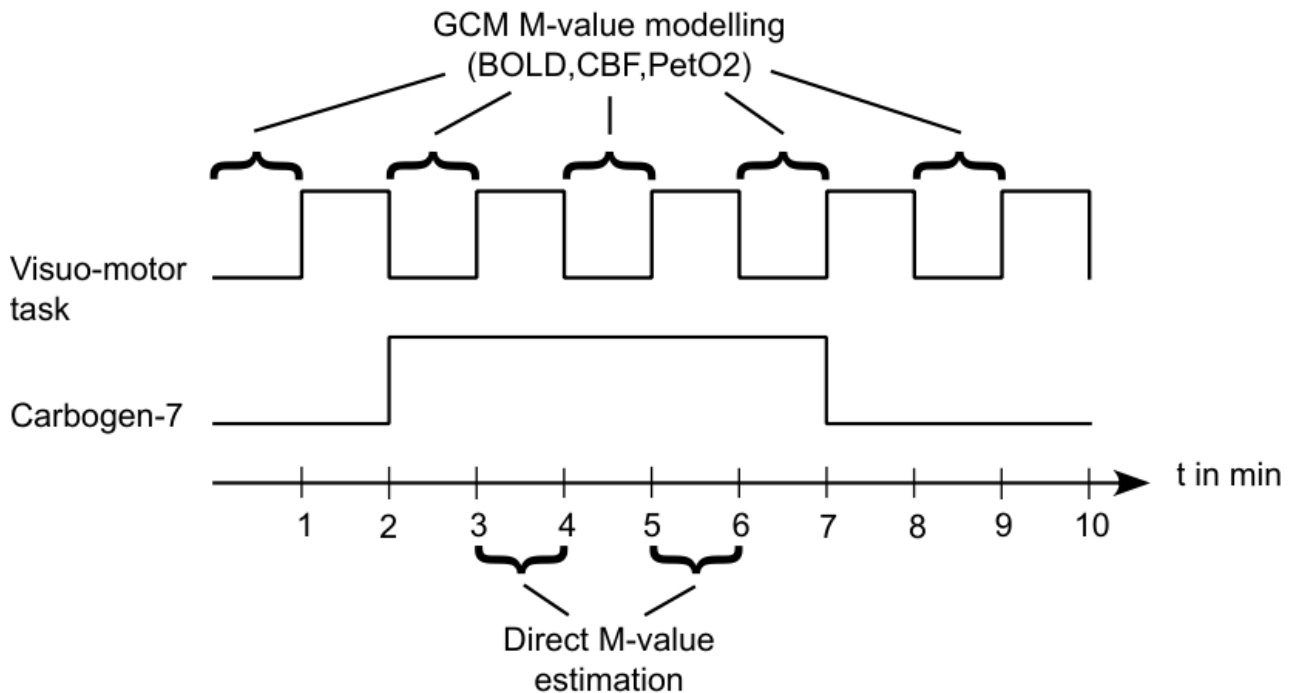


*Figure 33: A five minute carbogen-7 breathing challenge has been combined with a block design visuo-motor task alternating 60s blocks of rest and visuo-motor stimulation. BOLD and CBF-weighted MRI signals were acquired during the whole experiment via the pulsed arterial spin labelling technique. End-tidal $O_2$ and $CO_2$ were measured simultaneously also throughout the whole experiment.*

## 4.2.2 Visuo-Motor Task

The visuo-motor task used in this study involved the control, using a frictionless MRI-compatible joystick, of a short vertical bar displayed on a screen at the back of the scanner bore. Each participant was asked to use the joystick to precisely counteract the intrinsic movement of the vertical bar, and thus to maintain the bar in the centre of the screen. The intrinsic movement consisted of two continuous Gaussian functions (one negative and one positive) with an overall period of ten seconds. The 60 seconds trial duration of each block was chosen to allow the participants sufficient time to identify the pattern of the movement. A blank screen was shown during the 60 seconds rest block. Performance error was defined as the distance between the

moving bar and the centre of the screen.

## 4.2.3 Gas Manipulations

A mouthpiece was provided to the participants before they were positioned within the scanner. Subjects were asked to adjust the mouthpiece to avoid leakage of inflowing or exhaled air. The mouthpiece was connected to a three-way valve separating the inflowing air (either normal air or carbogen-7 – 7% $CO_2$/ 93% $O_2$) from the air exhaled by the subject. Gas flows were adjusted manually on the flow-meter to keep a total flow rate of 15 litres per minute. A medical doctor was present in the scanner room at all times during the breathing manipulation and was responsible for adjusting and controlling the flow rate. The doctor also monitored pulse rate and arterial $O_2$ saturation measured via a pulse-oxymeter on the subject's index finger. In case of hyperventilation or collapse of the reservoir bag affixed to the flow-meter during the breathing manipulation, flow rates were temporarily increased to maintain a constant filling of the reservoir bag. An alarm was provided to all participants to allow them to interrupt the experiment in case of discomfort.

End-tidal $O_2$ and $CO_2$ values were recorded for all subjects throughout the whole scanning procedure. The three-way valve inside the scanner was directly connected to the gas sensors of the $CO_2$ and $O_2$ modules of the MP150 BIOPAC physiological monitoring system (BIOPAC systems Inc., Goleta, CA, USA). This system was calibrated before each measurement by adjusting the input resistances for both module sensors to the partial pressures of the two gas mixtures not used during the actual experiment. The following gas-pressure combinations were used for calibration:

gas 1 (0% $CO_2$, 100% $O_2$) $\quad\rightarrow\quad$ p($CO_2$)=0mmHg $\qquad$ p($O_2$)=760mmHg

gas 2 (7% $CO_2$, 21% $O_2$) $\quad\rightarrow\quad$ p($CO_2$)=53.2mmHg $\qquad$ p($O_2$)=159.6mmHg

## 4.2.4 Scanning Parameters

Simultaneous BOLD and CBF functional MRI acquisitions were performed during the whole design depicted in Fig 33 with a PASL FAIR (Kim, 1995) QUIPSSII (Wong et al., 1998a) sequence and a tr-FOCI pulse (Hurley et al., 2010). A short inversion pulse duration of 5.5ms together with a high RF amplitude of 400V was used to maximise inversion efficiency. 25 slices with no slice gap were acquired within a *TR* of 4 seconds and a *TE* of 8.1ms using a standard EPI readout with a 90° flip angle. A GRAPPA factor of 3 and partial Fourier factor of 6/8 were used. The nominal isotropic resolution used was 3 mm with a FOV of 192mm x 192mm resulting in a matrix size of 64 x 64. The inversion times were $TI_1 = 700\, ms$ and $TI_2 = 1700\, ms$ and the tag-width was 90mm.

### 4.2.5 Data Analysis

All PASL datasets were corrected for motion using the Neurolens data analysis software package ([www.neurolens.org](www.neurolens.org)). Functional regions of interest (ROI) were defined on an individual basis using a general linear model (GLM) analysis of the visuo-motor data. Maps for ROI definition were obtained using the fMRI expert analysis tool (FEAT) v. 5.98 from the FSL software package using a 3mm smoothing kernel. Smoothing was used only for the purpose of ROI generation. In the final analysis of the data no smoothing was used, to preserve spatial information. Cluster thresholded activation maps for CBF signals ($p<0.05$, corrected for multiple comparison) and BOLD signals ($p<0.05$ multiple comparison corrected) were calculated for periods with visuo-motor task activation without gas inhalation. ROIs were defined using the intersection of significant CBF and BOLD signal changes. These individual intersection masks were manually separated into a visual-related ROI (including parts of the primary visual cortex V1 and visual motor cortex V5) and a motor-related ROI (including parts of the primary motor cortex, premotor area and supplementary motor area) to quantify physiological parameters on a regional basis. All ROI results are presented here as average ± standard deviation across voxels. Errors in modelled parameters were estimated through propagation of uncertainty.

All subsequent steps of the data analysis were performed with in-house Mathworks Matlab (v. 8.0.0.783, R2012b) code. Voxel-wise surround subtraction with linear interpolation of neighbouring time points was used to calculate CBF-weighted time courses, and surround addition to create BOLD-weighted signals. Addition and subtraction time courses were averaged over each ROI. CBF and BOLD-weighted signal baselines were defined as the average signal during the first minute of each time series. Relative CBF signal changes were corrected for $T_1$ shortening during carbogen-7 inhalation. Exact $T_1$ correction for the shortening effects of hyperoxia cannot be performed at 7T, since the $T_1$ value of blood during hyperoxia has not yet been measured accurately. A 10% increase in CBF was assumed to account for $T_1$ shortening effects, since this approximation was found to be most compatible with data acquired at other gas concentrations and field strengths through in-house modelling (data not shown).

### 4.2.6 *M*-value Modelling

ROI-based *M*-values were calculated for each subject using the generalized calibration model (GCM) (Gauthier & Hoge, 2013). This model may be used for any breathing manipulation that includes increases in oxygen content and/or blood flow, including simultaneous hypercapnia and hyperoxia manipulations (in this case carbogen-7 breathing). Using this model, the calibration

constant $M$ can be calculated as follows:

$$M = \frac{rBOLD}{1 - rCBF^{\alpha}\left(\dfrac{1 - Sv_{O_2}}{1 - Sv_{O_2|0}}\right)^{\beta}} \tag{90}$$

where $\alpha$ represents the power law exponent describing the relationship between changes in cerebral blood flow and cerebral blood volume, assumed here to be 0.18 (Chen & Pike, 2010). The exponent $\beta$ (Driver et al., 2010; Yablonskiy & Haacke, 1994) is used to model the influence of deoxygenated haemoglobin on transverse relaxation (Boxerman et al., 1995) and is here assumed to have a value of 1.0 due to the high magnetic field used (Martindale et al., 2008; Kida et al., 2000). $Sv_{O_2}$ and $Sv_{O_2|0}$ represent venous $O_2$ saturation during gas breathing periods and baseline (air breathing) periods respectively. Venous $O_2$ saturation values were obtained from GCM modelling with an assumed value of 0.35 for baseline OEF. For more detailed information on the specific calibration model used in this study refer to (Gauthier & Hoge, 2013). The relative BOLD and CBF-weighted signals used to extrapolate the $M$-value using the GCM were taken from periods with gas inhalation, but without visuo-motor stimulation (see Fig 33) to avoid the confounding effects of an unknown local metabolism increase. The modelling parameter values used here can be found in Table 1.

### 4.2.7 Direct $M$-Value Estimation

Direct estimation of $M$, based on previous work in our lab (Ivanov et al., 2012), relies on the method described in Gauthier et al. (2011) which attempts to measure the $M$-value directly, without additional modelling (Gauthier & Hoge, 2013). This approach assumes that the BOLD signal increase measured during a combined hypercapnia and hyperoxia manipulation is already very close to its theoretical upper limit $M$, due to very high venous $O_2$ saturation from the combination of increased $O_2$ content and increased blood flow. While data presented in Gauthier et al. (2011) suggests that inhalation of 7% $CO_2$ is expected to yield almost complete saturation levels, a visuo-motor task was nevertheless added to further increase blood flow and saturation of the BOLD signal. This additional saturation from combined stimulation arises from the approximate 2:1 flow-metabolic coupling (Buxton, 2010) and we expected complete or near-complete deoxyhaemoglobin dilution to be reached using this combined stimulus. The direct method was therefore used to estimate the $M$ parameter using the BOLD data from the periods with combined carbogen-7 inhalation and performance of the visuo-motor task (33).

| Parameter | Description | Value | Reference |
|---|---|---|---|
| α | Grubb value describing CBV-CBF coupling | 0.18 | (Chen & Pike, 2010; Kida et al., 2007) |
| β | Relationship between extravascular transverse relaxation and blood oxygen fraction | 1 | (Kida et al., 2000; Martindale et al., 2008) |
| φ | Haemoglobin $O_2$ capacity | 1.34 | (Rhoades & Bell, 2009; Chiarelli, Bulte, Wise, et al., 2007) |
| $[Hb]$ | Haemoglobin content in blood | 15 | (Rhoades & Bell, 2009; Chiarelli, Bulte, Wise, et al., 2007) |
| ε | Solubility of $O_2$ in plasma | 0.0013 | (Rhoades & Bell, 2009; Chiarelli, Bulte, Wise, et al., 2007) |
| OEF | Oxygen extraction fraction | 0.35 | (Gauthier et al., 2012; Gauthier, Krieger, et al., 2013; Fan et al., 2013; Menon et al., 2013; Chiarelli, Bulte, Wise, et al., 2007) |

*Table 1: Physiological parameters used for GCM estimation.*

Since single-subject analyses suffer from a low signal-to-noise ratio, further signal averaging is desirable. Additional analyses were therefore performed on group-averaged BOLD signal time courses for the visual-related ROI. The direct and modelled *M* estimation methods were applied to this time course and the amplitude of the task component during air and carbogen-7 breathing periods was assessed in order to determine whether complete BOLD signal saturation was obtained using carbogen-7 inhalation. Because of the design of the experiment, high-pass filtering could not be applied to account for signal drifts. However, testing for drifts within one-minute blocks of the experiment did not reveal the presence of significant signal drifts within our data. Therefore, since signal averaging over short one-minute blocks was used to estimate BOLD signal changes for both modelling and direct methods, no filtering for low frequency drifts was applied.

## *4.3 Results*

Baseline $O_2$ and $CO_2$ partial pressures were comparable for all subjects. The average $P_{etO2}$ and $P_{etCO2}$ at rest were 107.8±2.4mmHg and 40.2±2.2mmHg, respectively. End-tidal partial pressures of $CO_2$ during carbogen inhalation showed an average of 53.8±2.3mmHg. The average manipulated $P_{etO2}$

was 600.5±64.5mmHg. Participants' end-tidal partial pressures of $O_2$ ($P_{etO2}$) and $CO_2$ ($P_{etCO2}$) measured during rest and gas manipulation periods are given in Table 2.

| Subject | PetO$_{2|rest}$ | PetO$_{2|carb}$ | PetCO$_{2|rest}$ | PetCO$_{2|carb}$ | SvO$_{2|visual}$ (%) | SvO$_{2|motor}$ (%) |
|---|---|---|---|---|---|---|
| 1 | 112±2 | 572±3 | 36±1 | 52±1 | 89.9±1.5 | 92.1±2.4 |
| 2 | 109±1 | 684±2 | 41±1 | 57±1 | 91.1±4.1 | 88.7±3.2 |
| 3 | 109±2 | 572±5 | 38±1 | 56±1 | 88.2±1.5 | 90.9±2.8 |
| 4 | 107±2 | 617±4 | 40±1 | 54±1 | 92.0±4.0 | 94.3±3.6 |
| 5 | 111±2 | 598±10 | 38±1 | 51±1 | 94.0±5.1 | 94.0±4.3 |
| 6 | 102±2 | 548±11 | 44±1 | 53±1 | 90.6±1.9 | 86.7±4.4 |
| 7 | 106±3 | 600±13 | 41±1 | 54±3 | 91.8±3.4 | 93.0±4.4 |
| 8 | 107±1 | 438±3 | 41±1 | 51±1 | 89.7±5.5 | 89.7±6.3 |
| 9 | 109±1 | 596±7 | 38±1 | 50±1 | 90.8±3.4 | 92.5±2.4 |
| 10 | 110±3 | 608±9 | 40±1 | 54±1 | 82.5±2.9 | 80.2±4.0 |
| 11 | 107±2 | 643±15 | 42±2 | 54±1 | 97.4±2.0 | 95.9±4.0 |
| 12 | 108±3 | 678±3 | 40±1 | 56±1 | 93.0±1.7 | 95.3±4.1 |
| 13 | 105±2 | 541±11 | 44±1 | 57±2 | 90.9±3.7 | 90.9±3.0 |
| 14 | 107±1 | 690±3 | 40±1 | 55±1 | 90.1±5.9 | 85.7±3.9 |
| 15 | 109±3 | 623±9 | 41±1 | 53±3 | 94.4±5.0 | 97.1±2.5 |
| **Avg** | **107.8±2.4** | **600.5±64.5** | **40.2±2.2** | **53.8±2.3** | **91.1±3.3** | **91.1±4.5** |

*Table 2: Oxygen and carbon dioxide end-tidal values during resting and activation periods for all subjects and venous oxygen saturation values for visual-related and motor-related ROI based on GCM modelling.*

Visually-evoked ROI-based relative BOLD and CBF signal changes obtained during simultaneous task and gas inhalation periods and gas-only periods are given in Fig 34a and 34b. The average relative BOLD signal change during carbogen-7 inhalation for the visual-related ROI was 7.2±2.3%. CBF weighted signals for the same period showed an average increase of 97.7±33.4%. During simultaneous gas inhalation and task performance the relative BOLD signal change was 7.5±2.2% and the matching flow signal changes showed an average increase of 102.0±33.2%.

BOLD and flow weighted signal changes for the motor-related ROI are given in Fig 35a and 35b. Marginally larger BOLD changes were found in this brain region compared to the visual-related ROI, with an average of 7.8±2.8% during the gas-only period and 8.1±2.6% for simultaneous gas inhalation and task performance periods. CBF signal changes were also somewhat higher in the motor-related ROI than in the visual-related ROI. CBF signal increases of 102.3±42.4% and 121.7±56.6% were found for gas-only and simultaneous gas inhalation and task performance periods, respectively.
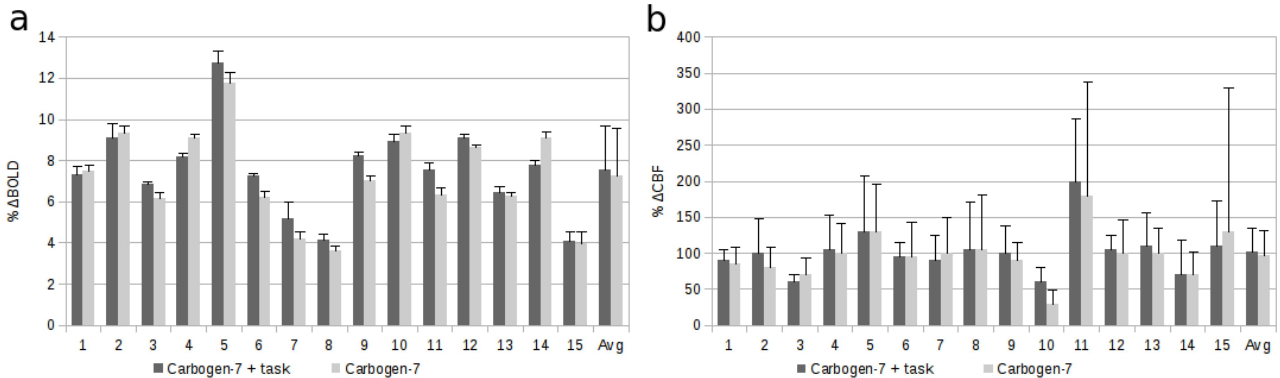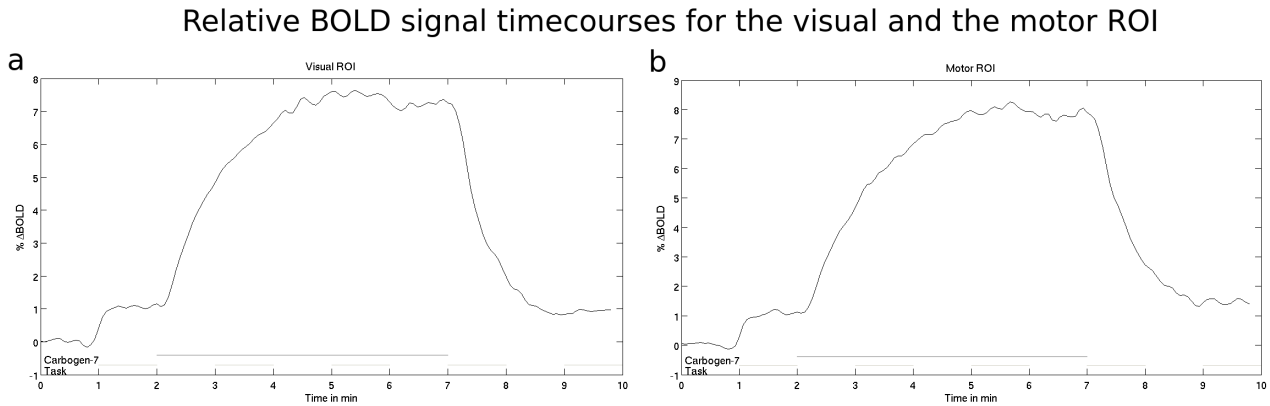
*Figure 34: Relative BOLD (a) and CBF (b) signal changes obtained during simultaneous task performance and gas periods (dark grey) and gas-only periods (light grey) for the visual ROI. Errorbars represent standard deviation across voxels.*



*Figure 35: Relative BOLD (a) and CBF (b) signal changes obtained during simultaneous task performance and gas periods (dark grey) and gas-only periods (light grey) for the motor ROI. Errorbars represent standard deviation across voxels.*

Relative BOLD signal time courses normalised to baseline for the entire ten minute acquisition period can be found in Fig 36a for the visual-related ROI and in Fig 36b for the motor-related ROI. These time courses were obtained by averaging over all voxels within the specific ROI and all subjects. The group-average visual and motor-related ROI BOLD time courses show a significant task-induced signal increase of 1.1% in the absence of carbogen inhalation (first task block). The following task block is not readily detectable in the BOLD time course plot as it occurs during the ramp-up phase of oxygenation following the beginning of gas inhalation (the fourth task block suffers from the same effect in the ramp-down phase of gas-induced oxygenation phase). The third

task block can be identified in the averaged BOLD time course, overlaid on the BOLD increase caused by gas inhalation with a BOLD signal increase of 7.5% and 8.1% for the visual and the motor-related ROIs, respectively. The last task block shows BOLD signal changes of 1.0% in the visual area and 1.5% in the motor area.

## Relative BOLD signal timecourses for the visual and the motor ROI



*Figure 36: Relative BOLD signal change time courses averaged over all subjects and the visual ROI (a) and motor ROI (b), respectively. Blocks of visuo-motor stimulus are indicated by a lightgrey line at the bottom of the graphs and the gas inhalation block with a dark grey line.*

*M*-values were obtained both via direct measurements during combined gas and visuo-motor stimulations, and using the GCM-based approach with the gas-only data. The modelling parameters used for the GCM are given in Table 1. The results from both methods for the visual-related ROI can be found in Fig 37a. The average modelled *M*-value was 10.4±3.9% relative BOLD signal increase whereas the average *M*-value obtained via the direct method was 7.5±2.2%. This difference between both methods was found to be statistically significant (paired t-test t=4.1, p=0.0011). The visual-related ROI-based venous oxygen saturation value for each subject is given in Fig 37b. These values were obtained via the GCM and are therefore based on periods with gas inhalation, but without simultaneous visuo-motor stimulus. Group average venous oxygen saturation was found to be 91.1±3.3%.

Motor-related ROI *M*-values are given in Fig 38a. The modelled *M*-value averaged across subjects was 11.3±5.2%. The directly estimated average measured was 8.1±2.6%. The values derived from both methods were also found to be significantly different in this ROI (paired t-test t=3.3, p=0.0055). The venous oxygen saturation values for each subject for the motor-related ROI is given in Fig 38b, showing an average of 91.1±4.5%.
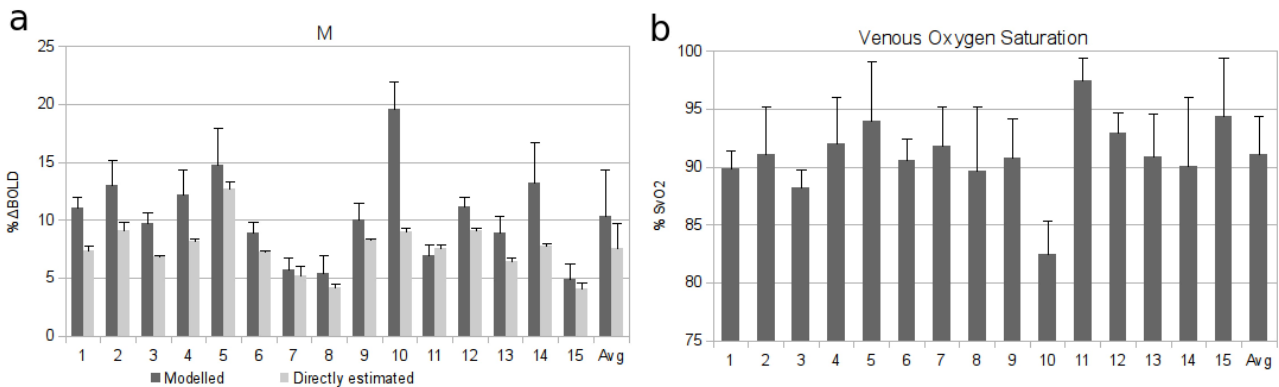
*Figure 37: The image on the left (a) shows the M-values for the visual ROI obtained via GCM modelling (dark grey) and the direct estimation method (light grey). The image on the right (b) depicts the venous oxygen saturation values during gas inhalation periods. These values have been obtained via GCM modelling. Error bars represent the standard deviation across voxels, measured from propagated error estimates of BOLD, CBF and end-tidal $pO_2$ data.*
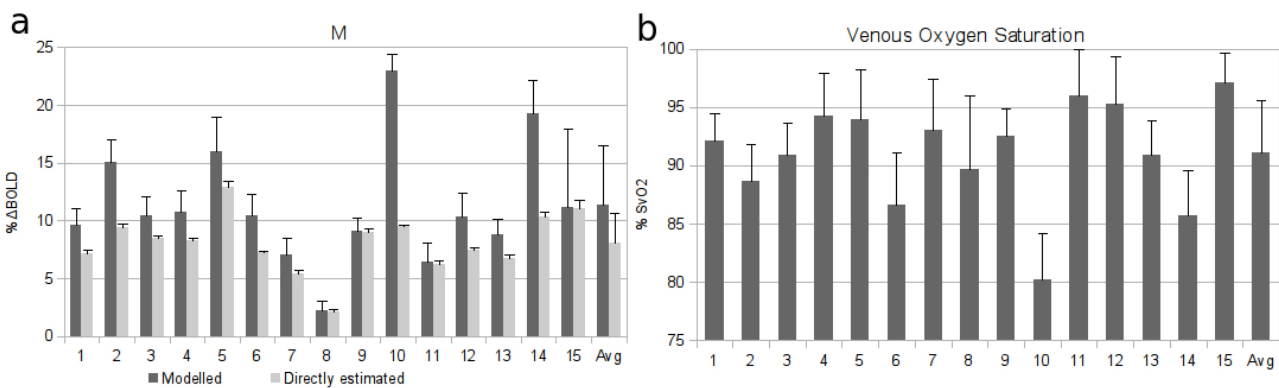


*Figure 38: The image on the left (a) shows the M-values for the motor ROI obtained via GCM modelling (dark grey) and the direct estimation method (light grey). The image on the right (b) depicts the venous oxygen saturation values during gas inhalation periods. These values have been obtained via GCM modelling. Error bars represent the standard deviation across voxels, measured from propagated error estimates of BOLD, CBF and end-tidal $pO_2$ data.*

Example voxel-wise *M*-maps obtained from the best participant (subject number 4) via the direct method and the GCM can be found in Fig 39a (direct estimate) and Fig 39b (modelled). A single slice including both the primary visual and motor areas is shown. Large BOLD signal changes can be seen in occipital and prefrontal areas, whereas white matter showed no significant signal changes.
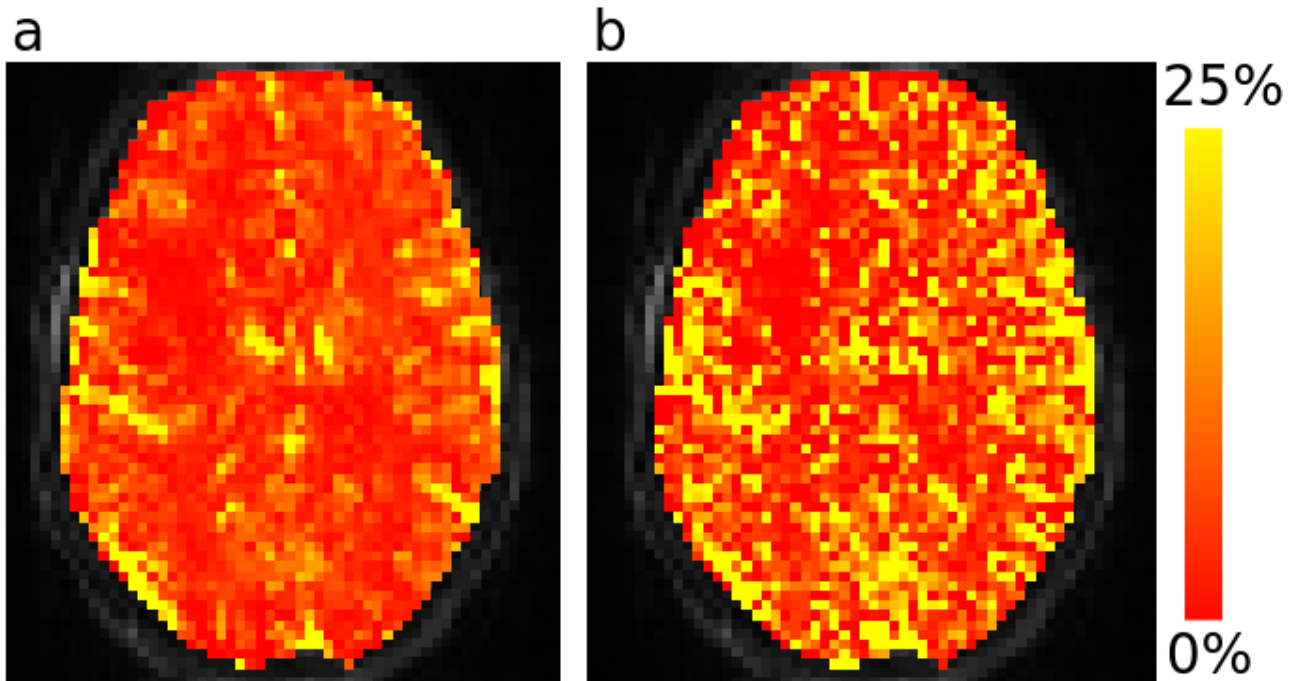
*Figure 39: Example M-maps obtained via the direct method (a) and modelling approach (b) from subject number 4.*

## 4.4 Discussion

In this study we applied and compared two concurrent calibrated BOLD techniques at 7T. The direct calibration method was used under the assumption that complete venous oxygen saturation could be reached using a combined hyperoxia-hypercapnia breathing challenge. To assess whether complete saturation of venous blood was reached using this challenge, subjects in this study also performed a visuo-motor task during gas inhalation. Venous oxygenation levels of 91.1% were obtained during gas inhalation without additional task performance. Average BOLD signal changes elicited by carbogen-7 inhalation were 7.8% in the motor-related ROI and 7.2% in the visual-related ROI. Additional performance of the visuo-motor task elevated the BOLD signal change to 8.1% (motor-related ROI) and 7.5% (visual-related ROI). The modelled *M*-values of 11.3% (motor-related ROI) and 10.4% (visual-related ROI) obtained were on average higher than those obtained directly during gas inhalation and simultaneous task performance.

### 4.4.1 *M*-value Estimation

Visual and motor-related ROI based *M*-values obtained lie within the expected physiological range. Published *M*-values at 3T for the visual cortex ranged from 4.5% up to 11.2% relative BOLD signal change (Ances et al., 2009; Ances et al., 2008; Bulte et al., 2012; Bulte et al., 2009; Chen & Parrish, 2009; Chiarelli, Bulte, Piechnik, et al., 2007; Chiarelli, Bulte, Wise, et al., 2007; Gauthier et al.,

2012; Gauthier et al., 2011; Gauthier & Hoge, 2013; Leontiev et al., 2007; Leontiev & Buxton, 2007; Lin et al., 2008; Mark et al., 2011; Mark & Pike, 2012; Perthen et al., 2008). At 3T, published motor cortex $M$-values range from 5.0% to 25.0% relative BOLD signal change (Ances et al., 2008; Chiarelli, Bulte, Wise, et al., 2007; Mark et al., 2011; Mark & Pike, 2012; Mohtasib et al., 2012; Uludağ et al., 2004). The higher $M$-values reported in this study are consistent with the increased amplitude of the BOLD contrast at 7 T. It is important to note however, that the conclusions that may be drawn from a quantitative comparison of $M$-values across field strengths are limited. Although there exists some published literature aiming to quantify $R_2$ and $R_2^*$ relaxation changes across field strengths (Blockley et al., 2013; Uludağ et al., 2009), these biophysical relationships are still only partly understood (Ivanov et al., 2013). Reported $M$-values at 7T can be found in Table 3. These have been adjusted to the echo time used in this study ($TE$=8.1ms) based on Hoge et al. (1999).

Published $M$-values at 7T adjusted to a $TE$ of 8.1 ms are in the same range, albeit somewhat smaller than those obtained by this study for the visual cortex. However, the extrapolation performed for the adjustment considers neither the difference in voxel size across studies, nor differences in intravascular and extravascular BOLD signal weighting (Triantafyllou et al., 2005). Huber et al. (Huber et al., 2013) used an isotropic resolution of 1.5mm, and therefore lower $M$-values can be expected due to reduced large vessel contributions and lower SNR compared to larger voxel sizes. Furthermore, the studies cited in Table 3 used different MRI techniques and breathing manipulations to obtain $M$, which is expected to increase the variance in $M$-value estimation between studies. The motor-related ROI $M$-values from this study are also in reasonable agreement with the adjusted $M$ estimates from studies in the motor area, and with similar voxel volumes (Hall et al., 2013; Driver et al., 2012).

Directly estimated $M$-values obtained in this study were consistently lower than their modelled counterpart for both visual- (p=0.0011) and motor-related ROIs (p=0.0055). While group average modelled and directly estimated $M$-values differed significantly, the difference between the two estimates varied between subjects. Some of this variability in modelled versus directly estimated difference may be attributable to inter-subject differences in carbogen-evoked flow increases. The largest relative differences between directly obtained and modelled $M$-values were found for subjects 10 and 14, both in the visual and motor-related ROIs. This larger difference between direct and modelled estimates may be partly explained by the fact that both participants showed flow changes in response to carbogen-7 inhalation below the group average. Because of its role in determining venous $O_2$ concentration, relative flow change in response to carbogen inhalation has a

major impact on GCM-based modelling (see equation 2 in (Gauthier & Hoge, 2013)). Venous saturation is typically much lower than arterial saturation (around 65% in venous versus about 98% in arteries), so that relatively modest flow increases due to carbogen inhalation only partly dilute the deoxyhaemoglobin generated through local baseline metabolism. Previous studies have shown that complete BOLD signal saturation occurs only at very high flow levels (Gauthier et al., 2011). As expected from their small CBF response, both subjects showed low estimated venous oxygen saturation during gas inhalation and consequently BOLD signals measured for these subjects were estimated to be well below the theoretical maximum. Therefore, in participants with a low CBF response to carbogen inhalation, the direct method underestimates the $M$-value, as the assumption of fully saturated oxygenation is not fulfilled.

In participants showing a large CBF response to carbogen inhalation, this effect disappears (compare subjects 10 and 14 to subjects 11 and 15). High blood flow in this case leads to small differences in oxygen concentration between the venous and the arterial vessel compartment from the large influx of fully saturated blood. Inhalation of carbogen leads to very high arterial $O_2$ content from an increased $O_2$ concentration in plasma. Combined with a large CBF increase, this high $O_2$ concentration may effectively compensate for any $O_2$ extraction in tissue due to local metabolism, leading to fully saturated venous blood. The venous oxygen saturation for these subjects was estimated to be high using the GCM. Thus modelled and directly estimated $M$-values in these participants were virtually identical. Results from these participants therefore suggest that, in participants with sufficiently high flow changes due to carbogen-7 inhalation, the direct method is applicable for the accurate determination of $M$ .

| Publication | Brain area | Original $TE$ in ms | $M$ in % | Adjusted $M$ in % |
|---|---|---|---|---|
| (Huber et al., 2013) | Visual | 19.0 | 14.3 | 6.1 |
| (Gauthier, Krieger, et al., 2013) | Visual | 19.4 | 14.5 | 6.1 |
| This study | Visual | 8.1 | 10.4 | 10.4 |
| (Driver et al., 2012) | Motor | 25.0 | 28.0 | 9.1 |
| (Hall et al., 2013) | Motor | 23.0 | 23.3-34.0 | 8.2-12.0 |
| This study | Motor | 8.1 | 11.3 | 11.3 |

*Table 3: Published visual and motor cortex M-values at 7 Tesla adjusted to TE=8.1ms.*

### 4.4.2 BOLD Time Courses

While most of the effects discussed so far rely on the accurate measurement of CBF using ASL, additional confirmation of these conclusions can be drawn from the BOLD time courses. Detection of a response to the task during carbogen inhalation is indicative that carbogen-7 alone is not sufficient to cause complete saturation. The amplitude of this response is however reduced by about two thirds as compared to the task-evoked response amplitude measured during air breathing. This diminished task-evoked response could at first sight be interpreted as showing that the combined stimulus leads to saturation. However, comparison of our data with the data presented by Gauthier et al. (Gauthier et al., 2011) indicates that this may not be the case. Gauthier et al. showed that a flashing checkerboard visual stimulus during simultaneous carbogen-7.5 gas inhalation led to reduced visually evoked BOLD signal changes. However the combined BOLD signal changes from task and carbogen-7.5 inhalation did not reach the maximum BOLD signal changes obtained by using carbogen-10. Therefore, the diminished amplitude of the task component seen in our data during carbogen-7 inhalation cannot be used to make inferences on overall BOLD signal saturation.

Our results further agree with the data presented by Gauthier et al. in terms of the relative amplitude of these effects. The amplitude of our direct $M$ estimate was around 75% of the modelled $M$ amplitude, which is comparable (when taking into consideration the lower $CO_2$ content and weaker visuo-motor stimulus used here) to the relative amplitudes of the BOLD signal changes obtained for carbogen-7.5 combined with visual stimulus and carbogen-10.

Interestingly, our results indicate a discrepancy between the visual and the motor-related ROI task-induced BOLD signal during last task block (between minutes 9 and 10). Whereas the amplitude of the last block was similar to the first for the visual-related ROI, the motor-related ROI shows an apparent increase in task-evoked BOLD signal during the last block. This could be due to the slower return to baseline of the BOLD signal after carbogen-7 inhalation seen in the motor as compared to the visual-related ROI (compare slopes in Fig 36a and 36b). Overall, the results obtained from the BOLD time course data support the conclusions drawn from time-averaged ROI-quantifications. Carbogen-7, even when combined with a task, does not increase venous oxygen saturation sufficiently for the direct measurement of the $M$-value.

### 4.4.3 $M$-Maps and Single Subject Analysis

In the ideal case, the $M$ parameter would be determined on a voxel-wise basis in every subject. This would allow assessment of more refined regional hypotheses and lead to important clinical applications. We assessed the feasibility of voxel-wise single-subject analysis for estimation of the

calibration factor $M$ in the visual cortex, as well as brain areas related to motor activation in our task, for a single subject with high quality data. Both areas showed large BOLD signal changes during simultaneous task and carbogen inhalation (Fig 39a). However, GCM modelling resulted in a noisier $M$-map (Fig 39b). This is unsurprising since calculation of the $M$-value using the modelling approach requires the incorporation of lower SNR perfusion signal changes to the BOLD signal change used in the direct method. Consequently, while the $M$ parameter can currently be mapped, higher quality $M$-maps would require further improvements of the PASL technique.

### 4.4.4 Effects on CMRO$_2$ Estimation

Accurate determination of the $M$ parameter is necessary for the estimation of task-evoked CMRO$_2$, and small errors in $M$ determination may lead to large errors in CMRO$_2$. In order to assess the significance of an accurate estimation of $M$ at ultra-high field, the effect of errors in estimated $M$-value on CMRO$_2$ estimates was assessed. Let $M_c$ be the correctly estimated $M$-value and $M_i$ the erroneous $M$-value with CMRO$_{2,c}$ as the correct cerebral metabolic rate of oxygen and CMRO$_{2,i}$ as its incorrectly estimated counterpart. Equation 91 expresses the relationship between correctly and incorrectly estimated CMRO$_2$. rCBF is defined as the relative CBF-weighted signal and rBOLD the relative BOLD signal change during functional activation. $\alpha$ represents the Grubb constant and $\beta$ models the influence of deoxygenated haemoglobin on transverse relaxation.

$$\frac{CMRO2_c}{CMRO2_i} = \frac{rCBF^{1-\alpha/\beta}\left(1-\frac{rBOLD}{M_c}\right)^{1/\beta}}{rCBF^{1-\alpha/\beta}\left(1-\frac{rBOLD}{M_i}\right)^{1/\beta}} \tag{91}$$

When assuming that $\beta=1$ for 7 Tesla, equation 91 simplifies to equation 92.

$$\frac{CMRO2_c}{CMRO2_i} = \frac{1-\frac{rBOLD}{M_c}}{1-\frac{rBOLD}{M_i}} \tag{92}$$

A plot of equation 92 for fixed $M_c$ and $M_i$ can be found in Fig 40a. The results indicate that for a given $M_c$ and $M_i$ the CMRO$_2$ calculation error based on an erroneously estimated $M$-value is larger for higher BOLD signal changes during task performance. Fig 40a additionally underlines the

significance of a correct estimation of $M$ as error propagation to $CMRO_2$ values increases hyperbolically with linearly increasing error of $M$.

## $CMRO_2$ error propagation at 7 Tesla
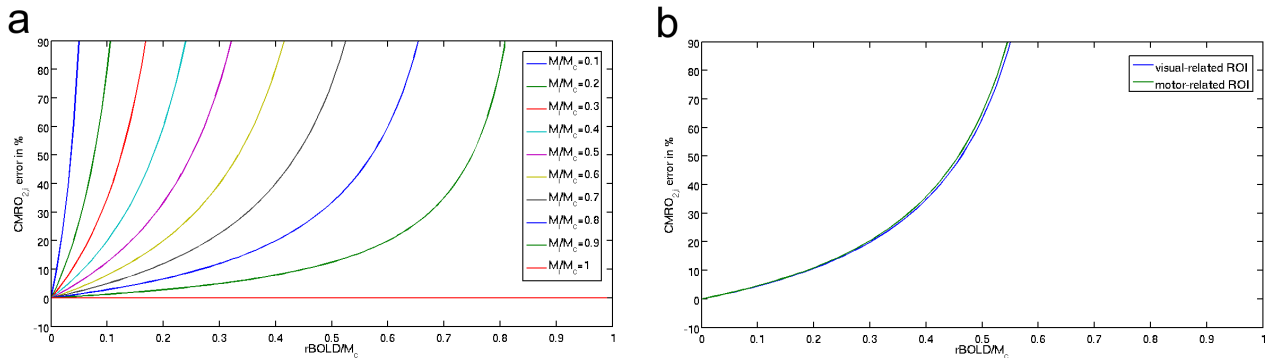


*Figure 40: The effect of errors in M estimation on calculated $CMRO_2$ estimates. Equation 92 is plotted for fixed $M_c / M_i$ ratios in panel a. Relative BOLD signal changes during task performance (rBOLD) are expressed relative to $M_c$. Errors in $CMRO_2$ estimation increases with larger rBOLD. A linear increase in the M estimation error results in exponentially increases in error in $CMRO_2$. Panel b depicts errors in $CMRO_2$ estimation for the specific M-values obtained for the visual-related and motorrelated ROI, at various rBOLD estimates.*

By replacing $M_c$ and $M_i$ with the modelled and directly estimated $M$-values obtained in this study the plots shown in Fig 40b were obtained for the visual-related and the motor-related mask. Based on Fig 40b and the estimated rBOLD values obtained during the visuo-motor task, $CMRO_2$ estimation errors between 10% and 30% can be expected during visuo-motor task performance for the echo time used in this study.

### 4.4.5 Technical Limitations and Implications for Calibrated fMRI

Some subjects showed slightly higher measured BOLD signal changes during gas-only periods than during gas inhalation with additional task performance. This may be a consequence of the specific method used here to calculate BOLD and CBF changes. Because these values were estimated by averaging the raw signals rather than using the results of a GLM, and since different paradigm periods were used for the two methods (simultaneous gas and task for the direct method and gas alone for the modelled method), experimental noise may lead to this non-intuitive result. This may be especially likely if, as seen here in all participants, the task component has a low signal amplitude during carbogen breathing. This result could also stem from a reduction or absence of a CBF response to the task when performed during the gas inhalation challenge, as observed in a previous study (Zappe, Kâmil Uludağ, et al., 2008). In that study, the authors observed a suppressed haemodynamic response to a functional task during 6% $CO_2$ inhalation in anaesthetised monkeys.

The authors interpreted the negative task-related BOLD signal changed obtained as an absence of flow increase in the presence of a task-evoked increase in deoxyhaemoglobin concentration. However, these results are inconsistent with more recent data obtained in awake humans, showing a positive task-evoked BOLD response during similar, and even higher $CO_2$ gas-mixtures (Gauthier et al., 2011). Furthermore, data from Gauthier et al. (Gauthier et al., 2011) show that this BOLD signal increase is accompanied by a preserved flow increase to the visual task during carbogen-10 inhalation. These results have recently been confirmed via optical imaging spectroscopy in rats (Kennerley et al., 2012).

Correct modelling-based $M$-value estimation relies on accurately estimated CBF changes during gas inhalation. Data quality for the ASL data collected here can be seen in 41. As previously discussed, high flow changes usually reflect high venous oxygen saturation (e.g. subjects 11 and 15), while underestimation of CBF can lead to an overestimation of $M$. This last scenario may occur in cases of low SNR perfusion measurements or low voxel numbers within the specific ROI, which may be biased towards larger vessels. Subject number 10 may be a good example for this effect. This subject was found to have the lowest venous oxygen saturation values for both ROIs and also showed the lowest measured CBF signal changes, especially during gas inhalation periods without additional task performance. As carbogen-7 inhalation typically results in CBF increases higher than 50% (Schwarzbauer & Hoehn, 2000; Zappe, Kâmil Uludağ, et al., 2008; Gauthier et al., 2011) the CBF increase may in fact be underestimated in this participant, leading to inflation of the modelled $M$-value. Additionally, changes in arterial transit times caused by the stimuli may result in decreased quality of CBF signal estimation (Gonzalez-At et al., 2000; Hernandez-Garcia et al., 2005). While arterial transit time changes were not taken into account here, future studies could measure and correct for differences in arterial transit time to increase the accuracy of the ASL measurement. Moreover, the choice of echo time will determine the amount and compartment-specificity of BOLD contamination of the CBF-weighted signal. At the short echo time used here, although extravascular BOLD is minimised, intravascular BOLD may contaminate measured CBF signals, especially in regions with large veins (Ivanov et al., 2013). However, as intravascular BOLD signal is expected to be smaller than its extravascular counterpart, especially at 7 Tesla, the effect on CBF estimation is likely to be minor (Duong et al., 2003; Kim & Ogawa, 2012; Uludağ et al., 2009). Finally, recent studies also revealed that changes in cerebrospinal fluid (CSF) relaxation rates due to oxygenation changes (Zaharchuk et al., 2006; Zaharchuk et al., 2005) could affect the quantification of CBF signal changes. Future studies could seek to correct for this effect.

An important aspect of all fMRI acquisition is the trade-off between increased SNR at larger voxel

sizes and higher field strength and the concurrent increase in the amplitude of physiological noise (Krüger & Glover, 2001; Triantafyllou et al., 2005). At 7 Tesla, the voxel size chosen in this study corresponds to the point where the SNR gain from going to larger voxel sizes tapers off, thereby representing a compromise to minimise the impact of physiological noise on the data acquired. Post-hoc physiological noise correction techniques also exist and could be applied in future studies to improve quality of the data (Triantafyllou et al., 2005).

The CBF changes shown here differ somewhat from the CBF changes measured in a previous MRI study using carbogen-7 (Gauthier & Hoge, 2013). Some of these differences could be attributed to differences in ASL implementations (pseudo-continuous versus pulsed ASL). However, the most significant source of difference between these two studies may be the implementation of the breathing manipulation, since the end-tidal value reached for a given gas mixture is highly dependent on the efficiency of the delivery mode. In the previous study, a non-rebreathing face mask was used, while a mouthpiece with nose clip was used in the current study. Since the face mask used in the earlier study was not sealed to the face, a significant amount of contamination with room air occurred, leading to lower and more variable end-tidal values. When taking these differences into account, the vascular reactivity (in percent CBF change per mmHg $CO_2$ change) was found to be similar for the two studies (data not shown).


The generalized calibration model predicts maximum BOLD signal changes for 100% oxygen saturation of the venous blood and the modelled $M$-value is calculated under this assumption. A recent study however suggests that susceptibility effects of different intravascular and extravascular compartments may lead the maximal BOLD signal at slightly lower oxygen saturation (Griffeth & Buxton, 2011). These effects could partly explain differences between directly and modelled $M$-values found in this study. However, further work is needed to understand the importance of this effect at ultra-high field, where the contribution of various tissue compartments is expected to be different, and the implications of this finding on the definition of the $M$ parameter. Given these sources of uncertainty as to the importance of this effect at this field strength, the original definition of the $M$ parameter has been retained here.

Another possible caveat leading to biased $M$-value estimation arises from putative changes in oxygen metabolism during $O_2$ (Xu, Uh, et al., 2011) and $CO_2$ gas inhalation (Jones et al., 2005; Xu, Uh, et al., 2011; Zappe, K Uludağ, et al., 2008). Additionally, the modelling approach relies on the assumption of several physiological parameters whose values are still the subject of some debate, including the $\alpha$, $\beta$ and OEF parameters. The biases arising from misattribution of the correct value

for these parameters has been discussed elsewhere (Griffeth & Buxton, 2011; Buxton, 2010; Buxton et al., 2004; Blockley, Griffeth & Buxton, 2012; Blockley, Griffeth, Simon, et al., 2012; Gauthier & Hoge, 2013; Chiarelli, Bulte, Piechnik, et al., 2007; Chen & Pike, 2010; Chen & Pike, 2009). The GCM has been shown to lead to more robust determination of $M$ in a previous study. It nevertheless suffers from some weaknesses of both original calibrated fMRI methods, since it relies on the low SNR measurement of flow changes during breathing manipulations (from the hypercapnia model) and assumptions on baseline oxygen usage (from the hyperoxia model). In contrast, the direct $M$-value estimation method measures the maximum BOLD response directly and is therefore independent of low SNR CBF measurements and could circumvent issues related to $M$-value modelling. However, the major drawback of the direct method is that it requires complete venous oxygen saturation due to gas inhalation. Our results suggest that this requirement is not met in most participants using carbogen-7 inhalation, even when combined with simultaneous task performance. Our results also highlight the fact that incomplete saturation from the breathing manipulation may not be compensated readily with the addition of a task, although it is possible that longer task blocks with a more intense stimulus may help reach complete saturation. The visuo-motor task used here was chosen to assess the possibility to use these techniques at ultra-high field in a context relevant for future applications in cognitive neuroscience. The use of a simple task such as the flashing checkerboard used in previous studies did not allow the assessment of the applicability of this technique to the more subtle cognitive tasks that would benefit from the additional physiological specificity of calibrated fMRI.

Modelling of the $M$-value using the GCM or other modelling approaches suffers from a variety of assumptions, possible biases and a lower SNR from the incorporation of noisy flow values. The direct method, while immune to many of these issues, suffers however from a few method-specific biases when carbogen inhalation is combined with a task to determine $M$. Because breathing of carbogen-7 or -10 causes breathing discomfort in most participants (Gauthier et al., 2011; Gauthier & Hoge, 2013), this could lead to a decrease in behavioural performance when the task is performed during the breathing manipulation. This may be particularly problematic in the case of a task with a significant cognitive component. This possible source of bias was, however, not a significant problem here, as behavioural performance on the visuo-motor task was found to be equivalent in task blocks during air and carbogen breathing.

Another source of error in this implementation of the direct method might arise from the fact that the sources of the combined haemodynamic changes have different spatial characteristics. The response to carbogen inhalation is global, but the response to the task is local. While the impact of

this may be partly minimized by strict functionally-based ROI selection criteria, there is no guarantee that all tissue within the ROI is activated by the task and therefore contributes to task-evoked CBF increase. However, while not all neurons of the area may be active, different neurons share local vascular resources. Because the vascular response to a stimulus is known to be much larger than the metabolic increase, the extra dilution from even a partial volume activation component may, in cases of near-saturation, be enough to lead to complete saturation over the whole ROI volume.
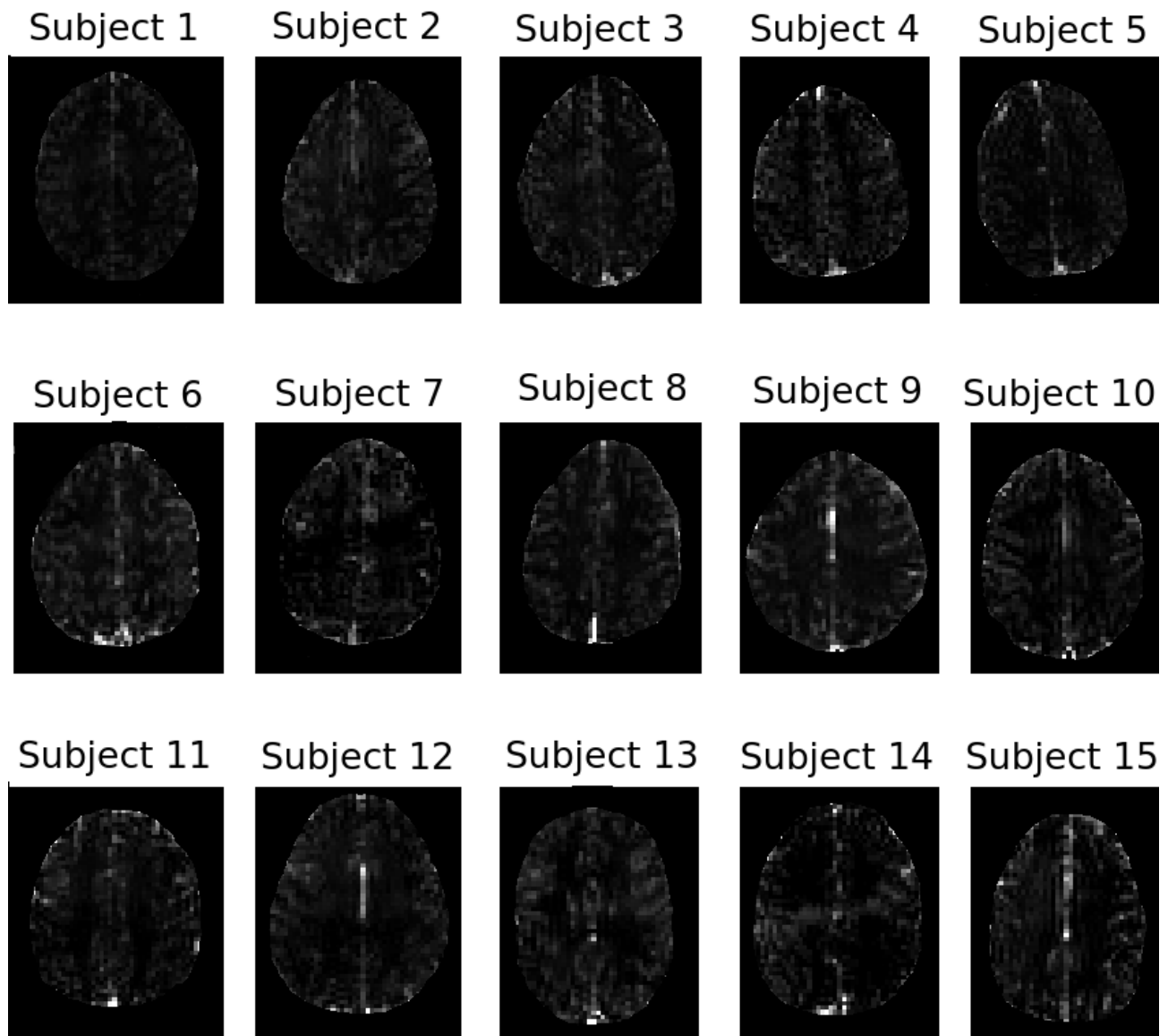


*Figure 41: Example ASL data obtained in this study.*

Overall, the results of the current study suggest that the modelling approach used in the existing literature is the most accurate method available for calibrating the BOLD signal. The current modelling methods have the further advantage of being usable for the additional measurement of

baseline metabolic parameters when combined with more than one breathing manipulation. Therefore, while more speculative in terms of assumed physiological parameters, the modelling approach allows the estimation of a more complete metabolic profile than the direct method.

## *4.5 Conclusion*

In this calibrated fMRI study, we compared the direct estimation of calibrated BOLD $M$-values to the generalized calibration model-based approach. Calibrated BOLD modelling suffers from important drawbacks, such as the reliance on assumed parameters whose values have not been fully validated. Additionally, $M$-value modelling is vulnerable to errors in CBF signal quantification. While the direct method does not suffer from these sources of error, it relies on complete venous oxygen saturation during the calibration period. Our data suggests that this cannot be achieved for all subjects when using carbogen-7, even when applying an additional visuo-motor task during gas inhalation. Therefore, despite the theoretical advantages of direct $M$-value estimation, incomplete venous saturation using carbogen mixtures with less than 10% $CO_2$, make the modelling approach necessary for accurate $M$ estimation. This accurate determination of $M$ is crucial to estimate valid task-evoked $CMRO_2$ since, as shown here, even modest errors in $M$ estimation may lead to large errors in $CMRO_2$ estimates. Future studies applying GCM-based modelling would benefit from improved flow-weighted data, making possible the estimation of more accurate $M$-value averages and $M$-maps with higher SNR. This quantitative mapping of oxygen metabolism would provide insight into the physiological and neuronal mechanisms of the human brain and could be used to study metabolic properties in health and disease.

# 5 Experiment II: Reproducibility of BOLD, ASL and Calibrated fMRI

This study has been published in Neuroimage (2014) 101:8-20.

## *5.1 Background Information*

The results obtained in the previous study (Krieger et al., 2014) provided evidence that GCM modelling might be the more accurate way of determining the calibration parameter *M* compared to the saturation technique. In this chapter the reproducibility of GCM based calibrated fMRI is assessed and compared to BOLD and ASL based fMRI techniques.

The calibrated BOLD technique inherently provides superior spatial specificity and offers physiologically more meaningful measures, compared with the classical BOLD approach. Importantly, this method has been shown to provide good stability characteristics at lower field strengths with simple functional stimuli (Leontiev & Buxton, 2007). Despite its theoretical advantages, few groups have adopted calibrated fMRI for studies of cognition and neuroplasticity (Kida et al., 2007; Gauthier, Madjar, et al., 2013; Herman et al., 2013). One reason may be the greater complexity of calibrated BOLD compared with classical BOLD, in terms of MRI setup, acquisition time and data analysis. Furthermore, most functional MRI software packages do not include tools to analyse calibrated BOLD data, and there is a lack of practical guidelines available for the adoption of this technique. Finally, the stability of calibrated BOLD for low-contrast and cognitive tasks has not been assessed, making it difficult to determine the benefit that a specific cognitive neuroimaging study could obtain by using calibrated BOLD compared with the effort required to implement the technique.

This study explores the applicability and reproducibility of a state-of-the-art calibrated BOLD technique when applying complex low-contrast functional tasks at 7 Tesla. Ultra-high field fMRI provides increased spatial resolution, specificity and sensitivity compared to lower magnetic field approaches (Triantafyllou et al., 2005; Uludağ et al., 2009). We show that calibrated BOLD can be reliably used for fMRI studies that apply complex low-contrast stimuli, such as cognitive tasks, also at high magnetic field strengths, with stability characteristics comparable to lower field strengths (Leontiev & Buxton, 2007). While this study was based on ultra-high field measurements, our conclusions extend beyond this field strength and help establish guidelines for the implementation of calibrated fMRI for both cross-sectional and longitudinal cognitive studies. We have assessed calibrated BOLD reproducibility across subjects and across days, and across runs within the same subjects. Furthermore, these estimates were compared with CBF and BOLD-based reproducibility

estimates for the same group of subjects.

## 5.2 Methods

Thirteen healthy participants (7 women, 27 ± 3 years) were scanned using the scanner setup described in chapter 3.1 according to the guidelines set by the local review board (Ethics Commission, Leipzig University). All participants gave written informed consent for participation in the study.

### 5.2.1 Experimental Design

Three calibrated BOLD scanning sessions were performed on each subject within a period of 7 days, with a maximum total daily scanning time of 60 minutes. Each session consisted of one ten-minute run with a combined gas breathing challenge and visuo-motor task (see Fig 42) followed by three ten-minute runs with the visuo-motor task alone. A one-minute on/off block design was used for the task, starting with one minute rest. The first ten-minute run of each day included a combined visuo-motor and gas-inhalation design. Gas inhalation started after two minutes of acquisition and lasted five minutes, superimposed on the previously-described ten-minute task design (see Fig 42). Simultaneous acquisition of BOLD and CBF-weighted images was performed via pulsed arterial spin labelling for all functional runs. The functional stimulus, the gas-breathing stimulus and the scanning parameters were identical to those described in chapter 4. For detailed information please refer to chapters 4.2.2 to 4.2.4.

### 5.2.2 Data Analysis

FMRI datasets were corrected for motion, and all 12 runs of each subject were then co-registered using MCFLIRT (FSL, fMRIB, Oxford, UK). A general linear model (GLM) analysis across all functional runs from each subject was used to define two functional regions of interest (ROI) one including primary visual and the other including primary motor areas. The fMRI expert analysis tool (FEAT) v. 5.98 from the FSL software package was used to create activation maps using a 3 mm smoothing kernel. In order to preserve spatial information smoothing was only used for the ROI generation step. Cluster thresholding was used to define significant signal changes for BOLD and CBF-based ROI selection ($p<0.05$, corrected for multiple comparison). The intersection of significant BOLD and CBF signal changes was used to define the visual and motor ROIs. These ROIs were chosen, since primary areas were thought to be most likely to show detectable signal changes at the level of each individual, while being somewhat more immune to complex learning or habituation effects than areas exclusively involved in cognitive aspects of the task. This ROI selection is similar to the ones employed in longitudinal and learning studies. An additional grey

matter ROI was defined on the basis of thresholded absolute CBF maps generated via the Neurolens software package (www.neurolens.org). Voxels showing absolute flow values greater than 20ml/min/100g tissue were defined as grey matter and included in the mask (Pohmann, 2010).
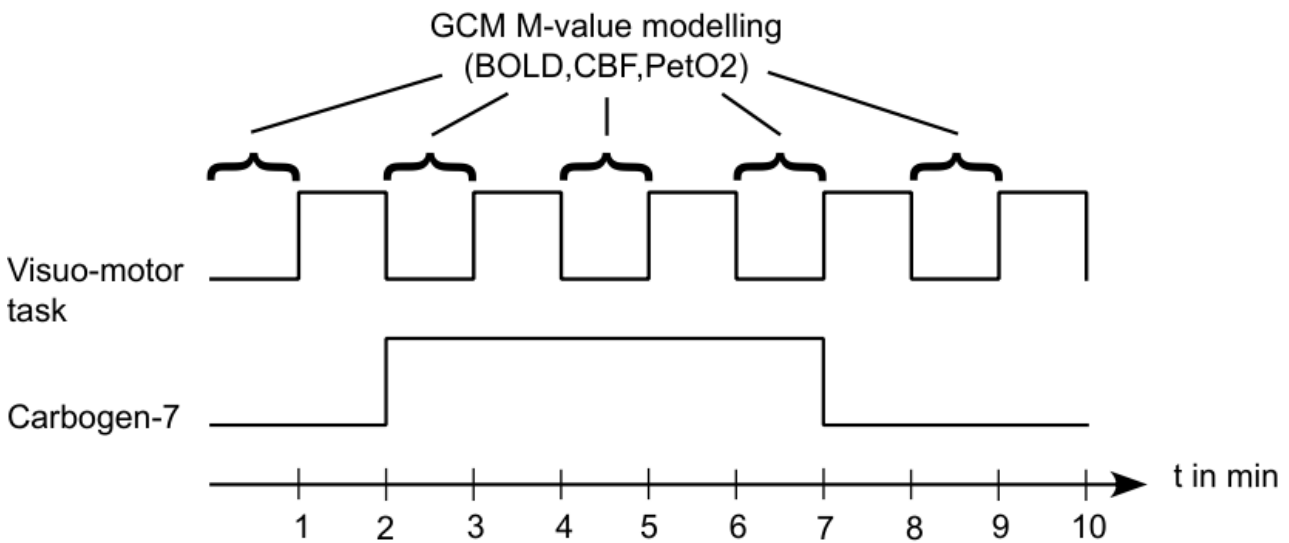


*Figure 42: Visualisation of the calibration acquisition design. During the first ten-minute run of each day, gas inhalation started after two minutes of acquisition and lasted five minutes, superposed on the 10-minute task as previously described.*

All subsequent steps of the data analysis were performed using in-house Mathworks Matlab (version 8.0.0.783 R2012b) code. Linear temporal interpolation was performed on tag and control datasets. Voxel-wise subtraction of interpolated control and label images resulted in CBF-weighted images. BOLD time series were obtained from voxel-wise addition. CBF and BOLD time courses were then ROI-averaged. Because there is no literature available describing the effects of hyperoxia on $T_1$ of arterial blood at 7 Tesla, a 10% underestimation of CBF was assumed, following the assumptions of earlier studies (Bulte et al., 2007; Gauthier & Hoge, 2013; Krieger et al., 2014). A linear BOLD signal drift correction was applied for runs without gas inhalation, although these corrections were only of minor amplitude. Furthermore, we tested for signal drifts within one-minute blocks during the calibration scans. No significant signal drifts were detected.

The calibration constant *M* is needed for estimation of functionally-induced changes in cerebral oxygen metabolism. This study used the generalised calibration model (GCM) to obtain *M*, since this model is compatible with combined hypercapnia and hyperoxia breathing manipulations such as carbogen-7 inhalation (Gauthier & Hoge, 2013). Based on the GCM the *M*-value can be calculated as follows:

$$M = \frac{BOLD_c}{1 - CBF_c^{\alpha}\left(\frac{1 - Sv_{O_2}}{1 - Sv_{O_{2,0}}}\right)^{\beta}} \qquad (93)$$

where $BOLD_c$ is the fractional change in BOLD signal and $CBF_c$ is the relative CBF signal due to carbogen inhalation, $\alpha$ represents the power law exponent describing the relationship between changes in cerebral blood flow and cerebral blood volume, assumed here to be 0.18 (Chen & Pike, 2010). The exponent $\beta$ (Driver et al., 2010; Yablonskiy & Haacke, 1994) is used to model the influence of deoxygenated haemoglobin on transverse relaxation (Boxerman et al., 1995) and is here assumed to have a value of 1.0 due to the high magnetic field used (Kida et al., 2000; Martindale et al., 2008). $SvO_2$ and $SvO_{2_0}$ represent venous $O_2$ saturation during gas breathing periods and baseline (air breathing) periods respectively. Venous $O_2$ saturation values were obtained from GCM modelling with an assumed value of 0.35 for baseline oxygen extraction fraction (OEF) (Bulte et al., 2012; Carpenter et al., 1991; Gauthier & Hoge, 2012; Lu & Ge, 2008). For more detailed information on the specific calibration model used in this study refer to (Gauthier & Hoge, 2013). $M$ was estimated on each measurement day for each subject, under the assumption that the physiological conditions remain stable during one scanning session, giving a total of three $M$-values for each subject. Cerebral oxygen metabolism was calculated for each of the three task-only runs, for a total of nine ROI-based $CMRO_2$ estimates per subject. Relative changes in $CMRO_2$ were estimated using equation 94 with $BOLD_t$ representing the fractional signal change of BOLD and $CBF_t$ the relative CBF signal during task stimulation.

$$CMRO_2 = \left(1 - \frac{BOLD_t}{M}\right)^{\frac{1}{\beta}} CBF_t^{1 - \frac{\alpha}{\beta}} \qquad (94)$$

The coupling between CBF and $CMRO_2$ is described as the index n, defined as the ratio between fractional changes in CBF and the fractional changes in $CMRO_2$ in response to a functional challenge.

### 5.2.3 Reproducibility

Variability in BOLD, CBF, $M$, $SvO_2$, $CMRO_2$ and n within and between MRI sessions was investigated. For that purpose three coefficients of variation (CV) (Tjandra et al., 2005) were computed. These characterised a) variability across runs on the same day for the same subject ($CV_1$), b) across days for the same subject ($CV_2$) and c) across all runs and sessions for all subjects ($CV_3$). The CV is defined as the standard deviation divided by the mean signal change within the

specific ROI, expressed as a percentage. A graphical representation of the different acquisitions included in each CV can be found in Fig 43.
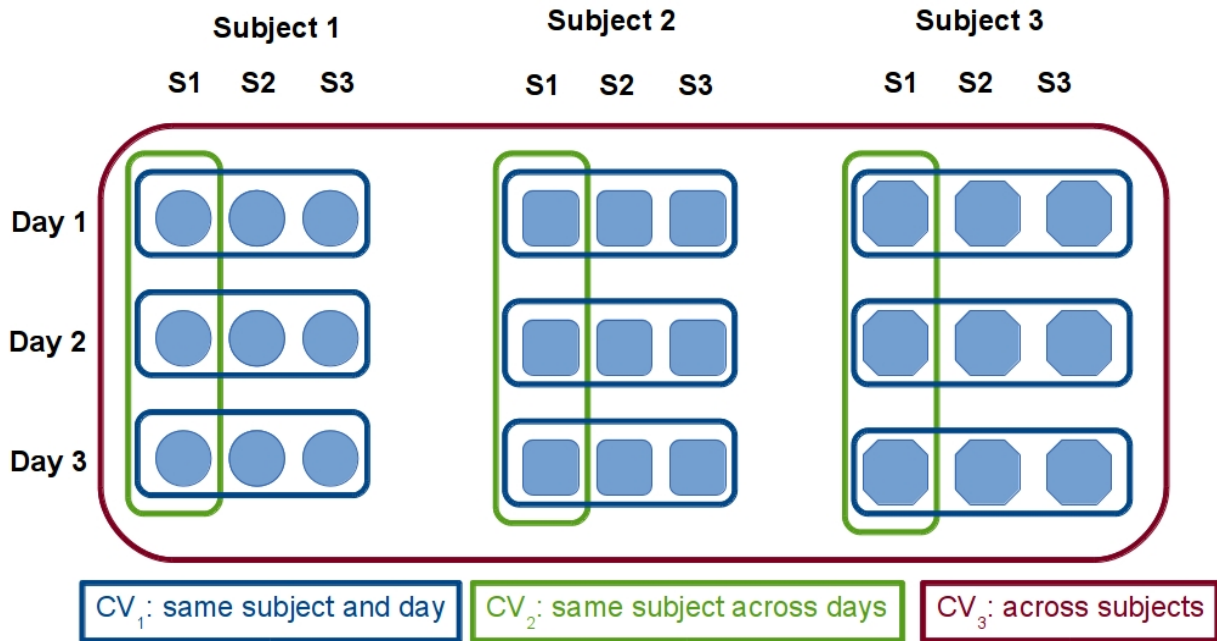


*Figure 43: A graphical representation of the different acquisitions included in each coefficient of variation. $CV_1$ is calculated for each subject and day, giving 3 estimates. These are averaged, leading to the intra-subject reproducibility across runs within the same day. The first ten-minute runs of each day are used to generate $CV_2$ representing the intra-subject reproducibility across days. All runs from all subjects are used to calculate the inter-subject $CV_3$.*

*$CV_1$ - Same subject and day*

Variability estimates for each subject were derived on a daily basis. Coefficients of variation were calculated separately for each subject and each day resulting in 3 CVs per subject.

*$CV_2$ - Same subject across days*

One coefficient of variation was calculated per subject using only the first run of each day.

*$CV_3$ - Across subjects*

All runs and sessions from all subjects and all days were used to calculate one inter-subject CV.

It should also be noted that task-evoked $BOLD_t$, $CBF_t$ and $CMRO_2$ were not calculated for the grey matter ROI as zero signal changes can be expected in response to the task within this mask since all task-relevant voxels were excluded from it. A statistical t-test was applied between the pooled data

from each ROI in order to determine statistical significance of the results.

## 5.2.4 Learning and Habituation Effects

To assess the impact of habituation and learning on the stability estimates, we used motor performance from each subject as an additional regressor for statistical data analysis. Improvement in motor performance was expected to lead to decreased functional signals in primary motor areas (Floyer-Lea & Matthews, 2004; Ungerleider et al., 2002). The residual signal following regression of performance on each individual acquisition was then used to perform the variability analyses previously described. These performance-corrected CVs may be useful to infer the variability of signals in longitudinal studies where no plasticity is expected to occur.

## *5.3 Results*

Complete datasets from 13 subjects were analysed. These datasets contain three scanning sessions within 7 days and four scanning runs per day, with the first being the calibration scan and the last three being functional scans. Example CBF maps can be found in Fig 44 for each subject. A good grey matter – white matter contrast was observed across all subjects. Frontal and occipital brain areas showed slightly higher flow values than the rest of the grey matter. End-tidal oxygen values increased from an average baseline of $110.8 \pm 6.0$ mmHg up to $588.2 \pm 104.8$ mmHg during carbogen-7 inhalation. Carbon-dioxide end-tidal values increased from $39.1 \pm 3.0$ mmHg to $53.5 \pm 3.6$ mmHg.

Table 4 summarises the mean values for each quantity obtained by averaging across all days, runs and subjects. Mean $BOLD_c$ and $CBF_c$ signal changes during carbogen inhalation were larger in the motor ROI than in the visual ROI (p=0.03). The average *M*-value was also larger in the motor ROI than in the visual ROI (p=0.04). The largest mean $BOLD_c$ signal changes and *M*-values were, however, found in the grey matter ROI (p=0.01). In the same region, $CBF_c$ changes due to carbogen inhalation were somewhat smaller than for the visual and motor ROI (p=0.01). A GCM extrapolation therefore led to a higher *M*-values in grey matter than in other ROIs (p=0.01).

In contrast with carbogen induced signal changes, similar $BOLD_t$ changes were found in both ROIs during functional activation. Task-evoked group average $CBF_t$ changes, however, were different in both regions, with larger changes observed in the motor ROI (p=0.05). Changes in oxygen metabolism were found to be comparable in both regions (p=0.23), leading to a higher flow-metabolism coupling constant in the motor ROI than in the visual ROI (p=0.01).

Fig 45a to 45c summarise the reproducibility results for the visual (Fig 45a), motor (Fig 45b) and grey matter (Fig 45c) ROI. $CV_1$ (red), $CV_2$ (blue) and $CV_3$ (green) are group averaged values across all subjects. Within-day stability could not be assessed for $M$, $SvO_2$, $CBF_c$ and $BOLD_c$, as only one

gas-breathing challenge was performed per day.
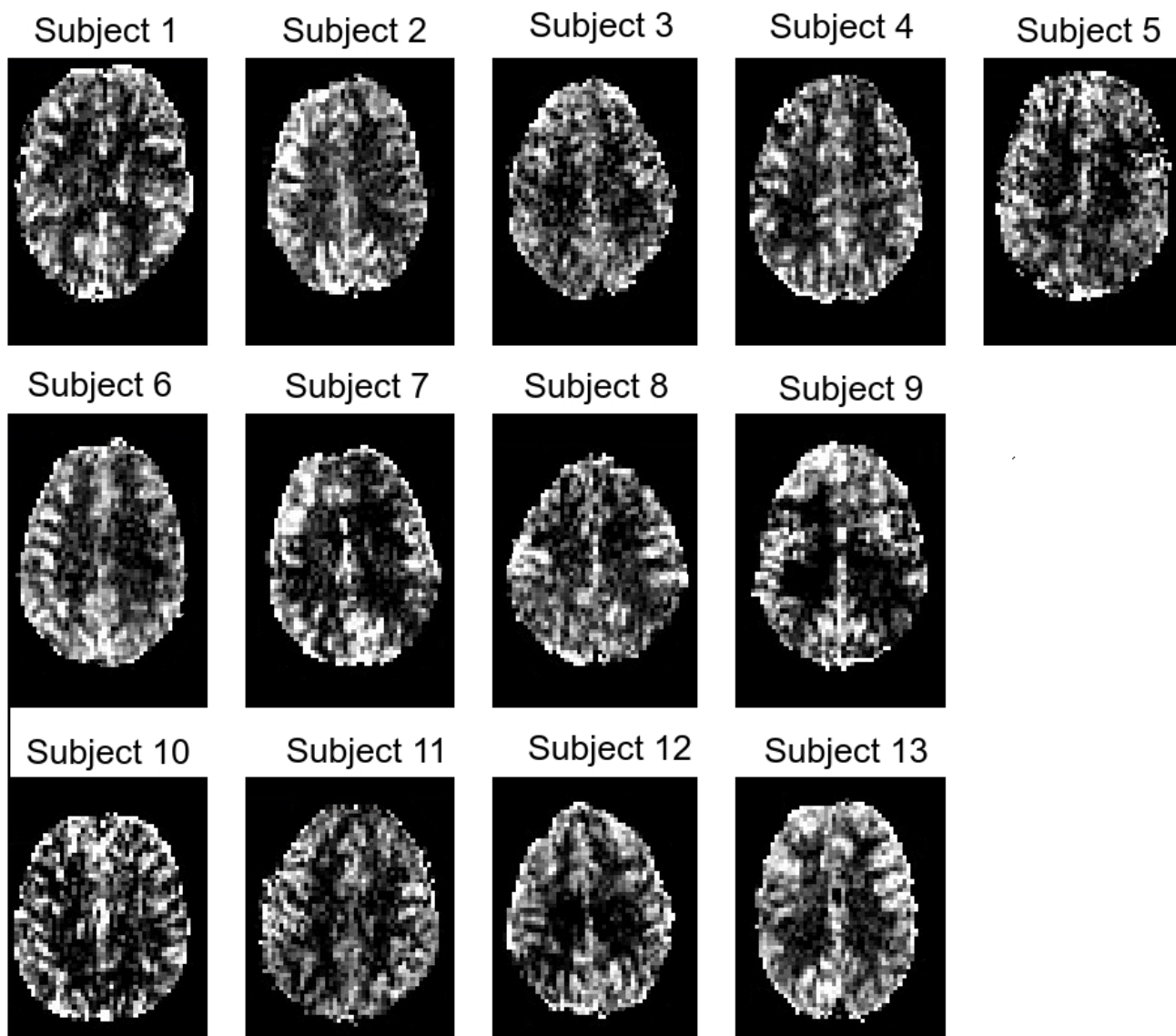


*Figure 44: Example cerebral blood flow maps for each subject. Higher blood flow values were detected in the occipital and frontal brain areas.*

The lowest coefficients of variation in all regions were found for venous oxygen saturation values showing a high consistency within and across subjects (CV<5%). It should be noted, however, that $SvO_2$ is expected to be close to 100% in all cases, since an OEF of 35% is assumed within the GCM and very high flow and end-tidal oxygen values are consistently observed after carbogen-7 inhalation. Gas induced $CBF_c$ signal changes showed lower variability across days and subjects ($CV_2$ and $CV_3$) than $BOLD_c$ and $M$ for all ROIs. $BOLD_c$ and $M$ variability was comparable within each ROI. A comparison across ROIs revealed that gas-related CVs across days and subjects for $CBF_c$, $BOLD_c$ and $M$ were largest within the motor ROI and lowest for the grey matter ROI. For all

gas-related quantities, variability across subjects ($CV_3$) was larger than variability within the same subject across days ($CV_2$).

| | Visual ROI | Motor ROI | Grey Matter ROI |
|---|---|---|---|
| **$BOLD_c$** | 5.7±0.6% [b c] | 6.6±0.8% [a c] | 7.3±0.7% [a b] |
| **$CBF_c$** | 73.3±9.2% [b c] | 85.3±2.0% [a c] | 58.9±6.2% [a b] |
| *M* | 9.1±1.0% [b c] | 9.9±1.0% [a c] | 12.2±1.2% [a b] |
| **$SvO_2$** | 88.2±0.4% [b c] | 89.3±0.6% [a c] | 84.1±4.3% [a b] |
| **$BOLD_t$** | 0.6±0.2% | 0.6±0.1% | n.a. |
| **$CBF_t$** | 31.5±3.0% [b] | 49.2±10.3% [a] | n.a. |
| **$CMRO_2$** | 20.3±4.1% | 20.2±4.8% | n.a. |
| **n** | 2.0±0.2 [b] | 2.9±0.5 [a] | n.a. |

*Table 4: The group averages and standard deviation across all subjects for three days and three runs per day for all measured quantities. Estimated average functionally induced changes in oxygen metabolism and $BOLD_t$ are comparable in visual and motor ROI. Functionally induced changes in CBF are higher in the motor ROI which leads to a larger flow-metabolism coupling constant in the motor ROI. The highest M-value could be measured in the grey matter ROI. [a], [b] and [c] denote a significant (p<0.05, multiple comparison corrected) difference to those values obtained in the visual, motor, and grey matter ROI, respectively.*
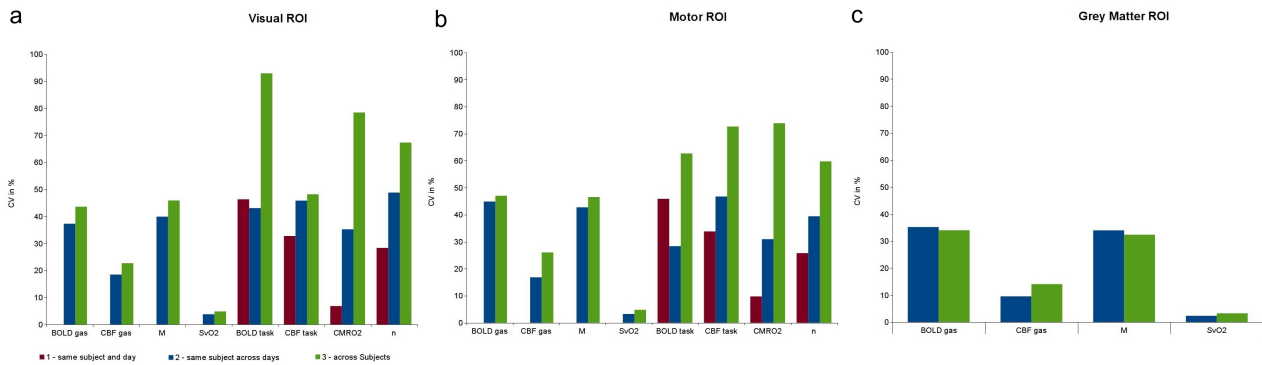


*Figure 45: Group averaged coefficients of variation for the visual (a), motor (b) and grey matter (c) ROI. $CV_2$ and $CV_3$ averaged across grey matter are smaller than those obtained in the visual and motor ROI. However, in all 3 ROIs only minor differences between across days intra-subject ($CV_2$) and inter-subject ($CV_3$) variability was observed. $CMRO_2$ shows the lowest $CV_1$ in both brain areas and $CV_2$ values comparable to BOLD.*

Amongst functionally-induced signal changes, $CMRO_2$ showed the best stability across runs ($CV_1$) in the visual and motor ROI. The largest $CV_1$ were found for $BOLD_t$ in both ROIs. $BOLD_t$, $CBF_t$ and $CMRO_2$ showed comparable $CV_1$ in motor and visual ROI. The smallest $CV_2$ across sessions

was found for $CMRO_2$ in the visual ROI and the motor ROI. However, CV of $BOLD_t$ in the motor ROI was in a similar range as CV of $CMRO_2$. Averaging across subjects ($CV_3$) revealed the CV of $CBF_t$ to be the lowest in both ROIs. Variability in $BOLD_t$, $CMRO_2$ and n showed coefficients greater than 50% whereas all intra-subject CVs ($CV_1$ and $CV_2$) were below 50%.

Inter-subject test-retest plots across days for each quantity can be found in Fig 46 and Fig 47. Averaged signal changes for each quantity are plotted for the second and third day against the averaged data obtained on day 1. Data from different ROIs can be distinguished by colour, whereas days are encoded by shapes. Stability is determined by the distance between a given point and the unity line. Linear regressions have been applied to the data of each graph and the average coefficients of determination can be found in each plot. Fig 46 shows the average signal changes related to gas inhalation and Fig 47 functionally induced signal changes. The *M*-value (Fig 46c) and blood flow plots (Fig 46b) show less scattering than BOLD visualising better stability across subjects and within subjects of *M* and CBF than BOLD (Fig 46a) due to gas inhalation. Changes in CBF are concentrated between 40% and 80% signal change (Fig 46b). Fig 47 shows larger scattering in BOLD (Fig 47a) than in any other quantity. Functionally induced changes in $CMRO_2$ are concentrated around 10%-30% (Fig 47c) while the flow-metabolism coupling constant n shows a similar behaviour (Fig 47d).

Fig 48 shows the intra-subject coefficients of variation ($CV_1$ and $CV_2$) of $BOLD_t$, $CBF_t$, $CMRO_2$ and n without (saturated red and blue bars) and with (semi-transparent red and blue bars) applied habituation correction within the motor ROI. Moderate to no changes between corrected and uncorrected signals were observed for $CV_1$. No changes in $CV_2$ were found for CBF and $CMRO_2$ while BOLD was the quantity most affected by the correction scheme applied, showing an approximate decrease in $CV_2$ of 15%.
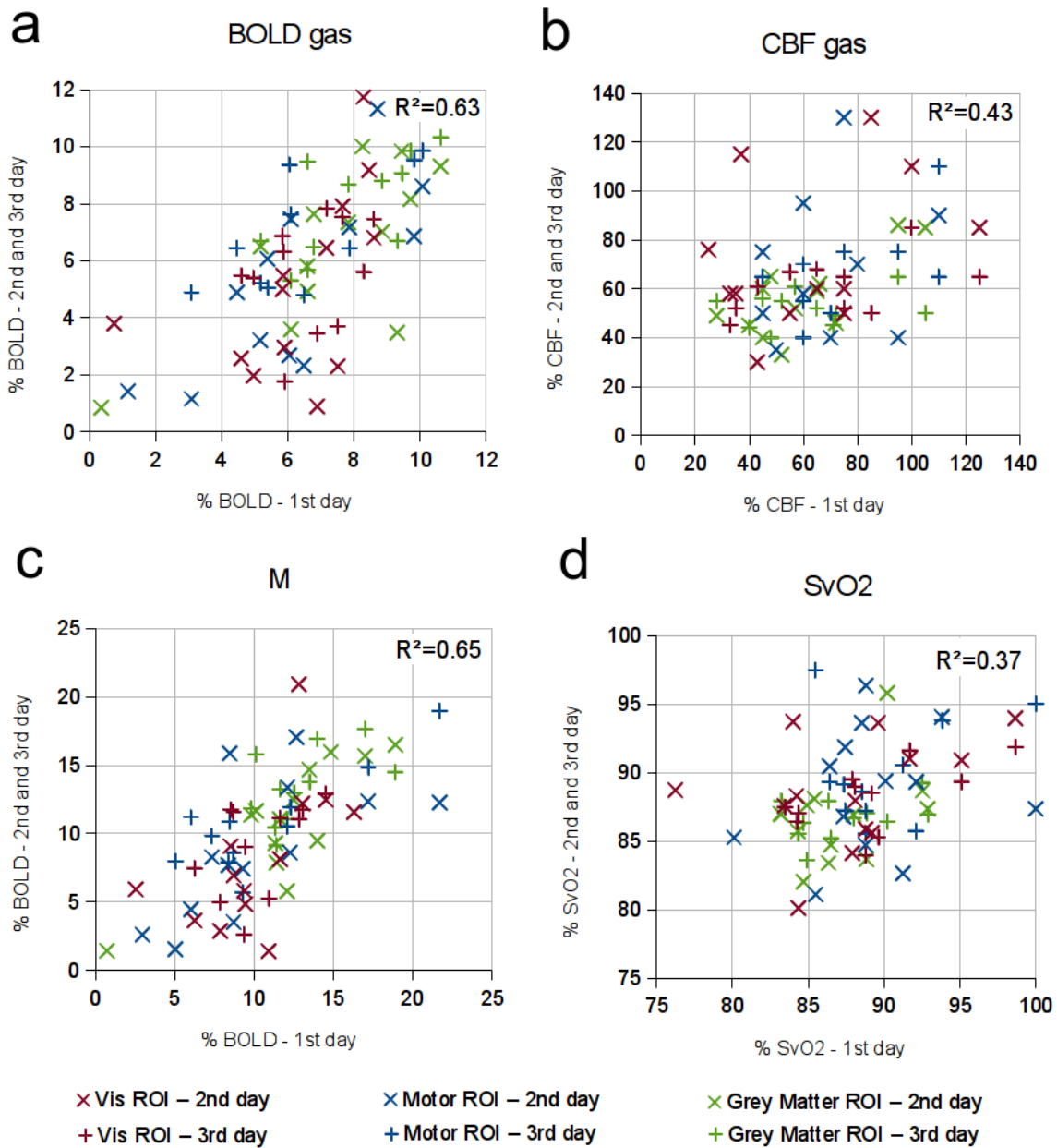
*Figure 46: Average gas induced signal changes are plotted for the second and third day against the averaged data obtained on day 1. Data from different ROIs can be distinguished by colour, whereas days are encoded by shapes. Stability is determined by the distance between a given point and the unity line. M and CBF were more consistent across days within subjects and across subjects than the BOLD signal. However, all quantities show significant scattering from the unity line.*
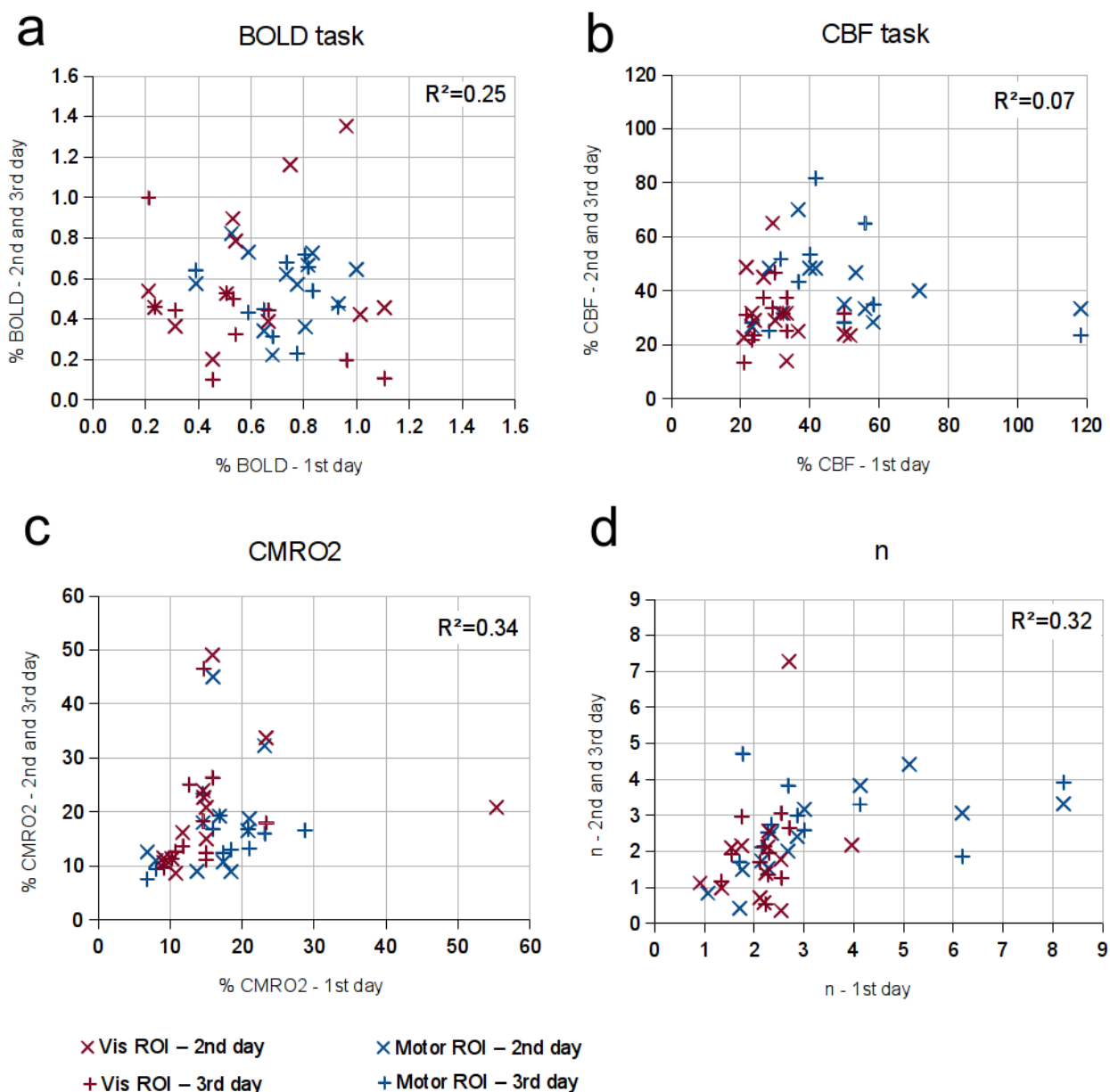
*Figure 47: Average functionally induced signal changes are plotted for the second and third day against the averaged data obtained on day 1. While the BOLD data points show widespread scattering, CMRO$_2$ data are close to the unity line reflecting matching data from each subject across days. Pooled data points in the CMRO$_2$ plot compared to BOLD also suggests more predictable inter-subject reproducibility.*

## 5.4 Discussion

Despite the physiological ambiguity, poor stability characteristics and low spatial specificity of classical BOLD contrast, it is still the most commonly used method in longitudinal and group studies that assess cognitive brain function and task-induced functional activation. The utilisation of more direct physiological measures such as cerebral oxygen metabolism may have been limited so

far by the lack of methodological validation and evidence for reasonable robustness and reproducibility. In this study, we have investigated the reproducibility characteristics of a state-of-the-art calibrated fMRI technique for cognitive studies, using a complex task with low-contrast primary sensory and cognitive components. Oxygen metabolism estimates showed lower intra-subject variation than BOLD and CBF. Inter-subject variation was relatively high for all quantities with $CMRO_2$ coefficients of variation being most consistent across ROIs. Taken together, these results indicate that calibrated fMRI may provide advantages over the BOLD signal, both in terms of greater physiological specificity and in terms of reproducibility.



**Comparison of coefficients of variation without and with correction schemes applied**
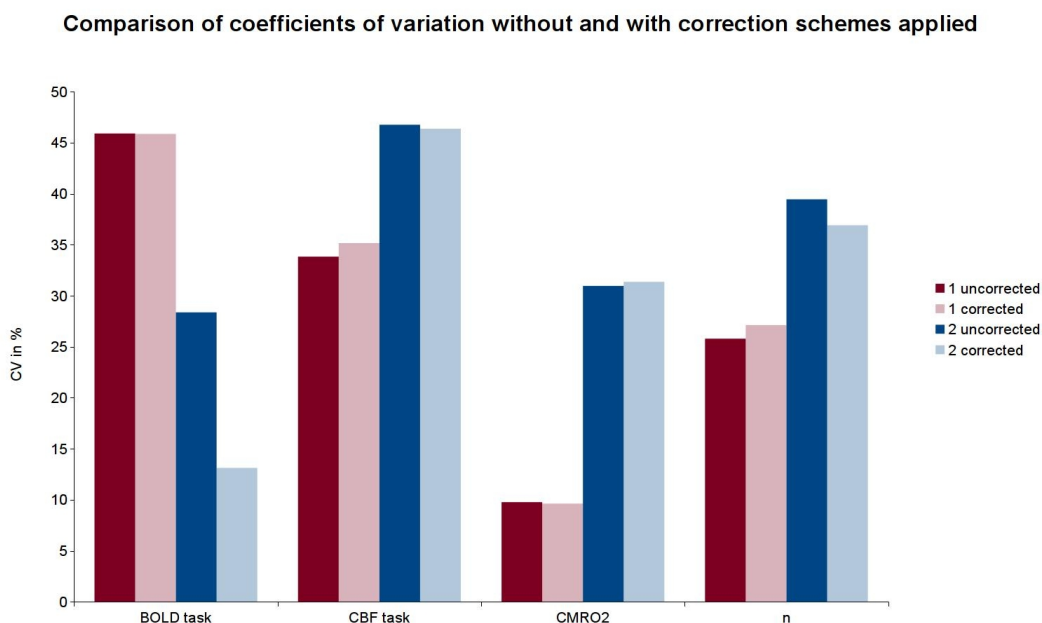
*Figure 48: Comparison of intra-subject coefficients of variation ($CV_1$ and $CV_2$) obtained with corrected (semi-transparent red and blue bars) and uncorrected (saturated red and blue bars) data for $BOLD_t$, $CBF_t$, $CMRO_2$ and n. The correction scheme used in this study only had minor effects on the intra-subject coefficients of variation. However, intra-subject variation across days $CV_2$ of BOLD reduced by approximately 15% after applying the correction algorithm.*

## 5.4.1 Breathing Manipulations

Carbogen-induced changes in all quantities of this study showed good reproducibility characteristics with $CV_2$ comparable to those obtained at lower field strengths (Leontiev & Buxton, 2007). $CV_2$ and $CV_3$ of gas induced $CBF_c$ changes found in this study were, however, smaller than those obtained for $BOLD_c$ and $M$, in contrast to an earlier study at 3 Tesla (Leontiev & Buxton, 2007). This discrepancy may be the result of implementation differences, both in terms of gas challenge and MRI acquisition. Different breathing manipulations may be used to perform a calibrated fMRI experiment, and each has its own advantages in terms of balancing assumptions

and the inclusion of low SNR measures which may reduce the reproducibility of the technique. The original calibrated BOLD approach was based on pure hypercapnic manipulations, under the assumption that this manipulation causes a purely vascular change (Davis et al., 1998; Hoge et al., 1999; Kim et al., 1999). The assumption of no change in $CMRO_2$ during hypercapnia has, however, been challenged recently (Xu, Uh, et al., 2011; Zappe, Kâmil Uludağ, et al., 2008) and the hyperoxia calibrated BOLD method was introduced to circumvent this issue and improve participant comfort.

It has also been postulated that the hyperoxia method may decrease variability compared to the hypercapnia approach since flow changes resulting from the breathing manipulation are not included in $M$ estimation (Chiarelli, Bulte, Wise, et al., 2007). The hyperoxia approach relies on the assumption of zero or negligible flow changes during oxygen inhalation, which has also been challenged (Bulte et al., 2007; Xu, Liu, et al., 2011). A generalised calibration technique allowing a combined hypercapnia-hyperoxia breathing challenge was utilised in this study, since this combination has been shown to lead to more robust estimations of the $M$ parameter (Gauthier & Hoge, 2013). Importantly, all these approaches suffer from the need to assume various physiological parameters such as flow-volume coupling $\alpha$ and the relationship between deoxyhaemoglobin concentration to the relaxation rate $R_2^*$ for hypercapnia, and haematocrit (Hct) and OEF for hyperoxia, which may show significant variability across subjects and brain regions (Blockley, Griffeth & Buxton, 2012). Various techniques have recently been used to estimate brain OEF and most results are in the range of 0.3 to 0.4 (Bulte et al., 2012; Carpenter et al., 1991; Gauthier & Hoge, 2012; He & Yablonskiy, 2007; Ito et al., 2004; Jain et al., 2010; Lu & Ge, 2008; Qin et al., 2011; Raichle et al., 2001; Wise et al., 2013). Simulation of error using our current GCM-based results indicate that within this range the maximum error in $M$ due to underestimated OEF would be approximately -30% while overestimation could lead to a maximum error of +20%. The potential effects of pathologies that impact OEF is yet unclear. For example, decreases in OEF have been found after brain injuries (Diringer et al., 2000) but the effect on $M$ and the accuracy of calibrated fMRI cannot be determined from the current data, as pathology would likely influence all measured components of the model. Recently, a hyperoxia calibrated fMRI approach has been introduced which is believed to overcome potential uncertainties in estimating $CMRO_2$ caused by assumption about flow-volume coupling and OEF (Driver et al., 2012). Furthermore, interleaved and combined hypercapnia and hyperoxia has been used to study absolute oxygen metabolism (Bulte et al., 2012; Gauthier & Hoge, 2012) as well as relative changes during functional activation while simultaneously estimating OEF, $\alpha$ and $\beta$ through a Bayesian modelling approach (Wise et al.,

2013). These promising techniques could lead to improvements in calibrated fMRI implementation, though their applicability and reproducibility characteristics have yet to be assessed.

Another potentially confounding factor of hyperoxia based calibrated BOLD techniques might be the underestimation of gas breathing induced changes in CBF due to a shortening effect in longitudinal relaxation time $T_1$ of blood (Bulte et al., 2007; Gauthier & Hoge, 2013; Krieger et al., 2014). Commonly a 10% underestimation of CBF is assumed based on increased oxygen saturation in arterial blood plasma. This value however, is based on theoretical modelling. Venous and arterial blood $T_1$ have been measured ex-vivo at 1.5 Tesla (Lu et al., 2003), 3 Tesla (Lu, Clingman, et al., 2004; Noeske et al., 2000; Stanisz et al., 2005), 4.7 Tesla (Dobre et al., 2007; Silvennoinen et al., 2003), 7 Tesla (Dobre et al., 2007; Francis et al., 2008; Rane & Gore, 2013) and 9.4 Tesla (Dobre et al., 2007). Only few studies have investigated venous blood $T_1$ in-vivo at these field strengths (Qin et al., 2011; Rane & Gore, 2013; Rooney et al., 2007; Wu et al., 2010; Zhang et al., 2013) and there is no in-vivo data available for arterial blood $T_1$. This lack of information is compounded by the fact that studies started investigating the effects of hyperoxia and hypercapnia on the longitudinal relaxation time of blood only very recently, and the results obtained so far do not provide reliable quantitative estimates (Dethrage et al., 2014; Ma et al., 2014). Future studies will be necessary to quantitatively assess the effect of breathing gases to blood $T_1$, especially with regards to the consistency of these effects across subjects.

The oxygen and carbon dioxide concentrations of delivered gas mixtures vary between studies. Higher concentrations of oxygen and $CO_2$ result in larger BOLD signal changes, bringing the measured BOLD signal closer to $M$ on the iso-$CMRO_2$ contour (Hoge et al., 1999). SNR-limited techniques such as ASL could benefit from increased signal changes induced by higher $CO_2$ concentrations and lead to improved reproducibility characteristics of the calibrated BOLD technique. On the other hand, high carbon-dioxide concentrations can induce significant levels of air hunger, discomfort or breathlessness, which can affect physiology and metabolism of cortical and sub-cortical brain regions (Brannan et al., 2001; Liotti et al., 2001). It is therefore important to use accurate control and recording systems for end-tidal gas values, as well as physiological correlates such as heart and breathing rate. Future studies could compare effects of various gas-mixtures to calibrated BOLD reproducibility.

Gas delivery also plays an important role in technical reliability. Whereas face masks and nasal cannulas are the most common modes of gas delivery, we have used a mouthpiece combined with a nose clip. This setup guaranteed that only the carbogen-7 gas mixture was inhaled, and no outside

air can be entrained into the breathing circuit. Larger changes in end-tidal partial gas pressures and CBF have typically been observed for the same gas concentration when mouth pieces were used instead of face masks (Gauthier & Hoge, 2013; Krieger et al., 2014). Most face masks are not sealed, which leads to contamination of inhaled gas by room air. Cannulas commonly lead to even greater contamination from room air since there is still space in the nose around the cannula. Therefore end-tidal values are both lower and more variable than with face masks and cannulas than with mouthpieces. This variability in gas concentration inhaled by the subjects introduces greater uncertainty in calibrated BOLD acquisitions, thereby influencing their reliability. Furthermore, there is evidence that breathing through face masks induces larger air hunger than breathing through mouth pieces (Liotti et al., 2001). Air hunger in turn can result in significant neuronal cerebral activation which may diminish the effectiveness and accuracy of the calibration procedure (Brannan et al., 2001; Liotti et al., 2001). While the gas delivery method used here has shown good reproducibility, further improvements could be obtained using an end-tidal gas control system (Mark et al., 2011; Mark et al., 2010; Slessarev et al., 2007). This technique uses a feed-forward physiological model to precisely target a predefined end-tidal partial gas pressure. Cerebro-vascular reactivity (CVR) has been found to be higher when using an end-tidal control system compared to fixed gas concentrations (Tancredi & Hoge, 2013). This technique, while a possible improvement in terms of reproducibility, comes at the cost of further scanner time and represents an additional equipment investment. An alternative approach uses computer controlled feedback on a breath-by-breath basis to alter the inspired gas partial pressures to meet pre-determined end-tidal gas pressures (Wise et al., 2007). Future studies could determine whether the use of these gas-inhalation techniques provide an improvement in reliability which outweighs their additional cost.

In addition to the previously described gas inhalation based fMRI approaches, recent studies have demonstrated the possibility of conducting calibrated fMRI experiments without any breathing manipulation. Combined gradient and spin echo data have been used to measure the relaxation rates $R_2$ and $R_2^*$ A biophysical model was then used to calculate the calibration constant based on the transverse relaxation rates (Blockley, Griffeth & Buxton, 2012; Herman et al., 2013; Hyder et al., 2001; Kida et al., 2000). An alternative technique uses $T_2$-Relaxation-Under-Spin-Tagging (TRUST) MRI to quantify oxygen metabolism as a whole-brain average (Xu et al., 2009). TRUST MRI-based estimation of global cerebral oxygen metabolism has been found to be a very reliable method showing low intra-subject and inter-subject coefficients of variation (Liu, Xu, et al., 2013). The major advantage of these techniques compared with gas inhalation based calibrated fMRI is that no additional gas breathing equipment is needed, which makes the setup more cost-effective

and reproducible across sites. The disadvantages and restrictions of the techniques described can, however, be severe, depending on the purpose of the specific study and the MRI setup available. Whereas TRUST MRI might be a powerful tool for measuring a global average in oxygen metabolism, this technique does not provide information about regional oxygen usage. Functional experiments can therefore not be conducted using this technique. The relatively large amount of RF pulses applied in this sequence restricts its application to lower field MRI due to specific absorption rate (SAR) limits. Similar power deposition restrictions are valid for the $R_2'$ calibrated fMRI techniques (Blockley, Griffeth & Buxton, 2012; Herman et al., 2013). Additionally, the $R_2'$ approach has been found to be less reliable than hypercapnia or hyperoxia fMRI, potentially due to its greater sensitivity to magnetic field inhomogeneity (Blockley, Griffeth & Buxton, 2012). Due to these restrictions, this study was conducted using a gas inhalation based calibrated fMRI technique rather than any of the promising non-gas inhalation based techniques mentioned.

A number of gas-induced reproducibility features must be considered. All gas inhalation related repeatability measures across days ($CV_2$) were slightly lower within the grey matter ROI than within the visual and motor ROIs, confirming trends observed in ASL and calibrated fMRI at lower field strengths (Stone et al., 2013; Wang et al., 2011). This may be attributable to the relative sizes of each ROI. The visual and motor ROI represent only a relatively small section of the total grey matter, thereby leading to more variability than when signal is averaged across the whole non task-specific cortical voxels of the brain.

The calibration parameter $M$ obtained in this study are somewhat smaller than those obtained by earlier 7 Tesla studies (Driver et al., 2012; Gauthier, Krieger, et al., 2013; Hall et al., 2013; Huber et al., 2013). This is an expected result due to the relatively short echo time used in this study. However, absolute comparisons of $M$-values across studies are generally difficult since different calibration approaches, MRI techniques, acquisition parameters and breathing manipulations can affect $M$ (Krieger et al., 2014). Along these lines, the higher inter-session variability of $M$ compared to $CBF_c$ found in this study demonstrates the importance of measuring $M$ for each subject and each day separately. Wrongly estimated $M$-values can lead to deviations in $CMRO_2$ which may diminish the conclusiveness of a specific study (Krieger et al., 2014). While variability in $M$ originating from technical uncertainty could be reduced by using an end-tidal gas control technique (Mark et al., 2010; Wise et al., 2007), physiological variability can only be accounted for by estimating $M$ during each scanning session. Furthermore, our results indicate that regional differences in flow-metabolism coupling (n) and maximum BOLD signal changes $M$ across ROIs may lead to inaccurate results when the calibration procedure is based on a global average rather

than separate averaging for each brain region (Chiarelli, Bulte, Gallichan, et al., 2007). In this context, future calibrated BOLD studies could seek to increase the spatial resolution of this technique to investigate the potential impact of partial volume effects on the estimation of $M$ and $CMRO_2$. Furthermore, higher resolution data would allow comparison with results obtained in recent rat studies which established the uniformity of $M$ across cortical laminae (Herman et al., 2013).

Finally, venous oxygen saturation was associated with lower CVs than any other measure. This is not surprising as this measurement is expected to always reside within a very limited range of values. $SvO_2$ is estimated via the GCM under the assumption of an OEF of 35%, and combined with the end-tidal $O_2$ partial pressure values at baseline and during gas inhalation. Since baseline $O_2$ partial pressure is similar both within and across subjects in healthy adults, and since gas-induced end-tidal values are reliably high within and across subjects, $SvO_2$ variability is expected to be low.

## 5.4.2 Functional Reproducibility

Several studies have assessed the reproducibility characteristics of BOLD and ASL for high-contrast motor and visual tasks (e.g. finger tapping or flickering checkerboard) at lower field strengths. There is evidence that using CBF as a marker for cerebral neuronal activity provides better intra-subject and inter-subject reproducibility than BOLD, especially over long periods of time (Chen et al., 2011; Tjandra et al., 2005; Wang et al., 2003; Wang et al., 2011). The ASL signal originates from the capillary and arteriolar vessel system, thereby providing better spatial specificity than BOLD, which is biased towards draining venules and veins that can be further away from the actual area of functional activation (Detre & Wang, 2002; Turner, 2002). Furthermore, the BOLD signal is vulnerable to susceptibility artefacts and baseline drifts, which have a less important impact on ASL (Detre & Wang, 2002). Task-evoked BOLD signal changes have also been found to be modulated by baseline blood oxygenation and cerebro-vascular reactivity, which contributes to the reduced reproducibility of BOLD (Liu, Hebrank, Rodrigue, Kennedy, Park, et al., 2013; Lu et al., 2008). The results obtained in this study indicate how these trends translate to ultra-high field and more complex cognitive tasks that lead to lower signal changes. Functional CBF changes showed better within-day intra-subject reproducibility ($CV_1$) than BOLD, confirming the results of studies at lower field strengths (Tjandra et al., 2005; Wang et al., 2003; Wang et al., 2011). BOLD variability across days ($CV_2$) was similar to variability across runs from the same day ($CV_1$) which confirms results obtained by earlier studies of BOLD variability (Smith et al., 2005), leading to comparable reproducibility of BOLD and CBF over longer time periods. To our knowledge, there is no published literature comparing BOLD and CBF intra-subject reproducibility on a time scale of

seven days. Our results suggest that the superior sensitivity of BOLD may balance out against the lower signal to noise ratio of PASL, despite the technical advantages of PASL in terms of long-term reproducibility, when using more complex cognitive tasks that only lead to modest functional signal changes.

A viable alternative to BOLD and CBF as surrogate neuronal markers of functional cerebral activation could be $CMRO_2$. Earlier studies at 3 Tesla observed comparable intra-subject repeatability for all three quantities (Leontiev & Buxton, 2007; Stone et al., 2013). The results of this study provide evidence that $CMRO_2$ is superior to BOLD and CBF in terms of intra-subject stability when using more complex cognitive tasks (Fig 45a, 45b and 47a to 47d). This effect may be enhanced by the use of ultra-high magnetic field. $CMRO_2$ variability estimates across runs within the same day were found to be well below those of $BOLD_t$ and $CBF_t$. These results confirm recent findings at 3 Tesla with visual stimulation showing that calculated responses such as $CMRO_2$ and n are relatively insensitive to baseline $CBF_t$ changes across runs. Due to flow-metabolism coupling, changes in CBF can be assumed to affect the BOLD signal by a similar relative amount, leading to lower variation in $CMRO_2$ and n than in CBF and BOLD (Leontiev & Buxton, 2007). Only recently, cerebral oxygen metabolism has started to be used to study cognitive processes (Ances et al., 2009; Gauthier, Madjar, et al., 2013; Mohtasib et al., 2012). The intra-subject repeatability characteristics found in this study indicate that calibrated BOLD is a promising alternative to classical functional techniques such as BOLD and ASL for this type of study.

The present study features some interesting results with regards to the coupling of cerebral blood flow and brain oxygen metabolism. The flow-metabolism coupling parameters n obtained in this study were comparable to those reported in earlier studies (Ances et al., 2008; Marrett & Gjedde, 1997; Roland et al., 1987; Seitz & Roland, 1992). The variability of n across brain areas and subjects found in this study could help explain and interpret the relatively large variability of the BOLD signal (Aguirre et al., 1998; Duff et al., 2007; Fox et al., 2005; Tjandra et al., 2005). The variability of n across sessions found in this study was smaller than that of $CBF_t$ and $BOLD_t$, though larger than the variability of $CMRO_2$. However, larger variability in n was observed within the same subject across days. Interestingly, *M* shows better intra-subject reproducibility across sessions than n in motor and visual ROIs which could be important for applications of calibrated fMRI to pathophysiology.

Inter-subject variability $CV_3$ was found, as expected from previous studies, to be larger than intra-subject variability for $BOLD_t$, $CBF_t$, $CMRO_2$ and n (Leontiev & Buxton, 2007; Stone et al., 2013; Tjandra et al., 2005). However, we anticipated that the relatively complex task used in this study

would lead to smaller signal changes and higher inter-subject variability values compared to those obtained with high-contrast tasks such as flickering checkerboard. Without explicit measures such as $B_1$ shimming or transmit SENSE, ultra-high field MRI scanners inevitably suffer from more severe transmit radio-frequency magnetic field inhomogeneities. Due to the higher field strength, these inhomogeneities also are larger across subjects than for lower field strengths. This may partly explain the higher inter-subject variability observed in this study. Calculated quantities such as $CMRO_2$ and n showed consistent $CV_3$ for both the visual and motor ROI, while $BOLD_t$ and $CBF_t$ showed greater differences in variability coefficients across regions (Stone et al., 2013). More consistent stability across brain regions may improve the reliability of studies assessing cognitive processes in several cerebral areas. Our results therefore suggest that calibrated BOLD could be a powerful alternative to BOLD and CBF scans alone.

### 5.4.3 Habituation Effects on Reproducibility

The nature of the functional task chosen for this study may have had an impact on the reproducibility estimates obtained. Cerebral functional changes related to motor learning can be expected, as well as habituation effects in task performance and visual stimulation. Linear regression of habituation and learning effects from task performance measures did not, however, have a major impact on our stability assessments. Only minor differences in $BOLD_t$, $CBF_t$, $CMRO_2$ and n CVs across runs or days in both visual and motor ROI were found following regression of performance changes (see Fig 41). CVs for most measures remained almost identical before and after applying the correction. It should however be noted, that the correction scheme we have applied is based on the assumption that motor performance is linearly related to all quantities and signal changes. It could be that this scheme underestimates the learning and habituation effects, if a more complex relationship is at play. However, most recent studies assume a linear relationship between performance and MRI signal amplitude changes and therefore this study followed this assumption (Fernández-Seara et al., 2009; Grafton et al., 2002; Steele & Penhune, 2010). Future studies could seek to implement other mathematical models to investigate non-linear correlation between MRI signal changes and motor performance or test for different weightings between physiological measures.

Day to day differences in motor performance and within session habituation effects leading to differences in cerebral functional activation may furthermore be responsible for counter-intuitive trends in $BOLD_t$ reproducibility. Coefficients of variation across runs ($CV_1$) were found to be larger than across days ($CV_2$) within the motor ROI for $BOLD_t$ (see Fig 45b). Increased motor activation was found at the beginning of each day. Participants require a certain period at the beginning of

each session to recover the low performance error observed in the previous session. This could be due to the fact that the initial performance of the task requires greater attention than subsequent runs, leading to a higher $BOLD_t$ signal at the beginning of each scanning day (Seidler et al., 2004; Steele & Penhune, 2010). This within-session habituation effect may lead to the observed lower $BOLD_t$ reproducibility across runs than across days. It is furthermore possible that this habituation effect is associated with changes in flow-metabolic coupling in different learning phases, thereby leading to different impacts on $BOLD_t$, $CBF_t$ and $CMRO_2$ stability. This interpretation is supported by the fact that the visual area does not show this counter-intuitive CV effect and CV across runs and days were found to have comparable values.

## 5.4.4 Technical Considerations for Calibrated fMRI

Compared to the classical BOLD contrast, calibrated BOLD typically relies on the simultaneous acquisition of CBF and BOLD signals. Commonly used labelling schemes include pulsed arterial spin labelling (PASL) schemes such as FAIR (Kim, 1995) and PICORE (Wong et al., 1997) or pseudo-continuous arterial spin labelling (pCASL) (Dai et al., 2008; Wu, Fernández-Seara, et al., 2007) techniques. Recent studies have found that the pCASL approach provides superior SNR and stability (Chen et al., 2011; Wu et al., 2013; Wu et al., 2011), so pCASL may be the best ASL technique to use when conducting a calibrated BOLD study at lower field strengths (Gauthier & Hoge, 2013). However, due to limits in specific absorption rate (SAR) related to radio-frequency pulse energy deposition, the use of pCASL and Q2TIPS at ultra-high field strengths is complicated (Ghariq et al., 2012). For this reason, an optimised FAIR QUIPSSII labelling scheme, found to provide superior reproducibility compared to PICORE QUIPSSII and PICORE Q2TIPS (Cavuşoğlu et al., 2009), was used in the current study.

The echo time is a crucial parameter when conducting PASL based calibrated fMRI studies, both in terms of BOLD signal scaling and compartmental origin, and with regards to potential BOLD contamination of the CBF-weighted MRI signal. Additional BOLD contribution to the PASL signal could lead to an overestimation of CBF, although extravascular BOLD signal contribution can be minimised by using short echo times, such as the one used in this study. However, the intravascular BOLD signal peaks at short echo times and may therefore contaminate the CBF-weighted PASL signal, especially in regions containing large veins (Ivanov et al., 2013). As the intravascular BOLD signal is believed to be smaller than its extravascular counterpart, minor BOLD contamination of the CBF-weighted PASL signal can be expected, especially at ultra-high magnetic field (Duong et al., 2003; Kim & Ogawa, 2012; Uludağ et al., 2009). Another confounding factor especially in ASL at ultra-high field is physiological noise, which scales with field strength. Larger voxel sizes

translate into better SNR but at the same time increase the amplitude of physiological noise (Krüger & Glover, 2001; Triantafyllou et al., 2005). In this study we have used a voxel size that showed optimal SNR while minimising the impact of physiological noise on our data. Background suppression techniques commonly rely on multiple inversion pulses to null the background signal at acquisition time (Garcia et al., 2005; Ishimori et al., 2011). As this approach relies on a well-defined nulling time of all background signals, its application is limited to 3D readout or a small number of slices. Furthermore, there is concern that background suppression will impact extravascular BOLD quantification and thereby change the relationship between blood flow and BOLD, which may lead to biases in calibrated fMRI quantification. Therefore background suppression has not been applied in this study. A short $TE$ will also result in lower BOLD signal changes. This would in turn lead to a smaller $M$ estimate. This is not expected to lead to biases in $CMRO_2$ quantification, however, if the task-based BOLD response is measured using the same $TE$ as both measures will then scale together. The BOLD signal in this case will however contain a larger intravascular contribution. A dual-echo sequence with a second $TE$ optimized for BOLD would reduce this bias and such sequences should be used whenever possible.

Another restriction at ultra-high magnetic fields arises from the radio-frequency transmitting hardware (Duyn, 2012; Yacoub et al., 2001). Whereas it is standard at lower field strengths to use a body or a neck coil to label arterial spins globally in FAIR sequences, or selectively spins in the carotid arteries in pCASL sequences, such equipment is not yet available at 7 Tesla. Therefore ASL at ultra-high field may suffer from reduction in functional SNR due to inflow of non-labelled spins. Fresh blood inflow may be especially problematic for hypercapnia-based calibrated BOLD. Carbon dioxide inhalation leads to global increases in blood flow and therefore rises in blood flow velocity, which in turn reduces the arterial arrival time. A shortening in arterial arrival time could diminish functional contrast of ASL at 7 Tesla. Therefore it is indispensable (at each field strength) to carefully adjust ASL inversion times $TI$ to achieve maximum functional SNR at rest and during gas inhalation. In this study the combination of $TI_1/TI_2 = 700\,ms/1700\,ms$ provided the optimal contrast-to-noise ratio while guaranteeing no fresh blood inflow into the imaging slab before the EPI readout. In summary, while some improvements in stability would be possible using other ASL implementations, SAR and hardware limitations at 7T have lead to the choice of the particular ASL implementation used in this study. Future studies could seek to use dedicated labelling coils to enable the use of better ASL techniques, thereby improving the reliability of calibrated fMRI experiments.

## *5.5 Conclusion*

Calibrated BOLD fMRI is a promising technique for investigating functional brain activity on the basis of physiologically meaningful quantities. This study investigated important technical considerations for the implementation of calibrated fMRI and assessed the applicability of the calibrated BOLD technique in the context of cognitive and learning studies. $CMRO_2$ was found to be more suitable for longitudinal studies than BOLD and CBF alone. $CMRO_2$ was furthermore associated with a more consistent variability across brain regions than BOLD and CBF, which may provide better reliability for studies looking into several brain regions. While calibrated BOLD studies require increased scanning times and additional equipment, these disadvantages may be outweighed by the increased stability, higher spatial specificity and greater physiological interpretability of $CMRO_2$ estimates.

# 6  Experiment III: Simultaneous Acquisition of BOLD, ASL and VASO Signals

This study has been published in Magnetic Resonance in Medicine (2014) In print.

## 6.1 Background Information

In the previous chapters calibrated fMRI has been shown to be a viable alternative to classic functional MRI approaches such as BOLD with regards to spatial specificity as well as reproducibility. However, the higher technical complexity of calibrated fMRI compared to standard fMRI techniques such as BOLD or ASL and VASO is not negligible. Depending on the requirements of the specific study such as robustness, spatial and temporal specificity, or spatial and temporal resolution the advantages and disadvantages of each technique require consideration to determine the most suitable technique for a specific experiment.

In this study a novel MRI technique is introduced for ultra-high magnetic field that enables the simultaneous detection of multiple MR signals. In this way it is possible to combine the advantages of each technique without adding additional scan time to the study. This technique is based on a recently introduced MRI technique to simultaneously map BOLD, CBF and CBV weighted MRI signals at 3 Tesla (Yang et al., 2004). This technique has already found a series of applications (Gu et al., 2005; Lin et al., 2008; Lin et al., 2009) and several technical developments have followed the original proposal (Gu et al., 2006; Glielmi et al., 2009; Ciris, Qiu & R Todd Constable, 2013; Ciris, Qiu & Robert Todd Constable, 2013). Based on Yang et al. we have developed a new method to simultaneously measure CBV, CBF and BOLD weighted MRI signals optimised for ultra-high magnetic field strength. The purpose of this study was to develop an MR sequence that addressed several potential drawbacks of Yang et al. while utilising the advantages of ultra-high magnetic fields.

The key modifications compared to the original technique developed by Yang et al. include the application of slice-saturation slab-inversion VASO (SS-SI-VASO) providing increased SNR in the CBV weighted images (Huber, Ivanov, et al., 2014). Furthermore, multiple EPI readouts are used to correct for BOLD signal contamination of the VASO and ASL images. High inversion efficiencies and sharp inversion profiles were achieved via an adiabatic inversion radio frequency (RF) pulse specifically designed for 7 Tesla (Hurley et al., 2010). Additionally, a separate BOLD acquisition at the end of the sequence minimises inversion effects on the BOLD signal. This technique can be used to study neurovascular coupling, quantification of oxygen metabolism and to investigate biophysical models of the BOLD signal.

## 6.2 Methods

### 6.2.1 SS-SI VASO Signal Acquisition

In order to obtain robust and uniform slab-selective inversion despite $B_1$ inhomogeneities and substantial SAR constraints, a slab-inversion tr-FOCI pulse (Hurley et al., 2010) was used to magnetically label blood water spins (pulse duration=5.5 ms, pulse amplitude=400 V, slab thickness=142.8mm) as suggested by Huber et al. (Huber, Ivanov, et al., 2014). At inversion time $TI_1 = 1330$ms a single slice positioned across the visual cortex was excited followed by two EPI readouts providing two VASO images at two different echo times ( $TE_{VASO,1} = 14\,ms$ , $TE_{VASO,2} = 37\,ms$ ). Imaging parameters for all acquisitions were: FOV=192mmx192mm, nominal isotropic resolution=(1.5mm)³; GRAPPA factor=3, partial Fourier factor=6/8, $TR = 3\,s$ .

### 6.2.2 ASL and BOLD Signal Acquisition

The second excitation was performed at $TI_2 = 1650\,ms$ followed by two consecutive EPI readouts ( $TE_{ASL,1} = 14\,ms$ , $TE_{ASL,2} = 37\,ms$ ) giving CBF weighted MRI images. No additional inversion pulse was applied between the VASO and ASL readouts. However, the delayed acquisition of the CBF weighted image provided enough time to have non-excited blood flowing into the imaging slice, and thus to avoid saturation effects due to earlier excitation RF pulses.

BOLD signals were acquired at $TI_3 = 2250\,ms$ in order to minimise the influence of earlier inversion pulses on the BOLD contrast. The echo time used for the BOLD image was $TE_{BOLD} = 22\,ms$ , which provided optimal contrast with minimal susceptibility induced void artefacts. The sequence diagram can be found in Fig 49.

### 6.2.3 Experimental Design

The data were acquired in five healthy participants on a Siemens Magnetom 7 Tesla whole body MRI scanner (Siemens Healthcare, Erlangen, Germany) equipped with a 24 channel head coil (NOVA Medical Inc, Wilmington, MA, USA). All participants gave written informed consent for participation in this study. Ethics approval was obtained from the local review board (Ethics Commission Leipzig University). Visual stimulation with an 8-Hz black and white radial checkerboard was presented on a screen inside the magnet with a standard block design of 30s rest followed by 30 activation periods. The complete procedure took 8 minutes.
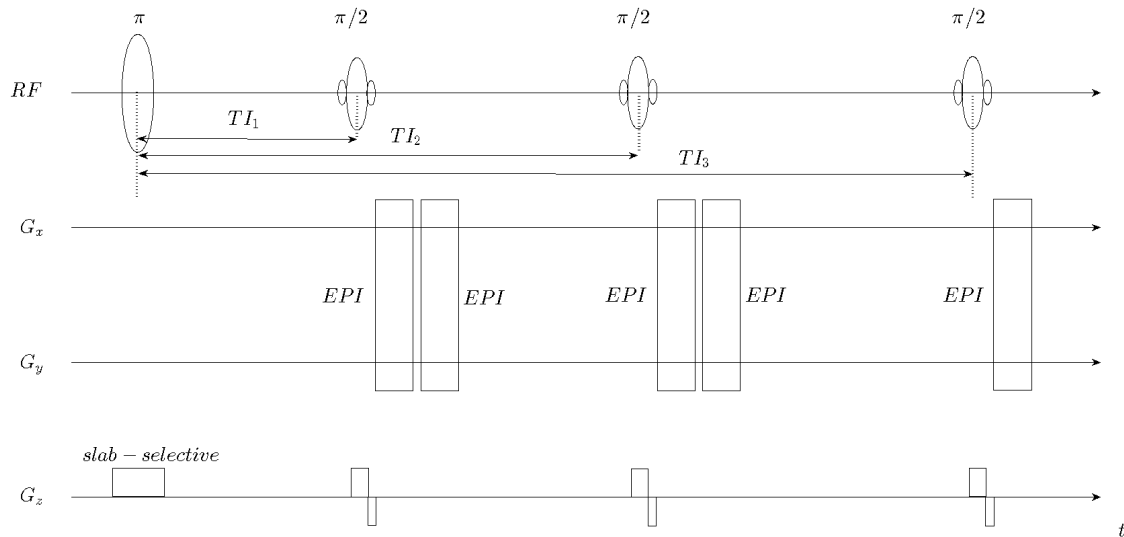
*Figure 49: Sequence diagram for simultaneous acquisition of VASO, ASL and BOLD weighted MRI images at 7T.*

## 6.2.4 Data Analysis

VASO and ASL images were extrapolated to $TE=0\,ms$ using a single compartment model (Lu & van Zijl, 2005). Extrapolated VASO and ASL images and the BOLD images were then corrected for in-plane motion using the fMRI expert analysis tool (FEAT) v. 5.98 from the FSL package using no smoothing kernel. SNR and temporal SNR (tSNR) was calculated in grey matter for all subjects based on the extrapolated SS-SI-VASO and ASL images at $TE=0\,ms$. Cluster thresholded activation maps (p<0.05, multiple comparison corrected) for VASO, ASL and BOLD signals were calculated using the same software. Time courses of significantly activated voxels were averaged in time using in-house analysis tools based on Matlab (v. 8.0.0.783, R2012b).

## *6.3 Results*

The average SNR in grey matter of the SS-SI-VASO and ASL images acquired via the simultaneous acquisition technique was 9.3±1.2 and 14.3±3.0, respectively. The corresponding tSNR of SS-SI-VASO and ASL in grey matter was 12.0±1.4 and 18.5±2.1, respectively. Statistical activation maps of CBV, CBF and BOLD from all subjects are shown in Fig 50. The relatively high spatial resolution used enabled the investigation of the differential spatial specificity of the different modalities. While BOLD contrast showed significant activation at the cortical surface, VASO and ASL signal changes appeared to peak only within grey matter, as expected. The CBV and CBF

activation maps were based on the VASO and ASL MRI images, when extrapolated to $TE=0\,ms$. Single subject time courses of VASO, ASL and BOLD signals averaged across all significantly activated voxels can be found in Fig 51 A, B and C, respectively. Group averages of each quantity are plotted in the same graphs. The time courses have been normalised to the baseline of each quantity, respectively.
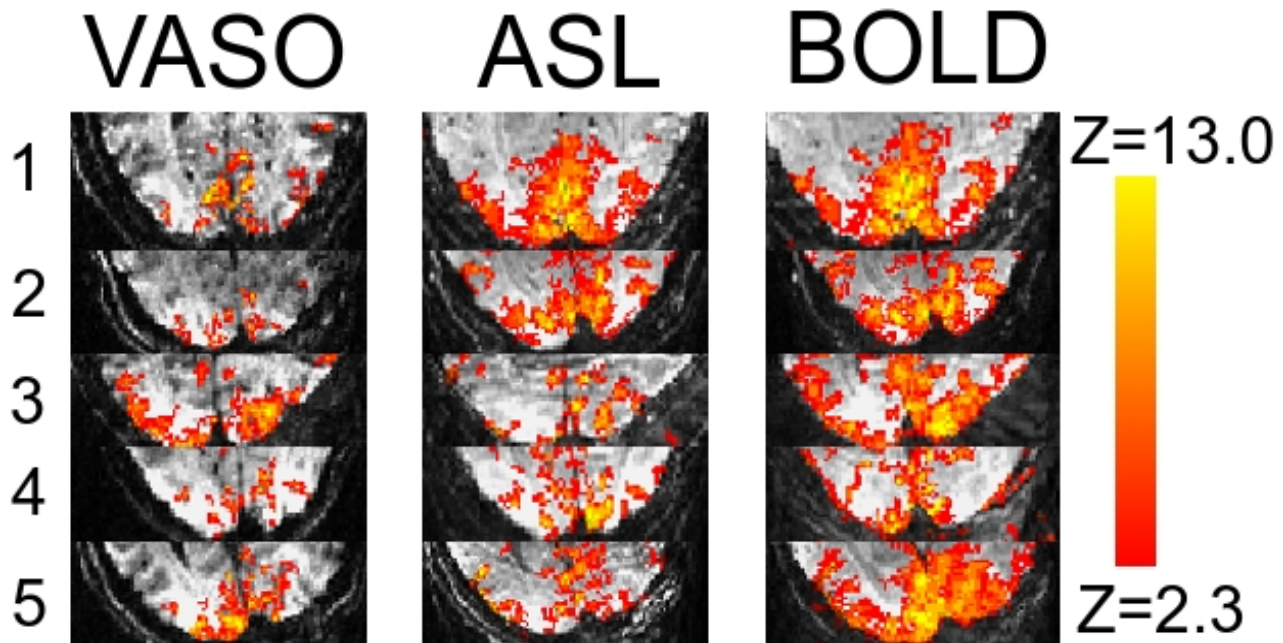


Figure 50: Statistical activation maps of VASO, ASL and BOLD weighted MRI images obtained via the simultaneous acquisition scheme.

## 6.4 Discussion

Based on the technique developed by Yang et al. (Yang et al., 2004) we have introduced an imaging technique to simultaneously acquire CBV, CBF and BOLD weighted MRI signals at ultra-high static magnetic field strength. The spatial and temporal SNR characteristics achieved in this study are comparable to those obtained in studies using the acquisition of a single quantity only at comparable spatial resolutions and field strengths (Huber, Ivanov, et al., 2014; Hua et al., 2012; Huber, Goense, et al., 2014). As expected BOLD weighted signals showed larger areas of significant functional activation than CBF and CBV weighted signals. BOLD signal changes were observed to occur not only at the site of neuronal activity, but also in downstream venules and veins, consistent with the reliance of the BOLD signal on changes in the oxy-deoxyhaemoglobin ratio which occur mainly on the venous vessel side (Turner, 2002; Buxton, 2010). In contrast, VASO and ASL signal changes originate mainly from arteries and capillaries, because the highest fractional changes in cerebral blood volume and flow occur in these compartments. Presumably due

to differences in the compartmental weighting of the VASO and the ASL signal, spatial differences in CBV and CBF activation maps are observable in Fig 50. Reduced partial volume effects because of the relatively high spatial resolution used in this study might highlight this effect. Furthermore, differences of blood $T_1$ across subjects might also lead to variations in the extent and amplitude of regional brain activation in ASL and VASO statistical activation maps.
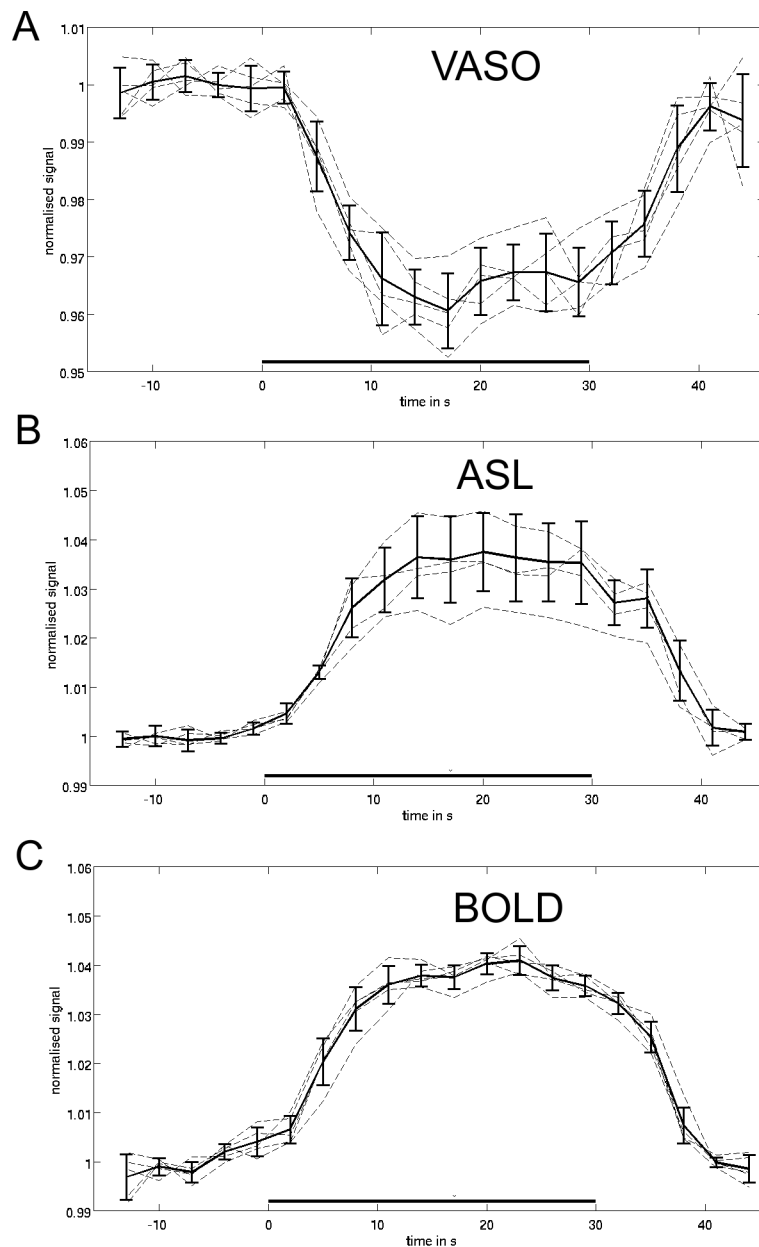


*Figure 51: Single subject (dotted lines) and group average (solid line) time courses of VASO (A), ASL (B) and BOLD (C) weighted MRI signals obtained via the simultaneous acquisition scheme.*

VASO and ASL suffer from an intrinsically lower sensitivity but provide increased spatial specificity as compared to BOLD contrast (Goense et al., 2012; Jin & Kim, 2008). When sequentially acquired MR signals are compared and interpreted, motion and image artefacts are major concerns. Furthermore attention and habituation effects have to be taken into account when comparing MR signals that are not acquired simultaneously, as these may affect the neuronal and haemodynamic response to functional stimuli. The pulse sequence introduced in this article thus enables study of brain function with combined high sensitivity and high specificity which may provide insight into the biophysics of the neurovascular response, a major practical advantage compared with sequential signal acquisition.

Despite the advantage of providing increased MR signals compared to lower static magnetic field strengths, 7 Tesla MRI entails several challenges when an inversion recovery sequence is used. For example, a reduced difference in longitudinal relaxation times $T_1$ of blood and tissue leads to small contrast-to-noise (CNR) of classic VASO (Hua et al., 2012) and positive BOLD signal changes increasingly counteract the negative VASO signal change (Lu & van Zijl, 2005). Furthermore, RF field inhomogeneities and SAR limits hamper efficient spin inversion. Use of a tr-FOCI pulse with SS-SI VASO was found to overcome these obstacles (Hurley et al., 2010) and increases SNR and CNR compared to classic VASO approaches. Slab-selective inversion enables labelled blood to be refreshed between each inversion pulse which leads to a steady-state tissue signal but a blood signal that has experienced only one inversion. The increased blood $T_1$ at higher field strengths provides higher SNR due to the slower decay of the labelled blood spins. A potential problem of the current implementation of this technique is inflow of fresh blood into the imaging slice before the VASO and the ASL signals have been acquired. Inflow of non-inverted spins could introduce a CBF-weighting in the SS-SI-VASO contrast. In future studies a partial inversion technique could be applied to reduce the blood nulling time and therefore reduce the vulnerability to inflow effects (Huber, Ivanov, et al., 2014). Furthermore, multi-slice acquisition could make this technique more robust against head motion since standard motion correction algorithms could be applied properly. In this study only experienced subjects that were known to show little movement during the scanning sessions were selected in order to avoid deviations resulting from head motion. A multi-slice extension of this technique would, however, be limited by the total acquisition time especially with regards to the VASO blood nulling condition. Also, energy deposition restrictions and effects on the ASL signal due to prior excitations would have to be assessed. Another potential drawback of the simultaneous acquisition of three physiological quantities is that advanced ASL techniques such as the application of saturation pulses to actively control the temporal width of the labelled bolus

(Wong et al., 1998b) and background suppression (Garcia et al., 2005; Ishimori et al., 2011) cannot be applied.

The technique introduced in this article involves three excitation pulses applied on one slice within one $TR$. Previous RF pulses might affect the ASL and the BOLD signal acquired at a later time point. Therefore it is crucial to maximise the time between the acquisition of the three contrasts to allow the blood inside the excited slice to refresh before the next acquisition takes place and avoid detrimental effects on the next acquisition. Longer $TI$ reduces the ASL signal, however, due to $T_1$ decay. We found optimal results for $TI_2 = 1650\,ms$ and $TI_3 = 2250\,ms$ while taking into account a fixed VASO inversion time. In order to minimise $T_1$ weighting associated with flow, the BOLD signal acquisition was performed at the end of the pulse sequence using a single RF excitation followed by a single EPI readout. This feature is especially necessary at high magnetic field strengths due to the increased longitudinal relaxation times of blood compared to lower field strengths.

The comparison and interpretation of simultaneously acquired signal time courses of CBV, CBF and BOLD may become a powerful strategy for future studies of brain function. The spatio-temporal characteristics of VASO, ASL and BOLD MRI signals have been found to rely on multiple parameters such as type of the functional task, brain area, task duration, age, sleep and awareness state (Aguirre et al., 1998; Duff et al., 2007; Liu, Hebrank, Rodrigue, Kennedy, Section, et al., 2013; Poser et al., 2011; Uludağ, 2008). Simultaneous acquisition of multiple physiological parameters could help investigate and quantify these dependencies. The time courses obtained in this study show the expected characteristics of VASO, ASL and BOLD (see Fig 51) (Yang et al., 2004). The increased CBV-weighted signal changes occurring during functional activation can be explained by the increased SNR of SS-SI-VASO at ultra-high field compared to classic VASO as well as reduced partial volume effects as a result of the high spatial resolution used (Pfeuffer et al., 2002; Huber, Ivanov, et al., 2014). However, comparable changes in VASO signal have already been found in earlier studies, even at lower field strengths (Hua et al., 2011; Hua et al., 2012). The VASO signal is acquired at the blood nulling time and therefore reflects the amount of grey matter signal in each voxel. During functional activation of a specific brain area, the blood vessels dilate and therefore reduce the remaining grey matter signal in these voxels, leading to a negative VASO signal. BOLD and ASL signal changes are positive as expected. The signal time courses of all three quantities are as expected for the single subject and group analyses.

## *6.5 Conclusion*

In this study we introduced a modified version of the MRI sequence introduced by Yang et al. (Yang et al., 2004) that enables simultaneous acquisition of CBV, CBF and BOLD weighted MR signals at 7 Tesla. The MR pulse sequence used in this study was optimised for use at ultra-high field, but with appropriate adjustment of the timing parameters, is equally applicable at clinical field strengths, albeit with lower SNR. Functional activation maps and time courses of CBV, CBF and BOLD weighted MRI signals obtained through this technique demonstrated the applicability of this novel approach. Simultaneous acquisition of VASO, ASL and BOLD based MRI signals can be a powerful tool for studies of brain function and a time efficient alternative for cognitive studies. Future studies could use our technique to investigate neurovascular coupling and its changes across diseases, age and pharmacological states. Furthermore, calibrated BOLD studies are expected to benefit from additional information about changes in CBV and overcome uncertainties related to the flow-volume coupling coefficient.

# 7 Conclusion and Outlook

Despite the large variety of alternative techniques available, the BOLD signal is still the contrast of choice for the majority of functional MRI studies. The advantage of the BOLD contrast compared to many other fMRI techniques is the simplicity of the MR sequence and the relatively high sensitivity. BOLD sequences are easily accessible and available for most MR scanner at many magnetic field strengths. Finally, the well-established analysis routines of BOLD based fMRI sequences still make this the most popular technique for functional MRI studies.

The problems and ambiguities associated with the use of BOLD fMRI can, however, be severe and could diminish the value of the results obtained by such studies. It is well known that the BOLD signal arises from simultaneous changes in CBF, CBV and $CMRO_2$. The quantitative relationships between these physiological parameters are, however, still not fully understood. Much effort has been devoted to the development of biophysical models that describe the quantitative relationships between these parameters but the complexity of brain physiology still limits our understanding of the quantitative origins of the BOLD signal. Furthermore, the spatial specificity of the BOLD contrast is limited. Downstream draining veins can show large BOLD signal changes during neuronal activation, even when not immediately proximal to the area of activation. Alternative fMRI techniques such as ASL, VASO or calibrated fMRI have the potential to circumvent the restrictions that are associated with BOLD fMRI by utilising a single physiological parameter as a tracer of neuronal activity. ASL and VASO use spin inversion to label the blood and changes in the MR signal are proportional to changes in CBF and CBV, respectively. As vascular changes during neuronal activation occur primarily in the capillary bed and the arterial vessel compartment, ASL and VASO signals are much closer to the location of functional activity than BOLD signals which can provide a significant advantage with regards to spatial specificity.

A novel approach of performing fMRI studies is to use simultaneous acquisition techniques to combine the advantages of each method. Additional information about neurophysiology can be obtained without additional scan time. The temporal and spatial characteristics of all parameters can be studied in various brain areas in multiple subjects without any additional cost. Although the recently introduced technique by Yang et al. has been used frequently at lower magnetic field strengths, an implementation at ultra-high field was still missing, although ultra-high field can provide significant boosts in SNR and CNR especially for inversion recovery based fMRI techniques such as VASO and ASL. Therefore we have implemented a modified version of this sequence at 7 Tesla which is optimised for the use at ultra-high magnetic field. The sequence timing

was optimised and potential drawbacks of the original sequence design were eliminated in order to obtain high SNR for all measures. The results obtained with this optimised sequence design were promising. Functional statistical activation maps of CBV, CBF and BOLD showed the typical activation patterns for each contrast, with BOLD showing the most extensive activation area. The activated areas of CBV and CBF were smaller than BOLD providing evidence for the microvascular origin of the signal changes suggesting higher specificity compared to BOLD signals.

The implementation of this sequence was a proof-of-concept study. The temporal and spatial results of all quantities measured were as expected and the successful application of the technique was demonstrated in multiple subjects. Therefore we suggest that this technique can be reliably applied in cognitive, psychological or physiological studies. Simultaneous acquisition of CBV and CBF could be used to study flow-volume coupling across brain areas and subjects. Several biophysical models assume a single coupling parameter (Grubb value), although there is no consensus with regards to its stability across cortical areas and subjects. Furthermore, time dependency of the Grubb value, especially during transition phases, has not yet been studied adequately. For example, calibrated BOLD fMRI usually relies on an assumed flow-volume coupling parameter in order to allow the estimation of the calibration parameter $M$ and to calculate changes in $CMRO_2$. The additional knowledge of CBV would help to address one of the most discussed disadvantages of calibrated fMRI modelling. Along these lines, current models of BOLD could be assessed with real data without the necessity to separately measure each quantity through separate studies. The estimation of oxygen metabolism via this novel sequence would allow the investigation of how the three quantifiable parameters CBV, CBF and $CMRO_2$ translate into the arbitrary unit of the BOLD signal. Where no calibrated fMRI equipment is available the technique would enable the examination of two physiologically and physically relevant parameters and comparison of these to BOLD signal changes, providing a more complete picture of haemodynamic changes.

A key objective of this thesis was the quantification of changes in oxygen metabolism via calibrated fMRI. Although calibrated fMRI has been available for more than ten years and despite the theoretical advantages of ultra-high fields, its application in more complex studies is still limited, especially at these magnetic field strengths. This may be due to the greater complexity of calibrated fMRI compared to classic BOLD in terms of MRI setup, acquisition time and data analysis. The stability and applicability of calibrated fMRI had also not yet been assessed with regards to low-contrast tasks at ultra-high field. The advantages from the additional efforts necessary to perform a calibrated BOLD study were hence difficult to estimate. Therefore we have focused our efforts on

assessing the applicability and reproducibility of a state-of-the-art calibrated fMRI approach and compared this approach with a direct calibration technique. The direct calibration is not applicable when using commonly available gas-mixtures, but our results suggest that the reproducibility characteristics of GCM modelling based calibrated fMRI are sufficient for studies that use low-contrast tasks. Our results furthermore provide evidence that at the single subject level, the use of $CMRO_2$ as a marker of neuronal activity can be an advantage compared to BOLD and ASL with regards to temporal signal variation. Future studies could follow up these ideas by studying motor learning via BOLD, CBF and $CMRO_2$. It would be informative to see whether the neuronal networks detected via each quantity are comparable or if results vary across the three measures.

The focus of this thesis was on the development, application and assessment of quantitative functional MRI techniques. Due to the numerous drawbacks of the BOLD contrast alternative fMRI approaches are required to gain deeper knowledge about brain physiology, haemodynamics and neuronal networks. ASL, VASO and calibrated fMRI measure physiological variables which can be used to quantify MR signal changes on a physical reasonable basis. The utilisation of the advantages of ultra-high magnetic fields led to increased SNR and spatial resolution compared to lower field strengths. Furthermore, this thesis has assessed the applicability of several quantitative functional fMRI techniques and the results confirmed that calibrated fMRI as well as simultaneous acquisition of VASO, ASL and BOLD signals are a viable alternative to classic BOLD studies. The methods developed and results obtained in these studies contribute significantly to the establishment of quantitative fMRI techniques in neuroscience.

# References

Abragam, A. (1983) *Principles of Nuclear Magnetism*. Auflage: Reprint. Oxford University Press, USA.

Aguirre, G.K., Zarahn, E. & D'esposito, M. (1998) The variability of human, BOLD hemodynamic responses. *Neuroimage* **8**(4):360–369.

Ances, B.M., Leontiev, O., Perthen, J.E., Liang, C., Lansing, A.E. & Buxton, R.B. (2008) Regional differences in the coupling of cerebral blood flow and oxygen metabolism changes in response to activation: implications for BOLD-fMRI. *Neuroimage* **39**(4):1510–1521.

Ances, B.M., Liang, C.L., Leontiev, O., Perthen, J.E., Fleisher, A.S., Lansing, A.E. & Buxton, R.B. (2009) Effects of aging on cerebral blood flow, oxygen metabolism, and blood oxygenation level dependent responses to visual stimulation. *Hum Brain Mapp* **30**(4):1120–1132.

An, H. & Lin, W. (2002a) Cerebral oxygen extraction fraction and cerebral venous blood volume measurements using MRI: effects of magnetic field variation. *Magn Reson Med* **47**(5):958–966.

An, H. & Lin, W. (2002b) Cerebral venous and arterial blood volumes can be estimated separately in humans using magnetic resonance imaging. *Magn Reson Med* **48**(4):583–588.

Attwell, D. & Iadecola, C. (2002) The neural basis of functional brain imaging signals. *Trends Neurosci.* **25**(12):621–625.

Attwell, D. & Laughlin, S.B. (2001) An energy budget for signaling in the grey matter of the brain. *J. Cereb. Blood Flow Metab.* **21**(10):1133–1145.

Banzett, R.B., Lansing, R.W., Evans, K.C. & Shea, S.A. (1996) Stimulus-response characteristics of CO2-induced air hunger in normal subjects. *Respir Physiol* **103**(1):19–31.

Bereczki, D., Wei, L., Otsuka, T., Acuff, V., Pettigrew, K., Patlak, C. & Fenstermacher, J. (1993) Hypoxia increases velocity of blood flow through parenchymal microvascular systems in rat brain. *J. Cereb. Blood Flow Metab.* **13**(3):475–486.

Berwick, J., Johnston, D., Jones, M., Martindale, J., Redgrave, P., McLoughlin, N., Schiessl, I. & Mayhew, J.E.W. (2005) Neurovascular coupling investigated with two-dimensional optical imaging spectroscopy in rat whisker barrel cortex. *Eur. J. Neurosci.* **22**(7):1655–1666.

Binder, J.R., Rao, S.M., Hammeke, T.A., Frost, J.A., Bandettini, P.A. & Hyde, J.S. (1994) Effects of stimulus rate on signal response during functional magnetic resonance imaging of auditory cortex. *Brain Res Cogn Brain Res* **2**(1):31–38.

Blockley, N.P., Griffeth, V.E., Jezzard, P. & Bulte, D.P. (2013) Cross-field analysis of the accuracy of hypercapnia calibrated BOLD. In: Proc ISMRM Salt Lake City.

Blockley, N.P., Griffeth, V.E.M. & Buxton, R.B. (2012) A general analysis of calibrated BOLD methodology for measuring CMRO2 responses: comparison of a new approach with existing methods. *Neuroimage* **60**(1):279–289.

Blockley, N.P., Griffeth, V.E.M., Simon, A.B. & Buxton, R.B. (2012) A review of calibrated blood

oxygenation level-dependent (BOLD) methods for the measurement of task-induced changes in brain oxygen metabolism. *NMR Biomed* **26**(8):987-1003.

Boxerman, J.L., Hamberg, L.M., Rosen, B.R. & Weisskoff, R.M. (1995) MR contrast due to intravascular magnetic susceptibility perturbations. *Magn Reson Med* **34**(4):555–566.

Brannan, S., Liotti, M., Egan, G., Shade, R., Madden, L., Robillard, R., Abplanalp, B., Stofer, K., Denton, D. & Fox, P.T. (2001) Neuroimaging of cerebral activations and deactivations associated with hypercapnia and hunger for air. *Proc. Natl. Acad. Sci. U.S.A.* **98**(4):2029–2034.

Bulte, D.P., Chiarelli, P.A., Wise, R.G. & Jezzard, P. (2007) Cerebral perfusion response to hyperoxia. *J. Cereb. Blood Flow Metab.* **27**(1):69–75.

Bulte, D.P., Drescher, K. & Jezzard, P. (2009) Comparison of hypercapnia-based calibration techniques for measurement of cerebral oxygen metabolism with MRI. *Magn Reson Med* **61**(2):391–398.

Bulte, D.P., Kelly, M., Germuska, M., Xie, J., Chappell, M.A., Okell, T.W., Bright, M.G. & Jezzard, P. (2012) Quantitative measurement of cerebral physiology using respiratory-calibrated MRI. *Neuroimage* **60**(1):582–591.

Buxton, R.B. (2012) Dynamic models of BOLD contrast. *Neuroimage* **62**(2):953–961.

Buxton, R.B. (2010) Interpreting oxygenation-based neuroimaging signals: the importance and the challenge of understanding brain oxygen metabolism. *Front Neuroenergetics* **2**:8.

Buxton, R.B. (2009) *Introduction to functional Magnetic Resonance Imaging - Principles and Techniques*. Second Edition. Cambridge University Press: Cambridge University Press The Edinburgh Building, Cambridge CB2 8RU, UK.

Buxton, R.B., Frank, L.R., Wong, E.C., Siewert, B., Warach, S. & Edelman, R.R. (1998) A general kinetic model for quantitative perfusion imaging with arterial spin labeling. *Magn Reson Med* **40**(3):383–396.

Buxton, R.B., Uludağ, K., Dubowitz, D.J. & Liu, T.T. (2004) Modeling the hemodynamic response to brain activation. *Neuroimage* **23 Suppl 1**:S220–233.

Carpenter, D.A., Grubb, R.L., Jr, Tempel, L.W. & Powers, W.J. (1991) Cerebral oxygen metabolism after aneurysmal subarachnoid hemorrhage. *J. Cereb. Blood Flow Metab.* **11**(5):837–844.

Cavuşoğlu, M., Pfeuffer, J., Uğurbil, K. & Uludağ, K. (2009) Comparison of pulsed arterial spin labeling encoding schemes and absolute perfusion quantification. *Magn Reson Imaging* **27**(8):1039–1045.

Chen, J.J. & Pike, G.B. (2009) BOLD-specific cerebral blood volume and blood flow changes during neuronal activation in humans. *NMR Biomed* **22**(10):1054–1062.

Chen, J.J. & Pike, G.B. (2010) MRI measurement of the BOLD-specific flow-volume relationship during hypercapnia and hypocapnia in humans. *Neuroimage* **53**(2):383–391.

Chen, Y. & Parrish, T.B. (2009) Caffeine dose effect on activation-induced BOLD and CBF responses. *Neuroimage* **46**(3):577–583.

Chen, Y., Wang, D.J.J. & Detre, J.A. (2012) Comparison of arterial transit times estimated using arterial spin labeling. *MAGMA* **25**(2):135–144.

Chen, Y., Wang, D.J.J. & Detre, J.A. (2011) Test-retest reliability of arterial spin labeling with common labeling strategies. *J Magn Reson Imaging* **33**(4):940–949.

Chiarelli, P.A., Bulte, D.P., Gallichan, D., Piechnik, S.K., Wise, R. & Jezzard, P. (2007) Flow-metabolism coupling in human visual, motor, and supplementary motor areas assessed by magnetic resonance imaging. *Magn Reson Med* **57**(3):538–547.

Chiarelli, P.A., Bulte, D.P., Piechnik, S. & Jezzard, P. (2007) Sources of systematic bias in hypercapnia-calibrated functional MRI estimation of oxygen metabolism. *Neuroimage* **34**(1):35–43.

Chiarelli, P.A., Bulte, D.P., Wise, R., Gallichan, D. & Jezzard, P. (2007) A calibration method for quantitative BOLD fMRI based on hyperoxia. *Neuroimage* **37**(3):808–820.

Cholet, N., Seylaz, J., Lacombe, P. & Bonvento, G. (1997) Local uncoupling of the cerebrovascular and metabolic responses to somatosensory stimulation after neuronal nitric oxide synthase inhibition. *J. Cereb. Blood Flow Metab.* **17**(11):1191–1201.

Ciris, P.A., Qiu, M. & Constable, R.T. (2013) Noninvasive MRI measurement of the absolute cerebral blood volume-cerebral blood flow relationship during visual stimulation in healthy humans. *Magn Reson Med* **72**(3):864-75.

Ciris, P.A., Qiu, M. & Constable, R.T. (2013) Non-invasive quantification of absolute cerebral blood volume during functional activation applicable to the whole human brain. *Magn Reson Med* In print. doi: 10.1002/mrm.24694.

Dai, W., Garcia, D., de Bazelaire, C. & Alsop, D.C. (2008) Continuous flow-driven inversion for arterial spin labeling using pulsed radio frequency and gradient fields. *Magn Reson Med* **60**(6):1488–1497.

Davis, T.L., Kwong, K.K., Weisskoff, R.M. & Rosen, B.R. (1998) Calibrated functional MRI: mapping the dynamics of oxidative metabolism. *Proc. Natl. Acad. Sci. U.S.A.* **95**(4):1834–1839.

Dechent, P., Schütze, G., Helms, G., Merboldt, K.D. & Frahm, J. (2011) Basal cerebral blood volume during the poststimulation undershoot in BOLD MRI of the human brain. *J. Cereb. Blood Flow Metab.* **31**(1):82–89.

Dethrage, L.M., Faraco, C.C., Strother, M.K. & Donahue, M.J. (2014) In vivo quantification of blood water R1 change during hypercarbic hyperoxia. In: Proc ISMRM Milano.

Detre, J.A., Alsop, D.C., Vives, L.R., Maccotta, L., Teener, J.W. & Raps, E.C. (1998) Noninvasive MRI evaluation of cerebral blood flow in cerebrovascular disease. *Neurology* **50**(3):633–641.

Detre, J.A., Leigh, J.S., Williams, D.S. & Koretsky, A.P. (1992) Perfusion imaging. *Magn Reson Med* **23**(1):37–45.

Detre, J.A. & Wang, J. (2002) Technical aspects and utility of fMRI using BOLD and ASL. *Clin Neurophysiol* **113**(5):621–634.

Devor, A., Hillman, E.M.C., Tian, P., Waeber, C., Teng, I.C., Ruvinskaya, L., Shalinsky, M.H., Zhu,

H., Haslinger, R.H., Narayanan, S.N., Ulbert, I., Dunn, A.K., Lo, E.H., Rosen, B.R., Dale, A.M., Kleinfeld, D. & Boas, D.A. (2008) Stimulus-induced changes in blood flow and 2-deoxyglucose uptake dissociate in ipsilateral somatosensory cortex. *J. Neurosci.* **28**(53):14347–14357.

Diringer, M.N., Yundt, K., Videen, T.O., Adams, R.E., Zazulia, A.R., Deibert, E., Aiyagari, V., Dacey, R.G., Jr, Grubb, R.L., Jr & Powers, W.J. (2000) No reduction in cerebral metabolism as a result of early moderate hyperventilation following severe traumatic brain injury. *J. Neurosurg.* **92**(1):7–13.

Dobre, M., Ugurbil, K. & Marjanska, M. (2007) Determination of blood longitudinal relaxation time (T1) at high magnetic field strengths. **25**(5):733–735.

Donahue, M.J., Lu, H., Jones, C.K., Edden, R.A.E., Pekar, J.J. & van Zijl, P.C.M. (2006) Theoretical and experimental investigation of the VASO contrast mechanism. *Magn Reson Med* **56**(6):1261–1273.

Donahue, M.J., Stevens, R.D., de Boorder, M., Pekar, J.J., Hendrikse, J. & van Zijl, P.C.M. (2009) Hemodynamic changes after visual stimulation and breath holding provide evidence for an uncoupling of cerebral blood flow and volume from oxygen metabolism. *J. Cereb. Blood Flow Metab.* **29**(1):176–185.

Drew, P.J., Shih, A.Y. & Kleinfeld, D. (2011) Fluctuating and sensory-induced vasodynamics in rodent cortex extend arteriole capacity. *Proc. Natl. Acad. Sci. U.S.A.* **108**(20):8473–8478.

Driver, I., Blockley, N., Fisher, J., Francis, S. & Gowland, P. (2010) The change in cerebrovascular reactivity between 3 T and 7 T measured using graded hypercapnia. *Neuroimage* **51**(1):274–279.

Driver, I.D., Hall, E.L., Wharton, S.J., Pritchard, S.E., Francis, S.T. & Gowland, P.A. (2012) Calibrated BOLD using direct measurement of changes in venous oxygenation. *Neuroimage* **63**(3):1178–1187.

Duff, E., Xiong, J., Wang, B., Cunnington, R., Fox, P. & Egan, G. (2007) Complex spatio-temporal dynamics of fMRI BOLD: A study of motor learning. *Neuroimage* **34**(1):156–168.

Duong, T.Q., Yacoub, E., Adriany, G., Hu, X., Ugurbil, K. & Kim, S.-G. (2003) Microvascular BOLD contribution at 4 and 7 T in the human brain: gradient-echo and spin-echo fMRI with suppression of blood effects. *Magn Reson Med* **49**(6):1019–1027.

Duyn, J.H. (2012) The future of ultra-high field MRI and fMRI for study of the human brain. *Neuroimage* **62**(2):1241–1248.

Edelman, R.R., Siewert, B., Darby, D.G., Thangaraj, V., Nobre, A.C., Mesulam, M.M. & Warach, S. (1994) Qualitative mapping of cerebral blood flow and functional localization with echo-planar MR imaging and signal targeting with alternating radio frequency. *Radiology* **192**(2):513–520.

Fan, A.P., Govindarajan, S.T., Kinkel, P.R., Rosen, B.R., Adalsteinsson, E. & Mainero, C. (2013) Intra-Observer and Scan-Rescan Reproducibility of Quantitative Oxygen Extraction Fraction from MRI Phase at 7 Tesla. In: Proc ISMRM Salt Lake City.

Faro, S.H. & Mohamed, F.B. (2010) *Bold Fmri: A Guide to Functional Imaging for Neuroscientists*. Auflage: 2010. Springer: New York.

Feinberg, D.A., Hale, J.D., Watts, J.C., Kaufman, L. & Mark, A. (1986) Halving MR imaging time by conjugation: demonstration at 3.5 kG. *Radiology* **161**(2):527–531.

Fernández-Seara, M.A., Aznárez-Sanado, M., Mengual, E., Loayza, F.R. & Pastor, M.A. (2009) Continuous performance of a novel motor sequence leads to highly correlated striatal and hippocampal perfusion increases. *Neuroimage* **47**(4):1797–1808.

Fernández-Seara, M.A., Wang, Z., Wang, J., Rao, H.-Y., Guenther, M., Feinberg, D.A. & Detre, J.A. (2005) Continuous arterial spin labeling perfusion measurements using single shot 3D GRASE at 3 T. *Magn Reson Med* **54**(5):1241–1247.

Floyer-Lea, A. & Matthews, P.M. (2004) Changing brain networks for visuomotor control with increased movement automaticity. *J. Neurophysiol.* **92**(4):2405–2412.

Fox, M.D., Snyder, A.Z., Barch, D.M., Gusnard, D.A. & Raichle, M.E. (2005) Transient BOLD responses at block transitions. *Neuroimage* **28**(4):956–966.

Fox, P.T. & Raichle, M.E. (1986) Focal physiological uncoupling of cerebral blood flow and oxidative metabolism during somatosensory stimulation in human subjects. *Proc. Natl. Acad. Sci. U.S.A.* **83**(4):1140–1144.

Fox, P.T. & Raichle, M.E. (1984) Stimulus rate dependence of regional cerebral blood flow in human striate cortex, demonstrated by positron emission tomography. *J. Neurophysiol.* **51**(5):1109–1120.

Fox, P.T., Raichle, M.E., Mintun, M.A. & Dence, C. (1988) Nonoxidative glucose consumption during focal physiologic neural activity. *Science* **241**(4864):462–464.

Francis, S. t., Bowtell, R. & Gowland, P. a. (2008) Modeling and optimization of look-locker spin labeling for measuring perfusion and transit time changes in activation studies taking into account arterial blood volume. *Magn. Reson. Med.* **59**(2):316–325.

Garcia, D.M., Duhamel, G. & Alsop, D.C. (2005) Efficiency of inversion pulses for background suppressed arterial spin labeling. *Magn Reson Med* **54**(2):366–372.

Gardener, A.G., Gowland, P.A. & Francis, S.T. (2009) Implementation of quantitative perfusion imaging using pulsed arterial spin labeling at ultra-high field. *Magn Reson Med* **61**(4):874–882.

Gauthier, C.J., Desjardins-Crépeau, L., Madjar, C., Bherer, L. & Hoge, R.D. (2012) Absolute quantification of resting oxygen metabolism and metabolic reactivity during functional activation using QUO2 MRI. *Neuroimage* **63**(3):1353–1363.

Gauthier, C.J. & Hoge, R.D. (2013) A generalized procedure for calibrated MRI incorporating hyperoxia and hypercapnia. *Hum Brain Mapp* **34**(5):1053–1069.

Gauthier, C.J. & Hoge, R.D. (2012) Magnetic resonance imaging of resting OEF and $CMRO_2$ using a generalized calibration model for hypercapnia and hyperoxia. *Neuroimage* **60**(2):1212–1225.

Gauthier, C.J., Krieger, S.N., Huber, L., Hoge, R.D. & Turner, R. (2013) Baseline oxygen metabolism quantification at 7T using QUO2. In: Proc HBM Seattle.

Gauthier, C.J., Madjar, C., Desjardins-Crépeau, L., Bellec, P., Bherer, L. & Hoge, R.D. (2013) Age

dependence of hemodynamic response characteristics in human functional magnetic resonance imaging. *Neurobiol. Aging* **34**(5):1469–1485.

Gauthier, C.J., Madjar, C., Tancredi, F.B., Stefanovic, B. & Hoge, R.D. (2011) Elimination of visually evoked BOLD responses during carbogen inhalation: implications for calibrated MRI. *Neuroimage* **54**(2):1001–1011.

Ghariq, E., Teeuwisse, W.M., Webb, A.G. & van Osch, M.J.P. (2012) Feasibility of pseudocontinuous arterial spin labeling at 7 T with whole-brain coverage. *MAGMA* **25**(2):83–93.

Ginsberg, M.D., Chang, J.Y., Kelley, R.E., Yoshii, F., Barker, W.W., Ingenito, G. & Boothe, T.E. (1988) Increases in both cerebral glucose utilization and blood flow during execution of a somatosensory task. *Ann. Neurol.* **23**(2):152–160.

Ginsberg, M.D., Dietrich, W.D. & Busto, R. (1987) Coupled forebrain increases of local cerebral glucose utilization and blood flow during physiologic stimulation of a somatosensory pathway in the rat: demonstration by double-label autoradiography. *Neurology* **37**(1):11–19.

Gjedde, A. (1987) Does deoxyglucose uptake in the brain reflect energy metabolism? *Biochem. Pharmacol.* **36**(12):1853–1861.

Glielmi, C.B., Schuchard, R.A. & Hu, X.P. (2009) Estimating cerebral blood volume with expanded vascular space occupancy slice coverage. *Magn Reson Med* **61**(5):1193–1200.

Goense, J., Merkle, H. & Logothetis, N.K. (2012) High-resolution fMRI reveals laminar differences in neurovascular coupling between positive and negative BOLD responses. *Neuron* **76**(3):629–639.

Golay, X. & Petersen, E.T. (2006) Arterial spin labeling: benefits and pitfalls of high magnetic field. *Neuroimaging Clin. N. Am.* **16**(2):259–268, x.

Golay, X., Petersen, E.T. & Hui, F. (2005) Pulsed star labeling of arterial regions (PULSAR): a robust regional perfusion technique for high field imaging. *Magn Reson Med* **53**(1):15–21.

Gonzalez-At, J.B., Alsop, D.C. & Detre, J.A. (2000) Cerebral perfusion and arterial transit time changes during task activation determined with continuous arterial spin labeling. *Magn Reson Med* **43**(5):739–746.

Grafton, S.T., Hazeltine, E. & Ivry, R.B. (2002) Motor sequence learning with the nondominant left hand. A PET functional imaging study. *Exp Brain Res* **146**(3):369–378.

Griffeth, V.E.M. & Buxton, R.B. (2011) A theoretical framework for estimating cerebral oxygen metabolism changes using the calibrated-BOLD method: modeling the effects of blood volume distribution, hematocrit, oxygen extraction fraction, and tissue signal properties on the BOLD signal. *Neuroimage* **58**(1):198–212.

Griswold, M.A., Jakob, P.M., Heidemann, R.M., Nittka, M., Jellus, V., Wang, J., Kiefer, B. & Haase, A. (2002) Generalized autocalibrating partially parallel acquisitions (GRAPPA). *Magn Reson Med* **47**(6):1202–1210.

Griswold, M.A., Jakob, P.M., Nittka, M., Goldfarb, J.W. & Haase, A. (2000) Partially parallel imaging with localized sensitivities (PILS). *Magn Reson Med* **44**(4):602–609.

Grubb, R.L., Raichle, M.E., Eichling, J.O. & Ter-Pogossian, M.M. (1974) The effects of changes in PaCO2 on cerebral blood volume, blood flow, and vascular mean transit time. *Stroke* **5**(5):630–639.

Gu, H., Lu, H., Ye, F.Q., Stein, E.A. & Yang, Y. (2006) Noninvasive quantification of cerebral blood volume in humans during functional activation. *Neuroimage* **30**(2):377–387.

Gu, H., Stein, E.A. & Yang, Y. (2005) Nonlinear responses of cerebral blood volume, blood flow and blood oxygenation signals during visual stimulation. *Magn Reson Imaging* **23**(9):921–928.

Gusnard, D.A., Raichle, M.E. & Raichle, M.E. (2001) Searching for a baseline: functional imaging and the resting human brain. *Nat. Rev. Neurosci.* **2**(10):685–694.

Hall, E.L., Driver, I.D., Pritchard, S.E., Gowland, P.A. & Francis, S.T. (2013) Voxel-wise Estimation of M and CMRO2 at 7T. In: Proc ISMRM Salt Lake City.

Heidemann, R.M., Griswold, M.A., Haase, A. & Jakob, P.M. (2001) VD-AUTO-SMASH imaging. *Magn Reson Med* **45**(6):1066–1074.

Herman, P., Sanganahalli, B.G., Blumenfeld, H., Rothman, D.L. & Hyder, F. (2013) Quantitative basis for neuroimaging of cortical laminae with calibrated functional MRI. *Proc. Natl. Acad. Sci. U.S.A.* **110**(37):15115–15120.

Hernandez-Garcia, L., Lee, G.R., Vazquez, A.L., Yip, C.-Y. & Noll, D.C. (2005) Quantification of perfusion fMRI using a numerical model of arterial spin labeling that accounts for dynamic transit time effects. *Magn Reson Med* **54**(4):955–964.

Hetzer, S., Mildner, T. & Möller, H.E. (2011) A Modified EPI sequence for high-resolution imaging at ultra-short echo time. *Magn. Reson. Med.* **65**(1):165–175.

He, X. & Yablonskiy, D.A. (2007) Quantitative BOLD: mapping of human cerebral deoxygenated blood volume and oxygen extraction fraction: default state. *Magn Reson Med* **57**(1):115–126.

Hillman, E.M.C., Devor, A., Bouchard, M.B., Dunn, A.K., Krauss, G.W., Skoch, J., Bacskai, B.J., Dale, A.M. & Boas, D.A. (2007) Depth-resolved optical imaging and microscopy of vascular compartment dynamics during somatosensory stimulation. *Neuroimage* **35**(1):89–104.

Hoge, R.D., Atkinson, J., Gill, B., Crelier, G.R., Marrett, S. & Pike, G.B. (1999) Investigation of BOLD signal dependence on cerebral blood flow and oxygen consumption: the deoxyhemoglobin dilution model. *Magn Reson Med* **42**(5):849–863.

Hoge, R.D., Atkinson, J., Gill, B., Crelier, G.R., Marrett, S. & Pike, G.B. (1999) Stimulus-dependent BOLD and perfusion dynamics in human V1. *Neuroimage* **9**(6 Pt 1):573–585.

Hua, J., Donahue, M.J., Zhao, J.M., Grgac, K., Huang, A.J., Zhou, J. & van Zijl, P.C.M. (2009) Magnetization transfer enhanced vascular-space-occupancy (MT-VASO) functional MRI. *Magn Reson Med* **61**(4):944–951.

Hua, J., Jones, C.K., Qin, Q. & van Zijl, P.C.M. (2012) Implementation of vascular-space-occupancy MRI at 7T. *Magn Reson Med*.

Hua, J., Qin, Q., Donahue, M.J., Zhou, J., Pekar, J.J. & van Zijl, P.C.M. (2011) Inflow-based vascular-space-occupancy (iVASO) MRI. *Magn Reson Med* **66**(1):40–56.

Huber, L., Goense, J., Kennerley, A.J., Ivanov, D., Krieger, S.N., Lepsien, J., Trampel, R., Turner, R. & Möller, H.E. (2014) Investigation of the neurovascular coupling in positive and negative BOLD responses in human brain at 7 T. *Neuroimage* **97**:349–362.

Huber, L., Ivanov, D., Gauthier, C., Roggenhofer, E., Henseler, I., Turner, R. & Moeller, H. (2013) Measurements of Cerebral Blood Volume and BOLD signal During Hypercapnia and Functional Stimulation in Humans at 7T: Application to Calibrated BOLD. In: Proc ISMRM Salt Lake City.

Huber, L., Ivanov, D., Krieger, S.N., Streicher, M.N., Mildner, T., Poser, B.A., Möller, H.E. & Turner, R. (2014) Slab-selective, BOLD-corrected VASO at 7 Tesla provides measures of cerebral blood volume reactivity with high signal-to-noise ratio. *Magn Reson Med* **72**(1):137–148.

Hudetz, A.G. (1997) Blood flow in the cerebral capillary network: a review emphasizing observations with intravital microscopy. *Microcirculation* **4**(2):233–252.

Huettel, S.A. (2009) *Functional Magnetic Resonance Imaging*. Auflage: 2nd Edition. Palgrave Macmillan: Sunderland, Mass.

Hurley, A.C., Al-Radaideh, A., Bai, L., Aickelin, U., Coxon, R., Glover, P. & Gowland, P.A. (2010) Tailored RF pulse for magnetization inversion at ultrahigh field. *Magn Reson Med* **63**(1):51–58.

Hyder, F. (2009) Dynamic imaging of brain function. *Methods Mol. Biol.* **489**:3–21.

Hyder, F., Kida, I., Behar, K.L., Kennan, R.P., Maciejewski, P.K. & Rothman, D.L. (2001) Quantitative functional imaging of the brain: towards mapping neuronal activity by BOLD fMRI. *NMR Biomed* **14**(7-8):413–431.

Hyder, F. & Rothman, D.L. (2011) Evidence for the importance of measuring total brain activity in neuroimaging. *Proc. Natl. Acad. Sci. U.S.A.* **108**(14):5475–5476.

Hyder, F. & Rothman, D.L. (2010) Neuronal correlate of BOLD signal fluctuations at rest: err on the side of the baseline. *Proc. Natl. Acad. Sci. U.S.A.* **107**(24):10773–10774.

Hyder, F., Sanganahalli, B.G., Herman, P., Coman, D., Maandag, N.J.G., Behar, K.L., Blumenfeld, H. & Rothman, D.L. (2010) Neurovascular and Neurometabolic Couplings in Dynamic Calibrated fMRI: Transient Oxidative Neuroenergetics for Block-Design and Event-Related Paradigms. *Front Neuroenergetics* **2**.

Iadecola, C. (2002) Intrinsic signals and functional brain mapping: caution, blood vessels at work. *Cereb. Cortex* **12**(3):223–224.

Iadecola, C. & Nedergaard, M. (2007) Glial regulation of the cerebral microvasculature. *Nat. Neurosci.* **10**(11):1369–1376.

Ishimori, Y., Monma, M., Kawamura, H. & Miyata, T. (2011) Time spatial labeling inversion pulse cerebral MR angiography without subtraction by use of dual inversion recovery background suppression. *Radiol Phys Technol* **4**(1):78–83.

Ito, H., Kanno, I., Kato, C., Sasaki, T., Ishii, K., Ouchi, Y., Iida, A., Okazawa, H., Hayashida, K., Tsuyuguchi, N., Ishii, K., Kuwabara, Y. & Senda, M. (2004) Database of normal human cerebral blood flow, cerebral blood volume, cerebral oxygen extraction fraction and cerebral metabolic rate of oxygen measured by positron emission tomography with 15O-labelled carbon dioxide or water,

carbon monoxide and oxygen: a multicentre study in Japan. *Eur. J. Nucl. Med. Mol. Imaging* **31**(5):635–643.

Ivanov, D., Huber, L., Kabisch, S., Streicher, M.N., Schloegl, H., Henseler, I., Roggenhofer, E., Heinke, W. & Turner, R. (2012) Mapping of CMRO2 changes in visual cortex during a visual motion paradigm at 7T. In: Proc ISMRM Melbourne.

Ivanov, D., Schäfer, A., Deistung, A., Streicher, M.N., Kabisch, S., Henseler, I., Roggenhofer, E., Joachimsen, T.H., Schweser, F., Reichenbach, J.R., Uludag, K. & Turner, R. (2013) In vivo estimation of the transverse relaxation time dependence of blood on oxygenation at 7 Tesla. In: Proc ISMRM Salt Lake City.

Jain, V., Langham, M.C. & Wehrli, F.W. (2010) MRI estimation of global brain oxygen consumption rate. *J. Cereb. Blood Flow Metab.* **30**(9):1598–1607.

Jin, T. & Kim, S.-G. (2008) Improved cortical-layer specificity of vascular space occupancy fMRI with slab inversion relative to spin-echo BOLD at 9.4 T. *Neuroimage* **40**(1):59–67.

Jin, T. & Kim, S.-G. (2006) Spatial dependence of CBV-fMRI: a comparison between VASO and contrast agent based methods. *Conf Proc IEEE Eng Med Biol Soc* **1**:25–28.

Jones, M., Berwick, J., Hewson-Stoate, N., Gias, C. & Mayhew, J. (2005) The effect of hypercapnia on the neural and hemodynamic responses to somatosensory stimulation. *Neuroimage* **27**(3):609–623.

Kennerley, A.J., Berwick, J., Martindale, J., Johnston, D., Papadakis, N. & Mayhew, J.E. (2005) Concurrent fMRI and optical measures for the investigation of the hemodynamic response function. *Magn Reson Med* **54**(2):354–365.

Kennerley, A.J., Harris, S., Bruyns-Haylett, M., Boorman, L., Zheng, Y., Jones, M. & Berwick, J. (2012) Early and late stimulus-evoked cortical hemodynamic responses provide insight into the neurogenic nature of neurovascular coupling. *J. Cereb. Blood Flow Metab.* **32**(3):468–480.

Kida, I. & Hyder, F. (2006) Physiology of functional magnetic resonance imaging: energetics and function. *Methods Mol. Med.* **124**:175–195.

Kida, I., Kennan, R.P., Rothman, D.L., Behar, K.L. & Hyder, F. (2000) High-resolution CMR(O2) mapping in rat cortex: a multiparametric approach to calibration of BOLD image contrast at 7 Tesla. *J. Cereb. Blood Flow Metab.* **20**(5):847–860.

Kida, I., Maciejewski, P.K. & Hyder, F. (2004) Dynamic imaging of perfusion and oxygenation by functional magnetic resonance imaging. *J. Cereb. Blood Flow Metab.* **24**(12):1369–1381.

Kida, I., Rothman, D.L. & Hyder, F. (2007) Dynamics of changes in blood flow, volume, and oxygenation: implications for dynamic functional magnetic resonance imaging calibration. *J. Cereb. Blood Flow Metab.* **27**(4):690–696.

Kim, S.G. (1995) Quantification of relative cerebral blood flow change by flow-sensitive alternating inversion recovery (FAIR) technique: application to functional mapping. *Magn Reson Med* **34**(3):293–301.

Kim, S.-G. & Ogawa, S. (2012) Biophysical and physiological origins of blood oxygenation level-

dependent fMRI signals. *J. Cereb. Blood Flow Metab.* **32**(7):1188–1206.

Kim, S.G., Rostrup, E., Larsson, H.B., Ogawa, S. & Paulson, O.B. (1999) Determination of relative CMRO2 from CBF and BOLD changes: significant increase of oxygen consumption rate during visual stimulation. *Magn Reson Med* **41**(6):1152–1161.

Kim, T. & Kim, S.-G. (2005) Quantification of cerebral arterial blood volume and cerebral blood flow using MRI with modulation of tissue and vessel (MOTIVE) signals. *Magn Reson Med* **54**(2):333–342.

Kim, T. & Kim, S.-G. (2011) Temporal dynamics and spatial specificity of arterial and venous blood volume changes during visual stimulation: implication for BOLD quantification. *J. Cereb. Blood Flow Metab.* **31**(5):1211–1222.

Kleinfeld, D., Mitra, P.P., Helmchen, F. & Denk, W. (1998) Fluctuations and stimulus-induced changes in blood flow observed in individual capillaries in layers 2 through 4 of rat neocortex. *Proc. Natl. Acad. Sci. U.S.A.* **95**(26):15741–15746.

Krieger, S.N., Ivanov, D., Huber, L., Roggenhofer, E., Sehm, B., Turner, R., Egan, G.F. & Gauthier, C.J. (2014) Using carbogen for calibrated fMRI at 7Tesla: comparison of direct and modelled estimation of the M parameter. *Neuroimage* **84**:605–614.

Krieger, S.N., Streicher, M.N., Trampel, R. & Turner, R. (2012) Cerebral blood volume changes during brain activation. *J. Cereb. Blood Flow Metab.* **32**(8):1618–1631.

Krüger, G. & Glover, G.H. (2001) Physiological noise in oxygenation-sensitive magnetic resonance imaging. *Magn Reson Med* **46**(4):631–637.

Kwong, K.K., Chesler, D.A., Weisskoff, R.M., Donahue, K.M., Davis, T.L., Ostergaard, L., Campbell, T.A. & Rosen, B.R. (1995) MR perfusion studies with T1-weighted echo planar imaging. *Magn Reson Med* **34**(6):878–887.

Lauterbur, P.C. (1973) Image Formation by Induced Local Interactions: Examples Employing Nuclear Magnetic Resonance. *Nature* **242**(5394):190–191.

Law, C.S. & Glover, G.H. (2009) Interleaved spiral-in/out with application to functional MRI (fMRI). *Magn Reson Med* **62**(3):829–834.

Lee, S.P., Duong, T.Q., Yang, G., Iadecola, C. & Kim, S.G. (2001) Relative changes of cerebral arterial and venous blood volumes during increased cerebral blood flow: implications for BOLD fMRI. *Magn Reson Med* **45**(5):791–800.

Leite, F.P., Tsao, D., Vanduffel, W., Fize, D., Sasaki, Y., Wald, L.L., Dale, A.M., Kwong, K.K., Orban, G.A., Rosen, B.R., Tootell, R.B.H. & Mandeville, J.B. (2002) Repeated fMRI using iron oxide contrast agent in awake, behaving macaques at 3 Tesla. *Neuroimage* **16**(2):283–294.

Leontiev, O. & Buxton, R.B. (2007) Reproducibility of BOLD, perfusion, and CMRO2 measurements with calibrated-BOLD fMRI. *Neuroimage* **35**(1):175–184.

Leontiev, O., Dubowitz, D.J. & Buxton, R.B. (2007) CBF/CMRO2 coupling measured with calibrated BOLD fMRI: sources of bias. *Neuroimage* **36**(4):1110–1122.

Lin, A.-L., Fox, P.T., Yang, Y., Lu, H., Tan, L.-H. & Gao, J.-H. (2008) Evaluation of MRI models in the measurement of CMRO2 and its relationship with CBF. *Magn Reson Med* **60**(2):380–389.

Lin, A.-L., Fox, P.T., Yang, Y., Lu, H., Tan, L.-H. & Gao, J.-H. (2009) Time-dependent correlation of cerebral blood flow with oxygen metabolism in activated human visual cortex as measured by fMRI. *Neuroimage* **44**(1):16–22.

Liotti, M., Brannan, S., Egan, G., Shade, R., Madden, L., Abplanalp, B., Robillard, R., Lancaster, J., Zamarripa, F.E., Fox, P.T. & Denton, D. (2001) Brain responses associated with consciousness of breathlessness (air hunger). *Proc. Natl. Acad. Sci. U.S.A.* **98**(4):2035–2040.

Liu, P., Hebrank, A.C., Rodrigue, K.M., Kennedy, K.M., Park, D.C. & Lu, H. (2013) A comparison of physiologic modulators of fMRI signals. *Hum Brain Mapp* **34**(9):2078–2088.

Liu, P., Hebrank, A.C., Rodrigue, K.M., Kennedy, K.M., Section, J., Park, D.C. & Lu, H. (2013) Age-related differences in memory-encoding fMRI responses after accounting for decline in vascular reactivity. *Neuroimage* **78**:415–425.

Liu, P., Xu, F. & Lu, H. (2013) Test-retest reproducibility of a rapid method to measure brain oxygen metabolism. *Magn Reson Med* **69**(3):675–681.

Lu, H., Clingman, C., Golay, X. & van Zijl, P.C.M. (2004) Determining the longitudinal relaxation time (T1) of blood at 3.0 Tesla. *Magn Reson Med* **52**(3):679–682.

Lu, H. & Ge, Y. (2008) Quantitative evaluation of oxygenation in venous vessels using T2-Relaxation-Under-Spin-Tagging MRI. *Magn Reson Med* **60**(2):357–363.

Lu, H., Golay, X., Pekar, J.J. & Van Zijl, P.C.M. (2003) Functional magnetic resonance imaging based on changes in vascular space occupancy. *Magn Reson Med* **50**(2):263–274.

Lu, H., Law, M., Johnson, G., Ge, Y., van Zijl, P.C.M. & Helpern, J.A. (2005) Novel approach to the measurement of absolute cerebral blood volume using vascular-space-occupancy magnetic resonance imaging. *Magn Reson Med* **54**(6):1403–1411.

Luh, W.M., Wong, E.C., Bandettini, P.A. & Hyde, J.S. (1999) QUIPSS II with thin-slice TI1 periodic saturation: a method for improving accuracy of quantitative perfusion imaging using pulsed arterial spin labeling. *Magn Reson Med* **41**(6):1246–1254.

Lu, H., Zhao, C., Ge, Y. & Lewis-Amezcua, K. (2008) Baseline blood oxygenation modulates response amplitude: Physiologic basis for intersubject variations in functional MRI signals. **60**(2):364–372.

Lu, H. & van Zijl, P.C.M. (2012) A review of the development of Vascular-Space-Occupancy (VASO) fMRI. *Neuroimage* **62**(2):736–742.

Lu, H. & van Zijl, P.C.M. (2005) Experimental measurement of extravascular parenchymal BOLD effects and tissue oxygen extraction fractions using multi-echo VASO fMRI at 1.5 and 3.0 T. *Magn Reson Med* **53**(4):808–816.

Lu, H., van Zijl, P.C.M., Hendrikse, J. & Golay, X. (2004) Multiple acquisitions with global inversion cycling (MAGIC): a multislice technique for vascular-space-occupancy dependent fMRI. *Magn Reson Med* **51**(1):9–15.

Mandeville, J.B., Marota, J.J., Ayata, C., Zaharchuk, G., Moskowitz, M.A., Rosen, B.R. & Weisskoff, R.M. (1999) Evidence of a cerebrovascular postarteriole windkessel with delayed compliance. *J. Cereb. Blood Flow Metab.* **19**(6):679–689.

Mansfield, P. (1977) Multi-planar image formation using NMR spin echoes. *J. Phys. C: Solid State Phys.* **10**(3):L55.

Mark, C.I., Fisher, J.A. & Pike, G.B. (2011) Improved fMRI calibration: precisely controlled hyperoxic versus hypercapnic stimuli. *Neuroimage* **54**(2):1102–1111.

Mark, C.I. & Pike, G.B. (2012) Indication of BOLD-specific venous flow-volume changes from precisely controlled hyperoxic vs. hypercapnic calibration. *J. Cereb. Blood Flow Metab.* **32**(4):709–719.

Mark, C.I., Slessarev, M., Ito, S., Han, J., Fisher, J.A. & Pike, G.B. (2010) Precise control of end-tidal carbon dioxide and oxygen improves BOLD and ASL cerebrovascular reactivity measures. *Magn Reson Med* **64**(3):749–756.

Marrett, S. & Gjedde, A. (1997) Changes of blood flow and oxygen consumption in visual cortex of living humans. *Adv. Exp. Med. Biol.* **413**:205–208.

Martindale, J., Kennerley, A.J., Johnston, D., Zheng, Y. & Mayhew, J.E. (2008) Theory and generalization of Monte Carlo models of the BOLD signal source. *Magn Reson Med* **59**(3):607–618.

Ma, Y., Berman, A.J. & Pike, G.B. (2014) The effect of dissolved oxygen on relaxation rates of blood plasma. In: Proc ISMRM Milano.

Menon, R.G., Walsh, E.G., Twieg, D.B. & Carroll, T.J. (2013) A Parse-MRI Based Technique to Measure Cerebral Oxygen Extraction Fraction (OEF). In: Proc ISMRM Salt Lake City.

Mildner, T., Müller, K., Hetzer, S., Trampel, R., Driesel, W. & Möller, H.E. (2014) Mapping of arterial transit time by intravascular signal selection. *NMR Biomed* **27**(5):594–609.

Mildner, T., Trampel, R., Möller, H.E., Schäfer, A., Wiggins, C.J. & Norris, D.G. (2003) Functional perfusion imaging using continuous arterial spin labeling with separate labeling and imaging coils at 3 T. *Magn Reson Med* **49**(5):791–795.

Mohtasib, R.S., Lumley, G., Goodwin, J.A., Emsley, H.C.A., Sluming, V. & Parkes, L.M. (2012) Calibrated fMRI during a cognitive Stroop task reveals reduced metabolic response with increasing age. *Neuroimage* **59**(2):1143–1151.

Noeske, R., Seifert, F., Rhein, K.-H. & Rinneberg, H. (2000) Human cardiac imaging at 3 T using phased array coils. *Magn. Reson. Med.* **44**(6):978–982.

Ogawa, S., Lee, T.M., Kay, A.R. & Tank, D.W. (1990) Brain magnetic resonance imaging with contrast dependent on blood oxygenation. *Proc. Natl. Acad. Sci. U.S.A.* **87**(24):9868–9872.

Oldendorf, W.H. (1971) Brain uptake of radiolabeled amino acids, amines, and hexoses after arterial injection. *Am. J. Physiol.* **221**(6):1629–1639.

Ordidge, R.J., Wylezinska, M., Hugg, J.W., Butterworth, E. & Franconi, F. (1996) Frequency offset

corrected inversion (FOCI) pulses for use in localized spectroscopy. *Magn Reson Med* **36**(4):562–566.

Pawlik, G., Rackl, A. & Bing, R.J. (1981) Quantitative capillary topography and blood flow in the cerebral cortex of cats: an in vivo microscopic study. *Brain Res.* **208**(1):35–58.

Pell, G.S., Thomas, D.L., Lythgoe, M.F., Calamante, F., Howseman, A.M., Gadian, D.G. & Ordidge, R.J. (1999) Implementation of quantitative FAIR perfusion imaging with a short repetition time in time-course studies. *Magn Reson Med* **41**(4):829–840.

Perthen, J.E., Lansing, A.E., Liau, J., Liu, T.T. & Buxton, R.B. (2008) Caffeine-induced uncoupling of cerebral blood flow and oxygen metabolism: a calibrated BOLD fMRI study. *Neuroimage* **40**(1):237–247.

Pfeuffer, J., Adriany, G., Shmuel, A., Yacoub, E., Van De Moortele, P.-F., Hu, X. & Ugurbil, K. (2002) Perfusion-based high-resolution functional imaging in the human brain at 7 Tesla. *Magn Reson Med* **47**(5):903–911.

Pohmann, R. (2010) Accurate, localized quantification of white matter perfusion with single-voxel ASL. *Magn Reson Med* **64**(4):1109–1113.

Poser, B.A., van Mierlo, E. & Norris, D.G. (2011) Exploring the post-stimulus undershoot with spin-echo fMRI: implications for models of neurovascular response. *Hum Brain Mapp* **32**(1):141–153.

Poser, B.A. & Norris, D.G. (2009) 3D single-shot VASO using a Maxwell gradient compensated GRASE sequence. *Magn Reson Med* **62**(1):255–262.

Poser, B.A. & Norris, D.G. (2007) Measurement of activation-related changes in cerebral blood volume: VASO with single-shot HASTE acquisition. *MAGMA* **20**(2):63–67.

Powers, W.J., Hirsch, I.B. & Cryer, P.E. (1996) Effect of stepped hypoglycemia on regional cerebral blood flow response to physiological brain activation. *Am. J. Physiol.* **270**(2 Pt 2):H554–559.

Pruessmann, K.P., Weiger, M., Scheidegger, M.B. & Boesiger, P. (1999) SENSE: sensitivity encoding for fast MRI. *Magn Reson Med* **42**(5):952–962.

Qin, Q., Grgac, K. & van Zijl, P.C.M. (2011) Determination of whole-brain oxygen extraction fractions by fast measurement of blood T(2) in the jugular vein. *Magn Reson Med* **65**(2):471–479.

Raichle, M.E., MacLeod, A.M., Snyder, A.Z., Powers, W.J., Gusnard, D.A. & Shulman, G.L. (2001) A default mode of brain function. *Proc. Natl. Acad. Sci. U.S.A.* **98**(2):676–682.

Rane, S. & Gore, J.C. (2013) Measurement of T1 of human arterial and venous blood at 7T. **31**(3):477–479.

Rhoades, R. & Bell, D. (2009) *Medical Physiology: Principles for Clinical Medicine*. 3rd ed. Lippincott Williams & Wilkins: Philadelphia, Pa; London.

Roland, P.E., Eriksson, L., Stone-Elander, S. & Widen, L. (1987) Does mental activity change the oxidative metabolism of the brain? *J. Neurosci.* **7**(8):2373–2389.

Roland, P.E., Eriksson, L., Widén, L. & Stone-Elander, S. (1989) Changes in Regional Cerebral Oxidative Metabolism Induced by Tactile Learning and Recognition in Man. *Eur. J. Neurosci.* **1**(1):3–18.

Rooney, W.D., Johnson, G., Li, X., Cohen, E.R., Kim, S.-G., Ugurbil, K. & Springer, C.S. (2007) Magnetic field and tissue dependencies of human brain longitudinal 1H2O relaxation in vivo. *Magn. Reson. Med.* **57**(2):308–318.

Schroeter, M.L., Kupka, T., Mildner, T., Uludağ, K. & von Cramon, D.Y. (2006) Investigating the post-stimulus undershoot of the BOLD signal--a simultaneous fMRI and fNIRS study. *Neuroimage* **30**(2):349–358.

Schwarzbauer, C. & Hoehn, M. (2000) The effect of transient hypercapnia on task-related changes in cerebral blood flow and blood oxygenation in awake normal humans: a functional magnetic resonance imaging study. *NMR Biomed* **13**(7):415–419.

Schwarzbauer, C., Morrissey, S.P. & Haase, A. (1996) Quantitative magnetic resonance imaging of perfusion using magnetic labeling of water proton spins within the detection slice. *Magn Reson Med* **35**(4):540–546.

Scouten, A. & Constable, R.T. (2007) Applications and limitations of whole-brain MAGIC VASO functional imaging. *Magn Reson Med* **58**(2):306–315.

Seidler, R.D., Noll, D.C. & Thiers, G. (2004) Feedforward and feedback processes in motor control. *Neuroimage* **22**(4):1775–1783.

Seitz, R.J. & Roland, P.E. (1992) Vibratory stimulation increases and decreases the regional cerebral blood flow and oxidative metabolism: a positron emission tomography (PET) study. *Acta Neurol. Scand.* **86**(1):60–67.

Severinghaus, J.W. (1979a) Current trends in continuous blood gas monitoring. *Biotelem Patient Monit* **6**(1-2):9–15.

Severinghaus, J.W. (1979b) Simple, accurate equations for human blood O2 dissociation computations. *J Appl Physiol Respir Environ Exerc Physiol* **46**(3):599–602.

Shen, Y., Kauppinen, R.A., Vidyasagar, R. & Golay, X. (2009) A functional magnetic resonance imaging technique based on nulling extravascular gray matter signal. *J. Cereb. Blood Flow Metab.* **29**(1):144–156.

Shulman, R.G., Rothman, D.L. & Hyder, F. (2007) A BOLD search for baseline. *Neuroimage* **36**(2):277–281.

Silvennoinen, M.J., Kettunen, M.I. & Kauppinen, R.A. (2003) Effects of hematocrit and oxygen saturation level on blood spin-lattice relaxation. *Magn. Reson. Med.* **49**(3):568–571.

Silver, M.S., Joseph, R.I., Chen, C.-N., Sank, V.J. & Hoult, D.I. (1984) Selective population inversion in NMR. *Nature* **310**(5979):681–683.

Slessarev, M., Han, J., Mardimae, A., Prisman, E., Preiss, D., Volgyesi, G., Ansel, C., Duffin, J. & Fisher, J.A. (2007) Prospective targeting and control of end-tidal CO2 and O2 concentrations. *J. Physiol. (Lond.)* **581**(Pt 3):1207–1219.

Smith, S.M., Beckmann, C.F., Ramnani, N., Woolrich, M.W., Bannister, P.R., Jenkinson, M., Matthews, P.M. & McGonigle, D.J. (2005) Variability in fMRI: a re-examination of inter-session differences. *Hum Brain Mapp* **24**(3):248–257.

Stanisz, G.J., Odrobina, E.E., Pun, J., Escaravage, M., Graham, S.J., Bronskill, M.J. & Henkelman, R.M. (2005) T1, T2 relaxation and magnetization transfer in tissue at 3T. *Magn. Reson. Med.* **54**(3):507–512.

Steele, C.J. & Penhune, V.B. (2010) Specific increases within global decreases: a functional magnetic resonance imaging investigation of five days of motor sequence learning. *J. Neurosci.* **30**(24):8332–8341.

Stone, A.J., Murphy, K., Harris, A.D. & Wise, R.D. (2013) Efficient measurement of resting and elevated absolute CMRO2 and their within session repeatability in the human brain using calibrated FMRI. In: Proc ISMRM Salt Lake City.

Streicher, M.N., Schäfer, A., Reimer, E., Dhital, B., Trampel, R., Ivanov, D. & Turner, R. (2012) Effects of air susceptibility on proton resonance frequency MR thermometry. *MAGMA* **25**(1):41–47.

Tancredi, F.B. & Hoge, R.D. (2013) Comparison of cerebral vascular reactivity measures obtained using breath-holding and CO2 inhalation. *J. Cereb. Blood Flow Metab.* **33**(7):1066–1074.

Tan, H., Hoge, W.S., Hamilton, C.A., Günther, M. & Kraft, R.A. (2011) 3D GRASE PROPELLER: improved image acquisition technique for arterial spin labeling perfusion imaging. *Magn Reson Med* **66**(1):168–173.

Teeuwisse, W.M., Webb, A.G. & van Osch, M.J.P. (2010) Arterial spin labeling at ultra-high field: All that glitters is not gold. *Int. J. Imaging Syst. Technol.* **20**(1):62–70.

Tjandra, T., Brooks, J.C.W., Figueiredo, P., Wise, R., Matthews, P.M. & Tracey, I. (2005) Quantitative assessment of the reproducibility of functional activation measured with BOLD and MR perfusion imaging: implications for clinical trial design. *Neuroimage* **27**(2):393–401.

Triantafyllou, C., Hoge, R.D., Krueger, G., Wiggins, C.J., Potthast, A., Wiggins, G.C. & Wald, L.L. (2005) Comparison of physiological noise at 1.5 T, 3 T and 7 T and optimization of fMRI acquisition parameters. *Neuroimage* **26**(1):243–250.

Turner, R. (2002) How much cortex can a vein drain? Downstream dilution of activation-related cerebral blood oxygenation changes. *Neuroimage* **16**(4):1062–1067.

Turner, R., Jezzard, P., Wen, H., Kwong, K.K., Le Bihan, D., Zeffiro, T. & Balaban, R.S. (1993) Functional mapping of the human visual cortex at 4 and 1.5 tesla using deoxygenation contrast EPI. *Magn Reson Med* **29**(2):277–279.

Uludağ, K. (2008) Transient and sustained BOLD responses to sustained visual stimulation. *Magn Reson Imaging* **26**(7):863–869.

Uludağ, K., Dubowitz, D.J., Yoder, E.J., Restom, K., Liu, T.T. & Buxton, R.B. (2004) Coupling of cerebral blood flow and oxygen consumption during physiological activation and deactivation measured with fMRI. *Neuroimage* **23**(1):148–155.

Uludağ, K., Müller-Bierl, B. & Uğurbil, K. (2009) An integrative model for neuronal activity-

induced signal changes for gradient and spin echo functional imaging. *Neuroimage* **48**(1):150–165.

Ungerleider, L.G., Doyon, J. & Karni, A. (2002) Imaging brain plasticity during motor skill learning. *Neurobiol Learn Mem* **78**(3):553–564.

Vafaee, M.S., Marrett, S., Meyer, E., Evans, A.C. & Gjedde, A. (1998) Increased oxygen consumption in human visual cortex: response to visual stimulation. *Acta Neurol. Scand.* **98**(2):85–89.

Vafaee, M.S., Meyer, E., Marrett, S., Paus, T., Evans, A.C. & Gjedde, A. (1999) Frequency-dependent changes in cerebral metabolic rate of oxygen during activation of human visual cortex. *J. Cereb. Blood Flow Metab.* **19**(3):272–277.

Vaughan, J.T., Garwood, M., Collins, C.M., Liu, W., DelaBarre, L., Adriany, G., Andersen, P., Merkle, H., Goebel, R., Smith, M.B. & Ugurbil, K. (2001) 7T vs. 4T: RF power, homogeneity, and signal-to-noise comparison in head images. *Magn Reson Med* **46**(1):24–30.

Wang, J., Aguirre, G.K., Kimberg, D.Y., Roc, A.C., Li, L. & Detre, J.A. (2003) Arterial spin labeling perfusion fMRI with very low task frequency. *Magn Reson Med* **49**(5):796–802.

Wang, J., Alsop, D.C., Li, L., Listerud, J., Gonzalez-At, J.B., Schnall, M.D. & Detre, J.A. (2002) Comparison of quantitative perfusion imaging using arterial spin labeling at 1.5 and 4.0 Tesla. *Magn Reson Med* **48**(2):242–254.

Wang, Y., Saykin, A.J., Pfeuffer, J., Lin, C., Mosier, K.M., Shen, L., Kim, S. & Hutchins, G.D. (2011) Regional reproducibility of pulsed arterial spin labeling perfusion imaging at 3T. *Neuroimage* **54**(2):1188–1195.

Williams, D.S., Grandis, D.J., Zhang, W. & Koretsky, A.P. (1993) Magnetic resonance imaging of perfusion in the isolated rat heart using spin inversion of arterial water. *Magn Reson Med* **30**(3):361–365.

Wise, R.G., Harris, A.D., Stone, A.J. & Murphy, K. (2013) Measurement of OEF and absolute CMRO2: MRI-based methods using interleaved and combined hypercapnia and hyperoxia. *Neuroimage* **83**:135–147.

Wise, R.G., Pattinson, K.T.S., Bulte, D.P., Chiarelli, P.A., Mayhew, S.D., Balanos, G.M., O'Connor, D.F., Pragnell, T.R., Robbins, P.A., Tracey, I. & Jezzard, P. (2007) Dynamic forcing of end-tidal carbon dioxide and oxygen applied to functional magnetic resonance imaging. *J. Cereb. Blood Flow Metab.* **27**(8):1521–1532.

Wong, E.C., Buxton, R.B. & Frank, L.R. (1998a) A theoretical and experimental comparison of continuous and pulsed arterial spin labeling techniques for quantitative perfusion imaging. *Magn Reson Med* **40**(3):348–355.

Wong, E.C., Buxton, R.B. & Frank, L.R. (1997) Implementation of quantitative perfusion imaging techniques for functional brain mapping using pulsed arterial spin labeling. *NMR Biomed* **10**(4-5):237–249.

Wong, E.C., Buxton, R.B. & Frank, L.R. (1998b) Quantitative imaging of perfusion using a single subtraction (QUIPSS and QUIPSS II). *Magn Reson Med* **39**(5):702–708.

Wu, B., Lou, X., Wu, X. & Ma, L. (2013) Intra- and interscanner reliability and reproducibility of 3D whole-brain pseudo-continuous arterial spin-labeling MR perfusion at 3T. *J Magn Reson Imaging* **39**(2):402-9.

Wu, C.W., Chuang, K.-H., Wai, Y.-Y., Wan, Y.-L., Chen, J.-H. & Liu, H.-L. (2008) Vascular space occupancy-dependent functional MRI by tissue suppression. *J Magn Reson Imaging* **28**(1):219–226.

Wu, W.-C., Buxton, R.B. & Wong, E.C. (2007) Vascular space occupancy weighted imaging with control of residual blood signal and higher contrast-to-noise ratio. *IEEE Trans Med Imaging* **26**(10):1319–1327.

Wu, W.-C., Fernández-Seara, M., Detre, J.A., Wehrli, F.W. & Wang, J. (2007) A theoretical and experimental investigation of the tagging efficiency of pseudocontinuous arterial spin labeling. *Magn Reson Med* **58**(5):1020–1027.

Wu, W.-C., Jain, V., Li, C., Giannetta, M., Hurt, H., Wehrli, F.W. & Wang, D.J.J. (2010) In vivo Venous Blood T1 Measurement using Inversion Recovery TrueFISP in Children and Adults. *Magn Reson Med* **64**(4):1140–1147.

Wu, W.-C., Jiang, S.-F., Yang, S.-C. & Lien, S.-H. (2011) Pseudocontinuous arterial spin labeling perfusion magnetic resonance imaging--a normative study of reproducibility in the human brain. *Neuroimage* **56**(3):1244–1250.

Xu, F., Ge, Y. & Lu, H. (2009) Noninvasive quantification of whole-brain cerebral metabolic rate of oxygen (CMRO2) by MRI. *Magn Reson Med* **62**(1):141–148.

Xu, F., Liu, P. & Lu, H. (2011) Effect of graded O2 challenge on vascular and metabolic parameters. In: Proc HBM Montreal.

Xu, F., Uh, J., Brier, M.R., Hart, J., Jr, Yezhuvath, U.S., Gu, H., Yang, Y. & Lu, H. (2011) The influence of carbon dioxide on brain activity and metabolism in conscious humans. *J. Cereb. Blood Flow Metab.* **31**(1):58–67.

Yablonskiy, D.A. & Haacke, E.M. (1994) Theory of NMR signal behavior in magnetically inhomogeneous tissues: the static dephasing regime. *Magn Reson Med* **32**(6):749–763.

Yacoub, E., Shmuel, A., Pfeuffer, J., Van De Moortele, P.F., Adriany, G., Andersen, P., Vaughan, J.T., Merkle, H., Ugurbil, K. & Hu, X. (2001) Imaging brain function in humans at 7 Tesla. *Magn Reson Med* **45**(4):588–594.

Yang, Y., Frank, J.A., Hou, L., Ye, F.Q., McLaughlin, A.C. & Duyn, J.H. (1998) Multislice imaging of quantitative cerebral perfusion with pulsed arterial spin labeling. *Magn Reson Med* **39**(5):825–832.

Yang, Y., Gu, H. & Stein, E.A. (2004) Simultaneous MRI acquisition of blood volume, blood flow, and blood oxygenation information during brain activation. *Magn Reson Med* **52**(6):1407–1417.

Yarowsky, P.J. & Ingvar, D.H. (1981) Symposium summary. Neuronal activity and energy metabolism. *Fed. Proc.* **40**(9):2353–2362.

Ye, F.Q., Mattay, V.S., Jezzard, P., Frank, J.A., Weinberger, D.R. & McLaughlin, A.C. (1997) Correction for vascular artifacts in cerebral blood flow values measured by using arterial spin

tagging techniques. *Magn Reson Med* **37**(2):226–235.

Zaharchuk, G., Busse, R.F., Rosenthal, G., Manley, G.T., Glenn, O.A. & Dillon, W.P. (2006) Noninvasive oxygen partial pressure measurement of human body fluids in vivo using magnetic resonance imaging. *Acad Radiol* **13**(8):1016–1024.

Zaharchuk, G., Martin, A.J., Rosenthal, G., Manley, G.T. & Dillon, W.P. (2005) Measurement of cerebrospinal fluid oxygen partial pressure in humans using MRI. *Magn Reson Med* **54**(1):113–121.

Zappe, A.C., Uludağ, K. & Logothetis, N.K. (2008) Direct measurement of oxygen extraction with fMRI using 6% CO2 inhalation. *Magn Reson Imaging* **26**(7):961–967.

Zappe, A.C., Uludağ, K., Oeltermann, A., Uğurbil, K. & Logothetis, N.K. (2008) The influence of moderate hypercapnia on neural activity in the anesthetized nonhuman primate. *Cereb. Cortex* **18**(11):2666–2673.

Zhang, X., Petersen, E.T., Ghariq, E., De Vis, J.B., Webb, A.G., Teeuwisse, W.M., Hendrikse, J. & van Osch, M.J.P. (2013) In vivo blood T1 measurements at 1.5 T, 3 T, and 7 T. **70**(4):1082–1086.

Zhao, M., Beauregard, D.A., Loizou, L., Davletov, B. & Brindle, K.M. (2001) Non-invasive detection of apoptosis using magnetic resonance imaging and a targeted contrast agent. *Nat. Med.* **7**(11):1241–1244.

# List of Figures

multiplecombinations and constant. These images are averages over 3min (=45 repetitions with). Longerleads to blood perfusion from larger vessels into the microvasculature (capillaries) and tissue space. For shortGM with large vessels is bright. For longer(eg) all GM voxels have similar contrast values. For very large,decay leads to minimal contrast of GM/WM (eg)..........................75

# List of Tables

# Acknowledgements

# Erklärung über die Anerkennung der Promotionsodnung und die eigenständige Abfassung der Arbeit

Hiermit erkläre ich, dass ich die vorliegende Arbeit selbständig und ohne unzulässige Hilfe oder Benutzung anderer als der angegebenen Hilfsmittel angefertigt habe. Ich versichere, dass Dritte von mir weder unmittelbar noch mittelbar geldwerte Leistungen für Arbeiten erhalten haben, die im Zusammenhang mit dem Inhalt der vorgelegten Dissertation stehen, und dass die vorgelegte Arbeit weder im Inland noch im Ausland in gleicher oder ähnlicher Form einer anderen Prüfungsbehörde zum Zweck einer Promotion oder eines anderen Prüfungsverfahrens vorgelegt wurde. Alles aus anderen Quellen und von anderen Personen übernommene Material, das in der Arbeit verwendet wurde oder auf das direkt Bezug genommen wird, wurde als solches kenntlich gemacht. Insbesondere wurden alle Personen genannt, die direkt an der Entstehung der vorliegenden Arbeit beteiligt waren.

Hiermit erkenne ich die Promotionsordnung der Fakultät für Physik und Geowissenschaften der Universität Leipzig vom 23. März 2010 an.

**29.10.2014**                                                    **Steffen von Smuda**

# Zusammenfassung der wissenschaftlichen Ergebnisse zur Dissertation

## Applicability of Quantitative Functional MRI Techniques for Studies of Brain Function at Ultra-High Magnetic Field

der Fakultät für Physik und Geowissenschaften der Universität Leipzig
eingereicht von

Dipl. Phys. Steffen Norbert von Smuda geb. Krieger

angefertigt am
Max-Plank Institut für Kognitions- und Neurowissenschaften
Abteilung Neurophysik
Oktober 2014

---

Magnetic resonance imaging (MRI) is the currently most widely used brain imaging technique and it can provide a wide variety of anatomical and physiological information. MRI is based on the physical phenomenon of nuclear magnetic resonance (NMR) which relies on the interaction of spin angular momentum of nuclei with external magnetic fields. Spin is an intrinsic characteristic of atomic nuclei. An external static magnetic field is used to generate two energy configurations. Transitions from one energy level to another are usually induced by external electromagnetic fields and for example relaxation effects, proton density, diffusion or perfusion are used to characterise the samples.

Functional MRI (fMRI) of the brain relies on the same physical basis as MRI but uses secondary, mostly haemodynamic effects that accompany cerebral neuronal activity (Buxton, 2010; Hyder et al., 2001). Compared to structural MRI, functional MRI offers increased temporal but usually reduced spatial resolution. Specifically designed functional tasks are used to modulate brain activity and induce haemodynamic changes. These changes can be detected via fMRI and therefore represent a surrogate marker of the neuronal response. The most common fMRI approach is the blood oxygenation level dependent (BOLD) contrast (Ogawa et al., 1990). The BOLD signal is generated by changes in the concentration of oxygenated blood, which is diamagnetic, and deoxygenated blood, which is paramagnetic. BOLD fMRI has several advantages: BOLD methods are readily available from most scanner manufacturers and field strengths. This technique is easy to use by non-expert scientists and BOLD fMRI has good sensitivity characteristics. Nevertheless, there are several important issues associated with BOLD fMRI: First, the BOLD signal originates from simultaneous changes in cerebral blood volume (CBV), cerebral blood flow (CBF) and cerebral metabolic rate of oxygen ($CMRO_2$). The complicated quantitative relationship between these parameters is not fully known yet, although there have been efforts to develop detailed biophysical models (Kim & Ogawa, 2012). Therefore, BOLD signal changes and results obtained via the BOLD technique have to be interpreted with caution (Hyder & Rothman, 2010). Furthermore, BOLD signal changes can occur at sites that are far away from the origin of neuronal activity changes (Turner, 2002). This is due to the fact that the BOLD signal relies on the oxy-deoxyhaemoglobin composition of blood which not only changes at the activation site but also downstream in the draining veins. Therefore, the spatial specificity of the BOLD contrast is limited.

Due to these drawbacks there have been efforts to develop alternative fMRI techniques that use a

single physiological parameter as marker of neuronal activity. Arterial spin labelling (ASL) MRI uses spin inversion to label blood water and therefore to generate an endogenous tracer of CBF (Detre et al., 1992). ASL therefore enables the quantification of changes in CBF. The vascular space occupancy (VASO) approach uses the same principle, but unlike ASL, VASO images are acquired at the time point when the blood signal is nulled (Lu et al., 2003). This concept allows the measurement of changes in total CBV. The main advantage of the ASL and VASO techniques compared to the BOLD contrast is improved spatial specificity since cerebral vascular changes in response to neural activation occur mainly in the capillary and arteriolar vessel compartments (Krieger et al., 2012). Furthermore, ASL and VASO provide physiologically and physically relevant measures which can be quantified and compared across scans, studies and subjects – a major advantage compared to the BOLD contrast.

ASL and VASO show better spatial specificity compared to BOLD fMRI but suffer from intrinsically low sensitivity. The application of ultra-high static magnetic fields can help to improve the signal-to-noise ratio (SNR) and therefore improve the sensitivity of such techniques. Increased SNR can be used to reduce voxel sizes or shorten the scanning time as less averaging is required. Another key advantage of ultra-high fields is the slower longitudinal signal decay allowing better microvascular weighting of ASL and VASO methods. However, beside these theoretical advantages of ultra-high field strengths there are several challenges that have to be overcome in order to actually improve the image quality obtained via fMRI. The decrease in transversal relaxation times require fast readout techniques that use intelligent readout acceleration approaches. Beside that, energy deposition in tissue is a major issue at ultra-high field. Increased static magnetic fields require RF pulses with higher frequency and therefore higher energy.

In this thesis a novel MRI technique is presented that enables the simultaneous acquisition of CBV (Huber et al., 2014), CBF and BOLD weighted MRI signals (Krieger, Huber, et al., 2014). This technique utilises the advantages and overcomes the challenges of ultra-high magnetic field. Simultaneous acquisition of multiple MRI parameters allows the combination of the spatial and temporal advantages of each technique without adding any scan time to the study. Whereas an earlier approach at 3 Tesla (Yang et al., 2004) already found a series of applications, the optimised technique introduced in this thesis may lead to a wider range of applications by utilising the advantages that ultra-high fields strength has to offer.

The spatial SNR ($SNR_{VASO}$=9.3±1.2, $SNR_{ASL}$=14.3±3.0) and temporal SNR ($tSNR_{VASO}$=12.0±1.4, $tSNR_{ASL}$=18.5±2.1) characteristics achieved with this novel approach were comparable to those
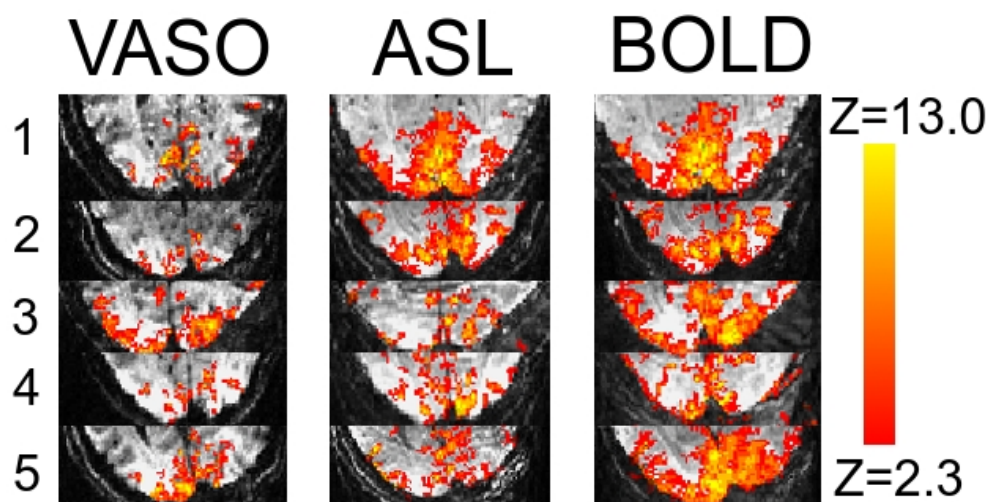


*Figure 1: Statistical maps of significant neuronal activation during a functional task based on VASO, ASL and BOLD weighted MRI signal changes obtained via the simultaneous acquisition scheme. While the BOLD contrast detects widespread activation patterns, VASO and ASL are more localised to the microvasculature.*

obtained in studies using the acquisition of each individual quantity at comparable field strengths and spatial resolutions. Also, CBV, CBF and BOLD activation patterns during a visual stimulus were as expected (Fig 1). CBV and CBF signal changes were found across visual grey matter only whereas BOLD signal changes occurred in a more wide-spread pattern. A time series analysis of CBV weighted fMRI signals showed a group average negative signal change of 3.2% during the visual stimulation which confirms increased blood vessel occupancy in the visual grey matter. CBF and BOLD weighted signal changes were 3.6% and 4.2%, respectively.

The technique introduced here is the first one that allows simultaneous acquisition of CBV, CBF and BOLD weighted fMRI signals in the human brain at 7 Tesla. Compared to lower field strengths simultaneous acquisition at ultra-high field allowed unprecedented small isotropic voxel sizes of 1.5mm and higher SNR for all quantities which could significantly improve the data quality. Simultaneous acquisition of the physically relevant measures of CBV and CBF will help to improve our understanding of the quantitative origins of the BOLD contrast in a time efficient manner.

The second focus of this thesis was on the quantitative measurement of changes in cerebral oxygen metabolism via calibrated fMRI at ultra-high field (Davis et al., 1998; Hoge et al., 1999). Changes in cerebral oxygen metabolism reflect the amount of thermodynamic work due to neural activity. $CMRO_2$ is therefore a significant physical measure in neuroscience (Herman et al., 2013). Calibrated fMRI relies on the simultaneous acquisition of BOLD and CBF weighted MRI signals during a gas-breathing challenge. A biophysical model (Gauthier & Hoge, 2013) with a set of assumptions is used to calculate the calibration parameter $M$ via equation 1

$$M = \frac{rBOLD_g}{1 - rCBF_g^{\alpha} \left( \frac{1 - Sv_{O_2}}{1 - Sv_{O_2|0}} \right)^{\beta}} \tag{1}$$

where $rBOLD_g$ and $rCBF_g$ represent the relative BOLD and CBF signal changes during gas inhalation, $SvO_2$ and $SvO_{2|0}$ are the measured venous oxygen saturation values during gas inhalation and rest periods. $\alpha$ and $\beta$ are assumed constants. In the following functional experiment changes in oxygen metabolism are determined via equation 2

$$CMRO_2 = \left( 1 - \frac{rBOLD_t}{M} \right)^{\frac{1}{\beta}} rCBF_t^{1 - \frac{\alpha}{\beta}} \tag{2}$$

where $rBOLD_t$ and $rCBF_t$ represent the relative BOLD and CBF signal changes during the functional task.

Using oxygen metabolism as a marker of neuronal activity can provide a measure that is temporally, spatially and physiologically closer to neuronal activation than the BOLD contrast (Kida et al., 2000). However, due to the greater complexity with regards to MRI hardware setup, acquisition time and data analysis calibrated fMRI has not yet been frequently used, especially not at ultra-high magnetic fields and combined with low-contrast tasks such as typically used in cognitive and psychological studies.

In this thesis a calibrated fMRI technique optimised for use at ultra-high field is presented. An adiabatic RF inversion pulse specifically designed for ultra-high field was implemented (Hurley et al., 2010). This RF pulse uses a time resampling function in order to modulate the RF amplitude, frequency and the magnetic gradient in an efficient manner. The RF inversion efficiency could be increased and the inversion profile improved while keeping the transmitted RF power low compared to other RF inversion pulses. Additionally, MR acquisition parameters were adjusted to the use at ultra-high field and the gas mixtures applied in the calibration experiments in order to achieve optimal signal and contrast.

Reproducibility of the calibrated fMRI technique introduced was assessed at ultra-high magnetic

field and compared to various fMRI contrasts such as ASL and BOLD (Krieger, Gauthier, et al., 2014). Furthermore the modelling based calibration method (see equations 1 and 2) was compared to a novel direct calibration approach (Krieger, Ivanov, et al., 2014). A low-contrast functional task was used to test its applicability for neuroscientific studies.

Calibrated fMRI modelling can suffer from drawbacks such as the reliance on assumed parameters whose values have not been fully validated or the fact that modelling of the calibration constant is vulnerable to errors in CBF signal quantification. The direct estimation approach does not suffer from these sources of errors since it relies on complete venous oxygen saturation during the calibration scan (Gauthier et al., 2011). This leads to less noise in the calibration maps as can be seen in Fig 2.
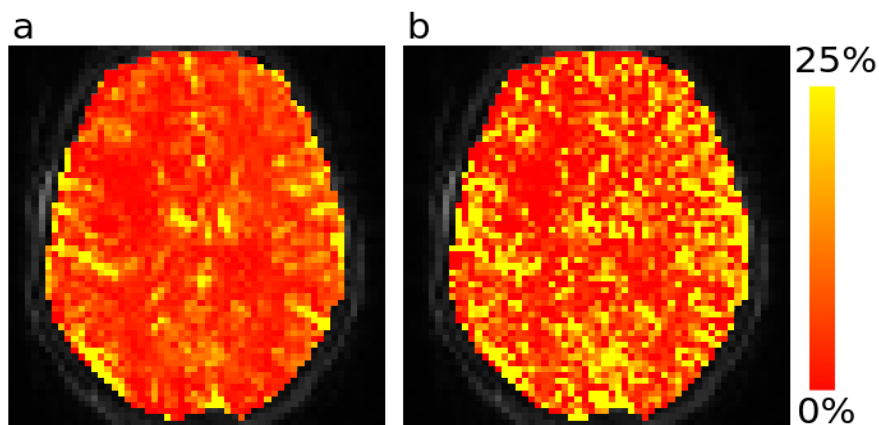


*Figure 2: Single subject voxel-based maps of the calibration parameter M in % BOLD signal change obtained via the direct calibration method (a) and the modelling based calibration (b). While the direct estimation technique shows improved SNR compared to modelling, the gas mixtures used in this study were not sufficient to fully oxygenate the venous vessel compartments.*

However, our data suggest that commonly applied gas-mixtures cannot achieve complete saturation since modelling consistently led to higher calibration constants than the direct method in the visual cortex ($M_{direct}$=7.5±2.2%, $M_{modelled}$=10.4±3.9%) as well as in the motor cortex ($M_{direct}$=8.1±2.6%, $M_{modelled}$=11.3±5.2%). Furthermore, the venous saturation values which were estimated during modelling were 91.1±3.3% in the visual cortex and 91.1±4.5% in the motor cortex and therefore our data suggest that modelling provides the more accurate calibration values. In this context a model was presented that allows the estimation of error in $CMRO_2$ based on an erroneous calibration constant $M$. The results shown in Fig 3 are valid for a 7 Tesla system and indicate the significance of the correct estimation of $M$. Since our results furthermore indicate that $M$ differs across brain regions and subjects it is crucial to calibrate each single scan rather than assuming calibration parameters.

In order to assess the applicability of the modelling approach of calibrated fMRI, its reproducibility was studied across multiple brain regions and compared to that of various physiologically relevant parameters. Coefficients of variation (CV) were calculated within subjects within days ($CV_1$), within subjects across days ($CV_2$) and across subjects and days ($CV_3$). The group averaged CVs (see Fig 4) suggest that $CMRO_2$ has the best intra-subject reproducibility. These results confirm those obtained by earlier studies performed at lower field strengths and high-contrast tasks (Leontiev & Buxton, 2007). The results presented here therefore provide evidence that calibrated fMRI is a viable alternative to the classic BOLD contrast with regards to spatial specificity as well as functional reproducibility. Our studies might help researchers and clinicians to predict the benefit that their studies can have from using calibrated fMRI. Furthermore, this thesis provides a detailed description about the technical details of how the studies were conducted which might help

scientists to set up future calibrated fMRI experiments.
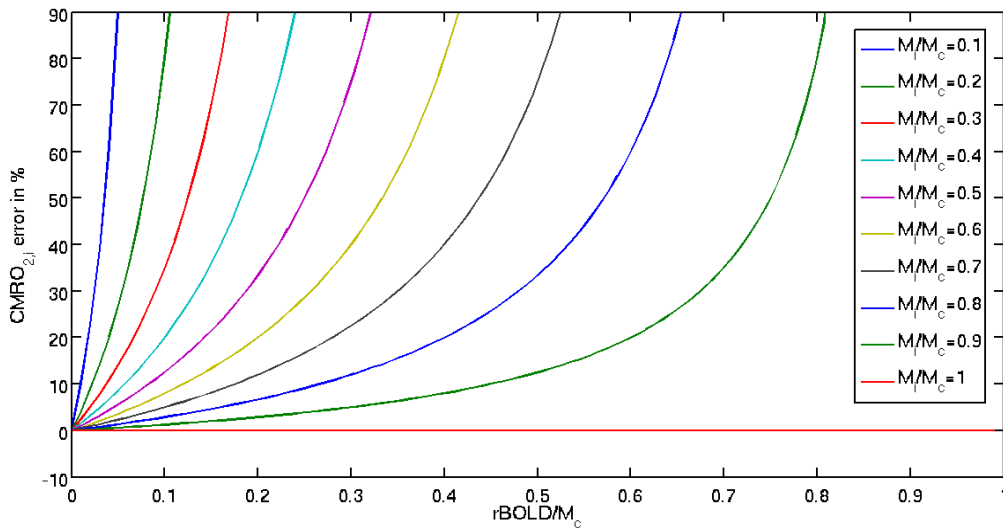
# CMRO$_2$ error propagation



*Figure 3: The effect of errors in the calibration procedure on calculated CMRO$_2$ estimates. A fixed ratio of correctly estimated calibration parameter (M$_c$) and erroneous calibration parameter (M$_i$) is used. Relative BOLD signal changes during task performance (rBOLD) are expressed relative to M$_c$. Errors in estimated CMRO$_2$ increase with larger rBOLD. A linear increase in the M estimation error results in exponential increases in error in CMRO$_2$.*



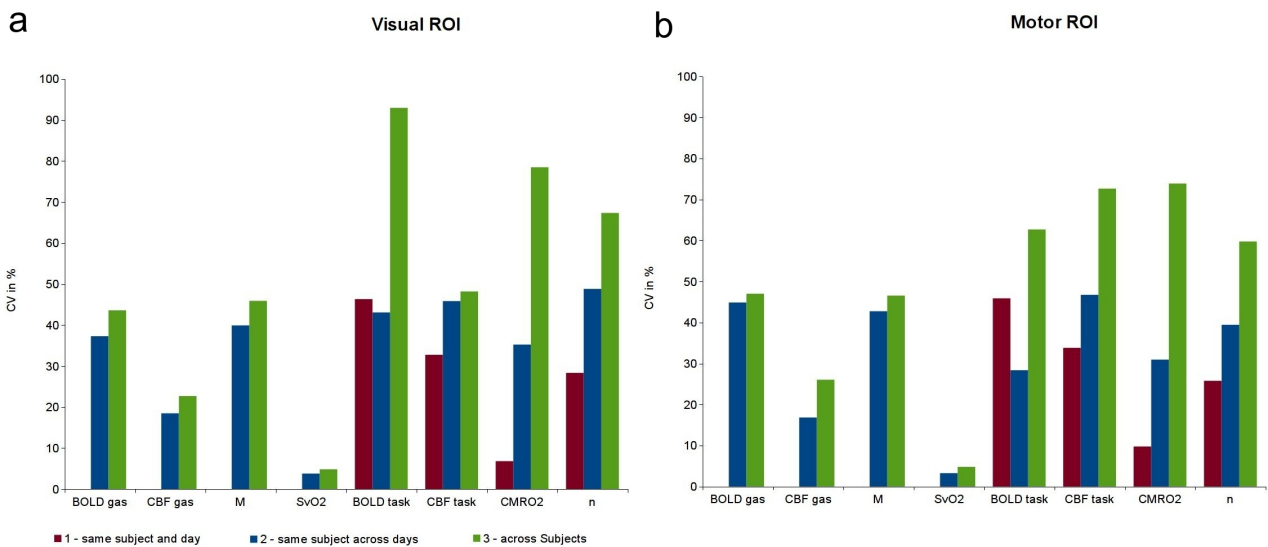*Figure 4: Group averaged coefficients of variation for the visual cortex (a) and the motor cortex (b).Within-day (1) and across-days (2) intra-subject coefficients of variation were the smallest for calibrated fMRI based estimates of CMRO$_2$.*

This thesis presents the development, optimisation, application and assessment of several quantitative fMRI techniques at ultra-high magnetic field. All techniques presented in this thesis utilise physically relevant physiological parameters in order to detect neural activity. The

simultaneous acquisition technique can provide a time efficient way of performing multimodal imaging studies with high SNR and high spatial resolution without additional scanning time requirements. CBV and CBF can be used to quantitatively estimate neural activity. Additional BOLD signal changes provide classic fMRI results that most researchers are used to. Calibrated fMRI at ultra-high field was found to be a reproducible technique which can be reliably applied to studies that rely on low-contrast tasks such as common in neuroscience. As $CMRO_2$ is believed to be spatially closer to neural activity than many other fMRI measures it might be the future technique with broad applications in neuroscience (Krieger & Egan, 2013; Hyder et al., 2010).

**References**

Buxton, R.B. (2010) Interpreting oxygenation-based neuroimaging signals: the importance and the challenge of understanding brain oxygen metabolism. *Front Neuroenergetics* **2**:8.

Davis, T.L., Kwong, K.K., Weisskoff, R.M. & Rosen, B.R. (1998) Calibrated functional MRI: mapping the dynamics of oxidative metabolism. *Proc. Natl. Acad. Sci. U.S.A.* **95**(4):1834–1839.

Detre, J.A., Leigh, J.S., Williams, D.S. & Koretsky, A.P. (1992) Perfusion imaging. *Magn Reson Med* **23**(1):37–45.

Gauthier, C.J. & Hoge, R.D. (2013) A generalized procedure for calibrated MRI incorporating hyperoxia and hypercapnia. *Hum Brain Mapp* **34**(5):1053–1069.

Gauthier, C.J., Madjar, C., Tancredi, F.B., Stefanovic, B. & Hoge, R.D. (2011) Elimination of visually evoked BOLD responses during carbogen inhalation: implications for calibrated MRI. *Neuroimage* **54**(2):1001–1011.

Herman, P., Sanganahalli, B.G., Blumenfeld, H., Rothman, D.L. & Hyder, F. (2013) Quantitative basis for neuroimaging of cortical laminae with calibrated functional MRI. *Proc. Natl. Acad. Sci. U.S.A.* **110**(37):15115–15120.

Hoge, R.D., Atkinson, J., Gill, B., Crelier, G.R., Marrett, S. & Pike, G.B. (1999) Investigation of BOLD signal dependence on cerebral blood flow and oxygen consumption: the deoxyhemoglobin dilution model. *Magn Reson Med* **42**(5):849–863.

Huber, L., Ivanov, D., Krieger, S.N., Streicher, M.N., Mildner, T., Poser, B.A., Möller, H.E. & Turner, R. (2014) Slab-selective, BOLD-corrected VASO at 7 Tesla provides measures of cerebral blood volume reactivity with high signal-to-noise ratio. *Magn Reson Med* **72**(1):137–148.

Hurley, A.C., Al-Radaideh, A., Bai, L., Aickelin, U., Coxon, R., Glover, P. & Gowland, P.A. (2010) Tailored RF pulse for magnetization inversion at ultrahigh field. *Magn Reson Med* **63**(1):51–58.

Hyder, F., Kida, I., Behar, K.L., Kennan, R.P., Maciejewski, P.K. & Rothman, D.L. (2001) Quantitative functional imaging of the brain: towards mapping neuronal activity by BOLD fMRI. *NMR Biomed* **14**(7-8):413–431.

Hyder, F. & Rothman, D.L. (2010) Neuronal correlate of BOLD signal fluctuations at rest: err on the side of the baseline. *Proc. Natl. Acad. Sci. U.S.A.* **107**(24):10773–10774.

Hyder, F., Sanganahalli, B.G., Herman, P., Coman, D., Maandag, N.J.G., Behar, K.L., Blumenfeld, H. & Rothman, D.L. (2010) Neurovascular and Neurometabolic Couplings in Dynamic Calibrated fMRI: Transient Oxidative Neuroenergetics for Block-Design and Event-Related Paradigms. *Front Neuroenergetics* **2**.

Kida, I., Kennan, R.P., Rothman, D.L., Behar, K.L. & Hyder, F. (2000) High-resolution CMR(O2) mapping in rat cortex: a multiparametric approach to calibration of BOLD image contrast at 7 Tesla. *J. Cereb. Blood Flow Metab.* **20**(5):847–860.

Kim, S.-G. & Ogawa, S. (2012) Biophysical and physiological origins of blood oxygenation level-dependent fMRI signals. *J. Cereb. Blood Flow Metab.* **32**(7):1188–1206.

Krieger, S.N. & Egan, G.F. (2013) Let the vessels rest. *Sleep* **36**(10):1415–1416.

Krieger, S.N., Gauthier, C.J., Ivanov, D., Huber, L., Roggenhofer, E., Sehm, B., Turner, R. & Egan, G.F. (2014) Regional reproducibility of calibrated BOLD functional MRI: Implications for the study of cognition and plasticity. *Neuroimage* **101**:8–20.

Krieger, S.N., Huber, L., Poser, B.A., Turner, R. & Egan, G.F. (2014) Simultaneous acquisition of cerebral blood volume-, blood flow-, and blood oxygenation-weighted MRI signals at ultra-high magnetic field. *Magn Reson Med*.

Krieger, S.N., Ivanov, D., Huber, L., Roggenhofer, E., Sehm, B., Turner, R., Egan, G.F. & Gauthier, C.J. (2014) Using carbogen for calibrated fMRI at 7Tesla: comparison of direct and modelled estimation of the M parameter. *Neuroimage* **84**:605–614.

Krieger, S.N., Streicher, M.N., Trampel, R. & Turner, R. (2012) Cerebral blood volume changes during brain activation. *J. Cereb. Blood Flow Metab.* **32**(8):1618–1631.

Leontiev, O. & Buxton, R.B. (2007) Reproducibility of BOLD, perfusion, and CMRO2 measurements with calibrated-BOLD fMRI. *Neuroimage* **35**(1):175–184.

Lu, H., Golay, X., Pekar, J.J. & Van Zijl, P.C.M. (2003) Functional magnetic resonance imaging based on changes in vascular space occupancy. *Magn Reson Med* **50**(2):263–274.

Ogawa, S., Lee, T.M., Kay, A.R. & Tank, D.W. (1990) Brain magnetic resonance imaging with contrast dependent on blood oxygenation. *Proc. Natl. Acad. Sci. U.S.A.* **87**(24):9868–9872.

Turner, R. (2002) How much cortex can a vein drain? Downstream dilution of activation-related cerebral blood oxygenation changes. *Neuroimage* **16**(4):1062–1067.

Yang, Y., Gu, H. & Stein, E.A. (2004) Simultaneous MRI acquisition of blood volume, blood flow, and blood oxygenation information during brain activation. *Magn Reson Med* **52**(6):1407–1417.